Dunne-film microlasers voor de integratie van elektronische en fotonische geïntegreerde circuits

Thin-Film Microlasers for the Integration of Electronic and Photonic Integrated Circuits

Joris Van Campenhout

Promotoren: prof. dr. ir. D. Van Thourhout, prof. dr. ir. R. Baets
Proefschrift ingediend tot het behalen van de graad van
Doctor in de Ingenieurswetenschappen: Elektrotechniek

Vakgroep Informatietechnologie
Voorzitter: prof. dr. ir. P. Lagasse
Faculteit Ingenieurswetenschappen
Academiejaar 2007 - 2008

UNIVERSITEIT
GENT

ISBN 978-90-8578-180-6
NUR 959
Wettelijk depot: D/2007/10.500/54

Promotoren:

Prof. dr. ir. D. Van Thourhout	Universiteit Gent, INTEC
Prof. dr. ir. R. Baets	Universiteit Gent, INTEC

Examencommissie:

Prof. dr. ir. D. De Zutter, voorzitter	Universiteit Gent, INTEC
Prof. dr. ir. D. Van Thourhout, promotor	Universiteit Gent, INTEC
Prof. dr. ir. R. Baets, promotor	Universiteit Gent, INTEC
Prof. dr. ir. G. Morthier, secretaris	Universiteit Gent, INTEC
Dr. ir. C. Seassal	Ecole Centrale de Lyon, INL
Prof. dr. ir. M. Smit	TU Eindhoven, OED
Prof. dr. ir. K. Neyts	Universiteit Gent, ELIS

Universiteit Gent
Faculteit Ingenieurswetenschappen

Vakgroep Informatietechnologie (INTEC)
Sint-Pietersnieuwstraat 41
9000 Gent
België

Tel.: +32-9-2643319
Fax: +32-9-2643593

Dit werk kwam tot stand in het kader van een specialisatiebeurs toegekend door het FWO-Vlaanderen (Fonds voor Wetenschappelijk Onderzoek Vlaanderen)
Part of this work was carried out in the framework of the European IST-PICMOS project.

Dankwoord

Vrijheid. Freedom. Voor Amerikanen lijkt het wel het hoogste goed. De vrijheid om als hardwerkende immigrant je leven uit te bouwen in The Land of Opportunity, ongeacht je afkomst, is één van de hoekstenen van de Amerikaanse samenleving. Momenteel wordt er op Ground Zero in New York City gebouwd aan de Freedom Tower, die deze kerngedachte nog eens moet herbevestigen. In hoeverre dit ideaal in de praktijk wordt ervaren door de miljoenen immigranten in de VS is natuurlijk een andere zaak. Hier in New York lijkt er alvast Opportunity genoeg. Maar waar eindigt vrijheid en begint luxe? Voor sommige Amerikanen lijkt vrijheid de mogelijkheid om met een nieuwe SUV naar de fitnesszaal om de hoek te kunnen rijden. De lijn tussen vrijheid en platte commercie lijkt hier soms wel eens bijzonder wazig.

Als doctoraatstudent ben je als het ware een immigrant in de wereld van het wetenschappelijk onderzoek. Je gaat op verkenning op een stukje relatief onontgonnen terrein, met tal van wenkende opportuniteiten. Daarbij dien je je een heel aantal nieuwe gewoontes en vaardigheden eigen te maken. Zelf heb ik daarbij gedurende vijf jaar van een uitgebreide vrijheid en luxe mogen genieten. Eerst en vooral de vrijheid om in die vijf jaar economisch totaal onproductief bezig te zijn. Maar wees gerust, ik heb er mijn slaap niet voor gelaten. De vrijheid om mijn werkschema en timing bijna volledig zelf te bepalen. De luxe om ondertussen ook nog enkele leuke plekjes op deze planeet te mogen verkennen. De relevante conferenties voor mijn doctoraatsonderzoek vonden toevallig altijd plaats op interessante bestemmingen. Wie zoekt die vindt was hierbij misschien wel al eens een verklarende factor.

Je merkt het al, ik heb vijf jaar lang kunnen werken in een stimulerende omgeving. Daarom wil ik prof. Roel Baets bedanken om een werkomgeving te creëren die qua infrastructuur en ondersteuning de mogelijkheid biedt om relevant wetenschappelijk werk uit te voeren, en de opmerkelijke vrijheid die elk individu in de onderzoeksgroep daarbij mag ervaren. Mijn promotoren prof. Dries Van Thourhout en prof. Roel Baets wil ik ook bedanken voor de nuttige prikkels en kritiek die ze al die jaren leverden, zonder dewelke ik ergens onderweg het noorden was kwijtgeraakt. Ik wil ook Steven bedanken voor het vele werk bij de fabricage van mijn componenten - quote Steven: ”tot ik er scheel van zie”. In dit werk hebben we de limiet van ons fabricageproces afgetast, waarbij jouw ervaring en vaardigheden een grote impact hadden op het mooie eindresultaat. Ik wil ook Liesbet en Jonathan bedanken voor het vele FIB/SEM werk. *Je veux aussi remercier dr. Christian Seassal et dr. Pedro Rojo Romeo de INL, pour la collaboration intense et exceptionelle.*

Maar wat echt telt zijn natuurlijk de collega's waarmee je elke dag doorbrengt. Ik moet zeggen dat ik het daarbij wel goed getroffen heb, eerst met Pieter en Gino op onze bureau in de 39. We hebben daar enkele surrealisitsche situaties meegemaakt. Nooit zal ik nog vergeten hoe luid een duivenjong kan schreeuwen. Later kwam daar nog Doos en Gunther bij in het Technicum. Als zij al geen vrienden waren voor dat ik aan mijn doctoraat begon, dan zijn ze het zeker geworden. Het was een eer samen met jullie allen te spelen, op het zinkend schip genaamd *TDC United*. Of moet dat zijn: zinkend vlot? Het moet gezegd: er lopen bij de photonics-groep op INTEC een heel pak fijne mensen rond, die samen een diverse bende vormt waarin het erg aangenaam is om te werken, en om koffie te drinken. Houden zo!

Een andere luxesituatie waarin ik de voorbije jaren ben terechtgekomen gaat genaamd onder de gevleugelde woorden *Freddy en de Freggels*. Dit sociaal gebeuren gaat gepaard met een hele hoop minivoetbalwedstrijden, maar vooral met veel plezier naast de lijnen, met alleen maar plezante, mooie mensen, die ik mijn vrienden mag noemen: Stinis, Greg, Tibi, Sven, Johan, Nico, Roel, Staf, Freddy, Frits, Ludwig, Luce, Kristoff, Shu-Xin, Wendy en alle al even sympathieke sympathisanten. Dit vriendenclubje is er één om te koesteren!

Maar wie het meest heeft geleden onder mijn vijfjarige queeste zijn ongetwijfeld mijn ouders en zussen. Moeke en vake, jullie voortdurende steun op alle mogelijke gebied hield mijn motor draaiende. De opvoeding die ik van jullie gekregen heb is een enorme troef in mijn leven. Johanna en Karen, 't betekent veel voor mij om te weten dat jullie altijd klaar staan om me te helpen wanneer nodig. Bedankt daarvoor!

Joris Van Campenhout
Astoria, NY, 5 November 2007

Samenvatting

Elektronisch-fotonische integratie

De rekenkracht van elektronische geïntegreerde circuits – vervaardigd met complementaire metaal-oxide technologie (CMOS) – kende de voorbije tientallen jaren een enorme vlucht. Een impressionante verbetering van de silicium nanofabricagetechnologie heeft tot een voortdurende toename geleid van de transistordensiteit en -snelheid. Er wordt verwacht dat deze evolutie – zoals voorspeld door de Wet van Moore – zich in de toekomst zal voortzetten. Hoewel steeds meer berekeningen kunnen uitgevoerd worden per eenheid van oppervlakte en tijd, kunnen de elektrische verbindingen (EI) in moderne systemen de toegenomen datastroom nog nauwelijks aan. Aangezien de bandbreedte van een elektrische verbinding fysisch bepaald wordt door haar doorsnede-lengteverhouding, treedt deze interconnectieflessenhals het eerst op voor de langste verbindingen in een systeem.

De bandbreedte van optische verbindingen (OI) wordt echter niet gelimiteerd door hun doorsnede-lengteverhouding. Hierdoor hebben optische-vezelverbindingen sinds de late jaren zeventig geleidelijk de elektrische verbindingen verdrongen voor communicatielinks die hoge bandbreedte-afstandproducten vereisen, zoals overzeese lange-afstandsverbindingen. Historisch gezien vond deze transitie plaats wanneer 10 Mb/s×km capaciteit vereist werd.

Communicatiesystemen gebaseerd op optische-vezeltechnologie vereisen verscheidene optische componenten voor lichtemissie, -detectie, -modulatie en routering. Zoals in de microelektronica is er een sterke tendens om zoveel mogelijk optische functies te integreren op één enkele chip, die dan een fotonisch geïntegreerd circuit (PIC) genoemd wordt. Men verwacht dat deze integratie tot een kostenreductie en verhoogde prestatie leidt. Bovendien kan men door verschillende componenten op één chip te integreren, de problematiek van het aligneren van vezel en component sterk reduceren.

Naarmate processors sneller worden, verkleint de afstand waarbij de EI-OI drempelwaarde optreedt. Voor toekomstige, hoogpresterende processors met meerdere kernen wordt verwacht dat deze afstand kleiner zal worden dan de afmetingen van de chip zelf. Daarom is er een groeiende wetenschappelijke interesse om optische netwerken te ontwikkelen die een hoge bandbreedte voor intra-chipcommunicatie zouden kunnen leveren.

Een veelbelovend platform waarop zulke integratie zou kunnen verwezenlijkt worden is silicium-op-isolator (SOI). Het hoge brekingsindexcontrast van dit mate-

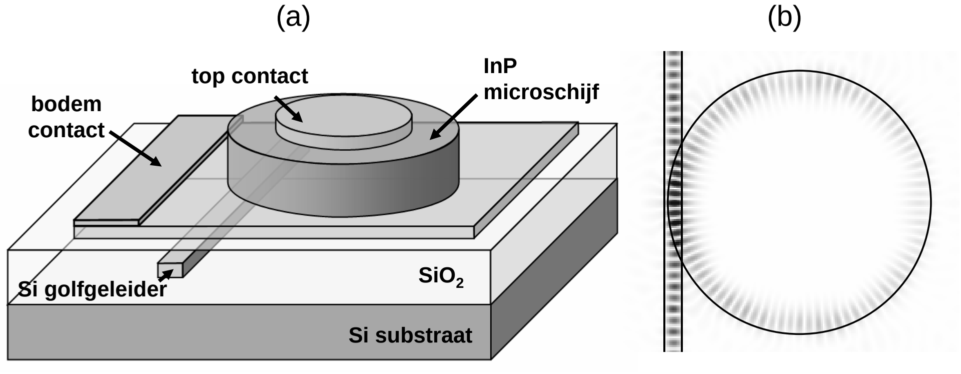

Figuur 1: (a) Schematische weergave van een SOI-geïntegreerde microschijflaser. (b) Fluistergallerijmode in de InP microschijf, gekoppeld met de SOI golfgeleider.

riaalsysteem maakt een hoge optische integratiedensiteit mogelijk. Bovendien kan CMOS-fabricagetechnologie gebruikt worden, wat tot een enorme kostenbesparing leidt. Ultra-compacte componenten met uitstekende passieve optische prestaties werden reeds gedemonstreerd. Een groot nadeel echter is dat lichtgeneratie en lichtversterking erg inefficiënt verloopt, vanwege de indirecte bandkloof van silicium.

Recentelijk zijn er enkele bemoedigende resultaten gerapporteerd betreffende relatief efficiënte lichtgeneratie in silicium. Een elektrisch-gedreven, efficiënte silicium lichtbron is echter nog niet voor morgen. Daarom zijn wij ervan overtuigd dat er, op de korte tot middellange termijn, halfgeleiders met een directe bandkloof – zoals InP – zullen moeten geïntegreerd worden teneinde efficiënte lichtgeneratie mogelijk te maken op de chip.

Heterogene integratie van InP op SOI door middel van een (moleculaire) aanhechtingstechniek is een veelbelovende aanpak om een dun laagje InP van hoge kwaliteit aan te brengen op het SOI-substraat. Vrijwel elke optische functie – bij telecomgolflengten – kan in principe geïmplementeerd worden op een heterogeen InP-SOI golfgeleiderplatform. Om die reden zouden InP-SOI PICs een kosteffectieve bouwsteen kunnen worden voor optische verbindingen op verscheidene systeemniveaus. Deze integratieroute heeft ook potentieel om de verwachte interconnectieproblematiek op de chip aan te pakken. Echter, op dit ogenblik dienen vrijwel alle vereiste optische geïntegreerde componenten nog ontwikkeld te worden.

Dit werk: geïntegreerde microlasers

Het doel van dit werk was de ontwikkeling van een ultra-compacte, elektrisch-aangedreven microlaser, gefabriceerd in een dunne InP film bovenop en gekoppeld met een SOI draadgolfgeleider. Zulk een microlaser is een sleutelcomponent voor elektronisch-fotonische integratie met hoge densiteit.

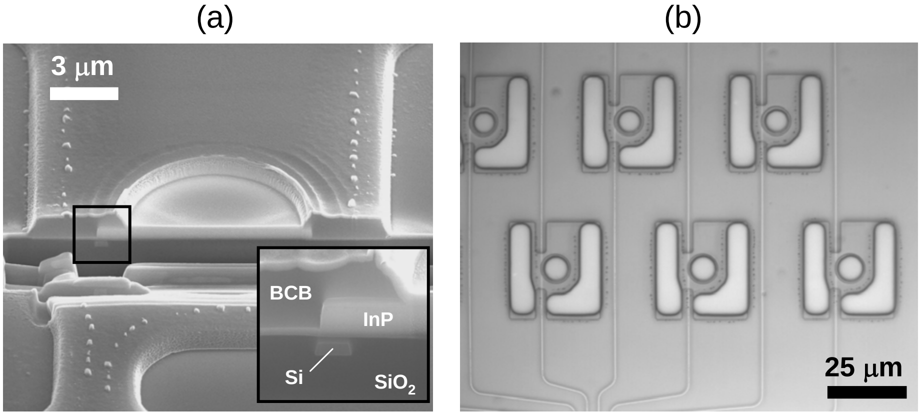

Figuur 2: (a) Dwarsdoorsnede gemaakt met FIB, en (b) bovenaanzicht van een microschijflaser, vóór metaaldepositie.

Bij het ontwerp van een elektrisch-gedreven microcaviteitslaser in een dunne film treden twee uitdagingen op. Ten eerste dienen de parasitaire optische verliezen zo laag mogelijk gehouden te worden, aangezien zij in direct verband staan met de drempelstroom en laserefficiëntie. Ten tweede dient de efficiëntie van de stroominjectie voldoend hoog te zijn, en dit voor voldoend lage spanning. Efficiënte stroominjectie vereist typisch het aanbrengen van zwaar gedopeerde contacteer- en metaallagen, die licht sterk absorberen. Daarom dient er een afweging gemaakt te worden tussen optische verliezen in de caviteit en de efficiëntie van de stroominjectie.

Tunneljunctie-gebaseerde microschijflasers

In een onderlinge vergelijking van meerdere geëvalueerde ontwerpen, werd het beste compromis tussen optisch verlies, injectie-efficiëntie, compactheid en gemak van fabricage gevonden voor een ontwerp gebaseerd op een microschijflasers met een injectie doorheen een tunneljunctie. De tunneljunctie (TJ) maakt het mogelijk om twee n-type InP ohmse contacten te gebruiken, die relatief gemakkelijk gerealiseerd kunnen worden zonder dat hiervoor sterk absorberende contacteerlagen nodig zijn. De microschijfresonator ondersteunt optische resonanties van het fluistergallerijtype, die een erg laag stralingsverlies vertonen, ook voor erg compacte caviteiten ($5\,\mu$m in doormeter). Bovendien propageren deze resonante modes aan de rand van de schijf en laten zo de mogelijk open om een metaalcontact aan te brengen in het centrum van de schijf, zonder extra absorptieverlies te veroorzaken (zie fig. 1). Het laserlicht kan via de uitdovende rand van de mode (evanescent) koppelen met de onderliggende SOI-golfgeleider. Een rigoureuze numerieke analyze werd uitgevoerd om de ultieme prestatie van dit type laser in te schatten. We vonden dat een geschikt ontworpen microschijflaser met tunneljunctie dezelfde – golfgeleider-

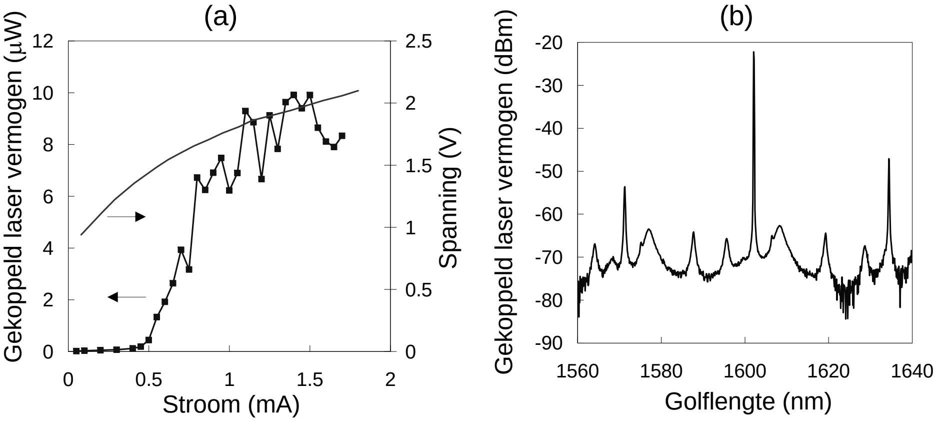

Figuur 3: (a) Gemeten SOI-gekoppeld uitgangsvermogen en spanning als functie van de stroom, voor een microschijflaser met een diameter van 7.5 μm, onder continue aansturing. (b) Laserspectrum voor 1.4 mA stroom.

gekoppelde – efficiëntie kan bereiken als conventionele InP-gebaseerde laserdiodes ($\sim 0.2 - 0.3$ W/A), echter met een sterk verlaagde drempelstroom ($\sim 100\,\mu$A).

Experimentele resultaten

In het kader van het Europees onderzoeksprogramma IST-PICMOS hebben onze projectpartners verbonden aan CEA-LETI een moleculair plak-op-plak en chip-op-plak aanhechtingstechologie ontwikkeld. Deze technologie werd gebruikt om microschijflasers te fabriceren, in combinatie met een reeks InP processen op de schaal van de volledige plak en de individuele chip. In principe kunnen alle fabricagestappen echter op volledige plakken uitgevoerd worden, wat een hoge fabricagecapaciteit garandeert. Enkele beelden van de microschijflasers tijdens het fabricageproces worden getoond in fig. 2.

In een eerste fabricagecyclus werden microschijflasers geïntegreerd op een naakte siliciumplak. Elektrisch-gedreven laserwerking bij kamertemperatuur werd vastgesteld voor meerdere structuren, met schijfdiameters tussen $6-9\,\mu$m. Laserwerking was enkel mogelijk in gepulst regime, vanwege een erg hoge elektrische weerstand in combinatie met een slechte warmteafvoer, wat resulteerde in een sterke zelfopwarming. Deze zelfopwarming hebben we experimenteel in kaart gebracht, en was in goede overeenstemming met thermische simulaties. De hoge elektrische weerstand werd toegeschreven aan een onvoldoend hoge dopering van de tunneljunctie. Niettemin was dit wereldwijd de eerste demonstratie van een elektrisch-gedreven microlaser, geïntegreerd op silicium.

Een tweede fabricagecyclus betrof de integratie van de microschijflasers op een SOI golfgeleiderplatform. Deze lasers vertoonden een lagere elektrische weerstand, als gevolg van de optimalisering van de TJ doperingniveaus tijdens epitaxiale groei (uitgevoerd door onze projectpartners verbonden aan het INL). De werkingsspanning varieerde tussen 1.5-3 V. Verscheidene structuren vertoonden elektrisch-gedreven laserwerking, met een substantiële lichtkoppeling naar de SOI golfgeleider. De drempelstroom was sterk gecorreleerd met de grootte en positie van het topcontact. De beste lasers vertoonden drempelstromen rond 500 μA (voor een schijfdiameter van 7.5 μm). Deze lasers werkten ook onder continue aansturing bij kamertemperatuur, met lichtopbrengsten tot 20 μW/mA gekoppeld in de SOI golfgeleider, per propagatierichting, zoals geïllustreerd in fig. 3. Dit was de eerste demonstratie van een SOI-gekoppelde elektrisch-gedreven microlaser onder continue aansturing bij kamertemperatuur. De statische laserkarakteristiek was bovendien in overeenstemming met het ontwikkelde microschijflasermodel, waarbij realistische parameterwaarden werden gebruikt.

De gemeten efficiëntie en aangetoonde opbrengst van het fabricageproces volstaan nog lang niet voor de meeste praktische toepassingen. Echter, de berekeningen tonen aan dat sterke prestatieverbetering mogelijk is door de structurele parameters van de microschijflaser te optimalizeren, en door een optimalisatie van het etsproces teneinde de oppervlakruwheid te verminderen. Om te besluiten kunnen we stellen dat dit werk de bruikbaarheid van heterogene InP-SOI integratie heeft aangetoond voor de implementatie van geïntegreerde, ultra-compacte, elektrisch-gedreven microlasers op een siliciumchip.

English Text

Summary

Electronic-photonic integration

The computation power of electronic integrated circuits – fabricated with complementary metal-oxide technology (CMOS) – has increased enormously over the past decades. Impressive progress in silicon nanofabrication technology has and will result in an ever increasing transistor density and speed, following Moore's Law. While more calculations can be performed in a given space and time, the electrical interconnects (EI) inside the systems cannot keep up with the increased data flow. Since the bandwidth of an EI is physically limited by its aspect ratio, this interconnect bottleneck arises first for the longest links in a computational system.

Optical interconnects (OI) don't suffer from such an aspect-ratio bandwidth limitation. As a result, since the late 1970s, fibre-optic communication has gradually being replacing electrical interconnections for links that require high bandwidth-distance products, such as long-haul interconnect, due to their immense power and bandwidth advantages. Historically, the transition from EI to OI has been at the $10\,\mathrm{Mb/s}\times\mathrm{km}$ threshold.

Fibre-optic communication systems require many optical functions, such as light emission, detection, modulation and routing. As is the case for electronics, there is a strong drive to integrate as many optical functionality as possible on a single chip, also known as a photonic integrated circuit (PIC). This integration is expected to result in cost reduction and increased performance. Furthermore, by putting many optical components on a chip, the need for time-consuming and expensive optical alignment between discrete components can be strongly reduced.

As processors get faster, the EI-to-OI transition threshold occurs at increasingly shorter link distances. For future high-performance multi-core processors, this distance is expected to become shorter than the chip's dimensions. Therefore, there is increased scientific interest to develop on-chip optical networks that could provide high-bandwidth on-chip optical communication.

An emerging material platform to implement these PICs is silicon-on-insulator (SOI). Its high refractive-index contrast allows for a high integration density. Moreover, CMOS technology can be used for fabricating SOI PICs, bringing tremendous cost and fabrication advantages. Excellent, ultra-compact passive optical functionality has been demonstrated. However, light emission and amplification is difficult, due to the indirect bandgap of silicon.

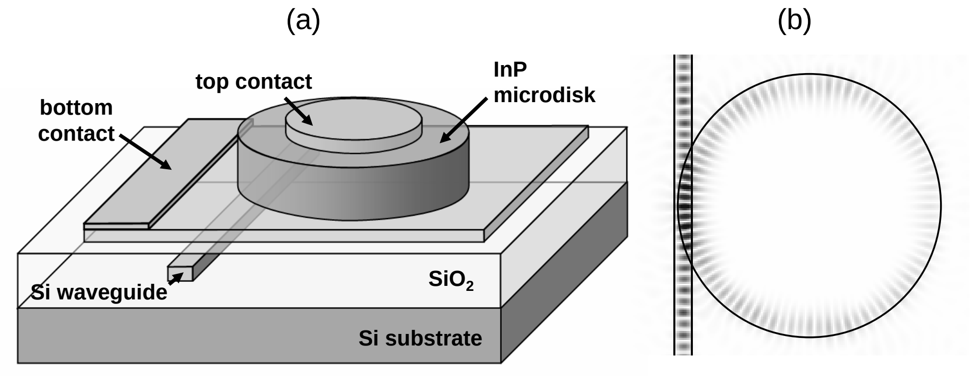

Figure 4: (a) Schematic representation of the SOI-integrated microdisk laser. (b) Whispering-gallery mode, evanescently coupled to the SOI wire.

Recently, there have been some encouraging efforts to achieve light generation on silicon. However, an efficient, electrically-injected silicon laser is not yet within reach. Therefore, we believe that in the near-to-medium time frame, direct-bandgap semiconductors such as InP will need to be integrated to achieve efficient on-chip light generation on a silicon chip.

Heterogenous integration of InP through bonding technology is a promising approach to transfer a thin InP layer on a SOI substrate. Any optical functionality – at telecom wavelengths – could in principle by implemented on a heterogeneous InP-SOI waveguide platform. As such, a heterogeneous InP-SOI PIC could become a cost-effective key element for implementing optical interconnections on various system levels. Potentially, this approach could also tackle the expected on-chip interconnection bottleneck. However, the majority of the required integrated optical components still need to be developed.

This work: integrated microlasers

The goal of this work was the development of an ultra-compact, electrically-injected microlaser, fabricated in a thin InP film bonded and coupled to an on-chip SOI wire waveguide circuit. Such a microlaser is a key component for dense electronic-photonic integration.

When designing a thin-film, electrically-injected microcavity laser, two main issues arise. First, the parasitic losses of the optical resonator should be minimized to ensure low threshold currents and high efficiencies. Second, current injection should be efficient and with low applied voltages. The latter typically requires the use of highly absorptive contact layers and metals, possibly in close proximity with the optical field, causing excessive optical absorption. As a result, a trade-off exists between obtaining low cavity loss and efficient current injection.

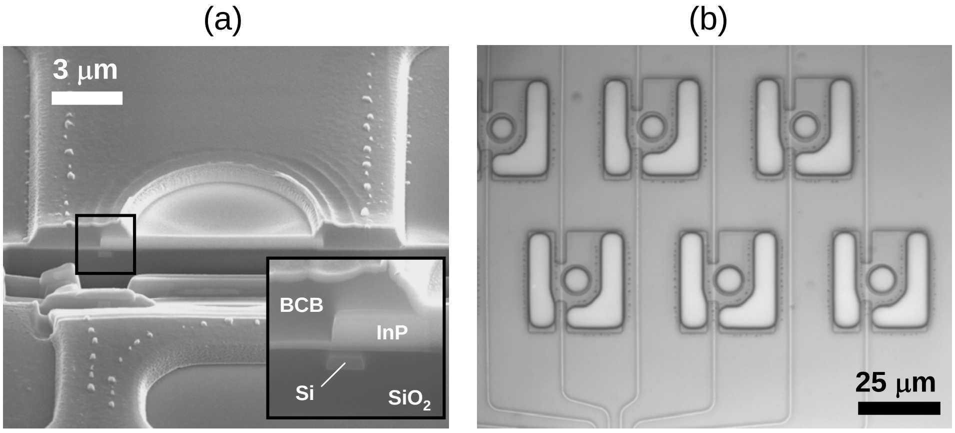

Figure 5: (a) FIB cross section, and (b) top down microscope image of a microdisk laser before metallization.

Tunnel-junction-based microdisk lasers

A design based on a microdisk resonator and a tunnel-junction-based (TJ) current injection scheme was found to offer the best trade-off between optical loss, injection efficiency, compactness and ease of fabrication, out of several evaluated alternatives. The tunnel junction enables the use of two ohmic n-type contacts, which are easily obtained without requiring absorptive contact layers. The microdisk resonator supports high-quality whispering-gallery modes (WGM), which are confined to the edges of the disk, as illustrated in fig. 4. As a result, a metal contact can be applied in the center of the disk without causing extra loss. Furthermore, the laser output can be coupled evanescently into an underlying SOI waveguide. A rigorous numerical analysis was performed in order to estimate the performance that can be expected for a fully-optimized laser design. It was found that a properly designed TJ-based microdisk laser can operate with a comparable – waveguide-coupled – efficiency as a conventional InP-based laser diode ($\sim 0.2 - 0.3\,\mathrm{W/A}$), albeit with a much lower threshold current ($\sim 100\,\mu$A).

Experimental results

In the framework of the IST-PICMOS research project, our project partners at CEA-LETI developed a molecular wafer-to-wafer and die-to-wafer bonding process. Microdisk lasers were fabricated using this technology and a combination a wafer-scale and die-based InP processing. However, in principle, all Si and InP processing steps could be carried out on a wafer scale, enabling high through-put fabrication. Some images during the fabrication process are shown in figure 5.

In a first processing run, microdisk lasers were integrated on a plain silicon wafer. Electrically-injected laser operation at room temperature was obtained for several devices, for disk diameters in the range $6 - 9\,\mu$m. Only pulsed operation was possi-

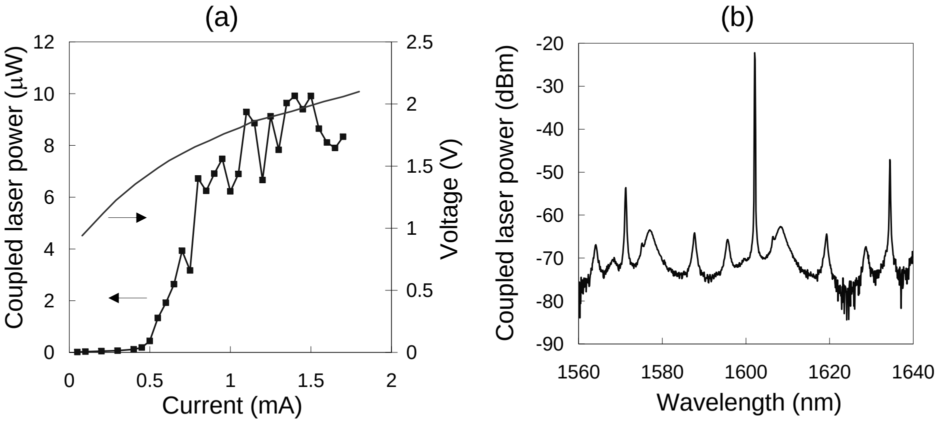

Figure 6: (a) Measured output power and voltage versus current for 7.5-μm-diameter microdisk. (b) Output spectrum for 1.4 mA drive current.

ble due to a high electrical resistance in combination with poor heat sinking, which resulted in excessive self heating. The self-heating effect was experimentally characterized, and was found to be in good agreement with thermal simulations. The high resistance was attributed to inadequate doping levels in the tunnel junction. Nevertheless, this was the first demonstration of an electrically-injected, silicon-integrated microlaser.

A second processing run involved the integration of microdisk lasers on the SOI waveguide platform. These devices exhibited a lower electrical resistance, as a result of optimizing the TJ doping levels during epitaxial growth (at INL). The operating voltages were found to be in the range 1.5-3 V. Several fabricated lasers exhibited electrically-injected lasing, with substantial optical coupling into the SOI waveguide. The threshold current was found to be strongly correlated to the size and position of the top contact. The best lasers featured threshold currents around 500 μA (microdisks with a diameter of 7.5μm). For these lasers, continuous-wave operation was possible at room temperature, with up to 20 μW/mA CW power coupled unidirectionally into the SOI waveguide, as illustrated in fig. 6. To our knowledge, this was the first demonstration of an electrically-driven microlaser, integrated on and coupled to a SOI waveguide circuit. The static performance of the best performing lasers was in agreement with the developed microdisk laser model, using realistic parameter values.

The demonstrated efficiency and yield of the heterogeneous microdisk lasers is still much lower than what would be needed for practical applications. However, as the calculations show, the performance could be strongly improved by optimizing the structural dimensions, and optimizing the etching process for low surface roughness. In conclusion, this work succeeded at proving the viability of heterogeneous InP-Si integration for the implementation of integrated, ultra-compact, electrically-injected microlasers.

Contents

Dankwoord i

Samenvatting iii

Summary xi

Table of Contents xvi

List of Acronyms xxi

List of Symbols xxiii

1 Introduction: Electronic-Photonic Integration 1

2 Thin-film microlasers: general design aspects 23

3 Design of SOI-integrated microdisk lasers 65

4 Fabrication of SOI-integrated microdisk lasers 105

5 Experimental results 119

6 Conclusions and Outlook 143

A DBR microlaser modeling 147

B Radially-dependent rate equations: calculation details 155

C Mask layouts 157

D Publications and awards 161

List of Figures 165

List of Tables 175

Bibliography **177**

Contents

Dankwoord **i**

Samenvatting **iii**

Summary **xi**

Table of Contents **xvi**

List of Acronyms **xxi**

List of Symbols **xxiii**

1 Introduction: Electronic-Photonic Integration **1**
- 1.1 Hardware of the Information Age 1
  - 1.1.1 Microelectronics 1
  - 1.1.2 Fibre-optic communication 2
- 1.2 Optical versus electrical interconnects 4
  - 1.2.1 Classification of interconnects 4
  - 1.2.2 Limitations of electrical interconnects 5
  - 1.2.3 Benefits of optical interconnects 6
- 1.3 Electronic-photonic integration 6
  - 1.3.1 Material systems for photonics 7
  - 1.3.2 Silicon-based electronic-photonic integration 8
  - 1.3.3 Integration of III-Vs on Si 10
- 1.4 This work 13
- 1.5 Applications 13
  - 1.5.1 Intra-chip optical interconnect 13
  - 1.5.2 Optical signal processing 16
  - 1.5.3 Sensing 17
- 1.6 State of the art 17
  - 1.6.1 Microcavity laser diodes 17
  - 1.6.2 Electrically-injected heterogeneous Si-InP laser diodes 19
- 1.7 Thesis overview and results obtained 20

2 Thin-film microlasers: general design aspects 23
- 2.1 Design goals 23
- 2.2 Semiconductor laser resonances 24
  - 2.2.1 Resonance condition 24
  - 2.2.2 Parasitic photon losses 27
  - 2.2.3 Photon extraction efficiency 32
- 2.3 Carrier recombination and optical gain 33
  - 2.3.1 Carrier recombination mechanisms 33
  - 2.3.2 Optical gain 34
- 2.4 Electrical injection 40
  - 2.4.1 Basic elements 40
  - 2.4.2 Injection efficiency 44
  - 2.4.3 Band diagram 47
- 2.5 Laser performance 47
  - 2.5.1 Rate equations 47
  - 2.5.2 Threshold current 49
  - 2.5.3 Differential efficiency 49
  - 2.5.4 Modulation bandwidth 49
  - 2.5.5 Temperature dependence 51
- 2.6 Thin-film microlaser design 52
  - 2.6.1 Epitaxial layer design 52
  - 2.6.2 Optical confinement in a microcavity 53
  - 2.6.3 Evanescent coupling to a passive waveguide 56
  - 2.6.4 Thin-film electrical injection schemes 57
- 2.7 Microcavity effects on laser performance 61
  - 2.7.1 The spontaneous-emission coupling factor 61
  - 2.7.2 The Purcell effect 62
  - 2.7.3 Impact on laser performance 62
- 2.8 Conclusion 63

3 Design of SOI-integrated microdisk lasers 65
- 3.1 Integrated microdisk laser layout 65
- 3.2 Optical resonances in a microdisk 66
  - 3.2.1 Whispering-gallery modes 66
  - 3.2.2 Bending loss 70
  - 3.2.3 Scattering loss 72
- 3.3 Coupling to the SOI waveguide 73
- 3.4 Tunnel-junction-based epilayer design 75
- 3.5 Electrical injection efficiency 79
- 3.6 Thermal resistance 82
- 3.7 Steady-state laser characteristics 86
  - 3.7.1 Lateral diffusion 87
  - 3.7.2 Surface recombination 87
  - 3.7.3 Non-uniform injection 89
- 3.8 Approximate laser models 90
  - 3.8.1 Model 1: no lateral diffusion current 90

3.8.2 Model 2: including a lateral diffusion current 91
3.9 Static performance optimization 92
3.10 Dynamic laser characteristics 95
3.10.1 Intrinsic modulation speed 95
3.10.2 Influence of lateral diffusion 96
3.11 Ultra-thin microdisk lasers 100
3.12 Conclusion 102

4 Fabrication of SOI-integrated microdisk lasers 105
4.1 Global overview 105
4.2 SOI waveguide technology 106
4.2.1 Deep-UV lithography 106
4.2.2 Si etching 106
4.3 InP-to-Si/SOI bonding technology 107
4.3.1 Direct molecular bonding 107
4.3.2 Adhesive DVS-BCB bonding 108
4.3.3 InP substrate removal 108
4.3.4 Wafer-to-wafer versus die-to-wafer bonding 109
4.3.5 Bonding results 109
4.4 InP processing 111
4.4.1 Microdisk definition 111
4.4.2 InP etching 112
4.4.3 DVS-BCB planarization and isolation 114
4.4.4 Metal contacts 115
4.5 Conclusion 118

5 Experimental results 119
5.1 Measurement setups 119
5.1.1 Optical pumping 119
5.1.2 Electrical injection 121
5.2 Generation 1: Si-integrated microdisk lasers 122
5.2.1 Thick G1 microdisk lasers 123
5.2.2 Thin G1 microdisks lasers 124
5.3 Generation 2: SOI-integrated microdisk lasers 129
5.3.1 Optical pumping 130
5.3.2 Electrical pumping 131
5.3.3 Theoretical fit to measured lasing characteristics 135
5.4 Full optical link on G2 samples 136
5.5 Preliminary results from G3 samples 139
5.6 Conclusion 140

6 Conclusions and Outlook 143
6.1 Overview 143
6.2 Conclusion 145
6.3 Recommendations 145

A DBR microlaser modeling 147

B Radially-dependent rate equations: calculation details 155

C Mask layouts 157

D Publications and awards 161
D.1 International Journals 161
D.2 International Conference Proceedings 162
D.3 National Conference Proceedings 164
D.4 Awards 164

List of Figures 165

List of Tables 175

Bibliography 177

List of Acronyms

BCB	Benzocyclobutene
CMOS	Complementary Metal-Oxide-Semiconductor
CMP	Chemical-Mechanical Polishing
DBBA	Direct Band-to-Band Absorption
DBR	Distributed Bragg Mirror
DUV	Deep Ultra-Violet
FC	Fibre Coupler
FCA	Free-Carrier Absorption
FDTD	Finite-Difference Time-Domain
FIB	Focused Ion Beam
G1, G2, G3	Generation 1, 2, 3
ICP	Inductively Coupled Plasma
MQW	Multiple Quantum Well
OCL	Optical Confinement Cayer
PBG	Photonic Band Gap
PhC	Photonic Crystal
PIC	Photonic Integrated Circuit
QD	Quantum Dot
Qλ	Quaternary material with bandgap wavelength λ
QW	Quantum Well
RIE	Reactive Ion Etch
SEM	Scanning Electron Microscope
SOI	Silicon-on-Insulator
SRH	Shockley-Read-Hall
TE	Transverse Electric
TJ	Tunnel Junction
TM	Transverse Magnetic
VCSEL	Vertical-Cavity Surface-Emitting Laser
WDM	Wavelength Division Multiplexing
WGM	Whispering-Gallery Mode
WPE	Wall-plug Efficiency

List of Symbols

A	SRH recombination coefficient
a	Differential gain
α	Modal propagation loss
α_b	Bending loss
α_{int}	Internal loss
α_s	Scattering loss
α_c	Coupling loss
B	Spontaneous recombination coefficient
β	Spontaneous emission coupling factor
C	Auger recombination coefficient
c	Speed of light in vacuum, specific heat
D	Ambipolar in-plane diffusion constant
$\Delta\lambda$	Free spectral range
η_e	Photon extraction efficiency
E_G	Band-gap energy
ϵ	Gain compression coefficient
η_d	Differential efficiency
η_i	Below-threshold injection efficiency
η_i^d	Differential injection efficiency
G	Material gain
Γ	Confinement factor
γ	Damping factor
G_0	Gain coefficient
I	Device current
I_L	Lateral leakage current
I_V	Vertical leakage current
I_{th}	Threshold current
J_P	Esaki peak tunnelling current density
K	Vertical mode number
κ	Thermal conductivity, amplitude coupling coefficient
k_B	Boltzmann constant
$k_{n/p}$	Free-carrier absorption coefficient for free electrons/holes
λ	Wavelength
L	Radial mode number, cavity length

L_c	Roughness correlation length
λ_G	Band-gap wavelength
M	Azimuthal mode number
n	Refractive index, diode ideality factor, free electron concentration
N	Free carrier density
N_0	Transparency carrier density
N_a	p-type doping level
N_d	n-type doping level
n_e	Effective index
N_e	Carrier density in thermal equilibrium
n_g	Group velocity
ν	Laser frequency
ω_R	Relaxation oscillation pulsation
p	Free hole density
P	Optical output power
Φ_b	Schottky barrier height
Q	Quality factor
R	Microdisk radius, resistance
R_{th}	Thermal resistance
ρ	Mass density
ϱ_c	Contact resistivity
σ	Roughness rms value
S	Photon density
T	Temperature
t	Total III-V film thickness
T_0	Characteristic temperature
t_a	Thickness active layer
t_d	Turn-on delay
t_s	Thickness bottom slab
τ_p	Photon lifetime
t_{ox}	Oxide bonding layer thickness
V	Device voltage
v_g	Group velocity
V_P	Esaki peak tunneling voltage
V_a	Active region volume
V_d	Diode voltage
V_m	Mode volume
v_s	Surface recombination velocity

Chapter 1

Introduction: Electronic-Photonic Integration

1.1 Hardware of the Information Age

1.1.1 Microelectronics

The last decades have witnessed an ever increasing computing power of digital electronic integrated circuits (ICs). This is the result of an impressive progress in silicon-based nanofabrication technology, which has led to a steady increase of the density of functional elements – such as transistors – per unit area on a computer chip. Current state-of-the-art microprocessor chips contain up to one billion transistors per square centimeter. Apart from the increasing integration density, the transistor switching speed also keeps increasing, which further adds to the intrinsic signal processing capacity of the circuit. This evolution was predicted by Moore in 1965, who claimed that the computing processing power would double every 18 months. This law still holds today and it is expected that the electronics industry will continue along this path, provided that some critical roadblocks are removed.

An important problem for current and future ICs is the excessive power dissipation and associated heat build-up, which scales with clock frequency. Since current microprocessors already dissipate 100s of Watts, it is difficult to further increase the clock speed. To circumvent this problem, the microelectronics industry now has shifted gears towards parallel computing systems, a technique that has long been used in supercomputers. A recent example of such a multiprocessor – used in consumer electronics – is the Sony-IBM-Toshiba Cell processor, which contains 8 processor cores, interconnected with a high-speed bus architecture, as shown in figure 1.1. Since this trend towards parallelization is expected to increase in the future, the on-chip communication bandwidth required to connect the cores will increase enormously. Assuming that each floating-point operation (FLOP) implies the transport of one bit, a TFLOP computer (which is only a few generations away) would need an on-chip bandwidth of 1 Tb/s! Since current global on-chip electrical interconnec-

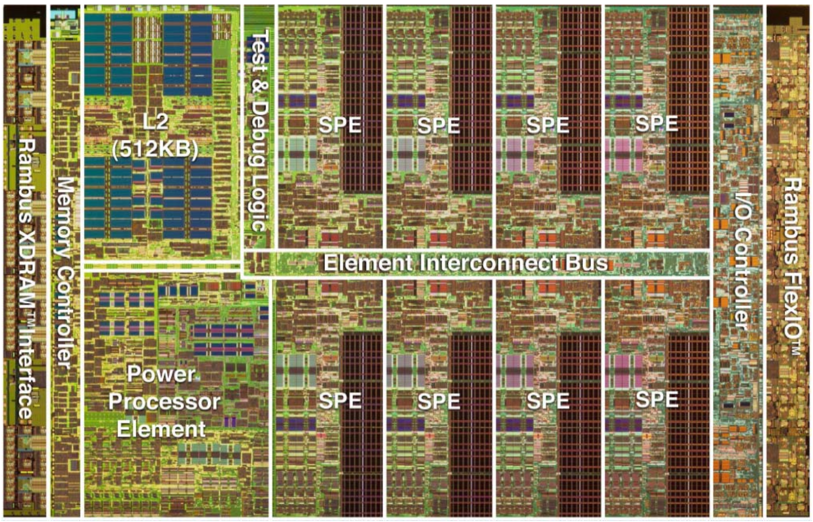

Figure 1.1: Layout of the Cell processor, containing 8 processor cores.

tions already have serious power, bandwidth and latency problems, it is clear that the microelectronics industry is facing a tremendous interconnect bottleneck.

1.1.2 Fibre-optic communication

Starting from the late 70s, fibre-optic connections have emerged as the most important method for long-distance high-bandwidth communication. They replaced electrical interconnections based on coaxial cables, which failed to deliver the required bandwidth capacity. As illustrated in fig. 1.2, the transition from electrical to optical systems occurred when bandwidth-distance products over 10 Mb/s×km were required. Since then, the information capacity of fibre-optic systems has doubled almost every 2.5 years. The success of these systems is largely due to the low signal power loss of 0.2-0.3 dB/km in glass optical fibres, for a wavelength transmission window around 1.55 μm, as compared to 10 dB/km at 1 MHz for coaxial cable. Also, the availability of efficient, narrow-linewidth laser diodes emitting in the 1.55-μm transmission window range was indispensable, enabling low-dispersion signal propagation.

Wavelength Division Multiplexing

Intrinsically, a single-mode optical fibre can carry a bandwidth of about 25 Tb/s before the wavelength dependence of the propagation losses affects the transmission quality. A key technique to unleash this massive bandwidth is wavelength division multiplexing (WDM). In this technique, multiple optical carrier signals at slightly different wavelengths are launched into a single optical fibre, and are modulated

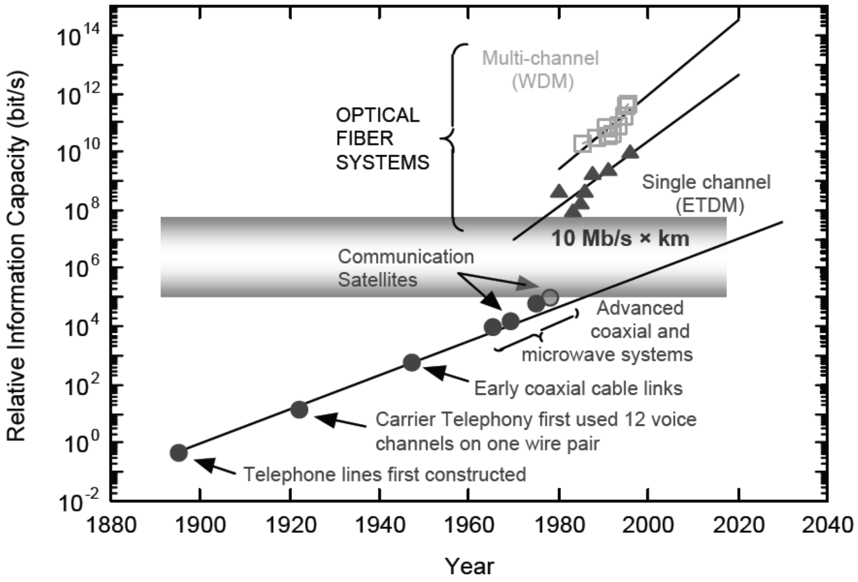

Figure 1.2: Evolution of the information capacity for various electrical and optical communication technologies (reproduced from [1]).

individually with different data signals. At the transmitter side of a fibre-optic connection, the output signals of an array of laser diodes – each emitting at a different wavelength – are combined with an optical multiplexer into the optical fibre. At the receiver side, the signal is split into the different carrier wavelength components, which are each sent to the corresponding detector. Current WDM systems contain 40 or even more wavelength channels. This technique allows to fully exploit the available fibre bandwidth, while not putting excessive burden on the lasers, modulators and detectors.

Photonic Integrated Circuits

An optical network requires several optical functions such as passive light routing, filtering, and multiplexing but also active functions such as light generation, detection, modulation and switching. As is the case for microelectronics, there is a strong drive to integrate as many photonic components as possible on a single chip, resulting in a photonic integrated circuit (PIC). It is expected that this integration effort will result in reduced cost and improved performance and compactness, as compared to systems based on discrete components. Integration of photonic functions also strongly relaxes the tight alignment tolerances that arise when coupling light between a fibre and an optical component, thereby strongly reducing the assembly cost. In a PIC, this alignment is obtained by collective lithographic processes, during fabrication.

The basic component on a PIC is the optical waveguide, which is a structure that guides the light between different locations on the PIC. Such waveguides typically consist of a dielectric or semiconductive core, surrounded by a cladding material with a lower refractive index than the core. These structures support guided electromagnetic modes as a result of total internal reflection at the core-cladding interface. Careful design of the transverse waveguide geometry results in single-mode waveguides. These are often preferred over multi-mode waveguides, as circuits based on the latter can suffer from unwanted mode conversion at waveguide discontinuities.

An important metric of an optical waveguide system is the refractive-index contrast between the waveguide core and the cladding layers. This contrast largely determines the minimum waveguide bend radius that can be used in the PIC, without causing excessive bending loss. Furthermore, it determines the minimum waveguide pitch that can be tolerated without causing excessive cross talk between neighboring waveguides. Since the maximum achievable integration density on a PIC depends strongly on the on-chip light routing density and thus on the minimum bend radius and waveguide pitch, we can conclude that the integration density scales with increasing refractive-index contrast.

Another important characteristic of a PIC is the degree to which efficient, active functionality can be implemented. Many active functions can be obtained by exploiting the non-linear effects of the waveguide material. The ability to achieve low-power non-linear functionality obviously depends on the intrinsic strength of these non-linear effects – which is a material property – but also on the transverse mode confinement in a waveguide. It should be noted that a high index contrast generally results in a tight transverse mode confinement, which results in an enhanced light intensity in the waveguide core as compared to low-contrast waveguides, and thus a lower required power to induce non-linear effects. While light generation in the 1.55-μm range can also be achieved by non-linear effects of an optical pumping beam, for efficient electrically-injected light generation, only direct-bandgap semiconductors are currently considered on a commercial scale. However, extensive research is going on to break this barrier, as will be discussed in 1.3.2.

From these considerations, an ideal PIC would consist of waveguide materials that combine a high refractive index contrast and low propagation loss for passive functionality, together with the (local) availability of strong non-linear effects and efficient light generation for active functions. Furthermore, the material cost should be low and a cost-effective high-throughput processing infrastructure should exist, to exploit economics of scale. Finally, efficient fibre-chip optical coupling should be possible. Unfortunately, no such material system exists today, as will be discussed in 1.3.1.

1.2 Optical versus electrical interconnects

1.2.1 Classification of interconnects

Interconnects can be found on several system levels. A distance-based classification is shown in figure 1.3 [2]. The interconnection lengths vary from a micrometer

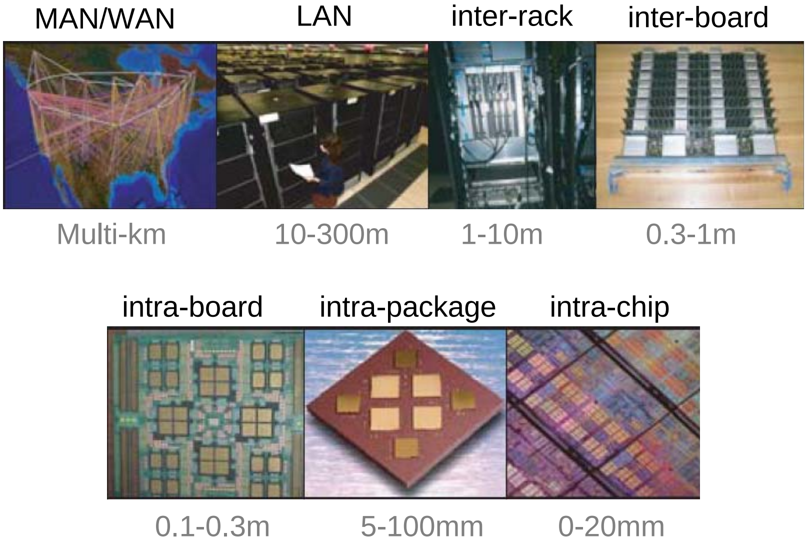

Figure 1.3: Physical interconnect hierarchy of interconnects in digital systems. The interconnects span a wide range of covered distances. Figures are reproduced from [2].

for intra-chip interconnect up to multiple kilometers, as is common for Metro/Wide Area Networks (MAN/WAN). In between these extremes, we find Local Area Networks (LAN), connecting machines within a building (10-100 m), inter-rack connections in a machine (1-10 m), inter-board (0.3-1 m), intra-board (0.1-0.3 m) and intra-package (5-100 mm) connections. Each of these interconnect levels has their own characteristics, in terms of physical implementation, bandwidth, density, latency and communication protocol. In this work, we will mainly target the intra-chip level, which features the highest interconnect density and level of integration.

1.2.2 Limitations of electrical interconnects

In [3], a general fundamental limit was formulated for the bandwidth of electrical interconnects (EI):

$$B \sim B_0 \frac{A}{L^2}, \tag{1.1}$$

where A is the total cross-sectional area of the wiring and dielectrics, L the wire length and where B_0 is in the range $\sim 10^{15} - 10^{18}$ b/s depending on the type of interconnect that is being considered. For simple lossy on-chip EI, $B_0 \sim 10^{16}$ b/s was found. By applying techniques such as repeatering and equalization, B_0 can be improved to $10^{17} - 10^{18}$ b/s, however at the expense of power and silicon real estate. From equation (1.1), it can be seen that the EI bandwidth is proportional to the aspect ratio A/L^2 of the interconnection. This is the physical reason for the EI bottleneck in modern electronic ICs: while transistor density and speed benefit from dimensional scaling, the EIs do not. Also, it is obvious that the EI performance is worst for the longest, global on-chip links.

To illustrate the global on-chip EI bottleneck for (future) multicore processors, let's consider a $2 \times 2\,\mathrm{cm}^2$ chip, with a 10-μm-thick interconnect layer. Assuming that for the longest link $L = 4\,\mathrm{cm}$ and that the full chip width can be used for the interconnect, results in $A/L^2 = 1.25 \times 10^{-4}$ and $B = 1.25\,\mathrm{Tb/s}$. It should be noted that this threshold value compares well with the historical transition bandwidth-length product of long-haul interconnect at $10\,\mathrm{Mb/s{\times}km} = 1\,\mathrm{Tb/s{\times}cm}$. It is interesting to note that the current Cell Microprocessor already features a $1\,\mathrm{Tb/s}$ on-chip electrical interconnect bus, based on a large number of electrical repeaters. However, this global interconnection consumes 30 to 50 percent of the total chip power!

1.2.3 Benefits of optical interconnects

Optical interconnects (OI) have several intrinsic benefits over EIs, many of which derive from the fact that OI uses a carrier signal frequency that is much higher than the data modulation frequency [4]. Therefore, OIs don't exhibit frequency dependent loss or cross talk, and there is no aspect-ratio limitation. Impedance matching and wave reflection problems can also be solved more easily, and the link is immune to electromagnetic noise. Because of these intrinsic benefits, optical links have long been used for long-haul interconnect, and are a common alternative for electrical links in LANs and server clusters. Due to the steady increase in required bandwidth for shorter links, and the gradual performance improvement and cost reduction of optical interconnects, optical links are increasingly being considered for I/O, memory, and system buses in multiprocessor systems [2].

As illustrated in the previous section, the electrical wiring bottleneck is also expected to reach the intra-chip level, albeit in a longer time frame (15-20 years). Also for that level, optical interconnections are considered as a promising solution. By using high index-contrast waveguide systems (see 1.3.1) in combination with WDM techniques, a high on-chip bandwidth density could be obtained. However, many (technological) issues exist today, as will be discussed below.

1.3 Electronic-photonic integration

Acknowledging the fact that optical interconnects intrinsically outperform electrical interconnects at high bandwidth-distance products, merging electronics with photonics appears to be a promising approach to solve the interconnect bottleneck, both on the inter and intra-chip level. However, to integrate electronic with photonic ICs, several obstacles need to be overcome. In this section, we focus on one very important technological issue: material and processing compatibility.

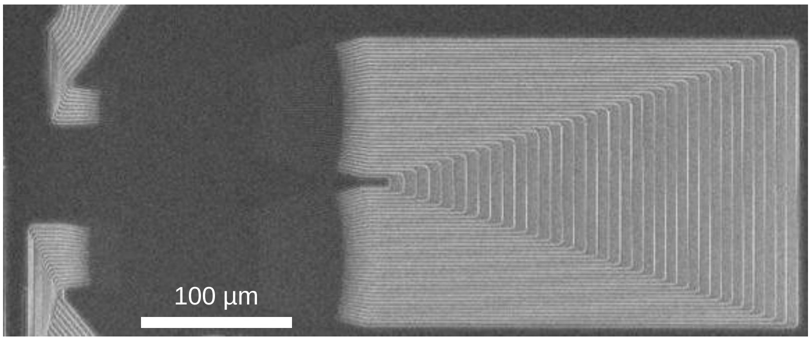

Figure 1.4: Ultra-compact passive 16-channel wavelength router based on an arrayed waveguide grating, fabricated on the silicon-on-insulator wire waveguide platform [5].

1.3.1 Material systems for photonics

PICs can be made in various material systems. A general – but not limiting – overview is given in this section.

Silica-on-silicon. A very mature and popular waveguide system is silica-on-silicon, which uses doped silica waveguide cores and undoped silica cladding layers on a silicon substrate. Since the waveguide core and cladding are essentially made in the same material type (glass), the refractive index contrast and the integration density are low. Basic silica waveguides were demonstrated in the early 80s, and the first silica-based multiplexer was developed in the early 90s.

Silicon-on-insulator. The silicon-on-insulator (SOI) waveguide material, which consists of a top Si waveguide layer separated from the silicon substrate by a SiO_2 cladding, has received extensive research interest over the last twenty years. SOI-based waveguide systems exist in two variants. A first is based on silicon rib waveguides, with a relatively large core cross section containing multiple square wavelengths (in the core material). By a careful control of the waveguide width, height and etching depth, single-mode operation can be obtained. While the vertical index contrast is high, the lateral is not, limiting the integration density. However, due to the large waveguide core dimension, optical fibre-chip coupling is relatively easy.

The second variant is based on silicon wire waveguides. These silicon wires are completely etched through the top silicon layer, and have a cross-sectional dimension of approximately $500 \times 200\,\text{nm}^2$ to achieve single-mode operation. Both the vertical and lateral index contrast is high ($\Delta n \sim 2$). SOI photonic wires currently allow for the highest photonic integration density[1]. Over the last couple of years, many research groups have demonstrated excellent passive performance, such as optical filters and wavelength routers, with remarkably small footprints (see fig. 1.4,

---

[1] Plasmonic waveguides allow for an even tighter lateral mode confinement, but exhibit much higher propagation loss.

[5]). A drawback of the high index contrast is that nm-scale variations on the characteristic features in optical components result in a strong alteration of the component performance. Therefore, many refer to this technology as the silicon *nanophotonic* waveguide platform. Due to the large mismatch between the optical mode size in a fibre and a silicon wire, specific coupling structures need to be designed for efficient fibre-chip coupling [6].

Since SOI is a material used for high-end electronics, the CMOS processing infrastructure can be used for the fabrication of SOI PICs, which brings enormous advantages in terms of fabrication and cost.

III-V materials. Other popular material systems are based on III-V semiconductor systems such as GaAs/AlGaAs and InP/InGaAsP. Since these are direct-bandgap semiconductors, they allow for efficient light generation. Ternary and quaternary alloys can be formed, with different refractive indices and emission wavelengths. The InP/InGaAsP is of particular use for telecommunications, since it enables efficient light emission and detection in both the 1.3 and 1.55-μm fibre-optic transmission windows. Furthermore, it allows for the monolithic integration of passive and active functions, through several techniques such as epitaxial regrowth, vertically multi-core waveguides, and quantum-well intermixing. While the vertical refractive index contrast is low, a high lateral contrast versus air can be obtained by etching through the waveguide core. Any optical functionality can be implemented with III-V materials, however the processing technology is much less mature and has a much lower yield as compared to Si processing, and is therefore much more expensive. However, it is the material of choice for the high-performance components that are required for long-haul optical interconnections.

Polymers. Polymers offer a cheap waveguide material system with rapid and cost-effective manufacturing. They exhibit a large thermo-optic effect, which allows for low-power thermo-optic switches. However, the refractive index contrast is low ($\Delta n \sim 0.1$) and there are some issues with reliability.

1.3.2 Silicon-based electronic-photonic integration

As mentioned in the previous section, a silicon nanophotonic PIC exhibits excellent passive optical performance with a high integration density. Furthermore, it is naturally CMOS-compatible and is therefore an ideal candidate to achieve electronic-photonic integration. However, implementing active optical functionality on this waveguide platform is more challenging. Substantial research effort is being spent on the development of Si-based lasers, modulators and detectors. Here, we shall briefly discuss some recent results on silicon lasers.

Silicon lasers

Since silicon has an indirect band gap, its radiative recombination rate is very slow and strongly outpaced by non-radiative recombination, limiting the internal quantum efficiency of bulk silicon luminescence. While a lot of functions can be implemented on a PIC without an on-chip light source, the availability of an integrated silicon laser will undoubtedly add significantly to the impact of silicon photonics. Therefore, the development of an efficient (electrically-injected) silicon laser is receiving much scientific interest.

In [7], electrically-injected free carriers were spatially localized by creating a nanostructured p-n-junction, by applying nano-patterned doping profiles in the silicon. It is believed that this localization saturates the non-radiative recombination centers, resulting in an increased non-radiative lifetime. Lasing was observed at room-temperature at a wavelength of 1.2 μm, and was attributed to a two-phonon-mediated indirect transition. While this was the first demonstration of an electrically-injected silicon laser, the efficiency was very low. Furthermore, since the original paper, no further results have been reported.

Another approach to achieve lasing in Si is to tailor the quantum confinement of the free carriers. In [8], optical gain was observed in silicon nanocrystals, embedded in a SiO_2 matrix. The peak gain wavelength was around 800 nm, and was attributed to radiative recombination through Si-SiO_2 interface states, but no lasing was reported. An important issue with such structures is how to achieve electrical injection of the nanocrystals through the oxide matrix. Injection schemes based on Fowler-Nordheim tunneling have been proposed and demonstrated [9]. However, they require high voltages. Another attempt was made in [10] with nano-patterned crystalline Si. Lasing was observed at 1278 nm under optical pumping for temperatures below 80 K, with very low external efficiencies. In this case, the radiative emission was attributed to direct recombination at Si vacancy defects that were created during processing of the nanoholes. It should be noted that purely Si-based emitters operate at wavelengths of about the bandgap wavelength of silicon (or shorter), and thus cannot be used in combination with silicon waveguides.

A strategy to obtain lasing around the telecom wavelength is to include rare-earth impurities such as erbium (Er^{3+}) in the Si or SiO_2 matrix. Er-doped fibre amplifiers (EDFAs) are already successfully being used in fibre-optic systems, and it is hoped that these gain elements can be used to achieve lasing on the silicon platform. While electroluminescence was observed in erbium-doped silicon [11], a SiO_2 matrix allows for a higher erbium doping level. The presence of silicon nanocrystals in the SiO_2 matrix has been reported to substantially increase the erbium excitation efficiency [12]. In [13], optically pumped lasing was obtained at 1.54 μm in a toroidal cavity sculpted into Er-doped silica. In [14], a slotted waveguide containing erbium-doped silica is proposed, which should enable electrically injected luminescent operation, and has potential to achieve lasing. However, high voltages (> 50 V) are required to achieve a sufficiently large drive current.

Finally, a radically different approach to achieve lasing in Si is to exploit stimulated Raman scattering. This non-linear effect arises when a photon from the pump beam – which has a wavelength above the bandgap wavelength – induces the creation of a phonon and a photon of lower energy than the pump photon. Optical gain can be obtained at the wavelength of the created photons. However, together with the Raman effect, two-photon-absorption is induced (another non-linear effect), which results in strong free-carrier absorption of both the pump beam and the signal

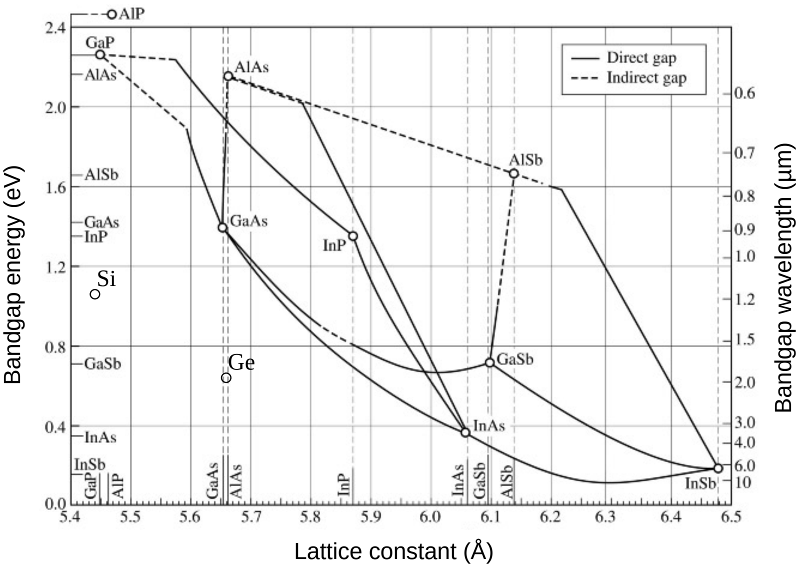

Figure 1.5: Bandgap energy and wavelength versus lattice constant for various III-V semiconductors, silicon and germanium [21].

beam. By sweeping these free carriers away in a reverse-biased p-n junction, net optical gain and lasing was obtained in [15]-[16]. However, due to its non-linear nature, only optically pumped lasing is possible. Another comparable approach is based on four-wave mixing [17]. In this case, two pump photons are converted to a signal and an idler photon, resulting in optical gain at the signal wavelength. The phase mismatch between the pump, signal and idler determines the optical bandwidth over which gain can be observed.

1.3.3 Integration of III-Vs on Si

While significant progress has been made on electro-optic modulation [18]-[19]-[20] and light detection on the SOI platform, electrically-injected light generation and amplification remains difficult, as discussed in 1.3.2. Therefore, we believe that to implement these functions, III-V materials will still be required, at least in the near-to-medium time frame. In this context, an attractive approach is to use silicon as a substrate and for passive waveguide functions, and to integrate III-Vs on the Si platform where light generation or amplification is needed. However, integrating III-Vs on Si is far from straightforward. Here, we discuss the main techniques that are currently being researched.

Hetero-epitaxy

It could be argued that the highest electronic-photonic integration density could be reached by directly growing the III-V material on the Si substrate. However, this is a huge technological challenge, since all III-V alloys – emitting in the 1.3-1.55-μm wavelength range – have a crystal lattice constant in the range 5.7-6.3 Å, whereas Si has a lattice constant of 5.43 Å, as illustrated in figure 1.5. Furthermore, there is a strong mismatch in thermal expansion coefficient. As a result, direct epitaxial growth of InP or GaAs on Si will result in a poor material quality, with a high concentration of dislocations and anti-phase domains. These defects act as efficient non-radiative recombination centers, thereby strongly reducing the luminescence quantum efficiency.

To circumvent this problem, several strategies are being considered. Since the lattice constant of GaAs (5.65 Å) is closer to that of Si, most results cover growth of GaAs-based materials on Si. In [22], continuous-wave lasing was demonstrated in a GaAs-based quantum-well structure, directly grown on silicon, with an intermediate buffer layer to accommodate crystal defects. However, the laser stability was very poor due to growth and migration of crystal defects into the active region. This problem can be tackled by epitaxial growth sequences that result in 2-D instead of 3-D crystal defects, concentrated at the interface between Si and the III-V. Such an approach was successfully applied in [23], where lasing in pulsed regime was obtained in InP-based layers. Other approaches include the implementation of a dislocation filter in the form of quantum dots [24], the use of a thin AlSb interfacial layer that relieves most of the strain [25] (see fig. 1.6 (a)), or the use of a SiGe interfacial layer [26].

As can be seen, significant improvement has been made in the quality of hetero-epitaxial growth of III-Vs on silicon. However, the device performance remains worse as compared to components on a GaAs or InP substrate. In many cases, thick buffer layers are needed. Coupling to the silicon waveguide circuit therefore seems difficult. Finally, it remains an open question if III-V epitaxial growth can be allowed during (front-end) CMOS processing.

Flip-chip technology

Another, more mature integration technology is flip-chip or hybrid technology. Flip-chipping is a well-known process, extensively used for attaching electronic dies on a printed-circuit board or a another common substrate. Typically, gold or solder bumps are used to attach the die to the substrate, at the same time providing an electrical connection. The same technology can be used to attach optoelectronic dies on a CMOS circuit [29], or to integrate InP-based laser dies on a silicon waveguide platform [27] (see fig. 1.6 (b)). The main challenge when flip-chipping optoelectronic dies is the strict alignment tolerance ($< 1\,\mu$m) that arises when coupling light from the active component into a fibre or on-chip waveguide. In [27], an alignment accuracy of 1 μm was achieved.

Flip-chip technology allows for the integration of high-performance optoelectronic components with electronics. Also, the components can be tested before in-

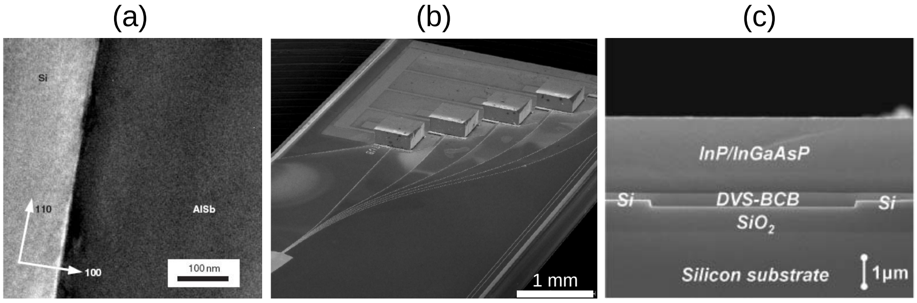

Figure 1.6: III-V/Si integration technology. (a) Hetero-epitaxy of AlSb on Si [25], (b) InP-based lasers flip chipped on SOI [27], and (c) InP-based layer bonded to SOI with adhesive BCB bonding [28].

tegration. Furthermore, it is a mature and CMOS-compatible technology. However, the alignment procedure has to be done on a die-per-die basis, which makes it slow and costly. The achievable integration density is low due to the presence of the bumps.

Bonding technology

Bonding technology involves the permanent attachment of two separately grown materials. Several techniques are being studied. *Metallic* bonding mostly uses eutectic metal mixtures, similar to the materials used for solder bumps. While it provides an excellent electrical and thermal interface, optical coupling to the underlying circuit is difficult. *Adhesive* bonding typically involves the use of polymers that spread on and interact with the to-be-bonded interfaces. After wetting the surfaces, a permanent attachment is obtained when polymer macromolecules are formed during the subsequent curing treatment at around 300 °C. An adhesive bonding process for optoelectronic III-V/Si integration was developed by G. Roelkens in [30], using the divinylsiloxane-bis-benzocyclobutene (DVS-BCB). Excellent bonding quality of III-V dies on silicon was obtained, with bonding layer thicknesses as low as 100 nm (see fig. 1.6 (c)). As most polymers are transparent, adhesive bonding allows for optical coupling between the III-V layer and the Si or SOI substrate. Finally, for *direct molecular* bonding, two ultra-clean and ultra-flat SiO_2 surfaces are brought together and are bonded through Vander Waals attraction at the intimate surface contact. During subsequent curing at around 300 °C, the O-H bonds are replaced by Si-O-Si bonds, providing a high bonding strength. This type of bonding was primarily used in this work. The bonding process was developed at CEA-LETI. This direct bonding technology is further discussed in section 4.3.

Bonding technology allows for the creation of a heterogeneous waveguide platform, with excellent passive and active functionality. An important benefit is the fact that all III-V component fabrication steps can be done after bonding, on a wafer scale and with CMOS tools. Alignment to the underlying SOI circuit is done during wafer-scale lithography. Bonding can be done on a wafer-to-wafer or die-to-wafer basis. The latter might be preferred, since III-V wafers are in general much smaller than Si or SOI wafers. Furthermore, die-to-wafer bonding allows to attach the III-V dies only where they are required (pick-and-place with coarse alignment), which can result in a cost reduction.

1.4 This work

The goal of this work was the design, fabrication and characterization of a compact and efficient, electrically-injected microlaser integrated on and coupled to a SOI nanophotonic waveguide circuit. The microcavity was to be fabricated using wafer-scale compatible processing in a thin InP-based film, which is bonded onto the SOI circuit. An emission wavelength around the telecom wavelength of $1.55\,\mu$m was targeted. For most practical applications, lasing should be possible in continuous-wave (CW) regime at room temperature. Furthermore, the laser should have a low threshold current ($\ll 1\,$mA), a slope efficiency comparable to that of conventional lasers ($\sim 0.3\,$W/A), and a compact footprint ($< 10 \times 10\,\mu\text{m}^2$) which enables a high level of integration with low power consumption. Additionally, high-speed operation should be possible ($> 10\,$Gb/s).

1.5 Applications

A silicon-integrated, electrically-injected microlaser can have many uses. The main application areas are intra-chip communication, optical signal processing and sensing.

1.5.1 Intra-chip optical interconnect

As discussed in section 1.2, future electronic circuits will suffer from an on-chip interconnection bottleneck, which could intrinsically be solved by using on-chip optical communication networks. For a complete on-chip optical link, two main alternatives are being considered, as illustrated in fig. 1.7. A first approach is to use integrated on-chip microlasers and microdetectors, coupled to a common on-chip waveguide. In this scheme, the electro-optical signal conversion is done by directly modulating the integrated lasers. In the second approach, light from a conventional off-chip laser is coupled onto the chip and split into several optical links. Each individual link contains an integrated electro-optic modulator and integrated detector. In this case, the optical power provided by the external laser doesn't contribute to the power consumed on the chip, relaxing the power budget. The available on-chip optical power is limited by the laser's maximum output power, the coupling efficiency from the laser to the on-chip waveguide and additional waveguide and splitter losses. It requires the development of compact, fast and low-power integrated optical modulators as opposed to compact, fast, and efficient integrated microlasers for the former

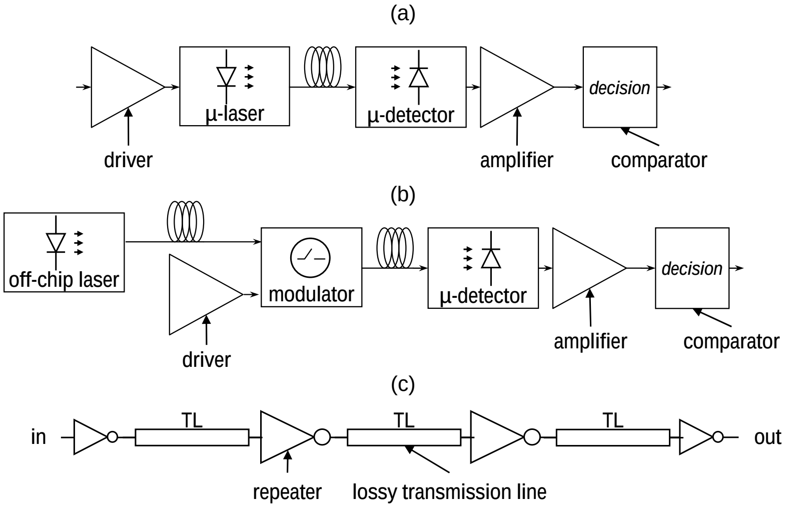

Figure 1.7: Schematic representation of future global on-chip interconnects. (a) Optical interconnect with on-chip lasers, (b) optical interconnect with off-chip laser source and on-chip modulators, and (c) electrical interconnect with repeaters.

approach. Keeping the laser off-chip has the additional benefit of not exposing it to high on-chip temperatures, which negatively affect laser performance.

Comparison of electrical and optical on-chip interconnect

In order to assess the benefits of introducing photonics as compared to an all-electrical implementation, the relevant metrics of on-chip interconnect should be estimated and compared, for current and future generation[2] ICs. Due to the absence of an efficient electrically-injected silicon-integrated laser, most studies on intra-chip optical interconnect found in literature involve the approach with an off-chip laser and on-chip modulators. The most important performance criteria are delay, bandwidth density and power. It should be noted that the choice of the waveguide material has a strong impact both on bandwidth density and delay. A high refractive-index contrast allows for high integration and bandwidth density. However, it generally comes at the expense of a higher group index n_g of the guided mode, which results in slower light propagation ($v = c/n_g$) and higher delay. The total delay also has contributions from opto-electronic conversion, which dominate for the shortest links.

In [32], scaled and non-scaled EIs are compared with optical interconnects, based on Si_3N_4 waveguides ($\Delta n \sim 0.5$, $n_{eff} = 1.7$), an off-chip laser and efficient modulators. The analysis included transmitter and receiver circuits. Considering a link length of 1 cm, it was found that for future IC generations, the delay of an OI is

---

[2] Most studies cover the technology nodes 90, 65, 45, and 32 nm, which are expected to arrive in 2004, 2007, 2010, 2013, and 2016 respectively [31].

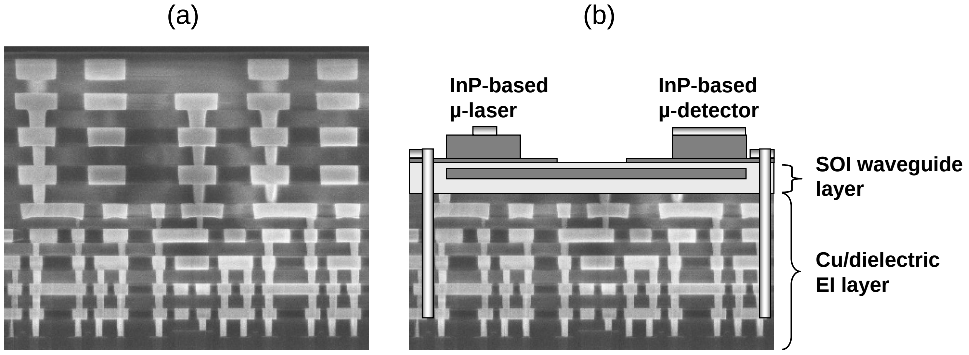

Figure 1.8: (a) Metallization levels in a modern electronic IC (AMD Athlon 64, 2003). (b) Proposed SOI-based optical interconnect (OI) layer, as studied in the PICMOS research project. Only the longest global electrical interconnections (EI) would be replaced by optical interconnects. The OI layer is based on a nanophotonic SOI waveguide with heterogeneous InP-based microlasers and microdetectors.

comparable to that of non-scaled EI, but significantly better than that of scaled EI. Bandwidth density was found to be worse for OI, both compared to scaled and non-scaled EIs. However, by applying coarse WDM techniques, the bandwidth density can be strongly increased, surpassing that of EIs. In [33], a comparable analysis was carried out, however with more up-to-date performance models for the modulator and also comparing polymer and SOI wire waveguides. They found that for $L = 1\,\mathrm{cm}$, OIs have 10-65% shorter delays than EIs, depending on the waveguide material (polymers are better) and technology node. Power consumption for OIs was found to be 15-75% smaller than that of EIs. OI bandwidth density was found to be about an order of magnitude smaller for polymer waveguides as compared to EI and SOI-based OI, which exhibit comparable bandwidth density. Once again, the use of WDM techniques can strongly increase this figure.

Heterogeneous integration for on-chip optical interconnect

Due to the absence of an efficient, electrically-injected silicon-integrated laser, an optical interconnection scheme involving on-chip light generation requires heterogeneous integration of InP on the silicon platform, to allow for the integration of efficient InP-based integrated microlasers. The feasibility of such an approach was studied in the EU-funded FP6 research project IST-PICMOS (Photonic Interconnect Layer on CMOS by wafer-scale integration). The goal of this project was to demonstrate an SOI-based optical link, including heterogeneously integrated InP-based microlasers and microdetectors. The optical interconnection layer would be bonded on top of a CMOS chip, replacing the longest, global EI layers, as is illustrated in figure 1.8.

The project also included a system study, to quantify the specifications for the various subcomponents, when targeting intra-chip communication. The results of this study are summarized in [34]. Power consumption, delay and gate area were compared, while assuming an identical line pitch of 1.1 μm both for EI and OI. The main conclusion was that for future generation ICs, OIs could result in an up to tenfold power reduction, a 60-fold gate area reduction, and a twofold reduction in delay as compared to EIs, for link lengths in the range 2.5-20 mm. However, this performance can only be expected provided that the microlasers have a threshold current $I_{th} < 150\,\mu$A, an operating voltage below 1.5 V, a slope efficiency of 0.3 W/A and occupy less than 100 μm^2. The detectors should be equally small, have a responsivity of at least 0.7 A/W, and a capacitance of not more than 10 fF. Furthermore, it was assumed that the modulation speed is equal to the clock frequency. Therefore, the laser and detector should have a modulation bandwidth in excess of this frequency, which is as high as 11 GHz for the 32-nm technology node. To obtain bandwidth densities significantly higher than for EI, WDM techniques should be implemented.

On-chip WDM and temperature stability issues

As is clear from the above studies, on-chip WDM techniques are most likely needed to achieve a convincing bandwidth improvement for OI as compared to future EIs. This implies that at the transmitter side, many wavelengths should be multiplexed into a common waveguide, and demultiplexed at the receiver side. Since the compact and low-power silicon-integrated modulators are currently based on a (ring) resonator, they have a limited spectral bandwidth ($<$ 1 nm). Furthermore, temperature variations change the resonant wavelength by about 75 pm/K [5]. Therefore, the spectral bandwidth of the modulators should be improved to a few nanometers, in order to be able to cope with on-chip temperature variations in the order of tens of degrees. The same problems arises for the (resonant) detectors.

For on-chip OI with integrated on-chip sources, the situation is even worse. Besides a changing emission wavelength with increasing temperature (about 100 pm/K for InP-based lasers), the laser threshold current increases exponentially, together with a (less important) decrease in slope efficiency [35]. While substantial improvement has been made on high-temperature laser performance, the threshold current at 100 °C can easily be five to ten times higher than at 20 °C.

1.5.2 Optical signal processing

The huge growth of Internet traffic requires an increased capacity and performance of the underlying optical networks. In current optical network nodes, the optical packet processing is done in the electrical domain, through hybrid optoelectronic node architectures. However, future network node functionality will have to be carried out in the optical domain, in order to align the packet forwarding capacity of the router with the increasing exploitation of the fibre transmission capacity [36]. A key component for complex optical processing is a compact, high-speed and low-power optical memory, which can be used for buffering of decisions and data. In [37], a fast and compact, low-power flip-flop optical memory was demonstrated on an InP-substrate, by coupling two microring lasers through a common waveguide. Two stable operating regimes exist, which can be monitored by inspecting the output power or wavelength at one end of the common waveguide. This memory element could be straightforwardly implemented on an SOI platform, by using heterogeneous InP-based microdisk lasers, probably resulting in a reduced cost and an increased integration density.

More generally, an array of coupled laser diodes is a promising implementation for an all-optical neural network. Two coupled laser diodes can be used to mimic the non-linear neuron function [38]. Neural networks are typically used for complex signal processing task such as pattern recognition. It can be expected that the processing capability scales with the number of neurons in the network. Therefore, a dense array of heterogeneous microlasers (and possibly other active elements such as amplifiers), interconnected by an SOI waveguide circuit might be a promising approach to implement a highly-integrated optical neural network.

1.5.3 Sensing

SOI nanophotonic PICs can also be used for sensing. Besides the already mentioned temperature dependence of ring resonators, they can also be used to measure strain [39]. Furthermore, since the guided modes supported by SOI wire waveguides have reasonably large tails in the cladding materials, a change in refractive index in their surroundings will result in a reasonably large change of the resonance wavelength of a (ring) resonator. This effect can be used for label-free detection of attached bio-molecules, if the wire surface is appropriately activated [40]. An important metric for these biosensors is the achievable sensitivity, which amongst others relates to the quality factor of the optical resonance. In [41], it is argued that resonators with internal optical gain allow for the detection of much smaller refractive index changes as compared to passive sensors. Integrating many InP-based microlasers on an SOI platform – each functionalized for detecting a different type of bio-molecule – might thus be a promising approach towards a versatile and highly sensitive lab-on-a-chip.

1.6 State of the art

Since both the silicon-integrated as the microcavity aspect of our to-be-developed laser is relevant, we give an overview of the state-of-the-art of both areas.

1.6.1 Microcavity laser diodes

In the past 15 years, many researchers have reported on several microlaser types, most of them on an InP substrate. The reported microlasers are mainly based on microdisk resonators or photonic-crystal structures.

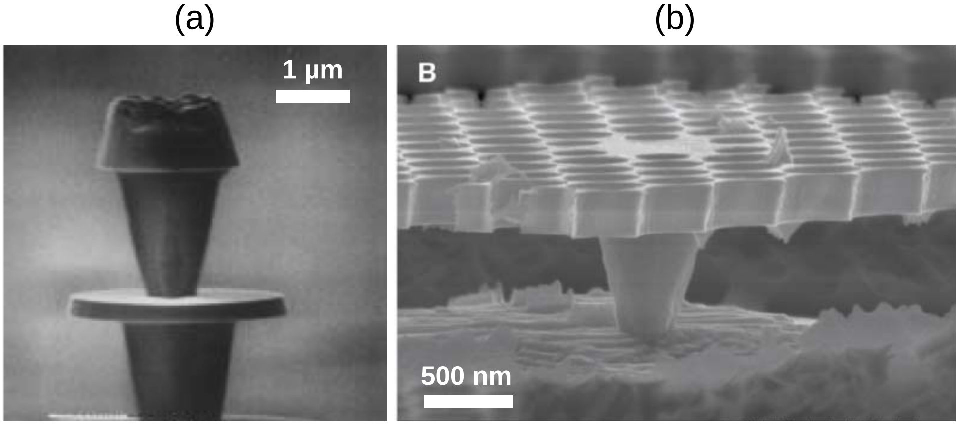

Figure 1.9: (a) Pedestal-supported microdisk laser structure [50]. (b) Pedestal-supported photonic-crystal laser structure [51].

Microdisk lasers

In 1992, Levi and coworkers reported on a new microlaser design, based on the whispering-gallery resonances in a semiconductor microdisk resonator [42]. Lasing was obtained for pedestal-supported microdisks with 5-μm diameter under pulsed optical pumping, for temperatures up to 273 K. When cooled with liquid nitrogen, threshold pump powers were as low as 100 μW. In the same year, electrically-injected operation was demonstrated at room temperature [43].

Since then, many authors have reported on improved lasing performance in various microdisk laser configurations. In [44], continuous-wave electrically-injected lasing was obtained from a 3-μm-diameter pedestal microdisk, with a threshold of 150 μA. A typical microdisk structure is shown in figure 1.9 (a). They are typically fabricated through a combination of dry etching to define a cylinder, and a selective wet underetching step to create the post. Current is injected through the central posts, and carriers diffuse in the thin disk towards the disk edges, where they recombine and can contribute to the whispering-gallery lasing operation. In [45], a record-low threshold current of 40 μA was obtained at room temperature. The mechanical stability of the pedestal structure was improved in [46], by embedding them in a polymer material (BCB). Lasing was also obtained under pulsed operation in the visible spectrum, using ZnSe quantum wells for emission in the blue-green [47], and GaN for emission around 400 nm [48]-[49].

Lasing has also been demonstrated under optical pumping for microdisks with quantum-dot active materials [52]-[53]. A recent demonstration [54] features ultra-low threshold pumping powers ($\sim 1\,\mu$W) for an AlGaAs microdisk with embedded InAs quantum dots, emitting around 1.3 μm.

In [55], microdisk lasers were coupled to passive output waveguides, by means of active-passive integration on an InP substrate, using bonding technology to allow double-sided processing. For a 16-μm-diameter microdisk, the CW threshold current was 5 mA, with up to 4 μW/mA coupled into the waveguide.

First attempts to integrate these III-V microlasers onto silicon or glass were reported in [56]. In this work, InP-based pedestal microdisks were fabricated on silicon, by means of metallic bonding. Also, microdisks without pedestal were fabricated in a molecularly bonded InP film on a glass substrate. Lasing (optically pumped) was only possible at liquid-nitrogen temperatures. In [57], CW optically pumped lasing was achieved for an InP-based laser, molecularly bonded on a silicon wafer. Coupling to an underlying SOI waveguide was achieved for these optically pumped microdisks, by molecular bonding onto an SOI waveguide wafer (as part of the PICMOS project) [58]. By comparing the quality factors of coupled and uncoupled microdisks, the coupling efficiency was estimated to be around 35%. However, no absolute output powers were measured. In this PhD work, we have built further upon this result to achieve electrically-injected, SOI-coupled operation.

As already mentioned, optically-pumped lasing around 1.5 μm was also obtained in erbium-doped SiO_2 toroidal structures, with pumping thresholds around 4.5 μW, for a device with a diameter of 40 μm [13]. Lasing was made possible by reducing the loss of the resonator, as illustrated by the measured Q factor of 3.9×10^7, for a passive structure. In [59], an optically pumped ZnO-SiO_2 microdisk laser integrated on silicon was demonstrated at room temperature. Optical gain was provided by ZnO nanocrystals, coated on top of the disk.

Photonic-crystal microlasers

Planar two-dimensional photonic crystals (PhC) are excellent structures to achieve micron-sized, high-quality optical resonators. Painter et al. were the first to demonstrate optically-pumped lasing in a PhC cavity [60], albeit only when cooled to 143 K and with a relatively large threshold power (6.75 mW). Since then, substantial progress has been made to reduce the threshold power [61]-[62]. In a very recent effort, optically-pumped CW operation was achieved, with an effective threshold pump power of only 1 μW [63].

While many optically-pumped PhC microlasers have been demonstrated, the reports on addressing electrical injection of these microlasers are far less numerous. To our knowledge, the only successful attempt at achieving electrically-injected lasing operation in PhC microcavities has been performed by Lee and coworkers [51]. In this work, hole injection in the cavity is done through a bottom post, as is the case for microdisk lasers. Electrons are injected through a highly doped n-type layer. The microcavity is shown in figure 1.9 (b). Pulsed lasing was achieved under electrical pumping at room temperature, with a threshold current of 260 μA. By optimizing the cavity, the threshold has recently been reduced to 100 μA [64].

1.6.2 Electrically-injected heterogeneous Si-InP laser diodes

Prior to this work, in [65] continuous-wave lasing at room temperature was reported for an InP-based laser, emitting at 1.3 μm, fabricated in an InP film molecularly bonded onto a silicon substrate. The threshold current was only slightly higher than for a comparable laser on an InP substrate (49 mA vs. 40 mA). However, the laser output was not coupled into an on-chip waveguide.

In [66], a Fabry-Perot laser diode was fabricated in an InP-based film, bonded onto an SOI nanophotonic circuit, by means of adhesive BCB bonding. The laser output was coupled into an on-chip SOI wire waveguide, by means of an adiabatic coupling structure. The threshold current was relatively high ($10.4\,\mathrm{kA/cm^2}$ for a 500-μm-long laser), due to a poor laser facet quality (which were dry etched), which only allowed for pulsed operation. However, up to $0.9\,\mathrm{mW}$ optical power was coupled into the SOI wire. This work was also performed in the context of the PICMOS project.

Almost at the same time, in [67], continuous-wave operation at room temperature was reported for a Fabry-Perot laser diode, fabricated in a hybrid SOI/AlGaInAs waveguide. Molecular bonding was used to fabricate the hybrid waveguide, containing a large-core SOI rib waveguide with a InP-based gain layer on top. The waveguide design was optimized to have sufficient optical overlap with the gain medium, while keeping enough confinement in the SOI for efficient coupling to a passive on-chip SOI waveguide. The lasing threshold was 65 mA. Building further on this work, a race-track laser was demonstrated in [68], which avoided the requirement of cleaved laser facets. However, bend radii needed to be larger than 150 μm, in order to avoid excessive bending loss, which seriously limits the achievable integration density.

1.7 Thesis overview and results obtained

In Chapter 2, we give an overview of the challenges that have to be met when designing electrically-injected thin-film microlasers. We review the standard semiconductor laser diode theory, which is as much as possible applied to the specific case of thin-film microcavity designs. Based on the general theory and available results in literature, some promising microlaser designs are proposed. Finally, a brief survey is given on microcavity effects that can be expected for ultra-compact laser diodes, based on results reported in literature.

Chapter 3 then proceeds with a detailed theoretical analysis of the performance of a thin-film SOI-integrated microdisk laser. This laser type has been the main subject of study in this PhD work, mainly due to its excellent performance and relatively easy fabrication. First, the resonant modes in a microdisk are studied, with a detailed assessment of all the loss factors. Then, the electrical characteristics are evaluated, for a structure containing a tunnel junction, followed by a thermal analysis. Finally, a rigorous radially-dependent rate-equation model is used to predict the static lasing performance. A simplified model is used to estimate the dynamic characteristics. Finally, an alternative microdisk laser design is proposed, exhibiting a better tolerance to variations in the bonding layer thickness.

In Chapter 4, an overview is given of the fabrication procedure of the SOI-integrated microdisk laser, including the SOI processing, InP-Si bonding, and III-V processing of the microdisk cavity.

Chapter 5 gives an overview of the most significant experimental results, obtained on Si- and SOI-integrated microdisk lasers. First, the used measurement setups are illustrated, both for optical an electrical pumping. Then we proceed with a review of the measurement results of both Si- and SOI-integrated microdisk lasers. Finally, Chapter 6 gives overall conclusions and perspectives.

The main experimental result of this PhD work was the world-wide first successful demonstration of electrically-injected laser operation in a microdisk laser integrated on and coupled to a nanophotonic SOI waveguide circuit, at room temperature and under continuous-wave regime. Threshold currents were as low as 500 μA, and up to 20 μW/mA optical power was coupled into the SOI wire. Operating voltages were in the range 1.5-3 V. Additionally, a theoretical analysis of the laser performance was carried out. Using this theoretical model, the design parameters were optimized, resulting in a significant theoretical improvement of the laser performance. The majority of the results presented in this thesis text have been published in the scientific literature.

Chapter 2

Thin-film microlasers: general design aspects

In this chapter, we give an overview of the challenges that arise when designing electrically-injected thin-film microlasers. We review the standard semiconductor laser diode theory, which is as much as possible applied to the specific case of thin-film microcavity designs. Based on the general theory and available results in literature, some promising microlaser designs are proposed. Finally, a brief survey is given on microcavity effects that can be expected for ultra-compact laser diodes, based on results reported in literature.

2.1 Design goals

As mentioned in the introductory chapter, an integrated microlaser can have many applications. While the performance requirements are specific for the different applications, high-density integration generally requires small device footprint and low power consumption. For on-chip optical interconnect, the following requirements for the laser performance were identified in the framework of the PICMOS project:

1. compact laser footprint ($< 10 \times 10\,\mu\mathrm{m}^2$)
2. electrically injected operation
3. threshold current $< 150\,\mu$A
4. SOI-coupled slope efficiency $> 200\,\mu$W/mA
5. low operating voltage < 1.5 V, and preferably even lower
6. modulation speed at least equal to on-chip clock frequency (11 GHz for the 32-nm technology node)
7. operation at high ambient temperatures ($70\,^\circ C$ and higher)

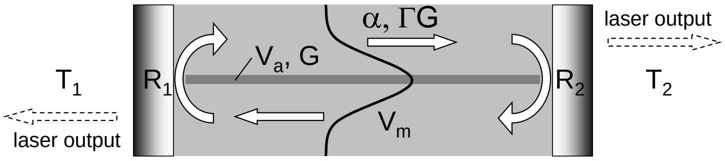

Figure 2.1: Schematic representation of a Fabry-Pérot laser

Coupling into a passive SOI-waveguide platform is considered here, since it features the highest interconnect density due to the high index contrast. However, if low latency is required, low-index polymer waveguides could be a better alternative, due to the higher propagation speed in this waveguide type [69].

2.2 Semiconductor laser resonances

2.2.1 Resonance condition

A laser is in general based on three key components: an active material that can amplify light by stimulated emission, an optical cavity that provides feedback to sustain the lasing action and a pumping mechanism that excites the active material to achieve population inversion. A photon traveling through a semiconductor can generate an identical second photon by stimulating the recombination of an electron-hole pair. This second photon has the same wavelength and phase as the original one, hence doubling the intensity of their monochromatic wave. By the competing process, photons can also be absorbed by generation of an electron-hole pair. Stimulated emission is therefore stronger than stimulated absorption only if more electrons are available in the conduction band than in the valence band. Thus, to achieve net optical gain, a semiconductor should be pumped to carrier inversion.

In order to achieve laser resonance, a fraction of the generated photons needs to be fed back into the laser cavity. Let's first consider the conventional Fabry-Perot laser type, as depicted in figure 2.1. For this cavity, two reflecting facets at both ends of the optical waveguide are used to achieve this optical feedback, with facet power reflectivities R_1 and R_2. They reflect a fraction R_i of the arriving photons back into the cavity, while a fraction $T_i = 1 - R_i$ is emitted as laser emission. The optical mode – guided by the waveguide – experiences a modal propagation loss α per unit length, for instance due to waveguide imperfections. Simultaneously, it is amplified by a factor ΓG per unit propagation length, where G is the optical material gain in the active region, and Γ is the optical confinement factor, which describes the overlap of the optical mode with the active region. The photon round-trip gain is then given by:

$$\text{round-trip gain} = R_1 R_2 e^{(\Gamma G-\alpha)2L} = e^{(\Gamma G-\alpha-\alpha_{mir})2L}, \tag{2.1}$$

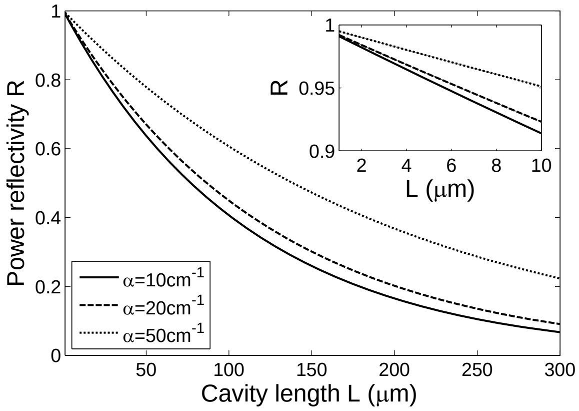

Figure 2.2: Minimum required mirror reflectivity to achieve lasing resonance versus cavity length and propagation loss.

where L is the laser cavity length. From this equation, it is clear that the local losses at the facets can also be considered as a distributed loss α_{mir}

$$\alpha_{mir} = -\frac{1}{2L} \ln\left(\frac{1}{R_1 R_2}\right) \tag{2.2}$$

The material optical gain G increases with increasing hole and electron concentrations in the active material. Lasing threshold is reached when the round-trip gain is unity, or equivalently, when

$$\Gamma G_{th} = \alpha_{tot} = \alpha + \alpha_{mir}, \tag{2.3}$$

where G_{th} is the threshold material gain. For a laser with two identical mirrors with reflectivity R, the required mirror reflectivity for achieving lasing resonance for a given loss α and a maximum modal gain ΓG_{max} can be calculated as

$$R_{min} = e^{-L(\Gamma G_{max} - \alpha)}. \tag{2.4}$$

From this equation, it can be seen that the required facet reflectivity R_{min} increases exponentially with decreasing cavity length L. Therefore, when designing microcavity lasers, specific attention has to be paid to the design of highly reflective cavity mirrors. This is illustrated in figure 2.2, where R_{min} is plotted as function of L for different α values, assuming a maximum modal gain $g_{max} = 100\,\mathrm{cm}^{-1}$, typical for InP-based lasers. For cavities shorter than $5\,\mu$m, the required mirror reflectivity exceeds 95%.

However, most optical microcavities support resonances of a more complicated nature than the simple 1-D laser mode of a Fabry-Perot resonator. Therefore, their optical loss is characterized by the quality factor or Q factor, which is a more general loss metric as opposed to mirror reflectivity and internal loss per unit length. The Q

factor can be measured easily, by inspecting the resonance linewidth $\delta\nu$ and using

$$Q = \frac{\nu_0}{\delta\nu}, \tag{2.5}$$

where ν_0 is the frequency of the resonance.

The resonance linewidth $\delta\nu$ is inversely proportional to the photon lifetime τ_p in the cavity:

$$\delta\nu = \frac{1}{2\pi\tau_p}. \tag{2.6}$$

However, τ_p can also be expressed as

$$\tau_p = \frac{1}{v_g\alpha_{tot}} = \frac{n_g}{c\alpha_{tot}}, \tag{2.7}$$

where v_g is the group velocity and $n_g = c/v_g$ the group index of the optical mode. Therefore, the Q factor relates with the total loss α_{tot} as

$$Q = \frac{2\pi n_g}{\alpha_{tot}\lambda_0}, \tag{2.8}$$

where λ_0 is the resonance wavelength. Assuming a maximum modal gain $\Gamma G = \alpha_{tot} = 100\,\mathrm{cm}^{-1}$, a group index $n_g = 3$ and $\lambda_0 = 1.55\,\mu$m results in a minimum required Q factor of 1216 to achieve laser resonance.

Lasing wavelength

In addition to the resonance condition (2.3), requiring unity round-trip gain, the resonance condition for the *phase* of the optical field requires a round-trip phase of $2\pi M$, where M is an integer. This condition can be written as

$$2L\frac{2\pi}{\lambda}n_e + \angle r_1 + \angle r_2 = 2\pi M, \tag{2.9}$$

where n_e is the effective index of the waveguide and $r_{1,2}$ is the amplitude reflectivity of mirror 1 or 2. Assuming – for simplicity – zero phase contribution from the mirrors, we obtain resonant wavelengths λ_M

$$\lambda_M = \frac{2Ln_e}{M}. \tag{2.10}$$

The resonant mode spacing $\Delta\lambda$ is derived as

$$\Delta\lambda = \frac{\lambda^2}{2Ln_g}, \tag{2.11}$$

where n_g is the waveguide group index. For a conventional Fabry-Perot laser with $L = 500\,\mu$m, $n_g = 3$ and $\lambda = 1.5\,\mu$m, one finds $\Delta\lambda = 1.5\,$nm. Since the optical gain typically has a spectral width of 50-100 nm, many modes can be lasing, at wavelengths around the peak optical gain wavelength. The spectral mode spacing increases rapidly with reducing cavity length. For a microlaser with $L = 10\,\mu$m, we find $\Delta\lambda = 75\,$nm. In this case, only one lasing mode will be spectrally aligned with the optical gain spectrum, resulting in single-mode lasing.

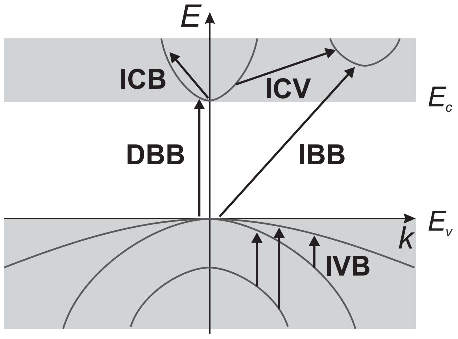

Figure 2.3: Absorption processes in a direct band semiconductor.

2.2.2 Parasitic photon losses

The propagation loss α in the laser cavity can have several contributions of different physical nature. In general, losses are due to internal absorption in the waveguide material (α_{int}) or are caused by external waveguide non-idealities, such as scattering at roughness at the waveguide surfaces (α_s) or radiation loss for leaky waveguide types (α_r). Moreover, since we are targeting electrically injected microlasers in thin semiconductor films, metal contacts need to be applied, which could be in close proximity with the optical field, thereby causing additional absorption (α_m). The total propagation loss can then be written as

$$\alpha = \alpha_{int} + \alpha_m + \alpha_s + \alpha_r. \tag{2.12}$$

Since none of the losses included in α contribute to the laser output, they can be considered as parasitic, and should be minimized to achieve optimum device performance.

Internal absorption loss α_{int}

The absorption processes in a direct band semiconductor are shown in figure 2.3 [35]. They include direct and indirect band-to-band absorption (DBBA and IBBA), intervalence-band absorption (IVBA), intraconduction-band absorption (ICBA) and intraconduction-band-valley absorption (ICVA). Obviously, these absorption mechanisms depend strongly on the wavelength of the interacting light. DBBA and IBBA are only important for wavelengths smaller than the bandgap wavelength λ_G of the semiconductor. For $\lambda > \lambda_G$, DBBA and IBBA decays and internal absorption is dominated by free-carrier losses (FCA) due to IVBA, ICBA and ICVA. FCA scales roughly linearly with the free-carrier concentrations n and p, so the material absorption coefficient can be written as

$$\alpha_{FCA} = k_n n + k_p p \tag{2.13}$$

FCA scales with wavelength as λ^s, with $s = 2 - 3$. Typical values for k_n at $1.55\,\mu$m for bulk InP/InGaAsP are $1 - 2 \times 10^{-18}$cm^2. k_p is in the range $20 - 60 \times 10^{-18}$cm^2 for

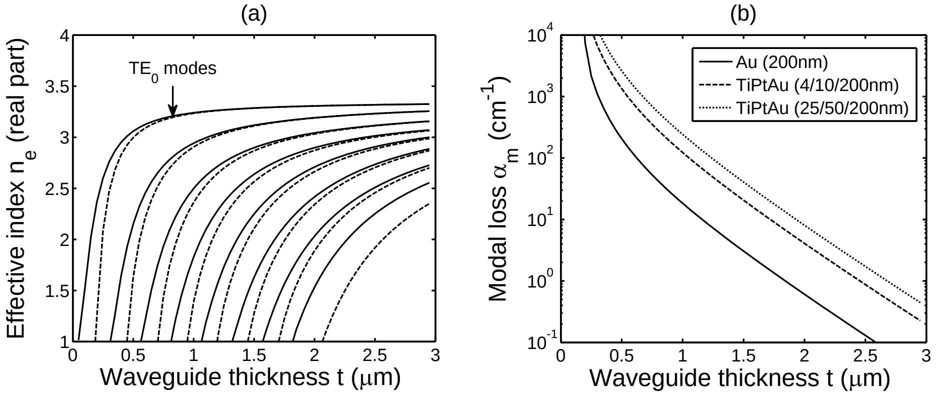

Figure 2.4: (a) Real part of the effective index n_e for an InP-based film waveguide, with (solid lines) and without (dashed lines) Au cladding, versus film thickness t (TE polarization). (b) Modal propagation loss of the fundamental TE$_0$ mode due to metal absorption, for various Au-based metal cladding versus waveguide thickness t. For both graphs, the InP waveguide contains a Q1.25 core with thickness $t/2$, and the wavelength is $1.55\,\mu$m.

bulk InP/InGaAsP [35], with in general lower values for InP than for InGaAsP. From these coefficients, it can be seen that FCA loss in p-type layers is much stronger than for n-type layers with the same doping level. For quantum wells, k_p is in the range $30 - 140 \times 10^{-18}$cm^2, depending on the material strain.

The modal internal loss α_{int} can for a given laser waveguide design be calculated as

$$\alpha_{int} = \Gamma_n k_n N_d + \Gamma_p k_p N_a + \Gamma_{BB} \alpha_{BB}^M, \tag{2.14}$$

where $\Gamma_{n/p}$ is the optical confinement factor of the n/p-type layer, $N_{a/d}$ are the acceptor and donor concentrations, and Γ_{BB}, α_{BB} are the confinement factor and material absorption of waveguide layers with $\lambda < \lambda_G$. Loss contributions from non-intentionally doped regions containing injected carriers should also be included in equation 2.14. Since optically thin films mostly exhibit tight optical confinement, the confinement factors $\Gamma_{n/p}$ will in general be relatively high, even when the doped layers are thin. Therefore, the position, size and doping level of highly p-type doped layers needs particular attention when designing a thin-film laser cavity.

Metal absorption loss α_m

A straightforward approach to electrically contact a thin-film optical resonator, is to add metal contacts at both thin-film surfaces. This approach is expected to exhibit optimal electrical injection efficiency. However, coating an optically thin film strongly alters the optical waveguiding properties, resulting in a modified dispersion relation and an excessive increase in optical absorption at the metal contacts. For a given operating wavelength and mode number, the strongest impact occurs near the cut-off thickness.

To illustrate this, we have calculated the effective index n_e of the guided modes of an InP-based thin-film slab waveguide, with and without Au coatings. In figure 2.4 (a), the real part of n_e is plotted as function of the waveguide thickness t, for a number of TE-polarized modes (**E** field parallel to film surface). It can be seen that the cut-off conditions change by applying the metal cladding. When t is much larger than the cut-off thickness of the non-metallized InP-waveguide, n_e of the gold-clad waveguide converges to that of the film with air cladding layers.

The modal loss of the TE_0 mode is plotted in figure 2.4 (b). Various Au-based metallizations were considered, including a pure Au and two TiPtAu-based metallizations: one with very thin Ti and Pt layers (4/10 nm) and one with slightly thicker Ti and Pt layers (25/50 nm). It can be seen that the lowest modal loss is obtained by applying a pure Au metallization, and that it increases with increasing Ti and Pt layer thickness. In general, noble metals such as Au, Ag and also Cu and Al result in the lowest absorption loss, whereas metals such as Ti, Pt and Ni yield much higher loss. This can be understood by inspecting their (complex) refractive index $n_{metal} = n_R - n_I j$, with $n_R, n_I > 0$. For wavelengths around $1.55\,\mu$m, noble metals have n_R values that are much smaller than n_I, and are therefore closer to the optical behavior of the ideal non-absorbing metal – which has a vanishing n_R and infinite n_I – as compared to non-noble metals. Gold for instance has $n = 0.56 - 9.81j$ at $1.55\,\mu$m, whereas Ti has approximately $n = 3.7 - 4.5j$. Therefore, from an optical point of view, the use of non-noble metals in close proximity with the optical field should be avoided. However, the standard, reliable metal contacts to InP involve the use of Ti and Pt. Ti is typically added to increase the adhesion of the Au film to the semiconductor, whereas the Pt layer acts as a diffusion barrier for Au, avoiding excessive Au-InP interaction during thermal annealing.

We will further discuss the options to achieve adequate electrical contact together with low optical loss in chapter 4. However, even when using a pure Au contact, when modal losses below $10\,\text{cm}^{-1}$ are required, the waveguide should be more than $1\,\mu$m thick. For this waveguide thickness, the film supports four TE-polarized modes, which could complicate the design of a resonator based on this type of waveguide. For standard TiPtAu contacts, the waveguide should be thicker than $2\,\mu$m. When thinner films are needed, a different contacting design should be used.

Radiation loss α_r

Radiation loss occurs in a waveguide when material with a refractive index larger than the effective index of the waveguide mode is present in the vicinity of the waveguide core. An illustrative example of such a situation can be found in the case of substrate loss. Consider the thin-film slab waveguide consisting of a thin InP film bonded onto a Si substrate with a SiO_2 bonding layer with thickness t_{ox}, as shown in figure 2.5. Since the Si substrate has a higher index than the InP waveguide core, truly guided modes don't exist. Since the mode decays exponentially in the cladding, the leakage into the Si substrate depends exponentially on the SiO_2 thickness, as is shown in figure 2.5 (a), for TE modes. For a 300-nm-thick InP slab, a SiO_2 of at least 550 nm is needed to obtain a substrate loss lower than $1\,\text{cm}^{-1}$. The **E**-field mode pro-

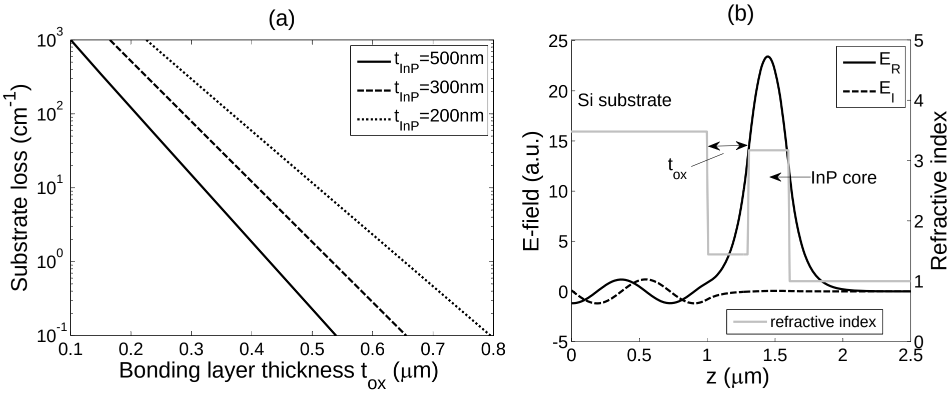

Figure 2.5: (a) Substrate loss for a thin-film slab waveguide consisting of a InP film bonded on a Si substrate vs. bonding layer thickness (TE modes, $\lambda = 1.55\,\mu$m). (b) **E**-field profile for $t_{ox} = t_{InP} = 300\,$nm.

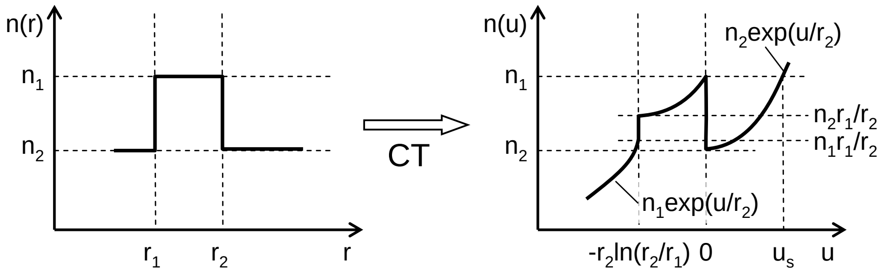

Figure 2.6: Conformal transformation, mapping a bent waveguide in the xy plane (or $r\varphi$ plane) to an equivalent straight waveguide in the uv plane.

file for $t_{ox} = 300\,$nm is shown in (b), illustrating the radiative character of the mode in the Si substrate.

Another example of this type of loss, relevant for microlaser design, is the radiation loss in bent waveguides, as used in microring and microdisk resonators. A common approach to calculate the waveguide properties of a curved waveguide is to apply a conformal transformation from the xy plane, or $r\varphi$ plane, containing the curved waveguide, to a uv plane such that the bent waveguide is transformed to a straight waveguide, albeit with a modified refractive index profile [70]. The conformal transformation that converts the original plane $z = re^{j\varphi} = x + jy$ into the new plane $w = u + jv$ is given by

$$w = f(z) = r_2 \ln(\frac{z}{r_2}). \tag{2.15}$$

Applying $f(z)$ to the the original Helmholtz equation then leads to

$$\left[\nabla_z^2 + k_0^2 n^2(r)\right] E(r,\varphi) = 0 \rightarrow \left[\nabla_w^2 + k_0^2 n^2(u)\exp(\frac{2u}{r_2})\right] E(u,v) = 0. \qquad (2.16)$$

This procedure is illustrated in figure 2.6. The resulting effective index profile $n(u)$ increases exponentially with increasing u. As a result, there will always exist a point u_s such that, for all $u > u_s$, we find $n(u) > n(0)$. Therefore, a bent waveguide always features a fundamental radiation loss that increases with decreasing bend radius and decreasing index contrast.

Scattering loss α_s

Light propagating in a waveguide can be scattered at imperfections at the waveguide sidewalls that are present due to imperfect fabrication. The amount of surface roughness can be statistically quantified by the root-mean-square (rms) value of the roughness σ and its correlation length L_c. Apart from these two parameters, the shape of the auto-correlation function should also be given for a complete description. Several functions are used in literature, including exponential, lorentzian and gaussian functions. For the latter, the exact formulation is given by

$$C(l) = \sigma^2 e^{-\pi(l/L_c)^2} \qquad (2.17)$$

In practice, the roughness auto-correlation function is fitted to experimental data obtained by scanning the sidewall profile, for instance with an AFM probe [71]. Typical values for InP-based waveguides are 3-20 nm for σ and 30-500 nm for L_c [71]-[72]-[73].

A simple expression for the scattering loss in traditional low index-contrast waveguides was formulated by Tien [74]:

$$\alpha_s = 2\sigma^2(n_1^2 - n_2^2)k_0^2\frac{k_x}{\beta}E_s^2, \qquad (2.18)$$

with n_1 the core refractive index, n_2 the cladding refractive index, k_x the transverse propagation constant in the cladding, β the propagation constant in the propagation direction and E_s the normalized electrical field at the waveguide edge. However, since the model doesn't include any information on the length scale of the roughness, its general validity is questionable. Nevertheless, this formula reveals a general rule of thumb that the scattering loss scales with increasing index contrast.

Due to the increasing interest in ring and disk-shaped optical resonators over the last twenty years, several authors have reported on theoretical calculations and experimental verification of scattering loss in such resonators [75][76][77]. The calculations are based on the volume-current method, and show very good agreement with experiment. Recently, a generalized and closed-form formulation for the scattering loss in microdisk resonators was derived in [77]. For an optically thin microdisk with thickness t and radius R, the loss is given by

$$\alpha_s = \frac{16\pi^3}{3R}\left(n_1^2 - n_2^2\right)^2\frac{\sigma^2 L_c}{n_1}\frac{t}{\lambda^4}. \qquad (2.19)$$

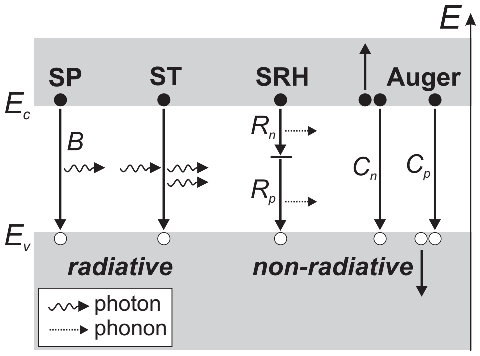

Figure 2.7: Carrier recombination processes

Again, it can be seen that α_s increases strongly with increasing index contrast, as opposed to the bending loss. The main limitation of this formula is that it is only valid for $L_c \ll \lambda/(2n_2)$.

2.2.3 Photon extraction efficiency

Next to the parasitic photon loss factors described in 2.2.2, the photon extraction that represents the useful laser emission acts as another loss factor α_u. In general, the photon extraction efficiency is given by

$$\eta_e = \frac{\alpha_u}{\alpha_{tot}} = \frac{\alpha_u}{\alpha_u + \alpha}. \tag{2.20}$$

For the Fabry-Perot laser, we have $\alpha_u = \alpha_{mir}$.

For a (micro-)resonator characterized by Q factors, we find

$$\eta_e = \frac{Q_{tot}}{Q_u}. \tag{2.21}$$

In this equation, Q_u is the quality factor associated with the useful loss, and Q_{tot} that of the total loss. They relate as

$$\frac{1}{Q_{tot}} = \frac{1}{Q_u} + \frac{1}{Q_{par}}, \tag{2.22}$$

where Q_{par} is the quality factor associated with the parasitic loss.

2.3 Carrier recombination and optical gain

2.3.1 Carrier recombination mechanisms

Radiative recombination

Carriers that are injected in a semiconductor by optical or electrical pumping can recombine in many ways, as illustrated in figure 2.7. First, they can recombine *radiatively* by emitting a photon, which can happen spontaneously or stimulated by an already present photon. The spontaneous emission rate for bulk material R_{sp} can – under the ambipolar approximation – be written as

$$R_{sp} = BN^2, \tag{2.23}$$

where N is the carrier concentration and B is a material parameter. Typically, $B \simeq 1 - 2 \times 10^{-10}\,\text{cm}^3 s^{-1}$ for InP-based semiconductors. Stimulated emission is the dual process of DBBA and is the origin of optical gain. It will be discussed in more detail in the next section.

Shockley-Read-Hall recombination

Non-radiative recombination occurs in III-V semiconductors by three dominant mechanisms. The first is Shockley-Read-Hall (SRH) recombination. It occurs when a carrier is trapped by a defect with energy level deep inside the band gap and recombines before it is released again. The SRH recombination rate is given by

$$R_{SRH} = AN. \tag{2.24}$$

For modern growth technologies, the defect concentration is low and SRH recombination is negligible compared with other carrier loss mechanisms ($A \approx 10^8\,\text{s}^{-1}$).

Auger recombination

In an Auger recombination event, the energy of an electron-hole recombination is transferred to a second electron or hole, exciting it within its respective band. This excited carrier then relaxes by emitting phonons. In the ambipolar approximation, the Auger recombination rate R_A can be written as

$$R_A = CN^3. \tag{2.25}$$

At room temperature, C lies typically in the range $10^{-29} - 10^{-27}\text{cm}^6 s^{-1}$ for InGaAsP materials [35]. It is also temperature dependent:

$$C(T) = C_0 \exp\left(\frac{-E_a}{k_B T}\right), \tag{2.26}$$

where T is the temperature, k_B the Boltzmann constant and typically $C_0 \simeq 2 \times 10^{-27}\text{cm}^6 s^{-1}$, and the activation energy $E_a \simeq 60\,\text{meV}$.

Surface recombination

Finally, carriers can recombine via the interface states at the surfaces of the semiconductor. The recombination mechanism is analogous to SRH recombination, however in the present case, the traps arise due to dangling bonds at the exposed surface, as a two-dimensional sheet density. Assuming a uniform carrier density N, the recombination rate can be written as

$$R_{sr} = \frac{A}{V} v_s N, \tag{2.27}$$

with A the exposed area, V the semiconductor volume and v_s the surface recombination velocity. v_s depends on the material, and increases strongly with increasing Ga content. GaAs for instance has $v_s \sim 5 \times 10^5$cm/s, whereas InGaAs has $v_s \sim 1 \times 10^5$cm/s and InP has $v_s \leq 1 \times 10^4$cm/s. v_s also depends on the surface condition, and passivation treatment with sulfur-containing compounds has been found to drastically reduce surface recombination in GaAs-based lasers [78]. Given the A/V dependence in (2.27), surface recombination can be problematic in microlasers, since they have a large surface-to-volume ratio.

2.3.2 Optical gain

The optical gain in a semiconductor for a transition from level i in the valence band to level j in the conduction band, with a transition energy $E_{ij} = E_j - E_i$ can be derived from Fermi's Golden Rule to be [79]:

$$G_{ij}(E_{ij}) = G_{max}(E_{ij})(f_j - f_i) \tag{2.28}$$

with

$$G_{max}(E_{ij}) = \frac{q^2 h}{2m_0^2 \varepsilon_0 nc} \frac{1}{E_{ij}} |M(E_{ij})| \rho_r(E_{ij}). \tag{2.29}$$

The second factor in (2.28) is a measure for the inversion level and thus depends on the injection level. It involves the Fermi factors f_i and f_j, which denote the occupation probabilities and are defined as

$$f_i = \frac{1}{e^{(E_i - E_{Fv})/kT} + 1} \tag{2.30}$$

$$f_j = \frac{1}{e^{(E_j - E_{Fc})/kT} + 1} \tag{2.31}$$

where E_{Fv} and E_{Fc} are the quasi-Fermi level in the valence and conduction band respectively. f_i and f_j can take values in between 0 and 1. As a result, the optical gain has a minimum of $-G_{max}$ (absorption) without pumping and saturates at high pumping levels to G_{max}. Net optical gain is achieved when the active material is pumped to inversion, that is $f_j > f_i$. This is approximately equivalent with $E_{Fc} - E_{Fv} > E_G$, where E_G is the band gap energy of the active material. Therefore, electrically injected lasers have to be biased at least above E_G/q to achieve laser output.

The maximum optical gain $G_{max}(E)$ at an optical frequency $\nu = E/h$ is a material parameter. As can be seen from (2.29), it depends on the refractive index n_r, but more importantly, on the transition matrix element $|M(E_{ij})|$ and the reduced density of states (DOS) $\rho_r(E_{ij})$. The transition matrix element describes the strength of the stimulated transition. It contains the overlap of the envelope functions of the interacting carrier states, which results in *allowed* and *forbidden* transitions, depending on the symmetry of the involved states. It can also be polarization-sensitive, since the interaction strength depends on the angle between the electron wave vector and the optical field vector ([79], [35]). It can be considered to be a constant for a given material system and given polarization[1].

The reduced density of states $\rho_r(E_{ij})$ depends strongly on the (quantum) confinement of the carriers in the active material. It is the main property that can be engineered to tailor the gain properties of a semiconductor active material. We shall briefly discuss this effect for bulk material (no quantum confinement), quantum wells (one-dimensional confinement) and quantum dots (three-dimensional confinement) below.

The lineshape of the optical transition is in general broadened due to the fact that the involved carriers interact with other carriers and phonons, thereby changing their energy. These scattering events typically occur every $\tau_{in} = 0.1\,\text{ps}$ at room temperature, which is much more frequent than radiative recombination events. As a result, the gain can be expressed as

$$G(h\nu) = \int G_{ij}(E_{ij})L(h\nu - E_{ij})dE_{ij}, \tag{2.32}$$

with

$$L(h\nu - E_{ij}) = \frac{1}{\pi}\frac{\hbar/\tau_{in}}{(\hbar/\tau_{in})^2 + (h\nu - E_{ij})^2}. \tag{2.33}$$

This *homogeneous* broadening limits the resolution of features in the gain spectrum, which is of particular importance for active materials with high quantum confinement (see below). The band structure and gain spectrum is shown schematically in fig. 2.8.

Bulk

For a bulk active layer with dimensions much greater than the de Broglie electron wavelength, carriers can move around as quasi-free particles obeying a parabolic-like dispersion relation near the band extremes[2]. The reduced density of states $\rho_r(E)$ is given by the well-known expression

$$\rho_r^{3D}(E) = \frac{1}{2\pi^2}\left(\frac{2m^*}{\hbar^2}\right)^{3/2}\sqrt{E - E_g} \tag{2.34}$$

---

[1] Excitonic effects can have a severe impact on M

[2] Band intermixing can result in strongly non-parabolic valence bands, also near the band extreme. In this case, the $\mathbf{k}\cdot\mathbf{p}$ perturbation method should be used to get a more accurate band dispersion relation.

with m^* the reduced carrier mass (see fig. **??**). For typical carrier densities, the peak gain depends in good approximation linearly on the carrier density:

$$G(N) = G_0(N - N_0) \tag{2.35}$$

where $G_0 = dG/dN$ is the differential gain and N_0 is the transparency carrier density. Typical values at room temperature are $G_0 = 4 \times 10^{-16}\,\mathrm{cm}^2$, $N_0 = 1.85 \times 10^{18}\,\mathrm{cm}^{-3}$ for bulk GaAs ($\lambda = 0.85\,\mu$m), and $N_0 = 1.1 \times 10^{18}\,\mathrm{cm}^{-3}$ for bulk $\mathrm{In}_{0.53}\mathrm{Ga}_{0.47}\mathrm{As}$ ($\lambda = 1.5\,\mu$m) [79].

Quantum wells

In a quantum well, carrier motion is restricted to the plane of the quantum well, which results in quasi-parabolic subbands. As a result, $\rho_r(E)$ contains a summation over all possible subband pairs. The summation can be restricted to pairs with the same quantum number, since the transition rates for other combinations are very low because in this case the transition matrix element is virtually zero due to symmetry mismatch (forbidden transition). This results in a staircase-like $\rho_r(E)$, with a discontinuity for energies E_m where a next subband pair comes into play:

$$\rho_r^{2D}(E) = \frac{2}{d_z} \sum_m \frac{m^*}{\pi\hbar^2} H(E - E_G - E_m) \tag{2.36}$$

with d_z the thickness of the quantum well, typically 3-15 nm. $H(x)$ the heaviside function (see fig. 2.8). In general, the gain from the lowest order subband pair is dominant. At high pumping levels, optical transitions from the second subband pair also contribute to the gain. The reduced DOS discontinuity is smoothed out in the gain spectrum at room temperature due to homogeneous broadening. The peak gain is in good approximation a logarithmic function of the carrier density:

$$G(N) = G_0 \ln\left(\frac{N}{N_0}\right) \tag{2.37}$$

where G_0 is the gain parameter and N_0 is the transparency carrier density. Typical values at room temperature are $G_0 = 2400\,\mathrm{cm}^{-1}$, $N_0 = 2.6 \times 10^{18}\,\mathrm{cm}^{-3}$ for GaAs-based quantum wells ($\lambda = 0.85\,\mu$m), and $G_0 = 1800\,\mathrm{cm}^{-1}$, $N_0 = 2.2 \times 10^{18}\,\mathrm{cm}^{-3}$ for InP-based quantum wells ($\lambda = 1.5\,\mu$m) [79].

Strain ($\pm 1 - 2\%$) can be incorporated into the quantum well by growing it in between barriers with a slightly different lattice constant. Compressive strain (+) occurs if the lattice constant of the quantum well material is larger than that of the surrounding barriers, and tensile strain (−) in the opposite situation. The thickness of the strained quantum well has a critical maximum. Exceeding this thickness results in increased non-radiative recombination due to an increased density of lattice defects. Strain has a big impact on the band structure of the active material and can have beneficial effects on the gain, by reducing the transparency carrier density and/or improving the differential gain. Compressive strain typically favors TE-polarized gain while quantum wells with tensile strain have larger TM gain. Typical

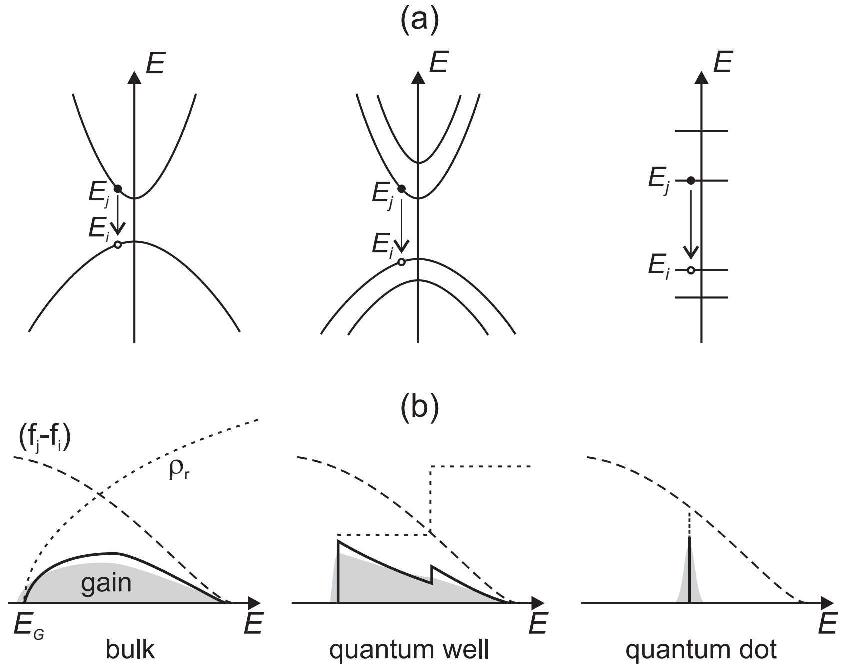

Figure 2.8: (a) Band structure. (b) Gain spectrum

values for strained InGaAs quantum wells are $G_0 = 4000\,\text{cm}^{-1}$, $N_0 = 3.3\times10^{18}\,\text{cm}^{-3}$ for $+1\%$ strain and $G_0 = 2300\,\text{cm}^{-1}$, $N_0 = 1.7\times10^{18}\,\text{cm}^{-3}$ for -1% strain [79]. Strained quantum wells outperform both bulk material and unstrained quantum wells in terms of peak optical gain.

Quantum dots

For ideal quantum dots (QD), carrier confinement is perfect. The reduced density of states features discrete peaks, at energies that agree with allowed transitions between the discrete electron and hole states. These states can be labeled by three mode numbers m, n and p. Higher-order carrier states can be degenerate when several (m, n, p) combinations have the same energy. $\rho_r(E)$ is then given by

$$\rho_r^{0D}(E) = \frac{2}{d_x d_y d_z} \sum_{m,n,p} \delta(E - E_G - E_{mnp}), \tag{2.38}$$

with d_x, d_y and d_z the dimensions of the quantum dot (see fig. 2.8). From these considerations, quantum dot active layers are expected to have a narrow gain spectrum, a reduced transparency carrier density and to have better performance at high temperatures. The precise mechanism behind gain in quantum dots is currently not completely understood. It appears that excitons play a significant role, especially at

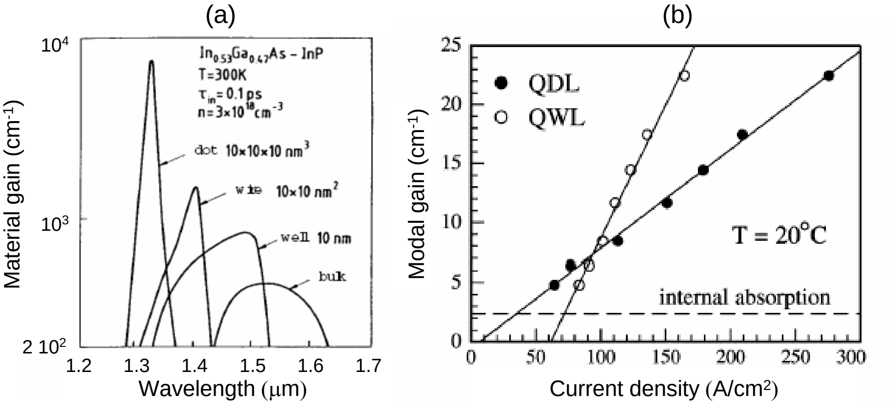

Figure 2.9: (a) Gain spectrum and peak material gain versus injected current for different quantum confinement. Reproduced from [81]. (b) Comparison of QW and QD modal gain ($\lambda = 980\,\mathrm{nm}$) as function of current density [82].

lower temperatures [80]. Some theoretical work indicates that the intrinsic material gain in a quantum dot can be as large as $50000\,\mathrm{cm}^{-1}$ (see fig. 2.9) [81],[83].

However, experimental modal gains measured in real, short-wavelength ($\lambda < 1\mu$m) quantum-dot devices are typically smaller than for comparable quantum-well devices, although with a lower transparency current (see fig. 2.9). For longer wavelengths, the saturated modal gain per quantum-dot layer is currently only about 3-10 cm^{-1} for the ground state transition ([82],[80]). The maximum gain from higher-order transitions is higher than that of the fundamental transition, due to their degeneracy. These low modal gains are due to several reasons. First, the quantum-dot sheet density is limited to about $3 \times 10^{10}\mathrm{cm}^{-2}$ with current fabrication methods, which results in low optical confinement factors Γ (< 0.005 per QD layer). Second, current fabrication methods yield quantum-dot layers with a strong size dispersion, which results in strong inhomogeneous broadening of the transition linewidth on top of the homogeneous linewidth broadening, together with a strongly reduced maximum gain.

The maximum modal gain can be increased by stacking several QD layers on top of each other. However, for situations where high gain is required, quantum wells are still a better choice. For lasers with low internal loss and a low distributed mirror loss, QD lasers outperform their quantum-well counterparts in terms of threshold current, with a record threshold current density of $33\,A/\mathrm{cm}^2$ [84]. However, it can be expected that the ongoing research in this field will yield QD layers with higher modal gains, also for telecom wavelengths. A big step in that direction was taken in [85], where a modal gain of $66.5\,\mathrm{cm}^{-1}$ at $1.5\,\mu$m was obtained from InAs QDs on a GaAs substrate.

Possible advantages of QD active layers over QWs include a reduced laser chirp and reduced lateral carrier diffusion. The latter can lead to improved current con-

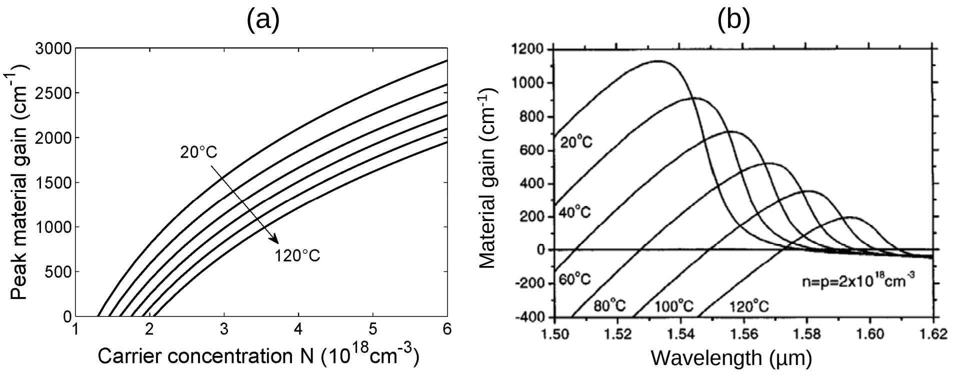

Figure 2.10: (a) Calculated quantum well peak material gain versus carrier concentration N, for increasing temperature. (b) Calculated gain spectrum for $N = 2 \times 10^{18}\mathrm{cm}^{-1}$ for increasing temperature [35].

finement, reduced surface recombination and diffusion-related parasitic effects during laser modulation.

Temperature dependence

With increasing temperature, the carriers are thermally excited to higher energy levels, resulting in a smoother Fermi distribution. For a given carrier density, this results in a lower $(f_j - f_i)$ factor, and thus in a lower material gain. The calculated peak material gain of a $+1\%$-strained 6.4-nm-wide InGaAsP quantum well is plotted as function of carrier concentration and temperature in figure 2.10 (a) [35]. This data can in good approximation be fitted to a temperature dependent gain coefficient $G_0(T)$ and transparency carrier density $N_0(T)$ as

$$G(N,T) = (G_{0i} + G_{0s}T)\ln\left(\frac{N}{N_{0i} + N_{0s}T}\right) \tag{2.39}$$

Together with a decrease of the peak gain, the gain spectrum shifts to longer wavelengths, as a result of bandgap shrinkage with increasing temperature. For InGaAsP quantum wells, the red shift is about $0.54\,\mathrm{nm/K}$ [35]. This effect is illustrated in figure 2.10 (b).

It could be expected that the peak gain in quantum dots is less temperature dependent, as the available carrier states have discrete energy levels, thus hampering thermal carrier excitation. Shchekin et al. report in [86] on a 1.3-μm QD-laser with a characteristic temperature for the threshold current (see section 2.5.5) of more than 160 K at room temperature and above, by optimizing p-type doping of the barrier material. However, this improvement went at the expense of higher threshold current at room temperature.

2.4 Electrical injection

2.4.1 Basic elements

The p-i-n junction

To achieve carrier inversion in the active region by electrical pumping, the active region is typically grown in the intrinsic region of a p-i-n junction. For a given carrier density N in the active region, the voltage drop V_d over this diode can be approximated by

$$V_d = V_0 \ln\left(1+\frac{N}{N_e}\right) = \frac{nk_BT}{q}\ln\left(1+\frac{N}{N_e}\right), \tag{2.40}$$

with n the diode ideality factor and N_e the equilibrium carrier density in the active region. The current in laser diodes is dominated by recombination current in the active region and therefore $n \simeq 2$.

Metal-semiconductor contacts

The metal-semiconductor contacts are the electrical interface between the laser diode and the electronic circuit. In order to obtain ultimate device performance, these contacts should be *ohmic*, requiring the contact voltage drop to be small as compared to the diode voltage, which equals approximately to E_G/q for achieving inversion. Assuming a contact area of 100 μm^2, the specific contact resistivity ϱ_c should be lower than $10^{-5}\,\Omega$cm^2 to obtain a contact voltage drop smaller than 10 mV.

When a metal is deposited on a semiconductor, band bending will occur in the semiconductor in order to line up the Fermi levels in the metal and the semiconductor, as well as the vacuum potentials. In most cases, this band bending results in the formation of a Schottky barrier Φ_B that needs to be overcome by carriers in order to flow from the metal into the semiconductor. For an ideal Schottky contact, the barrier height is given by

$$\begin{aligned} \Phi_{Bn} &= \Phi_M - \chi - \Delta\phi & (2.41)\\ \Phi_{Bp} &= E_G/q - \Phi_M + \chi - \Delta\phi & (2.42) \end{aligned}$$

where Φ_{Bn} is the barrier for an n-type contact, Φ_{Bp} for a p-type contact, Φ_M is the metal work function, χ the electron affinity of the semiconductor, and $\Delta\phi$ is the image-force barrier-lowering potential[3]. For the n-type contact, the barrier can be lowered by using a metal with a low work function Φ_M. For the p-type contact, a large Φ_M is needed, to overcome both the bandgap and electron affinity of the semiconductor.

However, for many semiconductor-metal contacts, the measured barrier height cannot be predicted by the simple model (2.41)-(2.42). Indeed, this simple model doesn't account for surface states at the metal-semiconductor interface. For a semiconductor with a large surface-state density, the band bending is completely determined by the surface properties and the semiconductor doping level. In this case, the Fermi level is pinned to a value $q\Phi_0$ above the valence band, and thus doesn't depend on the metal work function. The barrier height can then be expressed as

---

[3] which amounts for $\Delta\phi = \sqrt{\frac{q\mathcal{E}}{4\pi\varepsilon_0}}$, where $\mathcal{E}$ is the applied electrical field.

$$\begin{aligned} \Phi_{Bn} &= E_G/q - \Phi_0 - \Delta\phi && (2.43) \\ \Phi_{Bp} &= \Phi_0 - \Delta\phi. && (2.44) \end{aligned}$$

For most III-V semiconductors, the surface state density is very high, resulting in Fermi-level pinning. For many compounds, including GaAs, the Fermi level is pinned at roughly $E_G/3$ above the valence band. For InP, two pinning levels were identified by Hokelek et al. [87]. They found pinning levels at $0.4\,\mathrm{eV}$ and $0.5\,\mathrm{eV}$ below the conduction band edge, and correlated them to the metallurgical state of the metal-semiconductor interface. This correlation suggests that the Fermi level pinning is determined by the chemical reaction between the metal and the InP substrate, rather than by the metal work function and semiconductor electron affinity. For a gold contact, the measured barrier heights were $\Phi_{Bn} \sim 0.49\,\mathrm{eV}$ and $\Phi_{Bp} \sim 0.81\,\mathrm{eV}$. For many other metals, the barrier heights are similar.

Applying a positive bias to a moderately doped n-type metal-semiconductor contact results in a current that is determined by the thermionic emission process. In this case and at zero bias, ϱ_c can be calculated to be

$$\varrho_c \sim \left(\frac{k_B}{qA^*T}\right) \exp\left(\frac{q\Phi_{Bn}}{k_BT}\right), \qquad (2.45)$$

with A^* the effective Richardson constant. For highly doped semiconductors, the band bending will be steeper, resulting in a reduced barrier thickness. In this case, the tunneling process will dominate the current transport, resulting in a specific contact resistance

$$\varrho_c \sim \exp\left[\left(\frac{2\Phi_{Bn}}{\hbar}\right)\sqrt{\frac{\epsilon_0\epsilon_s m^*}{N_d}}\right], \qquad (2.46)$$

where N_d is the doping concentration. Similar expressions can be obtained for p-type contacts. It can be seen that in both cases, ϱ_c increases strongly with increasing Φ_B. From these expressions, it is clear that in the case of Fermi-level pinning, a low-resistance ohmic metal-semiconductor contact can be obtained by using heavily doped semiconductors with a small bandgap.

Contacts to n-type InP. For n-type InP, ϱ_c values lower than $10^{-6}\ \Omega\mathrm{cm}^2$ are commonly obtained by using NiAuGe metallization schemes, or pure Au contacts. Both contact types need an alloying treatment at 350-400°C, to drive the Ge dopants into the InP or to form low-bandgap Au-InP intermixed interfacial layers respectively. However, this intermixing is typically very violent, with deep metal spiking into the semiconductor. This can be problematic for thin-film devices, which have the functional semiconductor layers close to the metal contacts. Therefore, metal contacts with limited metal-InP intermixing should be used. This can be done by using metal contacts that don't need an alloying treatment, or that have reduced metal-semiconductor reactivity. For non-alloyed contacts, a low-bandgap intermediate contact layer such as n-type InGaAs should be introduced to achieve low ϱ_c. Metals such as Ti and Pt show lower reactivity with InP, and result in annealed contacts

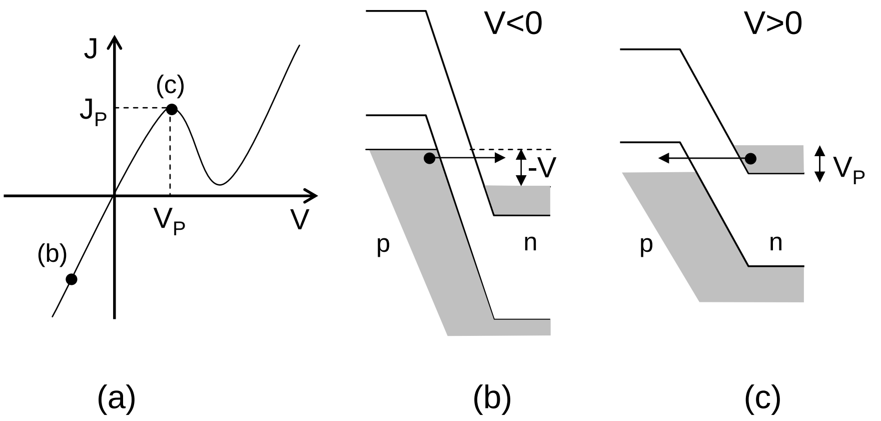

Figure 2.11: (a) Tunnel-junction current-voltage characteristic. Simplified band diagram for reverse bias (b) and forward bias V_P (c).

with better morphology. Furthermore, Pt acts as a diffusion barrier to Au, allowing for the deposition of a top Au layer to reduce metal resistance. A special Au-based contact with low ϱ_c and limited spiking was proposed in [88]. It is fabricated by depositing a Au layer of a few nm that is alloyed to form a thin low-bandgap Au_2P_3 interfacial layer. Then, an additional thick Au layer is deposited without alloying. We have studied this type of contact in terms of optical losses, and the results can be found in Chapter 4.

Contacts to p-type InP. Due to the higher barrier height for p-type InP, ohmic Au contacts to p-type InP are much more difficult to obtain than ohmic Au contacts to n-type InP. To obtain low ϱ_c, heavily doped low-bandgap contact layers such as p++ InGaAs need to be introduced. Typically, an alloyed TiPtAu contact is used, resulting in a contact resistance $\varrho_c < 10^{-5}\Omega\text{cm}^2$. In order to reduce DBBA and FCA loss, in [89], the InGaAs contact layer thickness is reduced from 100 nm to 15 nm in combination with a 100-nm InGaAsP contact layer, without an increase in contact resistivity.

Tunnel junction

Since ohmic contacts to p-type InP require heavily p-type doped contact layers with small band gaps, which have high optical absorption due to DBBA and FCA, this type of contact might be problematic to use in a thin-film optoelectronic device. Therefore, it can be interesting to replace it with another n-type contact in combination with a tunnel junction (TJ). Such a tunnel junction consists of a p-n junction with highly doped, degenerate p and n-layers. The Fermi level in the n-type layer is located inside the conduction band at an energy $E_c + qV_n$, while the Fermi level in the p-type part is located in the valence band at $E_v - qV_p$. While there can be

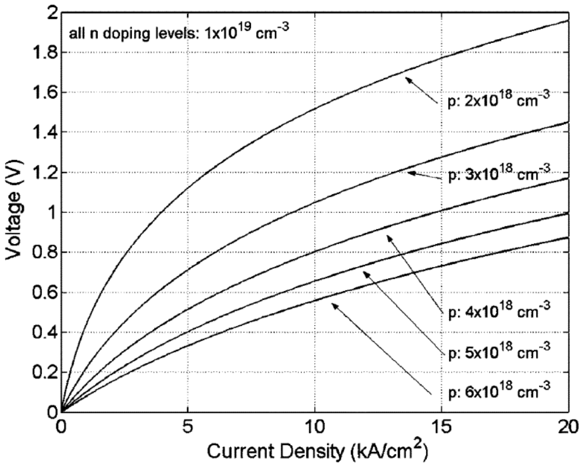

Figure 2.12: Calculated tunnel-junction J-V characteristic in reverse bias for an InP-based TJ as function of p-type doping N_a [90].

substantial FCA loss, the DBBA loss can be eliminated by using a TJ material with $\lambda_G < \lambda$.

A typical tunnel-junction current-voltage relation is shown in figure 2.11. Under forward bias, the current density exhibits a peak value J_P at a voltage V_P. For this bias, the energy of electrons in the energy interval $E_c \rightarrow E_F$ in the n-type layer are aligned with the hole energies $E_F \rightarrow E_v$ in the p-type layer, allowing electrons to tunnel from the n-type layer to the p-type layer through the thin barrier layer, as illustrated in figure 2.11 (c). For slightly higher biases, these energy levels are o longer aligned and the tunneling current decreases rapidly, resulting in a negative resistance region, as described by Esaki in 1958. For backward bias, the most energetic electrons in the p-type layer can tunnel to the vacancies above the Fermi level in the n-type layer, as shown in figure 2.11(b). The J-V characteristic of many experimental tunnel junctions can be fitted to

$$J = J_P \frac{V}{V_P} \exp\left(1 - \frac{V}{V_P}\right) \tag{2.47}$$

Demassa et al. showed in [91] that (2.47) is not only to be interpreted as a convenient fit to experimental data, but can also be used to evaluate the TJ performance *a priori*. Fermi statistics and Kane's tunneling theory [92] were used to obtain analytical expressions for J_P and V_P:

$$V_P \simeq \frac{V_n + V_p}{3} \tag{2.48}$$

$$J_P = \frac{qm^*}{36h^3} E_\perp D \exp\left[\frac{\pi m^{*1/2} E_G^{1/2}}{2^{3/2} hF}\right], \tag{2.49}$$

with

$$E_{\perp} = \frac{2^{1/2} h F}{\pi m^{*1/2} E_G^{1/2}} \tag{2.50}$$

$$F = \left(\frac{q^3}{2\epsilon}\right)^{1/2} \left(\frac{N_d N_a}{N_d + N_a}\right)^{1/2} V_d^{1/2}, \tag{2.51}$$

and where m^* is the reduced effective mass, D is the overlap integral, which is approximately equal to V_P, and V_d is the built-in diffusion potential, which can be approximated by E_G/q.

This analysis was carried out for an InP-based TJ in [90], in the context of the optimization of a long-wavelength VCSEL. It was found that the TJ resistance mainly depends on the p-type doping and TJ bandgap, and to a lesser extent on the n-type doping, as illustrated in figure 2.12. We will use this data in the design and analysis of the TJ-based microdisk lasers in Chapter 3.

2.4.2 Injection efficiency

Two different injection efficiencies can be defined, for below and above-threshold operation respectively. In literature, this difference is often misunderstood. However, injection efficiency is conceptually very different in above-threshold operation as compared to below-threshold operation.

Below-threshold injection efficiency

Below threshold, the injection efficiency of a QW laser is defined as the fraction of the injected current that recombines, both radiatively and non-radiatively, in the QW active region of the laser. A leakage current found in many laser designs is due to lateral carrier diffusion current and direct injection I_L outside of the lasing region, as is illustrated in figure 2.13 for the specific case of a ridge waveguide laser diode. A solution can be to etch the waveguide through the active layer, thus providing lateral carrier confinement. However, in this case the device can suffer from a possibly even worse surface recombination current.

Carriers can also escape vertically out of the active region by thermionic emission, contributing to the leakage current I_V. This vertical leakage depends strongly on the active region's temperature and the barrier height for electrons ΔE_c and holes ΔE_v, at the heterointerface between the quantum well and the barrier. For InGaAsP quantum wells, it is typically found that $Q_C = \Delta E_c/(\Delta E_v + \Delta E_c) = 0.4$ with respect to InP barriers. Therefore, electron leakage is expected to be more important than hole leakage for this type of quantum wells. However, InAsP quantum wells embedded in InP barriers have $Q_C = 0.7$ [93].

For simplicity, we will here assume equal leakage current for both carrier types. The escaped carriers populate the optical confinement layers (OCL), yielding a OCL carrier density N_{OCL}, which approximately relates to the active region carrier den-

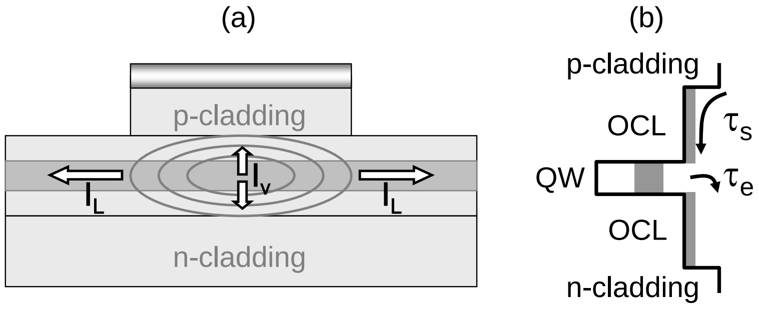

Figure 2.13: Origin of leakage current contributing to the threshold current. (a) Lateral and vertical leakage current in a ridge waveguide laser. (b) Vertical leakage is due to thermionic emission out of the active region (quantum wells), allowing carriers to recombine elsewhere without contributing to the laser operation.

sity N as [94]

$$N_{OCL} \simeq \frac{t_{QW}}{t_{OCL}} \frac{\tau_s}{\tau_e} N, \tag{2.52}$$

where t_{QW} is the total width of the active region (quantum wells), t_{OCL} the width of a OCL, τ_e is the QW carrier escape time, and τ_s the carrier diffusion time in the OCLs, given by $\tau_s = t_{OCL}^2 q/(4k_B T \mu_h)$, where μ_h is the hole mobility. In literature [79]-[94]-[95], τ_s can be found in the range $1 - 100\,\text{ps}$ whereas $\tau_e \sim 1 - 1000\,\text{ps}$, depending on the carrier type, barrier height, quantum well carrier concentration and temperature. Carriers in the OCL recombine without participating to the laser operation, giving rise to a vertical leakage current. The calculated vertical injection efficiency η_V is plotted as function of τ_e and t_{OCL} for $t_{QW} = 20\,\text{nm}$ in figure 2.14, assuming identical A, B and C recombination coefficients in the active region and OCL and no stimulated recombination. It can be seen that, according to this simple model, for relatively thin OCLs with $t_{OCL} < 100\,\text{nm}$, η_V remains higher than 90% for $\tau_e > 30\,\text{ps}$. For thicker OCLs, vertical carrier leakage is expected to be more severe. With increasing temperature, the carrier escape time decreases, resulting in increased vertical leakage. The temperature dependence of thermionic leakage current density J_V can be expressed as

$$J_V = \frac{4\pi q (k_B T)^2}{h^3} m_i^* \exp\left(-\frac{E_b - E_f}{k_B T}\right), \tag{2.53}$$

where E_b is the barrier energy level and E_f the quasi Fermi level.

Additional leakage can arise due to carrier escape into the cladding layers. This leakage was analyzed for an InGaAsP-based Fabry-Perot laser in [96]. The author concluded that this leakage only plays an important role at temperatures far exceeding 100°C.

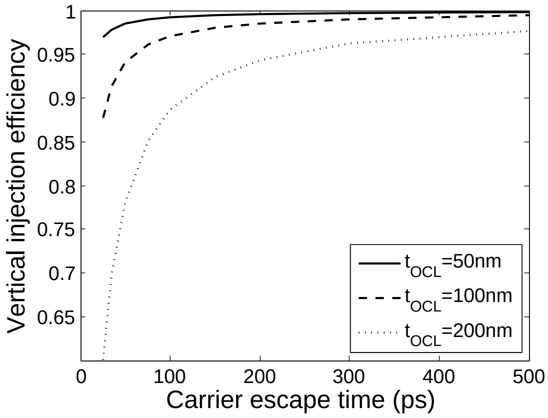

Figure 2.14: Vertical injection efficiency η_{iV} as function of τ_e and t_{OCL} for $t_{QW} = 20\,\text{nm}$.

The below-threshold injection efficiency η_i is then defined as

$$\eta_i = \eta_L \eta_V = \frac{I_{QW}}{I_L + I_V + I_{QW}}, \tag{2.54}$$

where I_{QW} stands for the current that recombines within the laser's active region.

Above-threshold differential injection efficiency

Above threshold, the average carrier density in the active region is assumed to be clamped at its threshold density. Therefore, we can assume that the carrier loss mechanisms are also clamped at threshold. As a result, each additional carrier injected above threshold should recombine by stimulated recombination, yielding a unity differential injection efficiency $\eta_i^d = 1$. However, some loss contributions are clearly not clamped, for instance for a structure where part of the current is injected outside of the active laser region. Moreover, it has been found that for a MQW structure, the carrier density in the individual QWs is not clamped in the strict sense [97], but clamping occurs rather for the average carrier density[4], with the carriers non-uniformly distributed over the QWs. For InGaAsP/InP MQW lasers, the largest carrier density in the QW occurs closest to the p-doped side, since electrons travel more easily through the MQW region than holes [97]. This non-uniformity gets worse with increasing pumping level. Since Auger recombination scales non-linearly with carrier density, this gives rise to a differential injection recombination efficiency $\eta_R^d < 1$. Other contributions to the above-threshold differential injection efficiency η_i^d include differential vertical leakage η_V^d and differential lateral leakage η_L^d, resulting in [96]

$$\eta_i^d = \eta_R^d \eta_V^d \eta_L^d = \frac{\Delta I_{stim}}{\Delta I_R + \Delta I_L + \Delta I_V + \Delta I_{stim}}. \tag{2.55}$$

---

[4] above threshold, the modal gain is clamped rather than the carrier density.

For the MQW (6 quantum wells) InGaAsP/InP Fabry-Perot laser in [96], it was found that $\eta_R^d = 0.75$, $\eta_V^d = 0.99$ and $\eta_L^d = 0.9$ at room temperature, and $\eta_R^d = 0.7$, $\eta_V^d = 0.5$ and $\eta_L^d = 0.9$ at $100°$C.

2.4.3 Band diagram

The band diagram under forward bias of a thin-film epitaxial layer p-i-n structure with good potential for efficient electrical injection is shown in figure 2.15 (a), for a forward bias of 0.9 V. Band bending at the contacts was not taken into account. The free electron and free hole concentrations are shown in (b), and the resulting spontaneous recombination is shown in (c).

To make an efficient microlaser in these structures, the doping, thickness, composition of the semiconductor layers should be optimized to minimize any detrimental effect on the optical resonator quality due to optical absorption. Strategies to achieve this goal are presented in section 2.6.

2.5 Laser performance

The interplay between photons and carriers in a laser is typically described by rate equations. From these equations, the static and dynamic performance characteristics of a laser diode can be extracted, including the threshold current, differential efficiency and modulation speed.

2.5.1 Rate equations

Under the ambipolar assumption, the spatially dependent rate equations for a laser with multiple laser modes are written as

$$\begin{aligned} \frac{\partial N(\mathbf{r},t)}{\partial t} &= \frac{\eta_i j(\mathbf{r},t)}{q t_a} - AN(\mathbf{r},t) - BN^2(\mathbf{r},t) - CN^3(\mathbf{r},t) \qquad (2.56) \\ &\quad + D\nabla^2 N(\mathbf{r},t) - v_g \Sigma_m G_m(N,S_m) S_m \\ \frac{\partial S_m(\mathbf{r},t)}{\partial t} &= -\frac{S_m}{\tau_p^m} + \beta_m \Gamma_m B N^2(\mathbf{r},t) + \Gamma_m v_g G_m(N,S_m) S_m \qquad (2.57) \end{aligned}$$

with $N(\mathbf{r},t)$ the spatiotemporal carrier density in the active layer, $D = (\mu_n D_p + \mu_p D_n)/(D_n + D_p)$ the ambipolar diffusion coefficient, m the laser mode number, S_m the photon density in the cavity, $G_m(N,S_m) = G_m(N)/(1+\varepsilon \Sigma_m S)$ the gain[5], τ_p^m the photon lifetime, β_m the spontaneous emission factor, and Γ_m the optical confinement factor of the m-th laser mode. Solving these rigorous equations requires substantial numerical resources due to the need of spatial discretization. However, in many cases, a good approximation can be made by assuming a uniform carrier density in

---

[5] ε is the gain compression factor, which describes gain saturation at high photon densities.

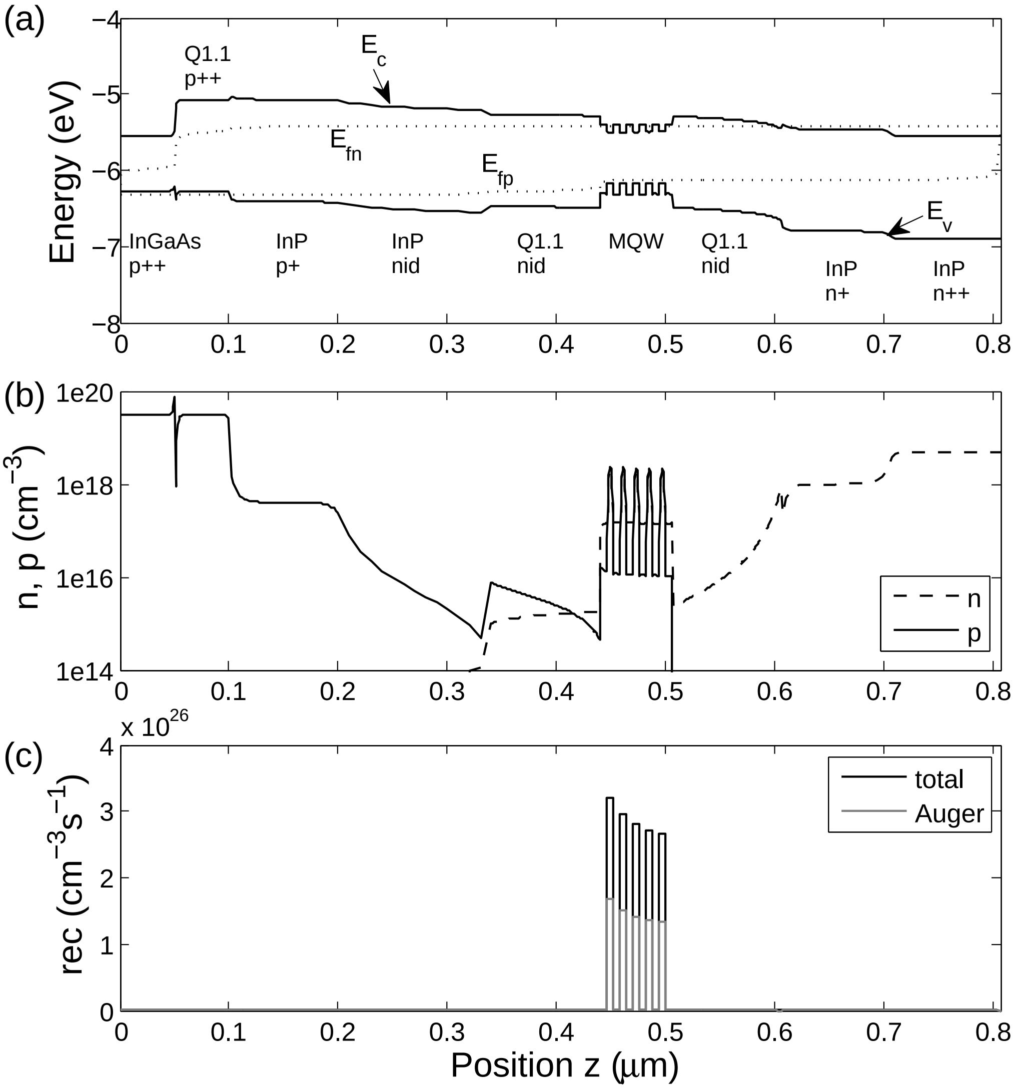

Figure 2.15: (a) Calculated band diagram under forward bias for a thin-film p-i-n diode structure with a InGaAs contact layer, (b) carrier concentrations, and (c) recombination rate for $0.9\,V$ forward bias. Calculations are performed with SIMWINDOWS. For all heterobarriers, $Q_C = 0.4$ was assumed. Band bending at the contacts is not included.

the active region and a single dominant laser mode. Under these assumptions, the rate equations read

$$\frac{dN(t)}{dt} = \frac{\eta_i I(t)}{qV_a} - AN(t) - BN^2(t) - CN^3(t) - v_g G(N,S)S(t) \quad (2.58)$$

$$\frac{dS(t)}{dt} = -\frac{S(t)}{\tau_p} + \beta\Gamma BN^2(t) + \Gamma v_g G(N,S)S(t). \quad (2.59)$$

2.5.2 Threshold current

Under steady-state regime and without photons in the cavity, it can be seen from (2.58) that at threshold

$$I_{th} = \frac{qV_a}{\eta_i}(AN_{th} + BN_{th}^2 + CN_{th}^3). \quad (2.60)$$

The threshold carrier density N_{th} can be calculated from (2.59) in steady-state regime, by neglecting the spontaneous emission term and dividing the remaining terms by S, resulting in

$$G(N_{th}) = \frac{1}{\Gamma v_g \tau_p} = \frac{\alpha_{tot}}{\Gamma}, \quad (2.61)$$

which is equivalent to (2.3). Assuming the logarithmic gain model (2.37) then results in

$$N_{th} = N_0 \exp\left(\frac{\alpha_{tot}}{\Gamma G_0}\right). \quad (2.62)$$

2.5.3 Differential efficiency

The laser output power P relates to the photon density S as

$$P = v_g \alpha_u h\nu \frac{V_a}{\Gamma} S = \frac{\eta_e h\nu V_a}{\Gamma \tau_p} S, \quad (2.63)$$

where ν is the laser frequency and η_e the photon extraction efficiency as defined in (2.20). The above-threshold steady state power-current characteristic can be deduced from the rate equations as

$$P(I) = \eta_i^d \eta_e \frac{h\nu}{q}(I - I_{th}) = \eta_d \frac{h\nu}{q}(I - I_{th}). \quad (2.64)$$

In this equation, η_d is referred to as the differential quantum efficiency. The slope efficiency is given by $\eta_d h\nu/q$.

2.5.4 Modulation bandwidth

From a differential analysis of the rate equations (2.58-2.59), the small-signal modulation transfer function can be deduced [79]:

$$H(\omega) = \frac{\omega_R^2}{\omega_R^2 - \omega^2 + j\omega\gamma}, \quad (2.65)$$

where ω_R is the relaxation resonance frequency and γ the damping factor. Above threshold, ω_R^2 and γ can be approximated as

$$\begin{aligned} \omega_R^2 &\simeq \frac{v_g a S}{\tau_p} && (2.66) \\ \gamma &= K f_R^2 + \gamma_0, && (2.67) \end{aligned}$$

with $a = [dG/dN]_{th}$ the differential gain, $K \simeq 4\pi^2\tau_p$ the K factor and $\gamma_0 \simeq 1/\tau_{\Delta N}$ the damping factor offset, with ΔN the differential carrier lifetime. From (2.66), it can be seen that ω_R increases with the square root of the photon density. This relation can be written more directly as a function of injected current I as

$$\omega_R^2 \simeq \frac{v_g a}{q V_p} \eta_i^d (I - I_{th}). \tag{2.68}$$

For a given pumping level and assuming low damping, the 3-dB modulation bandwidth is then approximated as $f_{3dB} \simeq 1.55 f_R$.

It should be noted that (2.68) represents the intrinsic modulation characteristic of a laser diode. Parasitic elements, such as electrical capacitance and resistance of the contact pads, can limit the maximum modulation speed due low-pass RC filtering of the injected current. Another parasitic effect can be found in the carrier transport in the OCLs. As already discussed in 2.4.2, carriers need to diffuse through the OCLs to reach the quantum wells and can also escape from them back into the OCLs. This effect can be accounted for by including an extra rate equation that describes the carrier population N_{OCL}. This analysis results in a transport factor $\chi \simeq 1 + \tau_s/\tau_e$, which reduces the modulation speed to $\omega_{tR}^2 = \omega_R^2/\chi$ [98]. By reducing the width of the OCLs, this low-pass filtering effect can be eliminated.

Turn-on delay

When a diode laser is switched on, a time t_d is required for the carrier density to build up to the threshold value before the laser resonance is activated. Such a turn-on delay can strongly affect the bit-error rate in high-speed optical links. For a zero initial bias and a final bias I_f, an approximate expression for t_d is given by

$$t_d \simeq \tau_{th} \ln\left(\frac{I_{th}}{I_f}\right), \tag{2.69}$$

where t_{th} is the carrier lifetime at threshold. For an initial bias I_i close to I_{th}, t_d is approximately given by [79]

$$t_d \simeq \tau_N \ln\left(\frac{I_f - I_i}{I_f - I_{th}}\right), \tag{2.70}$$

where a constant carrier lifetime τ_N was assumed. A large turn-on delay can thus be avoided by adjusting the bias level I_i close to threshold and increasing I_f as much as possible above threshold.

2.5.5 Temperature dependence

Most material parameters that appear in the rate equations depend on temperature. The most temperature-sensitive material properties for InP-based laser diodes include the optical gain $G(N, T)$, the internal loss α_i, the injection efficiencies η_i and η_i^d and the Auger recombination $C(T)$.

Temperature sensitivity of the threshold current

With increasing temperature, the maximum peak gain drops and the peak gain wavelength shifts to longer wavelengths as illustrated in figure 2.10. In general, this results in a higher threshold carrier density and therefore a higher threshold current. For a long Fabry-Perot laser, the dominant lasing wavelength will shift together with the gain spectrum ($\sim 0.54\,\mathrm{nm/K}$). For a microlaser with short cavity length, only one or two resonant modes are available within the gain spectrum. For an InP-based laser cavity, the resonant wavelength λ_M shifts at a rate of about 0.1 nm/K, due to the change in refractive index. Therefore, if the resonant mode is aligned with the peak gain wavelength λ_P at room temperature (20°C), it won't be aligned at higher temperatures. For instance, at 70°C, the cavity mode wavelength and the peak gain wavelength will be misaligned by more than 20 nm. This misalignment increases the temperature sensitivity of the threshold current. Alternatively, the cavity mode could be detuned at room temperature, in order to achieve a minimum lasing threshold at an elevated temperature. This situation is commonly encountered in the design of VCSELs.

Since higher N_{th} values are required at elevated temperatures, the carrier concentration in the barriers and OCLs will also increase, resulting in an increase in internal modal loss α_i and a decrease in photon extraction efficiency. Higher carrier densities also result in enhanced Auger recombination. Thermionic emission of carriers out of the active region is also enhanced with increasing temperature, which results in a decreasing η_i. All these effects are believed to add to the increase in threshold current.

In general, the threshold current of a laser diode increases exponentially with temperature

$$I_{th}(T) = I_0 \exp\left(\frac{T}{T_0}\right), \tag{2.71}$$

where I_0 is the threshold at zero degrees, and T_0 its characteristic temperature (all temperatures are in degrees Kelvin). Typical T_0 values for InGaAsP/InP laser diodes are in the range 50-70 K.

Temperature sensitivity of the differential efficiency

Since higher operating temperatures require higher carrier densities, the differential efficiency will drop as a result of the increase in internal loss α_i – due to increasing FCA – and a decrease in differential injection efficiency, due to the increased sensitivity to Auger recombination and thermionic emission. However, in general, the characteristic temperature T_η for the differential efficiency is two to three times larger than T_0 [79].

Self heating

When a laser is biased, a power P_D is dissipated as heat in the laser cavity

$$P_D = IV - P_{out}, \tag{2.72}$$

where P_{out} is the laser output power. This dissipated power needs to be evacuated to the substrate. The temperature increase ΔT that is associated with this heat dissipation is given by $\Delta T = Z_T P_D$, where Z_T is the thermal impedance. For steady-state operation, Z_T reduces to the thermal resistance R_T. This self heating results in a thermal roll-over behavior in which the laser output saturates and decreases at a given input current, due to the cavity temperature increase and the associated reduced performance.

Self heating can be expected to be problematic in bonded thin-film devices, since the bonding material has in general a low thermal conductivity κ. Assuming a one-dimensional heat flow results in a thermal resistance

$$R_T = \frac{t_{bonding}}{\kappa A}, \tag{2.73}$$

with κ the thermal conductivity, $t_{bonding}$ the thickness of the bonding layer and A the device area. For instance, a 1-μm-thick SiO_2 bonding layer with a thermal resistance $\kappa_{SiO_2} = 1\,\mathrm{W/Km}$ results in $R_T \times A = 10^{-6}\,\mathrm{m^2K/W}$. Since a typical heat dissipation is expected to be around 1-10 kW/cm^2, ΔT will be in the range 10-100 K, indicating serious self heating.

2.6 Thin-film microlaser design

2.6.1 Epitaxial layer design

The composition of the bonded epitaxial layers is of crucial importance for device performance: it should enable efficient carrier injection at low operating voltage while simultaneously provide light confinement with low internal absorption loss. A major bottleneck for the electrical current could occur at the p-type contact. As has been discussed in section 2.4.1, low-resistance contacts to p-type InP require heavily p-type doped, low bandgap contact layers such as p++ InGaAs. These layers have large optical absorption, due to band-to-band absorption and free-carrier absorption (FCA), as highly p-type doped layers have large intervalence band absorption (IVBA). In traditional substrate lasers, relatively thick ($> 1\,\mu$m) cladding layers provide optical isolation between the waveguide core and these very absorptive contact layers. However, for integration and fabrication purposes, the epitaxial layer should be as thin as possible. Thicker devices are more difficult to planarize and to etch with low surface roughness, thus making integration and fabrication more difficult. Also, the optical coupling to an underlying SOI waveguide is expected to be less efficient for thicker InP films, due to worsening phase matching conditions. Hence, we should avoid large quantities of InGaAs and/or heavily p-type doped layers in the epitaxial structure, while preserving good electrical behavior.

Basically, we see three approaches to achieve this goal in a thin-film device. In the first approach, the thickness of the InGaAs contact layer could be reduced while preserving the contact resistivity. This approach has been studied in [89] in the context of an integrated optical isolator. It was found that the InGaAs layer can be reduced down to 15 nm if used in combination with a semi-transparent Q1.15 contact layer. In the second strategy, a lateral contacting scheme could be applied where the contact layer and metal don't overlap with the optical field. In this approach, specific care has to be taken to achieve an adequate lateral injection efficiency, for instance by including current spreading layers and or current blocking layers. In the third approach, a tunnel junction in combination with an additional n-type contact replaces the p-type contact. It has been shown that TJs with a bandgap wavelength below the emission wavelength exhibit relatively low electrical resistance, provided that they are heavily doped ($> 10^{19}$ cm^3) to enhance the tunneling current (see also section 2.4.1). While such layers exhibit high IVBA, they don't suffer from DBBA and only need to be 10-20 nm thick. As a result, the associated modal internal loss can be relatively low. This approach has been demonstrated in the case of long-wavelength vertical-cavity surface-emitting lasers (VCSELs), with only a minor optical loss penalty, provided that the TJ is well positioned at a minimum of the optical field intensity [99]-[100].

2.6.2 Optical confinement in a microcavity

In a thin-film optical resonator, vertical optical confinement is provided by the refractive index contrast between the thin semiconductor film and the low-index dielectric or metal cladding layers. For the in-plane two-dimensional confinement, various strategies can be considered. To obtain a compact laser footprint, the laser cavity should be made very small. To achieve this goal, we can rely on index guiding or on distributed Bragg reflection. Depending on the design of the cavity, this can result in one-dimensional or two-dimensional laser resonances. We shall now proceed with discussing some promising approaches. Figure 2.16 gives an overview of some common cavity types, showing a SEM image of the laser cavity and the optical field (top view).

DBR microlasers

A first approach is based on a traditional high-contrast waveguide, terminated by Distributed-Bragg-Reflection (DBR) mirrors. The SEM photo shows an example of such a DBR microlaser, fabricated on a GaAs substrate. The laser resonance is one-dimensional standing wave and is very similar to that in a conventional Fabry-Perot laser, except for the shorter cavity length. Several (micro-)lasers with DBR mirrors can be found in literature, both on GaAs substrates [103]-[82] as on InP substrates [104]-[105]-[106]. Experimental DBR mirror reflectivities up to 95% were extracted and cavity lengths were as short as 12 μm. Threshold currents are as low as 5.7 mA,

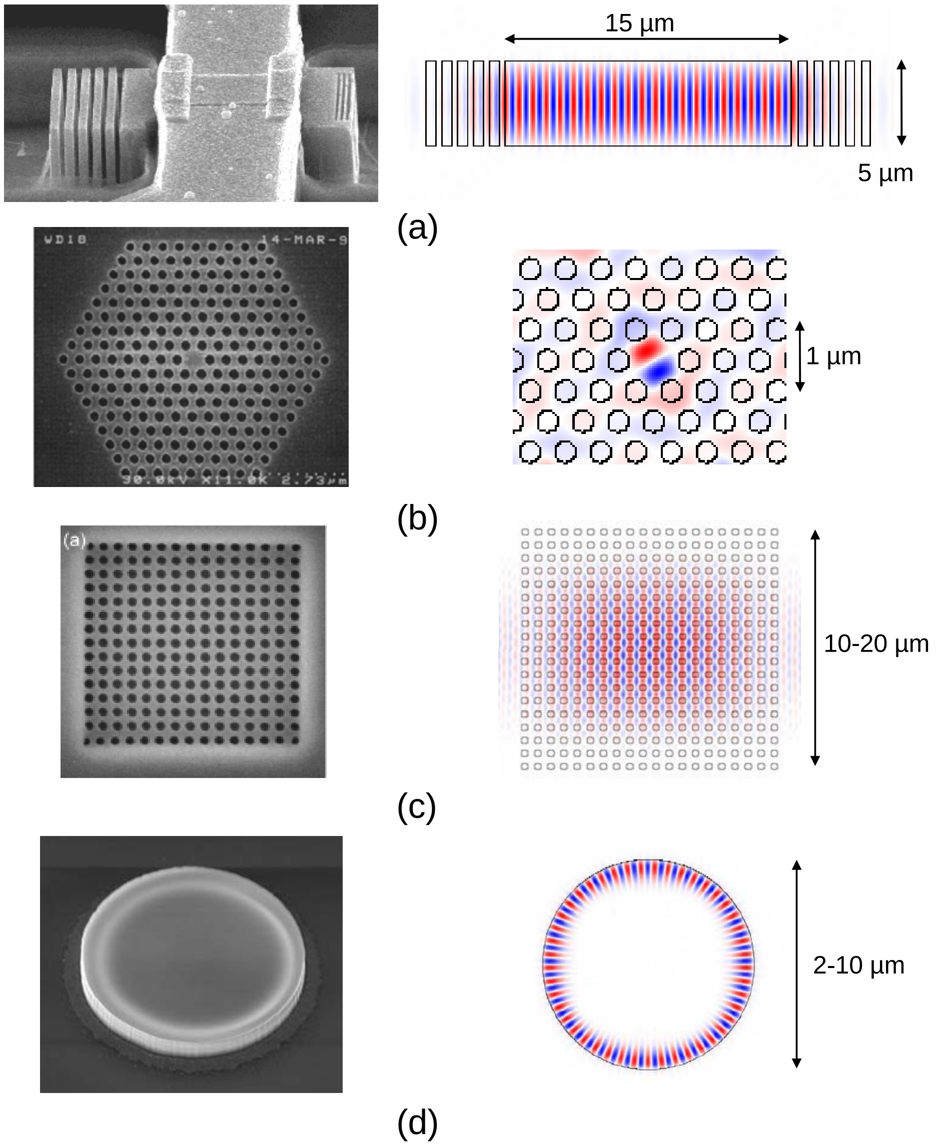
15 µm
5 µm
(a)
WD18
14-MAR-9
1 µm
(b)
(a)
10-20 µm
(c)
2-10 µm
(d)

Figure 2.16: In-plane micron-sized optical confinement schemes. (a) DBR microlaser (SEM image from [82]). (b) Defect-based photonic-crystal laser (SEM image from [101]). (c) Band-edge photonic crystal laser (SEM image from [102]). (d) Microdisk cavity.

with single-facet slope efficiencies in the order $100\,\mu\mathrm{W/mA}$. To achieve this performance, the deeply-etched DBR mirrors should have very steep sidewalls with low roughness. To achieve this goal, a specific etching process has to be developed. We have numerically investigated if this cavity design could be implemented in the thin-film approach. The results and discussion can be found in section 2.6.4, and in appendix A.

Photonic-crystal-based microlasers

A second cavity design is based on a two-dimensional photonic-crystal (PhC). This 2D PhC consists of a periodic array of etched holes into the thin semiconductor film. A properly designed PhC exhibits a 2D omni-directional photonic bandgap (PBG). Light with a frequency in the PBG cannot propagate in the crystal, regardless of the in-plane propagation direction. This is illustrated in figure 2.17, where the calculated band structure of a two-dimensional, triangular-lattice PhC is shown, for $r/a = 0.3$, with a the period of the lattice and r the radius of the holes. A photonic bandgap is apparent for reduced frequencies in the range $0.26 - 0.32\,a/\lambda$.

Defect-based microcavities. When a defect is introduced in the PhC, such as a missing hole, a cavity is formed, since light with a frequency in the PBG cannot leak away through the surrounding PhC. Due to the high index contrast, only a limited number of PhC layers is needed to achieve a high quality factor. The resonance can be of a one-dimensional or two-dimensional nature, depending on the shape of the defect. For one-dimensional resonances, the PhC defect cavity can be considered as a miniaturized version of the DBR microlaser.

The first demonstration of this type of microlaser was achieved by Painter et al. [60]. Optically pumped lasing was only observed in pulsed regime at 143 K, due to the small Q factor of only 250. Since then, much attention has been paid in the scientific community to improve the design and fabrication of ultra-compact and ultra-high-Q PhC cavities. Reducing the out-of-plane loss by tuning the PhC defect has resulted in optically pumped PhC lasers with thresholds in the μW range at room temperature, and recently also an electrically pumped version [51]. Recent work [107] has resulted in experimental Q values up to one million, for a micron-scale mode footprint. Due to its high Q/V ratio, this laser type is the most suited to achieve QED effects that can lead to improved device performance, as will be discussed in section 2.7.

Band-edge photonic-crystal microlasers. High-Q resonances can also be built up at the band edges of the bloch modes of a defect-free PhC. At these band edges, the group velocity $v_g = d\omega/dk$ of the propagating bloch mode approaches zero. For a finite-size PhC cavity with length L, this results in an increased time $t \sim L/v_g$ for a photon to propagate through the cavity, and a high Q factor (see equation 2.8). Alternatively, one could argue that the effective modal gain per unit length gets boosted by a factor $1/v_g$ [108]. At the edges of the PhC, the bloch mode approximately experiences an amplitude reflection $R \simeq \frac{n_g-1}{n_g+1}$, with $n_g = c/v_g$ the group index of the bloch mode [109]. The resulting optical resonance occupies the complete PhC region, and has a one- or two-dimensional nature, depending on the PhC band structure design

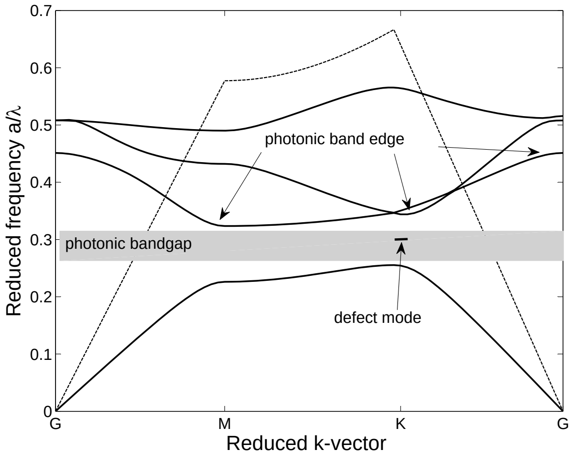

Figure 2.17: Band structure for a triangular 2D photonic crystal (2D calculation with $n_{eff} = 2.8$ in TE polarization, where only the four lower bands are shown).

and the resonance wavelength. In many aspects, this laser type can be considered as the high index-contrast version of the conventional DFB laser. While the minimum cavity size is on the order of tens of μm^2, the laser emission can be in-plane or out-of-plane, depending on the PhC design. Also, this cavity type allows for single-mode lasing even for relatively large cavity sizes. Furthermore, the band-edge resonator can be embedded in a PhC defect, which allows for advanced engineering of the mode properties.

Microdisk lasers

Finally, a simple and compact resonator can be found in the microring or microdisk resonator. For the microring, light is index-guided in the waveguide core, with very small bending loss, even for bend radii of one micrometer due to the high index contrast. Microdisk cavities support whispering-gallery modes that are confined to the edges of the disk, without the need for a guiding structure inside the disk. Electrically-injected pedestal-supported microdisk lasers with a diameter of $2\,\mu\text{m}$ and $40\,\mu\text{A}$ threshold current have already been demonstrated [45], illustrating the potential for compact device size and low power consumption with a relatively simple cavity design. This microlaser type is at the core of this PhD work and will be discussed in great detail in chapters 3, 4 and 5.

2.6.3 Evanescent coupling to a passive waveguide

When two waveguides are brought in close proximity, light can couple from one waveguide to the other and vice versa. This phenomenon is known as evanescent coupling, since it is triggered by the perturbation of the evanescent mode tails due to the presence of the neighboring waveguide. For weakly coupled waveguides, perturbation theory can be used to predict the amount of coupling. For two coupled waveguides with unperturbed propagation constants β_1 and β_2, the maximum power transfer is given by

$$P_{max} \simeq \frac{\kappa^2}{\kappa^2 + \Delta^2}, \tag{2.74}$$

and the coupling length L_c is given by

$$L_c \simeq \frac{\pi}{2\sqrt{\kappa^2 + \Delta^2}}, \tag{2.75}$$

where $\Delta \simeq (\beta_1 - \beta_2)/2$ is the phase mismatch between the two waveguide modes and κ is the coupling coefficient[6]. It can be seen that for perfect phase matching between the waveguide modes ($\Delta = 0$), complete power transfer is possible over a length scale that is inversely proportional to the coupling coefficient. For increasing phase mismatch between the waveguide modes, the maximum transferrable power decreases and the coupling length becomes shorter and less sensitive to the coupling strength κ. However, by bringing the waveguides closer together, the maximum power transfer can be increased. Furthermore, for most coupled microlasers, the optimum power coupling κ is in the range 1-5$\%$. Since typical coupling lengths are in the micrometer range, evanescent coupling is compatible with the required micron-sized laser footprint.

In practice, when designing microlasers, the coupling conditions are evaluated by purely numerical tools, as the coupling configurations typically involve curved waveguides or PhC-based confinement, which are difficult to treat (semi-)analytically. While coupling between passive ring resonators and waveguides is mostly characterized by the coupling factor κ, we have mostly used the Q factor or distributed loss α_c as a loss metric, as they compare more straightforwardly with the other cavity loss contributions.

2.6.4 Thin-film electrical injection schemes

Based on the considerations in sections 2.6.1 and 2.6.2, we shall now discuss some electrically-contacted microcavity designs that have potential to meet the microlaser performance requirements identified in 2.1. An overview of these designs is shown in figure 2.18. In these figures, the optical field profile is indicated by the semitransparent ellipse. The doping of the semiconductor layers is also indicated and the active region is assumed to be located in the center of the intrinsic (I) layer. For most designs, a p++ InGaAs contact layer is included. However, in principle, it could be replaced by a tunnel junction and n-type contact, as discussed in 2.4.1. Additionally, the order of the p-i-n layers could be reversed, resulting in an n-type top contact. Some of the presented strategies are inspired by previous work in literature. In those cases, a reference to the work is provided.

---

[6] For straight waveguides, κ can be approximated by $\kappa = \frac{k_0^2}{2\beta_1\beta_2}\sqrt{\int(n_{12}^2 - n_1^2)\psi_1\psi_2 dx \int(n_{12}^2 - n_2^2)\psi_1\psi_2 dx}$, where $n_{1,2}$ is the index profile and $\psi_{1,2}$ the waveguide mode of the unperturbed waveguide 1,2 and n_{12} is the total index profile

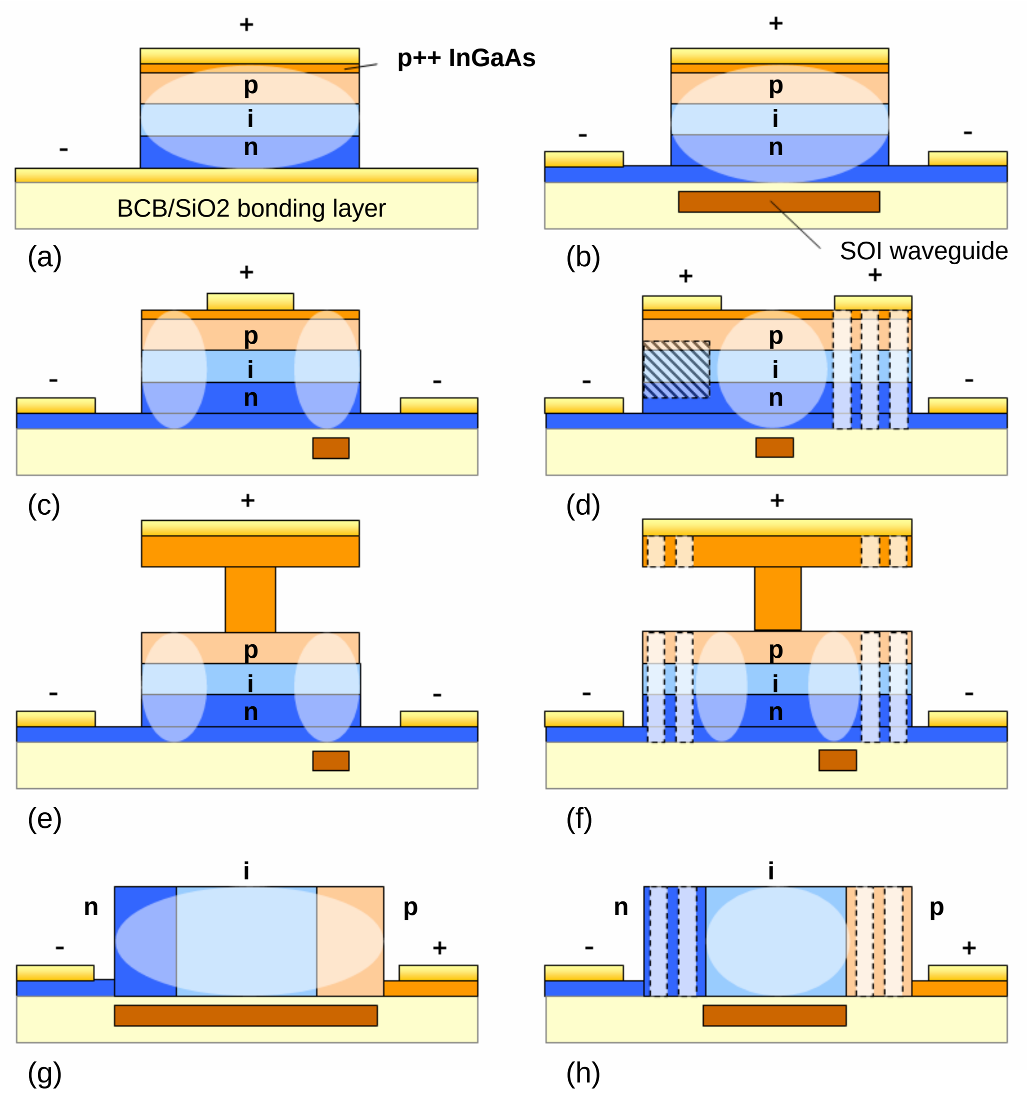
+
p++ InGaAs
p
i
n
-
BCB/SiO2 bonding layer
(a)
+
p
i
n
-
-
SOI waveguide
(b)
+
p
i
n
-
-
(c)
+
+
p
i
n
-
-
(d)
+
p
i
n
-
-
(e)
+
p
i
n
-
-
(f)
i
n
p
-
+
(g)
i
n
p
-
+
(h)

Figure 2.18: Overview of some promising thin-film microlaser contacting schemes. Double metal-clad film (a), single metal-clad film (b), microdisk resonator (c) and defect-based PhC resonator (d) with lateral contacts, post-contacted microdisk resonator (e) and defect-based PhC resonator (f), thin-film ridge (g) laser and PhC laser with lateral p-n junction.

Double metal-clad film

In the simplest contacting scheme (a), metal contacts are applied to each side of the thin film, the bottom one before bonding, and the top contact after bonding and substrate removal. To reduce absorption at the metal contacts ($\alpha_m < 1\,\mathrm{cm}^{-1}$), the semiconductor film should be sufficiently thick: $t > 1.8\,\mu$m for non-alloyed Au contacts, and $t > 2.5\,\mu$m for standard TiPtAu contacts. Lateral optical confinement can be achieved be any of the above mentioned strategies. However, since the film has to be relatively thick, the etching processes that have to be applied to define the cavity are expected to be quite challenging, especially for PhC-based resonators. For on-chip applications, the laser light could be butt-coupled to a polymer waveguide. Evanescent coupling to an underlying (SOI) waveguide is not possible, due the presence of the opaque bottom contact. We have studied the possibility of achieving band-edge lasing in such a structure, using 2D eigenmode expansion [110]. While these simulations indicate that a Au-clad 1-μm-thick band-edge resonator can support resonances with sufficiently high Q factors to achieve lasing, the metal absorption loss remains substantial, resulting in high threshold currents and low laser efficiency. Furthermore, for PhC-based resonators, the PhC needs to be designed in such a way to avoid mode coupling between the fundamental slab mode and the very lossy higher order modes [110]. The reliability of such a device with purely Au-based contacts is also expected to be poor. For the above reasons, we decided not to proceed with this approach.

Single metal-clad film

The second design (b) has only the top contact in close proximity with the optical field. The bottom contact is placed on a thin lateral semiconductor bottom contact layer. Both metal contacts are applied after bonding. The optical loss contribution due to the metal contacts is expected to be roughly half that of design (a), and can be further optimized by including optical confinement layers in the bottom of the waveguide, thus drawing the optical mode away from the top contact. Near-unity lateral injection efficiency can be expected.

We have performed a rigorous numerical optical analysis of a DBR microlaser with this injection design, including a tunnel junction or a ternary p-type contact layer. In summary, these calculations indicate threshold currents in the range 1.5-2.5 mA with slope efficiencies up to 0.2 W/A, for an optimized design. In order to use a TiPtAu contact, the InP-based film thickness should be at least 1.5 μm. If pure Au contacts are used, the required film thickness is about 1 μm. The optimum cavity length is in the range 15-30 μm. It was found that the DBR mirror reflectivity depends strongly on the sidewall slope of the DBR slits. A sidewall slope of five degrees with respect to the surface normal results in a decrease in reflectivity of up to ten percentage points. A more detailed summary of these modeling efforts can be found in appendix A.

Etching DBR mirrors with 180-nm slits in a 1-μm-thick InP film with an RIE process and a SiO_2 hard mask yielded sidewall slopes in the order of 5 degrees, due to hard mask erosion. While this figure could certainly be optimized by changing the etching parameters and mask composition, etching deep and fine slits with low surface roughness remains a big challenge, certainly for the 1.5 μm-thick InP films that are required for conventional contacts. For these reasons, we decided in the course of the PhD not to proceed with optimizing the deep DBR etch, but to focus on injection schemes compatible with conventional contacts.

Thin film with lateral metal contacts

The overlap between the metal and the optical field can be avoided by using a resonator that supports laser modes that are laterally confined inside the epitaxial layer. The top metal contact can then be applied in the regions with low optical field intensity, thus avoiding excessive absorption loss. From figure 2.16, it can be seen that photonic-crystal and microdisk cavities comply with this requirement. For a defect-based PhC cavity, the metal top contact could be placed around the defect, as illustrated in figure 2.18 (d). For the microdisk, the top contact can be placed in the center of the disk, as shown in figure 2.18 (c). However, the lateral injection efficiency in such structures may be poor, especially for the PhC cavity. Therefore, the doping of the p-type and n-type layers should be adjusted to enhance lateral current spreading in the device. Additionally, current blocking zones could be implemented by applying proton implantation in the regions with low optical intensity, as illustrated by the hatched area in figure 2.18 (d). It should be noted however that it is a non-trivial task to accurately control the proton implantation depth and lateral position without damaging the active region, especially for very compact cavities in thin single-mode semiconductor films [111]. The microdisk approach (c) is extensively studied in this PhD, both by simulation and experiment. The results and discussion are presented in chapters 3, 4 and 5.

Thin film with central post contact

The p-type contact can also be optically isolated from the lasing region by injecting the current through a thin central post, located at a minimum of the optical field. If the post is narrow enough and the gap between the topmost contact layer and the laser cavity is wide enough, the quality factor of an optical resonance will remain unchanged as compared to a structure without post.

This injection scheme is commonly used for electrically injected microdisk lasers [42]-[50]-[45]-[46]. These structures are typically fabricated by first dry etching a microcylinder in the substrate, followed by wet selective etch removing the cladding material and forming a thin microdisk. The wet etching time and rate has to be carefully controlled in order to optimize the thickness of the central post. A major drawback of this contacting scheme is that it relies on lateral carrier diffusion of centrally injected carriers to the edges of the disk where the laser mode is located, resulting in limited lateral injection efficiency. However, this can be improved by including thin, doped current spreading layers, at the expense of higher FCA losses.

A similar contacting approach was used in [51], where a bottom central post was used as a bottom p-type contact in a defect-based PhC cavity, in combination with a lateral top n-type contact. In this case, the PhC cavity was designed such that it supports a lasing mode with a intensity node in the center of the cavity. As a result, the optical loss due to the presence of the post is small [64]. Additionally, this structure included highly doped n-type current spreading layers. For integrated thin-film microlasers, a top post contact could be used in combination with a lateral bottom contact, as shown in figure 2.18 (e) and (f). While the microdisk laser (e) is easier to fabricate, the PhC laser (f) allows for smaller cavity size.

Thin film with lateral p-n junction

Finally, injection could be done through a lateral p-n junction as shown in figure 2.18 (g) and (h). This approach was proposed by Sugitatsu et al. [112] for a line-defect PhC cavity. In this case, all n-type layers and the MQWs are grown first, followed by p-dopant diffusion in a selected area, thereby controlling the diffusion front. Then, the PhC line-defect cavity is formed around the diffusion front. However, it might be difficult to use this approach for microlasers fabricated in bonded films, as the dopant diffusion typically requires temperatures in the range 500-700 °C, which are not compatible with current bonding technology.

2.7 Microcavity effects on laser performance

Shrinking down the laser cavity volume can yield microlasers for which the footprint and threshold current are scaled down proportional with the size reduction, with the same efficiency and intrinsic modulation characteristics as for large laser cavities, provided that the total photon losses can be kept low enough with decreasing cavity volume. However, when the cavity size is smaller than a certain limit, more effects come into play, which are basically a modification of the spontaneous emission.

2.7.1 The spontaneous-emission coupling factor

Spontaneous emission (SPE) is crucial for lasing operation, since it generates the initial photons that are needed to trigger stimulated emission. However, SPE can also be considered as an unwanted effect in a lasers, since it can have a significant contribution to the lasing threshold current, as well as to the laser linewidth above threshold. The traditional threshold definition states that the photon loss rate should be equal to the net stimulated photon emission rate, or equivalently, the photon round-trip gain should be unity. This is a useful definition, as it gives a very good approximation for the pumping current above which the phenomena associated with laser operation are achieved. These phenomena are an increase in quantum efficiency (visible as a kink in the P-I curve), an increase in temporal coherence and pinning of the carrier inversion and optical gain. The physical reason why this approximation gives good results for large laser cavities is that only a small fraction β of the spontaneously emitted photons BN^2V_a is coupled into the lasing mode. The fraction $1-\beta$ is coupled into non-lasing modes or lost to radiation modes. For large lasers, β is in the range $10^{-4}-10^{-5}$.

By shrinking the cavity volume, the number of resonant modes available within the SPE spectrum decreases strongly. As a result, β will increase with decreasing cavity volume. The ideal single-mode cavity would effectively exhibit $\beta = 1$. In that case, all SPE is coupled into the lasing mode. As such, SPE is no longer a carrier loss mechanism. Experimentally, β values up to 0.85 have already been demonstrated [113].

2.7.2 The Purcell effect

Another physical effect that arises for reduced cavity volumes is the enhancement of the SPE rate, also known as the *Purcell* effect. The Purcell factor is defined as the ratio of the SPE rate in a microcavity as compared to the bulk SPE rate. For an ideal emitter[7], the Purcell factor F is given by [114]

$$F = \frac{3}{4\pi^2}\frac{\lambda_m^3}{n^3}\frac{Q}{V_m}, \tag{2.76}$$

where V_m is the optical mode volume, and λ_m is the resonance wavelength. As can be seen from this equation, the Purcell effect is favored by a high Q/V_m ratio, which is typically obtained for ultra-compact, low-loss PhC resonators. The best physical implementation of an ideal emitter is a single, properly positioned, quantum dot. As such, most experimental work on characterizing the Purcell effect is carried out on defect-based PhC cavities, containing a single or multiple quantum dots [115], [113]. Purcell factors up to 75 have been demonstrated experimentally [116].

2.7.3 Impact on laser performance

The influence of these microcavity effects on the laser performance can in the simplest approximation be studied by inserting the Purcell factor F in the rate equations, and assuming an enhanced β value [117], [118]:

$$\frac{dN}{dt} = \frac{I}{qV_a} - F\frac{N}{\tau_{sp}^0} - \frac{N}{\tau_{nr}} - v_g GS \tag{2.77}$$

$$\frac{dS}{dt} = \Gamma v_g GS + \Gamma\beta F\frac{N}{\tau_{sp}^0} - \frac{S}{\tau_p} \tag{2.78}$$

Here, τ_{sp}^0 is the spontaneous emission lifetime for bulk material and τ_{nr} is the non-radiative lifetime.

Static performance

The first obvious effect of enhanced β values is a softening of the threshold kink in the P-I curve, and an enhanced quantum efficiency below threshold.

---

[7] An ideal emitter is defined as a dipole which is perfectly aligned with the cavity mode, both spatially and spectrally.

Dynamic performance

Performing a rigorous small-signal analysis of (2.77)-(2.78), which doesn't neglect SPE contributions, leads to the following expressions for the relaxation oscillation frequency ω_r and damping coefficient γ [79]:

$$\begin{aligned}
\omega_r^2 &\simeq \frac{v_g a S}{\tau_p} + \frac{\beta N_0 \Gamma}{(\tau_{sp}^0/F)S}\left(\frac{1}{\tau_{tot}} - \frac{\beta}{\tau_{sp}^0/F}\right) + \frac{\beta}{(\tau_{sp}^0/F)\tau_p} &\quad (2.79)\\
\gamma &\simeq v_g a S + \frac{1}{\tau_{tot}} + \frac{\Gamma \beta F N}{\tau_{sp}^0 S}, &\quad (2.80)
\end{aligned}$$

with τ_{tot} the total carrier lifetime. For large laser cavities, only the first term of (2.79) is considered, since it dominates the expression for typical photon densities. From these expressions, it can be seen that a combination of high β and high F results in an increase of ω_r, especially at low pumping levels, for which the first – conventional – term is low due the low photon number. Additionally, microcavity lasers are expected to exhibit higher damping coefficients. A recent experimental demonstration of the increased modulation speed in microlasers is given in [116], demonstrating a direct modulation speed of $100\,\mathrm{GHz}$ for an optically pumped photonic-crystal laser, with a measured Purcell factor $F = 75$.

In conclusion, microlasers with only one cavity mode within the transition spectrum of their gain material, which is concentrated at the anti-nodes of the cavity mode, exhibit an increased sub-threshold quantum efficiency and an increased sub-threshold modulation bandwidth, which are favorable properties for low-power, integrated light sources.

2.8 Conclusion

In this chapter, we have given an overview of the challenges that arise when designing electrically-injected thin-film microlasers. An important design aspect is to keep the parasitic optical loss of the resonator as low as possible, since it directly affects the laser threshold and efficiency. Contributions to this loss are due to radiation, scattering and absorption at metal contacts and internal absorption in doped layers and low-bandgap contact layers. However, achieving an adequate electrical injection efficiency with low voltage is equally important, requiring current-spreading layers, contact layers, and metal contacts, possibly in close proximity with the optical field. A critical electrical bottleneck can arise at the p-type contact, since heavily-doped, low-bandgap contact layers are required to achieve low contact resistivity. Therefore, a balanced trade-off has to be found between resonator loss and injection efficiency.

Several structures were considered, both concerning the position of the metal contacts and the optical confinement scheme. When the InP film is coated at one or both sides with a metal contact, in close proximity to the optical field, the film thickness needs to be 1.5 to 2.8 μm thick, in order to obtain sufficiently low optical absorption at conventional metal contacts. Using pure gold contacts can reduce this thickness, but such contacts are not reliable. For these thick films, the etching processes required to fabricate a microresonator are technologically very challenging. Furthermore, their multi-modality complicates the microresonator design, and evanescent coupling to an underlying waveguide is less efficient.

For the above reasons, an injection scheme with lateral metal contacts is preferred. However, such structures require current-spreading layers to achieve adequate lateral injection efficiency. Optical confinement schemes with lateral optical confinement include the microdisk resonator and photonic-crystal resonators. Microdisks are attractive as a thin-film resonator, as they offer a compact footprint ($< 10 \times 10\,\mu\mathrm{m}^2$), with the optical mode propagating at the edges of the disk, allowing for a metal contact to be placed in the center of the disk, without causing additional absorption. Furthermore, their fabrication is relatively easy. Defect-based photonic-crystal resonators offer the highest possible photon confinement, and allow for the exploitation of the Purcell effect that results in enhanced sub-threshold efficiency and enhanced modulation bandwidth. However, fabricating photonic-crystal structures with efficient electrical injection is far more challenging. As a result, we decided in the course of this work to focus on the microdisk laser.

Chapter 3

Design of SOI-integrated microdisk lasers

This chapter provides a detailed theoretical analysis of the performance of a thin-film, tunnel-junction-based SOI-integrated microdisk laser. This laser type has been the main subject of study in this PhD work, mainly due to its relatively easy fabrication and excellent performance. First, the resonant modes in a microdisk are studied, with a detailed assessment of all the loss factors. Then, the electrical characteristics are analyzed, for a structure containing a tunnel junction, followed by a thermal analysis. A rigorous radially-dependent rate-equation model is used to predict the static lasing performance. A simplified model is used both to optimize the static performance, as well as to estimate the dynamic characteristics. Finally, an alternative microdisk laser design is proposed, exhibiting an improved fabrication tolerance on the bonding layer thickness.

3.1 Integrated microdisk laser layout

The layout of the SOI-integrated microdisk laser is shown in figure 3.1. A microdisk is etched into an InP-based film with a total thickness t, bonded onto a patterned and planarized, passive SOI waveguide structure. The InP etch is incomplete, leaving a thin lateral bottom contact layer with thickness t_s. The top metal contact is placed in the center of the disk, without overlapping the whispering-gallery mode at the disk edge. The bottom metal contact is applied to the bottom contact layer. The disk edge is laterally aligned to an underlying SOI wire waveguide, with an intermediate SiO_2 thickness t_{ox}. The wire waveguide has a width w_{Si} and a height of 220 nm. The microdisk is also embedded in a low-refractive-index polymer or dielectric (not drawn on fig. 3.1), which both serves as an (optical) isolation and planarization layer. For fabricated devices, we typically used a Benzocyclobutene (BCB) polymer for this purpose.

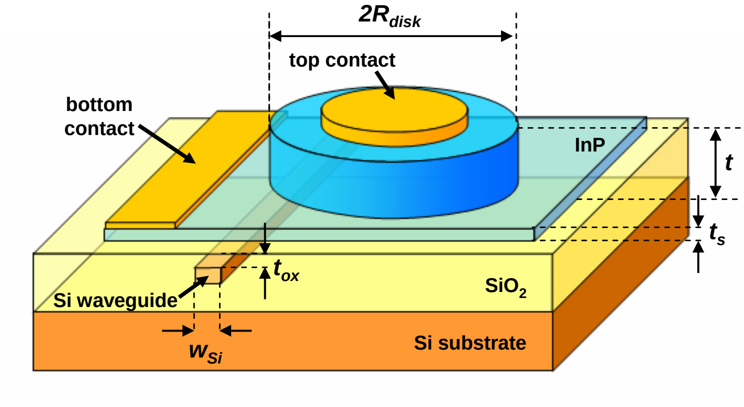

Figure 3.1: Schematic representation of the heterogeneous SOI-integrated microdisk laser.

3.2 Optical resonances in a microdisk

3.2.1 Whispering-gallery modes

Since a microdisk structure has cylindrical symmetry, solving for the optical field can be simplified by expressing the Helmholtz equation in cylindrical coordinates. Under the assumption[1] that the modes can be separated in TE- and TM-polarized modes, with respective components (E_r, E_ϕ, H_z) and (H_r, H_ϕ, E_z), the fully-vectorial Helmholtz equation can be reduced to the scalar equation

$$\left(\frac{\partial^2}{\partial z^2} + \frac{\partial^2}{\partial r^2} + \frac{1}{r}\frac{\partial}{\partial r} + \frac{1}{r^2}\frac{\partial^2}{\partial \varphi^2} + k^2 n^2(r)\right)\Psi_z(r,\varphi,z) = 0, \tag{3.1}$$

where Ψ_z is the H_z-component for TE modes and the E_z component for TM modes, and $n(r)$ the piecewise constant refractive index of the material. In order to pursue an analytical solution, some further simplifications are introduced [119]. First, the optical field profile in the z direction is assumed to be identical to that of a slab waveguide, resulting in an effective index n_{eff} that is then to be used in the remaining 2-D in-plane Helmholtz equation. Further, it is assumed that the optical field is propagating in the azimuthal direction, so that the mode can be further separated into a radially dependent part and an azimuthal phase factor: $\Psi_z(r,\varphi) = \Psi_z(r)e^{iM\varphi}$, with M the integer azimuthal eigenvalue. This leads to the Bessel equation for the radial field profile:

$$\left(\frac{\partial^2}{\partial r^2} + \frac{1}{r}\frac{\partial}{\partial r} + k^2 n^2(r) - \frac{M^2}{r^2}\right)\Psi_z(r) = 0. \tag{3.2}$$

---

[1] for microdisks with finite thickness, this assumption is only strictly valid for microdisks with vertical mirror symmetry, and even then only in this mirror symmetry plane.

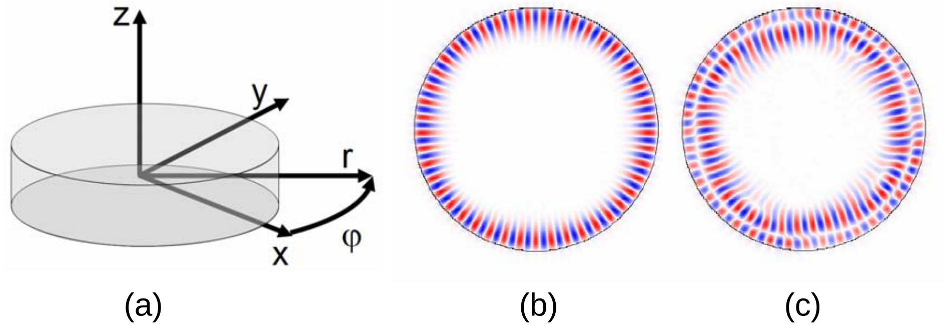

Figure 3.2: Definition of cylindrical coordinate system (a), and whispering-gallery mode H_z profiles for an InP disk with a radius of 4 μm (TE), calculated with 3-D FDTD, for $(K, L, M) = (0, 0, 45)$ (b), and $(K, L, M) = (0, 1, 40)$ (c).

The physically meaningful solutions to this equation are Bessel functions of the first kind $J_M(\tilde{k}n_{eff}r)$ inside the disk ($r < R$), and Hankel functions of the second kind $H_M^{(2)}(\tilde{k}n_0r)$ outside the disk ($r > R$, refractive index n_0), with a complex propagating constant $\tilde{k} = \tilde{\omega}/c$, or equivalently, a complex resonance frequency $\tilde{\omega} = \omega - i\gamma/2$. Applying the boundary conditions at the disk edge (requiring a continuous axial field) results in a transcendental dispersion relation for $\tilde{\omega}$. Solutions to this equation were numerically calculated in [77]-[120]-[121]-[75], for different normalized disk radii and refractive-index contrasts. For a given azimuthal order M, many discrete radial solutions exist (with eigenvalue L), scattered over the complex plane. All solutions have an imaginary part $\gamma/2$, which implies a continuous energy loss due to bending, and is directly related to the resonator quality factor $Q = \omega/\gamma$. A slightly different method was used in the original paper by Frateschi [119], where a complex azimuthal mode number $Z = M + i\alpha R$ was assumed. The bending loss α was then calculated by using conformal mapping.

The solutions can thus be labeled with radial and azimuthal mode numbers L and M, and additionally a vertical mode number K, if the slab waveguide is multimodal. The mode numbers K, and L represent the number of nodes of the field profile in their associated direction. Two of such resonant modes are shown in figure 3.2. It can be seen that the resonant modes are guided in a thin shell at the disk edge, and don't need an inner surface with a refractive index contrast for confinement. This situation is to some degree analogous to the propagation of acoustical waves at the walls of a chapel or a theater, which is why these modes are also known as *whispering-gallery* modes.

For laser operation, we are mainly interested in the fundamental whispering-gallery modes $(0, 0, M)$, which have the highest confinement and the lowest optical loss. M can be both positive or negative, illustrating the fact that each resonance exists in a clockwise and counterclockwise version. If both modes are excited with the same amplitude, they interfere to form a standing wave pattern with $2M$ azimuthal nodes. The degeneracy can be lifted in non-ideal microdisk resonators due to contradirectional coupling, for instance at sidewall roughness at the disk edge. In this case, two resonator modes with slightly different wavelengths arise for a mode number set, each exhibiting a partial standing-wave behavior [75].

Approximate analytical solution

A further approximation can be made by imposing the simple boundary condition $\Psi_z(r = R, \varphi) \equiv 0$ [119]. While this approach doesn't allow for an assessment of the bending loss, it is useful to obtain approximate field profiles. This boundary condition results in the resonant frequencies

$$\lambda^{LM} = \frac{2\pi}{X^{LM}} n_{eff} R, \tag{3.3}$$

where X^{LM} is the L-th zero of the Bessel function of M-th order J_M, and the radial field profile

$$H_z(r) = J_M(X^{LM}\frac{r}{R}). \tag{3.4}$$

The effective index n_e of the mode, defined at the microdisk edge, is then given by $n_e^{LM} = M/X^{LM} n_{eff}$. This is consistent with the general relation between the azimuthal mode number M and n_e^{LM}

$$M = \frac{2\pi R n_e^{LM}}{\lambda^{LM}}. \tag{3.5}$$

The mode separation $\Delta\lambda$, or free spectral range, is given by

$$\Delta\lambda = \frac{\lambda^2}{2\pi R n_g}, \tag{3.6}$$

with $n_g = n_e - \lambda dn_e/d\lambda$ the group index of the WGM.

Rigorous numerical solution

Since our microdisk structures incorporate a bottom contact layer which favors higher bending loss, it is difficult to use the above semi-analytical approach to calculate the bending loss with adequate precision. Therefore, we chose to model the bending loss with other, purely numerical tools. The first method is based on the commercial complex mode solver *FimmWave*, which uses eigenmode expansion. FimmWave allows for the calculation of the complex propagation constant and field profiles of the guided modes in bent waveguides. Since no azimuthal boundary conditions are involved, this tool yields the intrinsic properties of the bent waveguide modes that are at the basis of the whispering-gallery resonances, not only at wavelengths that comply with the azimuthal resonance condition, but at arbitrary wavelengths. The second tool *MEEP* [122] involves two-dimensional finite-difference time-domain (FDTD) calculations in the (r, z) plane, with a given azimuthal order M, or fully three-dimensional FDTD. These calculations yield the resonant wavelengths and quality factors of the spectrally discrete microdisk resonances.

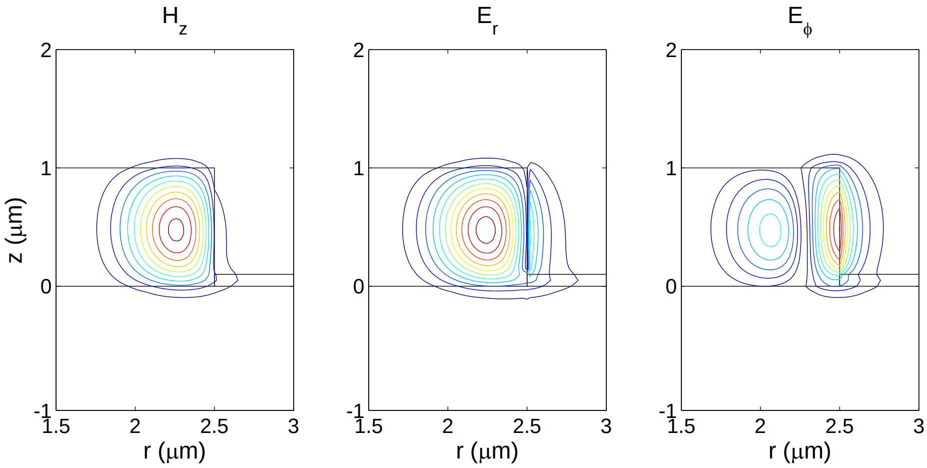

Figure 3.3: Cross-sectional $H_z(r,z)$, $E_r(r,z)$, $E_\phi(r,z)$ profiles for the fundamental TE-polarized WGM in a 5-μm-diameter 1-μm-thick microdisk (FimmWave, $\lambda = 1.55\,\mu$m). The contour level values are different for each graph.

In the following sections, we will focus on 0.5-μm-thick and 1-μm-thick microdisk structures, to which we shall refer as *thin* and *thick* films respectively. While for these thicknesses, the epitaxial film is multimodal, they allow for the incorporation of a tunnel-junction-based electrical injection scheme, as will be discussed in section 3.4. The cross-sectional mode profiles H_z, E_r and E_φ in the (r,z) plane of the fundamental TE-polarized bent waveguide mode in a 1-μm-thick, 2.5-μm-radius microdisk with a 100-nm-thick contact layer, calculated with FimmWave, are shown in figure 3.3. A simplified disk structure was assumed, with a refractive index of 3.2 for the disk and contact layer, 1.44 for the SiO_2 bonding layer and 1.54 for the Benzocyclobutene (BCB) cladding material. Figure 3.4 (a) shows the intensity mode profiles at half microdisk thickness, as well as the intensity of the approximate analytical solution J_M^2. It can be seen that the approximation produces a H_z^2 mode profile that is almost identical to the rigorously calculated H_z^2 mode profile. However, for the modeling of laser operation, the $|\mathbf{E}^2|$ profile is of more importance, since this is the field that physically interacts with the dipoles in the gain region. While the agreement between the $|\mathbf{E}^2|$ and the J_M^2 profile is of lower quality, due to the appearance of the mode tail outside the disk, it should be noted that the calculation of the lateral overlap between the optical field and the active region also involves the square of refractive index profile $n^2(r)$:

$$\Gamma_r = \frac{\int_0^R n^2(r)|\mathbf{E}^2(r)|2\pi r dr}{\int_0^\infty n^2(r)|\mathbf{E}^2(r)|2\pi r dr}. \tag{3.7}$$

Due to the high index contrast, the impact of this mode tail on the quality of the approximation is relatively low, at least for not too small microdisks. Indeed, for

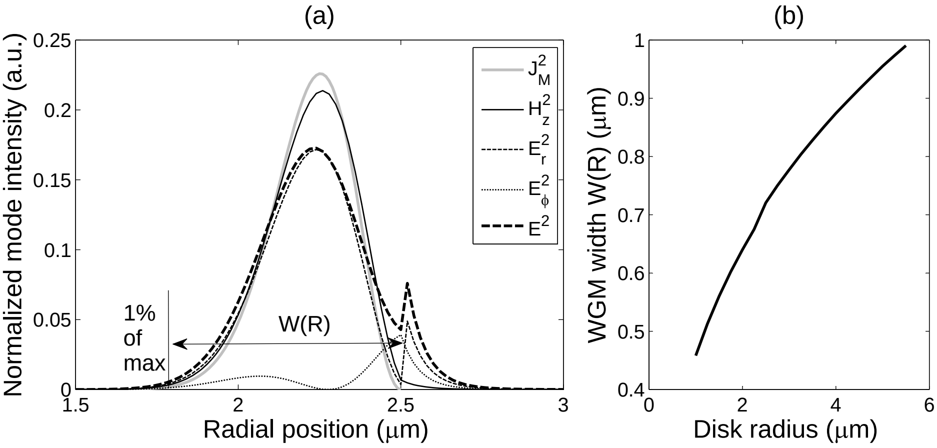

Figure 3.4: (a) Normalized $H_z^2(r)$, $E_r^2(r)$, $E_\phi^2(r)$ and $E^2(r)$ profiles at half microdisk thickness for the fundamental TE-polarized whispering-gallery mode, for 5-μm-diameter 1-μm-thick microdisk (FimmWave, $\lambda = 1.55\,\mu$m). A good approximation for the mode profile consists of a Bessel function of the first kind J_M inside the disk and a vanishing field outside the disk. (b) The WGM width $W(R)$ as a function of disk radius, calculated for $J_M(r)$.

$R > 2.5\,\mu$m, we calculate $\Gamma_r > 95\%$, justifying the approximation. We will rely extensively on this approximation when calculating the laser performance in section 3.7.

Using the approximate mode profiles, we now proceed with calculating the mode width $W(R)$, which we arbitrarily extract at 1% of the maximum mode intensity, as a function of disk radius. $W(R)$ is in the range 0.19-0.46R, with increasing absolute lateral confinement for smaller microdisk radii, as illustrated in figure 3.4 (b).

Finally, figure 3.5 shows the effective index n_e and group index n_g of the simplified 0.5-μm-thick microdisk as a function of disk radius. With an effective index in the range 2.2-2.6, we can expect to have relative efficient coupling between the WGM and the (curved) SOI wire waveguide, whose propagating modes have comparable effective indices [5].

3.2.2 Bending loss

Bending loss is typically very low for microdisk structures with a diameter of a few micrometer, given the high refractive index contrast between the disk and the surrounding medium (air). Ultra-compact, pedestal-supported microdisk lasers with diameters as small as $2\,\mu$m have been demonstrated [50]. However, our design includes a thin lateral bottom contact layer with thickness t_s, which might introduce additional bending loss, especially for thick contact layers and small disk diameters. Also, for planarization and isolation purposes, the surrounding medium is BCB rather than air (see chapter 4), which leads to higher bending loss due to the reduced index contrast. With the eigenmode-expansion method, the bending loss can

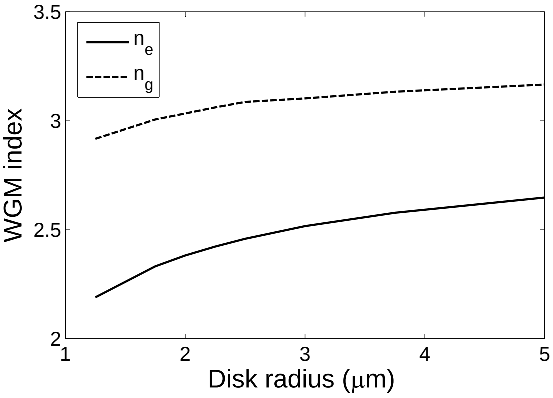

Figure 3.5: Effective index n_e and group index n_g for the fundamental TE-polarized WGM in a 0.5-μm-thick microdisk versus bend radius, calculated with FimmWave.

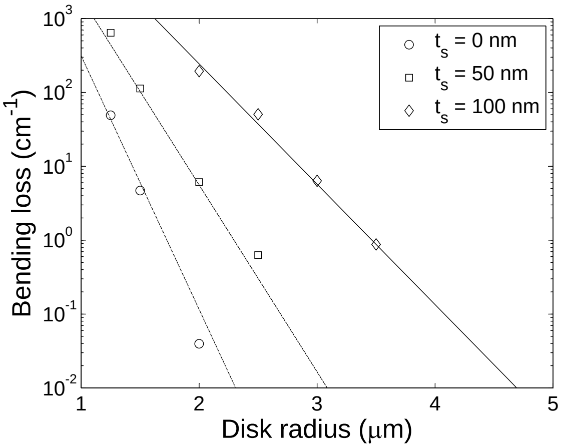

Figure 3.6: Bending loss α_b for the fundamental TE-polarized WGM, for thin microdisks versus diameter for different bottom contact layer thicknesses t_s. Lines represent eigenmode-expansion calculations, whereas the markers show 2-D FDTD results.

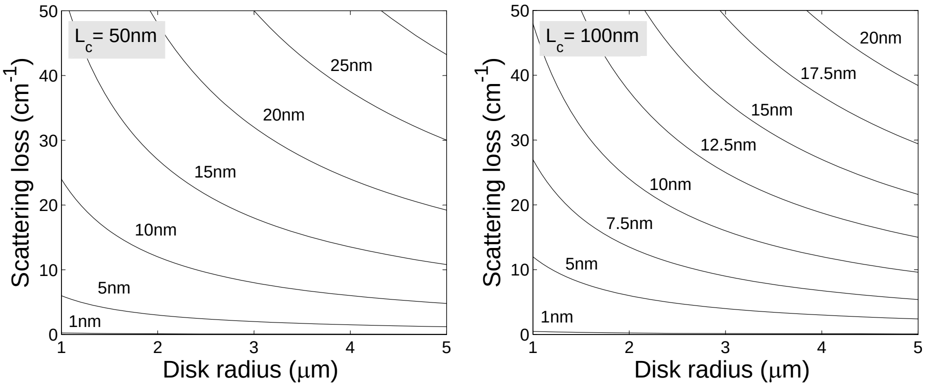

Figure 3.7: Calculated scattering loss [77] as a function of disk radius and sidewall roughness rms value σ, assuming a roughness correlation length S_c of 50 nm (left) and 100 nm (right).

be calculated directly from the imaginary part of the effective index of the calculated guided mode. For the FDTD simulations, the bending loss can be calculated as

$$\alpha_b = \frac{2\pi n_g}{Q_b \lambda_0} \tag{3.8}$$

with Q_b the quality factor of the resonance calculated for a transparent microdisk, n_g the group index of the mode and λ_0 the vacuum wavelength. For the eigenmode-expansion calculations, λ_0 was set to 1.55 μm, while for the FDTD calculations, the resonant mode with wavelength closest to 1.55 μm was considered. The bending loss was calculated for the thin structure for three values of t_s: 0, 50 and 100 nm. Only the TE-polarized WGMs were considered. The results can be found in figure 3.6. The group index was set to 3.15, based on calculations for 7.5-μm-diameter disks. Qualitative agreement was obtained between the two methods, with deviations being caused by discretization errors, since the bending loss is very sensitive to disk radius and contact layer thickness. For the FDTD simulations, a resolution of 20 nm was used, which is close to the dimension of the contact layer. For 1-μm-thick microdisks, bending loss behaves similarly, but is somewhat smaller. From these results, it is clear that disk diameters should be larger than 4.5 μm, assuming that $t_s = 50$ nm for proper electrical operation, and tolerating a maximum bending loss of 1 cm^{-1}.

3.2.3 Scattering loss

For an assessment of the scattering loss that can be expected in our microdisk structures, we rely on the closed-form expression obtained by the volume-current method in [77]:

$$\alpha_s = \frac{16\pi^3}{3R}\left(1 - \frac{n_0^2}{n_{eff}^2}\right)^2 \left(\frac{n_{eff}\sigma}{\lambda}\right)^2 \frac{n_{eff}L_c}{\lambda}\Gamma_z \frac{t}{\lambda}, \tag{3.9}$$

where n_{eff} is the effective index of the disk region, n_0 the index of the surrounding medium, σ the rms value and L_c the correlation length of the edge roughness, and Γ_z the vertical disk confinement factor. In figure 3.7, α_s is plotted as a function of σ and R, for a 1-μm-thick film and assuming a roughness correlation length $L_c = 50\,\text{nm}$ or $L_c = 100\,\text{nm}$. It can be seen that to suppress scattering loss, the roughness rms value should be as low as 1 nm.

3.3 Coupling to the SOI waveguide

In the previous sections, the optical losses were considered as parasitic and were to be minimized. Obviously, the coupling loss into the SOI waveguide is to be considered as a useful loss factor, and should be optimized for proper device operation. Here, we quantify this coupling loss as a function of the bonding layer thickness t_{ox}, which is defined as the total SiO_2 thickness between the Si wire waveguide and the InP disk, the SOI wire waveguide width w_{Si} and the lateral offset between the InP disk and the Si waveguide. For zero lateral offset, the disk edge is assumed to be vertically aligned with the outer edge of the SOI wire. For a positive lateral offset, the waveguide is shifted away from the microdisk center. Three-dimensional FDTD calculations were performed, again for the simplified microdisk structure. The analysis was done both for thin and thick disks, with a fixed disk diameter of 7.5 μm. The SOI wire waveguide is 500 nm or 600 nm wide and 220 nm thick. The Si refractive index was set to 3.48. First, the Q factor was calculated for a microdisk without Si waveguide, being Q_b. Then, the calculations were repeated for structures with Si waveguide, yielding *loaded* quality factors Q_L. The quality factor Q_c due to coupling to the waveguide was then estimated as

$$Q_c = \left(\frac{1}{Q_L} - \frac{1}{Q_b}\right)^{-1} \tag{3.10}$$

The distributed coupling loss α_c is then given by

$$\alpha_c = \frac{2\pi n_g}{Q_c \lambda_0}. \tag{3.11}$$

Only the fundamental resonances with wavelength closest to 1.55 μm were considered. The results for a 500-nm-wide SOI wire waveguide are shown in figure 3.8. For both structures, the coupling loss depends exponentially on t_{ox}:

$$\alpha_c(t_{ox}) = A(t)\exp(-t_{ox}/B(t)) \tag{3.12}$$

For a given bonding layer thickness, coupling is much more efficient for the thin structures. This could be expected since for the thick structures the WGM has a very weak evanescent tail in the bonding layer, which results in a low mode overlap with the SOI waveguide mode. Furthermore, the phase matching of the WGM mode with the Si waveguide mode gets worse with increasing disk thickness, due to the increasing WGM effective index n_e. For the thick microdisk, a coupling loss of

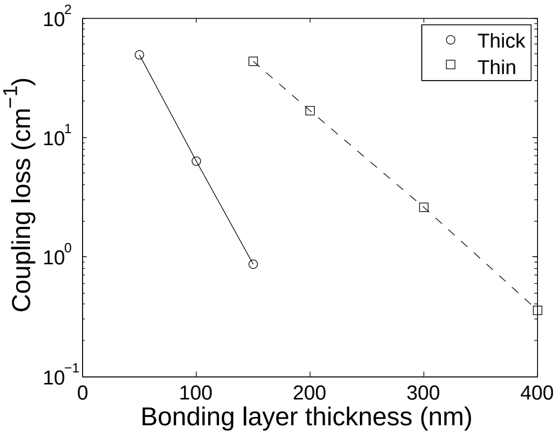

Figure 3.8: Distributed coupling loss α_c for thin and thick microdisks with 7.5-μm diameter and a 500-nm-wide SOI wire waveguide (without offset) versus bonding layer thickness t_{ox}.

20 cm^{-1} requires a 70-nm-thick bonding layer while a thin microdisk has the same coupling for a 190-nm-thick bonding layer. Moreover, the coupling is twice as sensitive to t_{ox} for thick structures than for the thin disks. The relative sensitivity of the coupling loss to variations in t_{ox} can be expressed as

$$\frac{1}{\alpha_c}\frac{d\alpha_c}{dt} = -\frac{1}{B} \tag{3.13}$$

For the thick microdisk, this sensitivity is $4\%/\mathrm{nm}$, whereas for the thin microdisk it is about $1.9\%/\mathrm{nm}$. This high sensitivity can be reduced by using even thinner InP films[2], which have less vertical confinement. However, in general this results in an increased internal loss, which limits the laser performance.

In figure 3.9, the coupling loss is shown as function of lateral waveguide-disk offset, for a thick microdisk and 500-nm and 600-nm-wide wires with a fixed bonding layer thickness of 100 nm. It can be seen that applying a lateral offset of 150 nm to a 500-nm-wide wire more than doubles the coupling efficiency, due to better phase matching. Increasing w_{Si} to 600 nm also improves the coupling efficiency, for the same reason. However, for this width, the SOI wire waveguide is no longer single mode. While FDTD images indicate dominant coupling to the fundamental wire mode, the wire should be tapered down to 500 nm to avoid mode conversion in the waveguide circuit. Lateral misalignment tolerances are clearly more relaxed as compared to the tolerance on the bonding layer thickness.

---

[2] An alternative strategy might be to use TM-polarized modes. These modes have less vertical confinement and are thus expected to exhibit stronger coupling to an underlying SOI wire with lower sensitivity to the bonding layer thickness. This approach would require an epitaxial structure with strong TM gain, based on quantum wells with tensile strain [123]. Also, the SOI circuit should be designed for TM polarization.

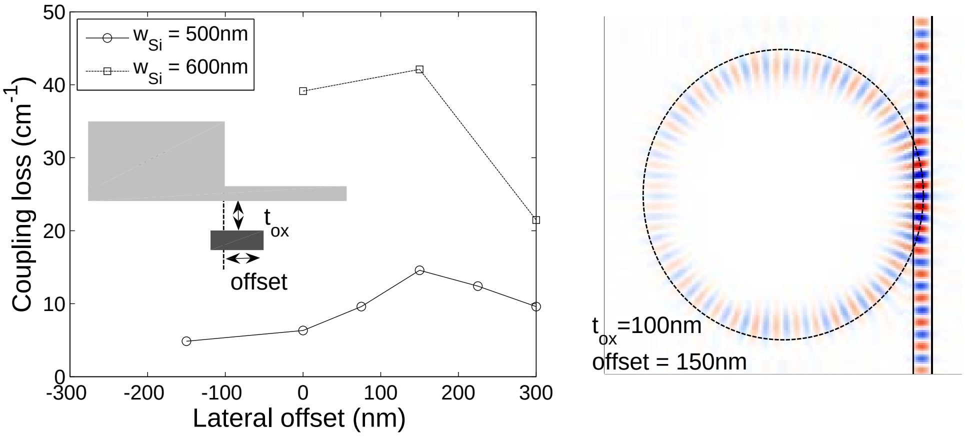

Figure 3.9: Left: distributed coupling loss α_c for a thick 7.5-μm microdisk, a bonding layer thickness $t_{ox} = 100\,\text{nm}$ and SOI wire waveguide widths $w_{Si} = 500\,\text{nm}$ and $600\,\text{nm}$, versus lateral disk-wire offset. Right: H_z profile in a plane between the disk and the Si waveguide, showing the evanescent tails of the WGM and the coupled light propagating in the Si wire.

3.4 Tunnel-junction-based epilayer design

Now, we investigate the performance of a tunnel-junction-based approach for a thin-film microdisk laser that has no metal contacts in close proximity with the optical field. We compare it with an approach based on a very thin InGaAs contact layer [89]. The tunnel junction is assumed to consist of two 20-nm-thick, heavily doped ($2\times10^{19}\,\text{cm}^{-3}$) InGaAsP layers with 1.2-μm bandgap wavelength (Q1.2). The active layer consists of three compressively strained (+1.7%) InAsP quantum wells, embedded in 20-nm-thick Q1.2 barriers, and surrounded with Q1.2 optical confinement layers (OCLs) with to-be-optimized thicknesses.

Three designs are considered, as shown in figure 3.10. Design A has the active layer in the center of the epitaxial structure, with the TJ below the active layer and symmetric OCLs, with identical thickness t_1, that is to be optimized for given total thickness t. Design B has the TJ in the upper part of the structure, but with potentially asymmetric OCLs (thickness t_1 and t_2) around the active layer, which doesn't have to be in the center of the epitaxial structure. This design allows for reducing TJ-related optical absorption loss by reducing optical confinement in the TJ while preserving optical overlap with the quantum wells and the underlying SOI waveguide. For a given total thickness t, t_1, t_2 and t_c should be optimized. Finally, design C is identical to design B except for the TJ and the top n-type contact layer which are replaced by a thin 15-nm p++ InGaAs contact layer and 100-nm p++ Q1.2 layer. Each of the designs includes an additional n-doped region ($5\times10^{18}\,\text{cm}^{-3}$) with thickness $d_n = t/3$, and an additional p-doped region ($5\times10^{17}\,\text{cm}^{-3}$) with thickness $d_p = t/7$, forming the p-

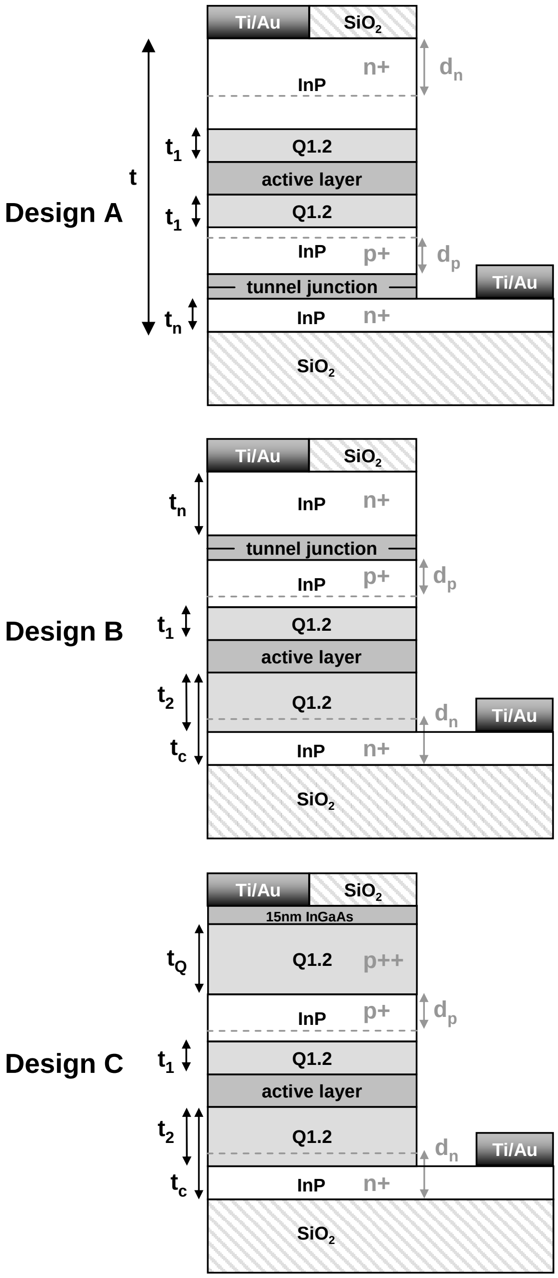
Design A
Ti/Au
SiO$_2$
t
InP
n+
d_n
t_1
Q1.2
active layer
t_1
Q1.2
InP
p+
d_p
tunnel junction
Ti/Au
t_n
InP
n+
SiO$_2$
Design B
Ti/Au
SiO$_2$
t_n
InP
n+
tunnel junction
InP
p+
d_p
t_1
Q1.2
active layer
t_2
Q1.2
d_n
Ti/Au
t_c
InP
n+
SiO$_2$
Design C
Ti/Au
SiO$_2$
15nm InGaAs
t_Q
Q1.2
p++
InP
p+
d_p
t_1
Q1.2
active layer
t_2
Q1.2
d_n
Ti/Au
t_c
InP
n+
SiO$_2$

Figure 3.10: Three epitaxial layer structure designs are under study: design A and B include a tunnel junction, whereas design C incorporates a thin ternary contact layer.

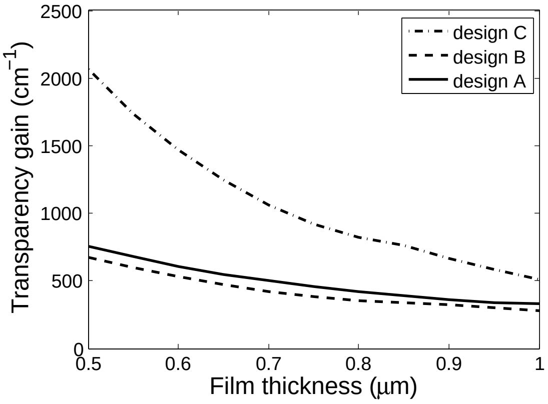

Figure 3.11: Optimized transparency gain G_{tr}, compensating for the internal loss, as a function of III-V film thickness t.

n junction. Designs A and B have an additional n-type contact layer with thickness $t_n = 100\,\mathrm{nm}$.

For each of the designs, the FCA is described by $\alpha = kP$ (in cm^{-1}), with P the doping level (in cm^{-3}) and k the loss coefficient. For n-type InP and InGaAsP we have used $k_n = 10^{-18}$cm^2, while for p-type InP $k_p^{InP} = 25 \times 10^{-18}$cm^2 and for p-type InGaAsP $k_p^Q = 40 \times 10^{-18}$cm^2 [35]. The OCLs are assumed to be filled with carriers with density $N_{OCL} = \frac{t_{QW}\tau_s}{t_{OCL}\tau_e} N_{QW}$, with t_{QW} the total thickness of the quantum wells, t_{OCL} the total OCL thickness, N_{QW} the carrier density in the quantum wells, τ_e the quantum well carrier escape time (25 ps), and τ_s the carrier diffusion time in the OCLs, given by $\tau_s = \frac{t^{*2}_{OCL} q}{4 k_B T \mu_h}$, with t^*_{OCL} the maximum of t_1 and t_2, q the elementary charge, k_B the Boltzmann constant, T the temperature (293 K) and μ_h the hole mobility in the OCL (70 cm^2/Vs) [94]. While a rigorous analysis should contain a self-consistent determination of N_{QW}, we have chosen a fixed value of 2.5×10^{18} cm^{-3}, which is a typical value at threshold.

For the three designs, we have optimized the relevant thicknesses to achieve the lowest material gain required to compensate for the internal loss, which can be calculated as $G_{tr} = \alpha_{int}/\Gamma_{QW}$, with Γ_{QW} the optical confinement factor of the quantum wells, for total film thicknesses in the range 0.5-1 μm, using a one-dimensional eigenmode-expansion technique [124]. The optimized G_{tr} values are shown in figure 3.11. For 500-nm-thick films, the TJ-based approaches A and B strongly outperform design C, with respective G_{tr} values of 755 cm^{-1} and 674 cm^{-1} versus 2061 cm^{-1}. For 1-μm-thick films, optimized G_{tr} values are 330 cm^{-1} and 278 cm^{-1} respectively, versus 513 cm^{-1}.

A breakdown of the loss contributions to the total internal loss for design A is shown in figure 3.12. For all thicknesses, the major contribution is due to IVBA in the p-side of the heavily doped TJ, followed by IVBA losses in the quantum wells, in the p-region and n-region of the diode and in the OCLs. For the remainder of

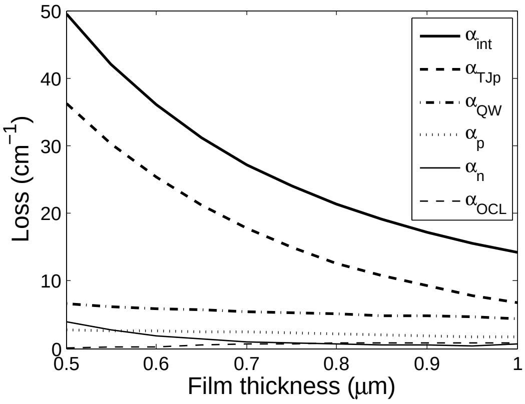

Figure 3.12: Breakdown of the internal loss contributions for design A versus III-V film thickness t. α_{int} is the total internal loss, α_{TJp} is the loss in the p-side of the tunnel junction, α_{QW} is the quantum-well contribution, $\alpha_{p/n}$ the loss in the diode p/n-doped layer and α_{OCL} is the loss in the optical confinement layers.

Parameter	Thin	Thick	Unit
t	0.5	1.0	μm
t_1	20	65	nm
α^0_{int}	13.3	7.5	cm^{-1}
Γ_{QW}	6.56	4.32	%
Γ_{TJp}	4.52	0.85	%

Table 3.1: Parameters for the two benchmark structures

the chapter, we will perform further device optimization for a *thin* (0.5 μm) and a *thick* (1 μm) benchmark structure, both based on design A. Although design B has slightly lower G_{tr} values, design A is used in fabricated devices. To avoid dopant diffusion into the active layer, the heavily p-type doped TJ-layer should be grown as one of the last layers. Since the epitaxial layer is bonded after growth, the TJ will indeed be located in between the active layer and the bonding interface.

In section 3.9, the TJ p-doping is considered as an optimization parameter, so the internal loss is split into a TJ-specific part, and a fixed contribution α^0_{int}, containing the other losses. The total internal loss then reads

$$\alpha_{int} = \alpha^0_{int} + \Gamma_{TJp} k^Q_p N_a \tag{3.14}$$

with N_a the TJ p-type doping level, and Γ_{TJp} the confinement factor of the TJ p-side. An overview of the relevant parameters for both structures is given in table 3.4.

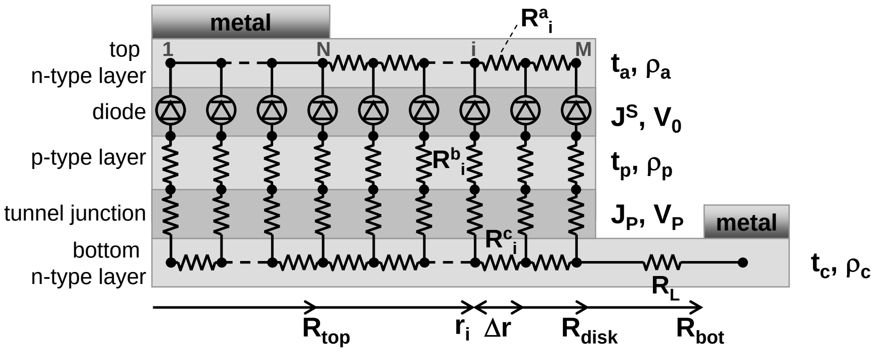

Figure 3.13: Lumped electrical network, used for analyzing the current path in the microdisk laser.

3.5 Electrical injection efficiency

Efficient laser operation also requires efficient current injection and low operating voltage. To analyze the current path in our TJ-based microdisk structure, we used an equivalent lumped circuit model as shown in figure 3.13. A two-dimensional network was used, exploiting the cylindrical symmetry of the disk. Another simplification was introduced by reducing the epitaxial layer structure to five functional layers, including an n-type contact and current spreading layer, a diode layer, a p-type layer, the tunnel-junction layer and a bottom n-type contact layer. Lateral drift current flow is expected to be mainly in the n-type layers, since they have the lowest effective resistivity. Lateral carrier diffusion was not taken into account. Each layer is characterized by its specific parameters. For the two n-type layers and the p-type layer, these are the thickness t_x of the layer and the resistivity ρ_x [125]. These parameters are then used to express the lumped resistors in the model:

$$\begin{aligned} R^a_i &= \rho_a \frac{\ln(r_i+\Delta r)-\ln(r_i)}{2\pi t_a}, r_i \geq R_{top} \\ &= 0, r_i < R_{top} \\ R^b_i &= \frac{\rho_p t_p}{\pi[(r_i+\Delta r)^2 - r_i^2]} \\ R^c_i &= \rho_c \frac{\ln(r_i+\Delta r)-\ln(r_i)}{2\pi t_c} \\ R_L &= \rho_c \frac{\ln(R_{bot})-\ln(R)}{2\pi t_c} \end{aligned} \tag{3.15}$$

with

$$\begin{aligned} \Delta r &= R/M \\ r_i &= \Delta r(i-1/2), i = 1 \ldots M \end{aligned} \tag{3.16}$$

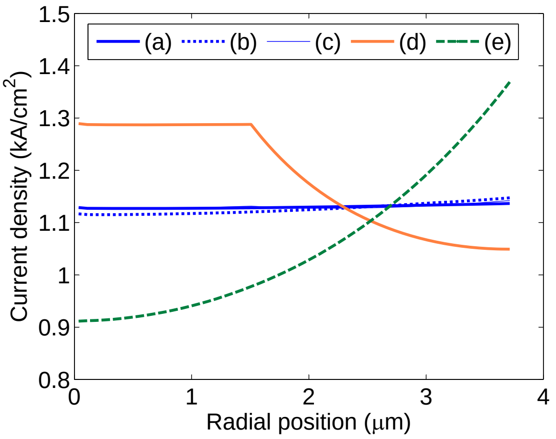

Figure 3.14: Current density versus radial position calculated for a 7.5-μm disk and $I = 0.5\,\mathrm{mA}$, calculated with the network shown in fig. 3.13, with the material parameters listed in table 3.5. Structures (a)-(d) include thick devices with $R_{top} = 0.4R$ or $0.8R$, and $N_a = 2 \times 10^{18}\mathrm{cm}^{-3}$ or $2 \times 10^{19}\mathrm{cm}^{-3}$, and show uniform current injection. Thin structures have comparable behavior. Structure (e) has a 10× worse conducting top n-layer and a 10× better conducting bottom n-layer, while (f) has the opposite composition.

The diode layer is characterized as a carrier-controlled voltage source:

$$V_i^{diode} = V_0 \ln\left(1 + \frac{N}{N_e}\right) = V_0 \ln\left(1 + \frac{I_i \tau_n}{q d_a A_i N_e}\right) \tag{3.17}$$

$$A_i = \pi[(r_i + \Delta r)^2 - r_i^2] \tag{3.18}$$

with N_e the intrinsic carrier density in the active region, τ_n the carrier lifetime and $V_0 = nk_BT/q$ where n is the diode's ideality factor.

Finally, the tunnel-junction layer is assumed to obey the voltage-current characteristic [91]

$$J_i^{TJ} = J_p \left(\frac{V_i^{TJ}}{V_p}\right) \exp\left(1 - \frac{V_i^{TJ}}{V_p}\right) \tag{3.19}$$

The parameters J_p and V_p depend on the bandgap and doping levels of the tunnel-junction layers. The explicit dependence was calculated in [90], for a similar InP-based tunnel junction, incorporated in a long-wavelength VCSEL. It was found that the TJ resistance decreases strongly with increasing p-doping level N_a in the TJ and with increasing bandgap wavelength of the TJ material, and to a lesser extent with increasing n-type doping level N_d. For our model, we rely upon the theoretical values for a 918-nm-bandgap InP TJ presented in [90]. Since our design includes a Q1.2 TJ, we expect to overestimate TJ voltage.

The nonlinear system containing the electrical network equations with $M = 51$ nodes was numerically solved for a total input current of 0.5 mA, using the parameter values shown in table 3.5. The calculated current density as function of radial

	Thin	Thick	Unit		Thin/Thick	Unit
ρ_a	17.5	25	$\mu\Omega\,$m	ϱ_c^{top}, ϱ_c^{bot}	2.0	$10^{-5}\,\Omega\,\text{cm}^2$
ρ_c	10	15	$\mu\Omega\,$m	τ_n	1	ns
t_p	100	220	nm	N_e	2.5	10^{11}cm^{-3}
ρ_p	3.0	3.0	m$\Omega\,$m	n	2	
t_a	160	340	nm	N_d	1	10^{19}cm^{-3}
t_c	100	100	nm	N_a	2, 6, 20	10^{18}cm^{-3}
$R_{bot} = R + 3.75\,\mu$m				V_P, J_P	from [90]	

Table 3.2: Parameter values used for the electrical analysis

position is plotted in figure 3.14, for different TJ doping levels, top contact sizes (a-d). For all cases, the current density is uniform with good approximation, indicating efficient current spreading in the n-type layers, even for $R_{top} = 0.4R$ and low TJ resistance. As a result, for sub-threshold operation, we expect a uniform carrier density profile. As such, neglecting carrier diffusion for the calculation of the injection profile was justified.

Two artificial, thick structures were also analyzed: structure (e) has a 10 times worse conducting top n-type layer and a 10 times better conducting bottom n-type layer, while (f) has the opposite composition. The first case clearly has worse lateral injection performance, since for $r > R_{top}$ the current preferably flows through the bottom n-type layer which has lower resistance. The latter has an increased injection density at the disk edge, which is advantageous for efficient laser operation, but it also has a 10 times bigger R_L resistance as compared to (a). Therefore the benefit of such an approach to increase laser efficiency might be limited. For the remainder of the chapter we will assume uniform injection for both benchmark structures.

Using this assumption, we now proceed with a more detailed assessment of the theoretical V-I characteristic. The device voltage contains contributions from the diode, the tunnel junction, the bottom contact layer, the metal-semiconductor contacts and current spreading:

$$V(I) = V^{diode}(I) + V^{TJ}(I) + (R_L + R_{cont} + R_{CS})I \tag{3.20}$$

with

$$\begin{align} R_{cont} &= \frac{\varrho_c^{top}}{\pi R_{top}^2} + \frac{\varrho_c^{bot}}{\pi((R_{bot}+l_t)^2 - R_{bot}^2)} \tag{3.21} \\ & \tag{3.22} \end{align}$$

and R_L as defined in (3.16), $V^{TJ}(I)$ as in (3.19) and $V^{diode}(I)$ as in (3.17), relative to the full microdisk area. $l_t = \sqrt{R_c^{bot} t_c/\varrho_c}$ is the carrier transfer length, which describes the effective length which carriers need to transfer from the metal into the semiconductor and vice versa. For the top contact, we assumed that the full contact area is used for carrier transfer. The metal contact resistivities ϱ_c^{top} and ϱ_c^{bot}

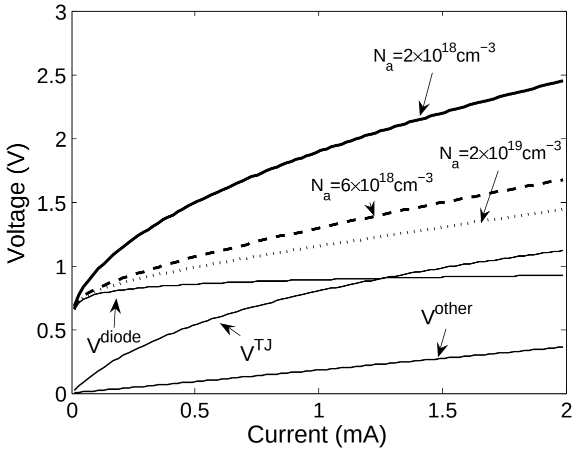

Figure 3.15: Calculated V-I curve for a thick 7.5-μm microdisk, assuming uniform injection, versus TJ p-doping level N_a. A breakdown of the device voltage is shown for $N_a = 2 \times 10^{18}\,\mathrm{cm}^{-3}$. For this doping level, the TJ voltage dominates other non-diode related voltage contributions.

were set to $5 \times 10^{-5}\,\Omega\,\mathrm{cm}^2$. The current spreading resistance R_{CS} is estimated to be $12\,\Omega$, based on the lumped network calculations. The calculated V-I curve for a thick 7.5-μm-diameter microdisk is shown in figure 3.15, for TJ p-doping levels N_a of $2{\times}10^{18}\,\mathrm{cm}^{-3}$, $6{\times}10^{18}\,\mathrm{cm}^{-3}$ and $2{\times}10^{19}\,\mathrm{cm}^{-3}$. Voltage contributions other than the diode voltage and TJ voltage are lumped together in V^{other}. The device voltage breakdown for $N_a = 2 \times 10^{18}\,\mathrm{cm}^{-3}$ is also shown. For these low TJ p-doping levels, V^{TJ} clearly dominates V^{other}. Increasing the TJ p-type doping level to $N_a = 2 \times 10^{19}\,\mathrm{cm}^{-3}$ substantially decreases device resistance. However, as indicated in section 3.4, higher p-type doping increases internal loss. Therefore, the optimum doping level represents the best trade-off between operating voltage and internal loss, and will be calculated in section 3.9.

3.6 Thermal resistance

In order to model the thermal impedance of the microdisk lasers, the heat equation should be solved:

$$\rho c \frac{\partial T}{\partial t} = q_v + \nabla \cdot (\kappa \nabla T) \tag{3.23}$$

where ρ is the density, c is the specific heat, $T(\mathbf{r}, t)$ is the temperature, t is the time, q_v is the heat dissipation per unit volume and κ is the thermal conductivity. Since the microdisk lasing structure has a cylindrical symmetry (except for the metal pads),

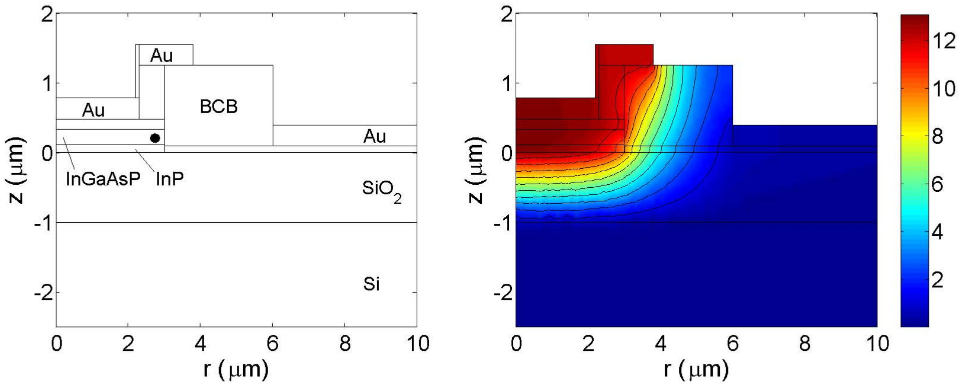

Figure 3.16: Left: geometry used for thermal simulations of generation 1 microdisk lasers. Right: steady-state temperature increase distribution for $P = 1\,\text{mW}$.

we can solve the problem in cylindrical coordinates:

$$r\rho c\frac{\partial T}{\partial t} = q_v r + \frac{\partial}{\partial r}\left(\kappa r\frac{\partial T}{\partial r}\right) + \frac{\partial}{\partial z}\left(\kappa r\frac{\partial T}{\partial z}\right) \tag{3.24}$$

with r and z the cylindrical coordinates. The laser structure that was used in the thermal model is depicted in figure 3.16. The geometry parameters were taken from the cross section of a fabricated structure of generation 1 ($t = 480\,\text{nm}$, $t_{ox} = 1\,\mu\text{m}$, see Chapter 5). A commercial finite-element tool was used to solve (3.24). Neumann boundary conditions were set on all boundaries of the structure, except for the bottom boundary, which is kept at a fixed temperature (Dirichlet boundary condition), and thus acts as a heat sink. Convection and radiation effects can be neglected and were not taken into account. To asses the impact of self heating on laser performance, we need to determine the temperature at the position of the maximum of the optical mode intensity in the active region. Therefore, the temperatures that are considered and presented in this section are extracted at $r = 0.9R$ at half thickness of the III-V membrane (the dot in figure 3.16). The heat is assumed to be dissipated homogeneously over the entire microdisk volume, so a total dissipated power P results in $q_v = P/(\pi R^2 t)$, with R the radius and t the thickness of the disk. The material parameters that were used in the simulation are listed in table 3.6. SiO_2 films can have a thermal conductivity κ in the range 0.8-1.4 W/Km, depending on the deposition technique [126]. Thermally grown SiO_2 films have $\kappa = 1.27\,\text{W/Km}$ whereas films deposited by Chemical Vapour Deposition (CVD) have $\kappa \sim 1\,\text{W/Km}$. For the simulations, $\kappa_{SiO_2} = 1.27\,\text{W/Km}$ was assumed, unless specified otherwise. The thermal conductivity of Au was set to half its bulk value, since the evaporated Au layer thicknesses were about 150 nm, and it is known that the thermal conductivity of Au decreases with decreasing film thickness [127]. For InP, the thermal conductivity was set to 40 W/Km, taking its high doping level into account (undoped InP has $\kappa = 68\,\text{W/Km}$).

Material	ρ	κ	c
	(g cm^{-3})	(Wm^{-1}K^{-1})	(Jg^{-1}K^{-1})
Si	2.3	130	0.70
SiO_2	2.2	0.8-1.4(1.27)	0.74
Au	19.3	150	0.13
BCB	1.0	0.3	2.18
InGaAsP	4.8	6	0.31
InP	4.8	40	0.31
Al_2O_3 (c)	3.9	36	0.93
Al_2O_3 (a)	3.9	2	0.93
MgO (μc)	3.6	4	0.88

Table 3.3: Material parameters used in the thermal simulation

The turn-on temperature evolution in a microdisk with $R = 3\,\mu$m was simulated for a dissipated power of 1 mW. The temperature step response is shown in figure 3.17 (left). In steady-state regime, a thermal resistance $R_{th} = 11.5\,\mathrm{K/mW}$ can be extracted. The heating transient behavior can be roughly fitted to an exponential heating curve, assuming a thermal time constant of $1.67\,\mu$s. The thermal resistance was calculated for disk radii in the range 1-5 μm and is inversely proportional to the disk diameter: $R_{th} \sim R^{-1.15}$ (fig. 3.17, right). The thermal resistance decreases slower with disk diameter as compared to the increase in disk area. So we can expect a better thermal behavior for smaller devices, assuming that the threshold power density for lasing doesn't depend on disk diameter. This is due to the fact that the heat flow at the edges of the disk becomes more dominant for smaller disk diameters. The thin lateral bottom contact layer indeed plays an important role in the heat evacuation for these smaller microdisks. A one-dimensional approximation for the thermal resistance $R_{th} = t_{ox}/\kappa_{ox}\pi R^2$ is also plotted (dotted line). It strongly overestimates the true thermal resistance, especially for smaller disks, since it doesn't account for the lateral heat flow.

The thermal resistance can be decreased by improving the heat flow through the bonding layer. Reducing the bonding layer thickness improves the heat evacuation, but too thin bonding layers will cause optical substrate leakage. Another option is to use a bonding material[3] with a better thermal conductivity and a low refractive index, such as crystalline Al_2O_3 or microcrystalline MgO (see table 3.6, [128], [129]). By replacing SiO_2 with Al_2O_3, the thermal resistance can be reduced by almost one

---

[3] For a microdisk integrated on an SOI circuit, the total SiO_2 thickness is mainly determined by the buried oxide layer of the carrier SOI wafer, which is typically 1-2 μm in order to achieve SOI waveguides with low substrate leakage. Therefore, the main heat flow bottleneck will arise in the SOI and the option to reduce thermal resistance by using thinner bonding and/or bonding layers with higher thermal conductivity layers is of little use for SOI-integrated microdisk lasers.

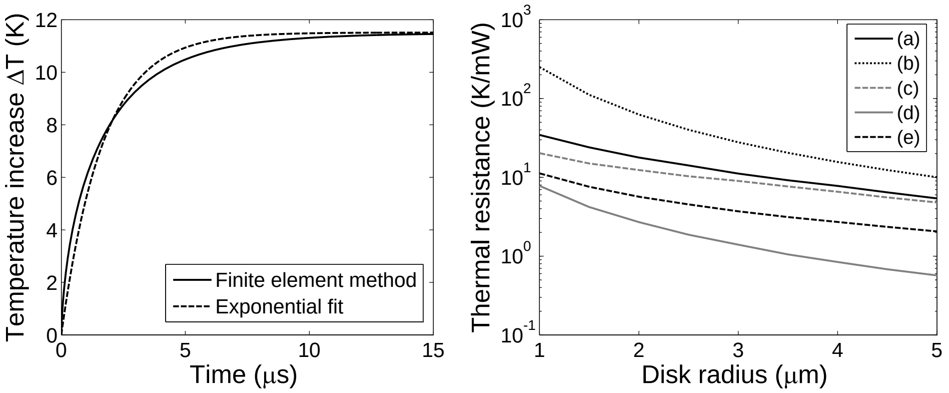

Figure 3.17: Left: temperature step response for $P = 1\,\mathrm{mW}$. Right: Thermal resistance versus microdisk radius, for disk geometry as in fig. 3.16 (a), 1D approximation $R_{th} = t_{ox}/\kappa_{ox}\pi R^2$ (b), BCB planarization layer replaced by amorphous Al_2O_3 (c), SiO_2 bonding layer replaced by crystalline Al_2O_3 (d), and microdisk with heat sink structure (e).

order of magnitude (figure 3.17 right, grey solid line). However, bonding with (crystalline) Al_2O_3 layers is technologically far less developed than SiO_2 bonding.

An alternative strategy is to spread the heat over a bigger area, so that the heat flows through a bigger part of the bonding layer. This effect is already present due to the thin lateral InP contact layer, but can be greatly enhanced if the BCB planarization layer is replaced with a better thermal conductor. It is highly unlikely that crystalline Al_2O_3 can be used as a planarization layer, since it needs to be deposited, so we assumed to have amorphous Al_2O_3 in this case ($\kappa = 2\,\mathrm{W/Km}$). The thermal resistance for structures where BCB is replaced by amorphous Al_2O_3 and with a SiO_2 bonding layer is also shown in figure 3.17 (right, grey dashed line). The thermal resistance is reduced by 10 to 40%, depending on the disk diameter. However, it should be noted that the refractive index of Al_2O_3 is about 1.7. As a result, bending loss will be higher than that of BCB-covered microdisks, and using Al_2O_3 for better lateral heat sinking is thus only of practical use for larger microdisk diameters.

Finally, another solution can be to create a thermal short circuit between the disk volume and the Si substrate, by etching a hole through the bonding layer and depositing a good thermal (metal) connection between the Si substrate and the microdisk. Assuming that this connection consists of a Au pad with a length L_{hs}, a thickness t_{hs}, and has the same width as the disk diameter, results in a shunt thermal resistance $R_{hs} = L_{hs}/2t_{hs}R\kappa_{Au}$. The total thermal resistance R_{th}^{tot} is then given by $R_{th}^{tot} = (1/R_{th} + 1/R_{hs})^{-1}$. We have done this calculation for $L_{hs} = 5\,\mu\mathrm{m}$ and $t_{hs} = 1\mu\mathrm{m}$, and the result is shown fig. 3.17 (right) as the black dashed line. The thermal resistance is about a factor 3 smaller as compared to the microdisk without thermal connection.

3.7 Steady-state laser characteristics

In order to model the static laser characteristics, we need to solve the spatially dependent rate equations (2.56), in steady-state regime. For a microdisk laser with perfect cylindrical symmetry containing one laser mode, these equations are simplified to[4]:

$$\begin{aligned} 0 &= -G\left[N(r), S\right] v_g \Psi^2(r) \Gamma \pi R^2 S - \left[AN(r) + BN^2(r) + CN^3(r)\right] + \\ & \quad D\left[\frac{dN(r)}{rdr} + \frac{d^2N(r)}{dr^2}\right] + \frac{\eta_v J(r)}{qt_a} \qquad (3.25) \\ 0 &= -\frac{S}{\tau_p} + \beta \int_0^R BN^2(r)\Psi^2(r) 2\pi r dr + S\Gamma \int_0^R G\left[N(r), S\right] v_g \Psi^2(r) 2\pi r dr \qquad (3.26) \end{aligned}$$

The following boundary conditions apply:

$$\begin{aligned} \left[\frac{dN}{dr}\right]_{r=0} &= 0 \qquad (3.27) \\ \left[\frac{dN}{dr}\right]_{r=R} &= \frac{-N(R)v_s}{D}, \qquad (3.28) \end{aligned}$$

which express zero lateral carrier current at the center of the disk due to symmetry, and surface recombination at the disk edge.

An overview of the used hypothetical (but realistic) material parameters that we used for the benchmark structure can be found in table 3.7. The mode profile $\Psi(r)$ was for simplicity approximated by the Bessel function $J_M(X_M r/R)$, where the mode number M corresponds to the resonance with wavelength closest to 1.55 μm. Also, we have used a single vertical injection efficiency $\eta_v = \eta_v^d$ both for below and above-threshold operation. The photon lifetime τ_p relates to the total modal loss α_{tot} as $\tau_p = 1/\alpha_{tot} v_g$. The total modal optical loss α_{tot} can be written as

$$\alpha_{tot} = \alpha_c + \alpha_b(R) + f(R)\alpha_{int} + \alpha_s(R), \qquad (3.29)$$

where $f(R)$ is a normalization factor that transforms the local internal loss to a modal loss defined with respect to the disk circumference, as are other loss contributions. $f(R)$ is calculated[5] as

$$f(R) = \int_0^R J_M^2(X_M \frac{r}{R}) \frac{r}{R} 2\pi r dr \qquad (3.30)$$

For $R = 2.5\,\mu$m, f is 0.866.

The output power P can be calculated from the photon density S as

$$P = \frac{1}{2}\pi R^2 t_a h\nu v_g \alpha_c S. \qquad (3.31)$$

---

[4] This analysis is based on [130]. As we expect the impact of microcavity effects to be weak for the relatively large microdisk lasers that are studied within this work, we simplified the expresssion for the contribution of the spontaneous emission to the photon density. Furthermore, the photon density S is defined with respect to the volume of the active region, yielding an additional factor Γ in equation 3.25.

[5] We assume $J_M(X_M r/R)$ normalized such that $\int_0^R J_M^2(X_M r/R) 2\pi r dr = 1$.

parameter	value	unit	parameter	value	unit
G_0	1500	cm^{-1}	α_i	10	cm^{-1}
N_0	1.5×10^{18}	cm^{-3}	α_c	10	cm^{-1}
ϵ	2×10^{-17}	cm^{-3}	α_s, α_b	0	cm^{-1}
A	10^{-8}	s^{-1}	Γ	4.32%	
B	2×10^{-10}	cm^3s^{-1}	v_g	c/3.4	
C	1.63×10^{-28}	cm^6s^{-1}	β	10^{-3}	
η_V, η_V^d	0.7		t_a	18	nm

Table 3.4: Model parameters used in rate equations

The factor 1/2 arises from the fact that we consider the unidirectional efficiency and the (ideal) microdisk supports two degenerate, counterpropagating laser modes that each couple into one direction of the SOI waveguide.

3.7.1 Lateral diffusion

As discussed in 3.5, uniform injection ($J(r) \equiv I/\pi R^2$) can be expected for structures that contain adequate current spreading layers. As a result, it can be expected that – for structures with negligible surface recombination – the threshold current doesn't depend on lateral diffusion, since in this case uniform injection results in a uniform sub-threshold carrier density profile. Above threshold, the photon density in the WGM builds up, burning a spatial hole in the carrier concentration. In fact, the carrier density in the laser region $R-W(R) < r < R$ gets clamped at its threshold value, while the carrier density in the center of the disk $0 < r < R-W(R)$ can grow above this value. Due the gradient in the carrier concentration, a lateral diffusion current will exist, which feeds additional carriers to the laser region. We have quantified this effect for a 5-μm-diameter microdisk as function of the ambipolar diffusion constant D. The impact of lateral diffusion on the differential efficiency is clear from figure 3.18: improved lateral diffusion results in a higher differential efficiency (a), and a more shallow spatial hole burnt into the carrier profile (b).

3.7.2 Surface recombination

As already mentioned in 2.3, the surface recombination velocity v_s depends on the Ga content of the active material. For InGaAsP quantum wells, v_s is of the order 10^4cm/s, whereas for InGaAs QWs, it is about 10^5cm/s. It is believed that for InAsP quantum wells, v_s is as low as for pure InP ($v_s < 10^4$cm/s). The impact of v_s on the static laser performance and the carrier density profile $N(r)$ for a 5-μm-diameter microdisk is shown in figure 3.19, for $v_s = 10^4$cm/s and $v_s = 10^5$cm/s, assuming $D = 8\,\text{cm}^2/\text{s}$. Below threshold, it is clear that surface recombination results in serious carrier depletion at the disk edge for $v_s = 10^5$cm/s, reducing the effective carrier density that can contribute to optical gain in the laser region and thereby

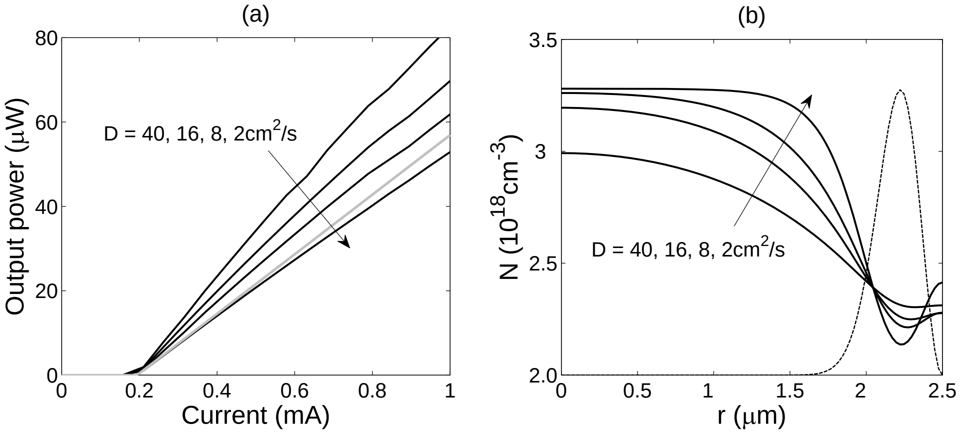

Figure 3.18: Lateral diffusion feeds extra carriers to the laser region, resulting in a higher differential efficiency (a), and a less distinct spatial hole burnt into the carrier density profile (b). The left part (a) also shows the P-I curve calculated under the assumption of no lateral current and an injection efficiency determined by the geometrical width of the WGM (grey line).

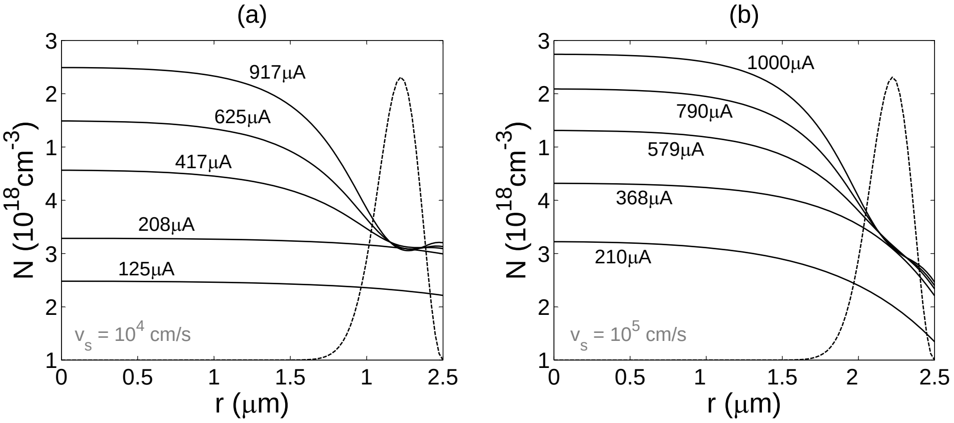

Figure 3.19: Radial carrier profile for a 5-μm-diameter microdisk as function of injection current. (a) $v_s = 10^4$cm/s, (b): $v_s = 10^5$cm/s, with $D = 8\,\text{cm}^2/\text{s}$. The WGM profile $\Psi^2(r)$ is also plotted as reference (dashed lines).

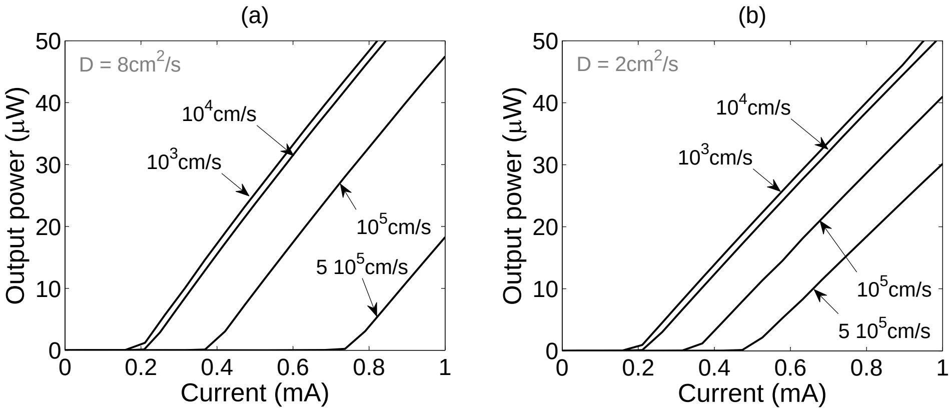

Figure 3.20: Impact of surface recombination on static laser performance. Enhanced lateral diffusion increases the performance penalty due to surface recombination.

giving rise to a threshold current penalty. For $v_s = 10^4$cm/s, the impact of surface recombination on threshold current is negligible, as can be seen from figure 3.20. The differential efficiency is in general less affected. As can be expected, the impact of surface recombination is minimized for a decreasing diffusion constant D.

3.7.3 Non-uniform injection

While the electrical analysis indicated uniform injection for the envisaged TJ-based epitaxial layer structure, these calculations were performed under the assumption of perfect cylindrical symmetry. This assumption might be questionable for some fabricated structures, for which the shape of the bottom contact doesn't have this symmetry (for technological reasons, see figs. 4.5(b) and C.2). Furthermore, the top contact might be misaligned with respect to the center of the microdisk. Such structures might suffer from current-crowding effects, which can have a strong impact on laser performance. To model these non-idealities, fully 3-D spatially dependent rate equations and electrical networks should be solved, which falls outside the scope of this work.

However, the effect of non-uniform injection for the specific case for which only a central part of the disk is pumped ($J(r) = I/\pi r_{inj}$ for $r \leq r_{inj}$, $J(r) = 0$ for $r > r_{inj}$) can provide some insight into the effects that are associated with non-uniform injection. Such a study was also performed in the case of post-injected microdisk lasers in [130]. It was found that laser threshold and differential efficiency depend strongly on the ambipolar diffusion constant D, since carriers need to diffuse from the center of the disk into the lasing region. Figure 3.21 shows the impact of this type of non-uniform injection on the static performance for our benchmark microdisk laser with $R = 2.5\,\mu$m (a). It is clear that both the threshold current and differential efficiency are strongly affected by increasingly non-uniform pumping. Fig. 3.21 (b) shows that

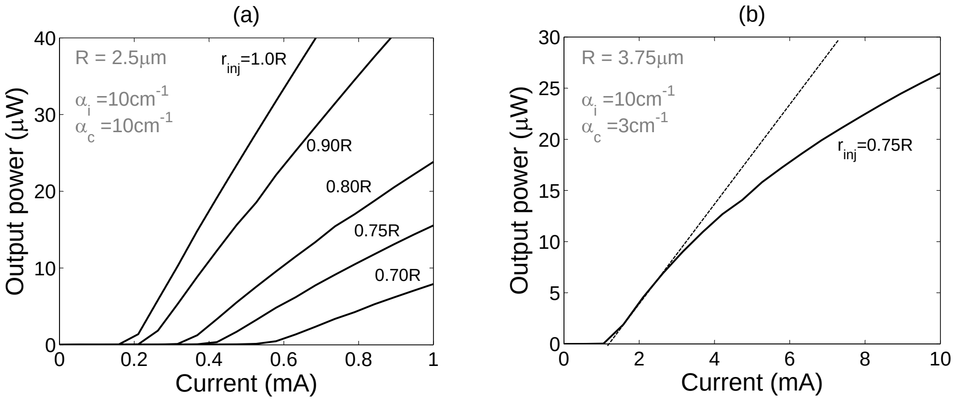

Figure 3.21: Impact of non-uniform injection (radially symmetric) on static laser performance ($D = 8\,\mathrm{cm}^2/\mathrm{s}$). (a) benchmark 2.5-$\mu$m-radius microdisk laser. (b) 3.75-μm-radius microdisk laser. The dashed line is a visual guide to illustrate the saturation effect.

non-uniform pumping can also cause a saturation effect in the laser output power at higher pumping levels (in this case for a bigger radius $R = 3.75\,\mu$m). This is due to a decreasing lateral injection efficiency, which is caused by the growing carrier loss due to Auger recombination in the injected region. This effect was also observed in [130].

3.8 Approximate laser models

3.8.1 Model 1: no lateral diffusion current

The simplest approximate model to calculate the static P-I characteristic is based on the assumption that there is no lateral current flow and that the lateral injection efficiency is simply determined by the ratio of the area occupied by the WGM compared to the total disk area. Assuming uniform injection then results in a lateral injection efficiency $\eta_L = 2W(R)/R - W^2(R)/R^2$, where $W(R)$ is the radial WGM width. This results in a injection efficiency $\eta_i = \eta_V \eta_L$. The optical extraction efficiency η_e is given by

$$\eta_e = \frac{\alpha_c}{\alpha_{tot}} \tag{3.32}$$

and the unidirectional differential efficiency η_d is then

$$\eta_d = \frac{1}{2}\eta_i \eta_e. \tag{3.33}$$

The threshold current can be written as

$$I_{th} = \left(AN_{th} + BN_{th}^2 + CN_{th}^3\right)\frac{V_a q}{\eta_i}. \tag{3.34}$$

N_{th} is the carrier density at threshold, and is calculated as

$$N_{th} = N_0 \exp\left(\frac{\alpha_{tot}}{\Gamma_{QW} G_0 f(R)}\right). \tag{3.35}$$

Clearly, the above expressions don't include gain suppression nor self-heating effects. Within this simple model, the above-threshold P-I curve is then given by

$$P = \eta_d \frac{h\nu}{q}(I - I_{th}), \tag{3.36}$$

with ν the laser frequency. We will use this simple model to optimize the static laser performance of the microdisk lasers in section 3.9

3.8.2 Model 2: including a lateral diffusion current

In order to take the lateral diffusion between the central disk region ($0 < r < R - W(R)$, carrier density N_1) and the laser region ($R - W(R) < r < R$, carrier density N_2) into account, the following rate-equation system can be used:

$$\begin{aligned}
\frac{dN_1}{dt} &= \frac{\eta_V J}{q t_a} - \frac{N_1}{\tau(N_1)} + \frac{2D(N_2 - N_1)}{R_1 L(N_1, N_2)} && (3.37)\\
\frac{dN_2}{dt} &= \frac{\eta_V J}{q t_a} - \frac{N_2}{\tau(N_2)} - \frac{2DR_1(N_2 - N_1)}{(R^2 - R_1^2)L(N_1, N_2)} - G v_g S && (3.38)\\
\frac{dS}{dt} &= -\frac{S}{\tau_p} + \beta \Gamma B N_2^2 + \Gamma G v_g S, && (3.39)
\end{aligned}$$

with

$$\begin{aligned}
\tau(N) &= (A + BN + CN^2)^{-1} && (3.40)\\
L(N_1, N_2) &= \sqrt{D\frac{\tau(N_1) + \tau(N_2)}{2}} && (3.41)
\end{aligned}$$

where $L(N_1, N_2)$ is the average diffusion length, and $R_1 = R - W(R)$. The diffusion-related terms in (3.37)-(3.38) were derived by approximating the lateral diffusion current density J_{diff} as

$$J_{diff} \simeq -D\frac{N_2 - N_1}{L}. \tag{3.42}$$

In (3.37)-(3.39), uniform injection was assumed, via the constant injection current density J. However, the equations can be easily altered to model a microdisk with only injection in the central part. When D is set to zero, Model 2 is reduced to Model 1.

Figure 3.22 shows the comparison of the static P-I curves calculated with the fully radially-dependent rate equations and Model 2. As could be expected, Model 2 accurately reproduces the threshold current in the case of uniform injection ($r_{inj} = R$). Without lateral diffusion ($D = 0$), the lumped model slightly overestimates the

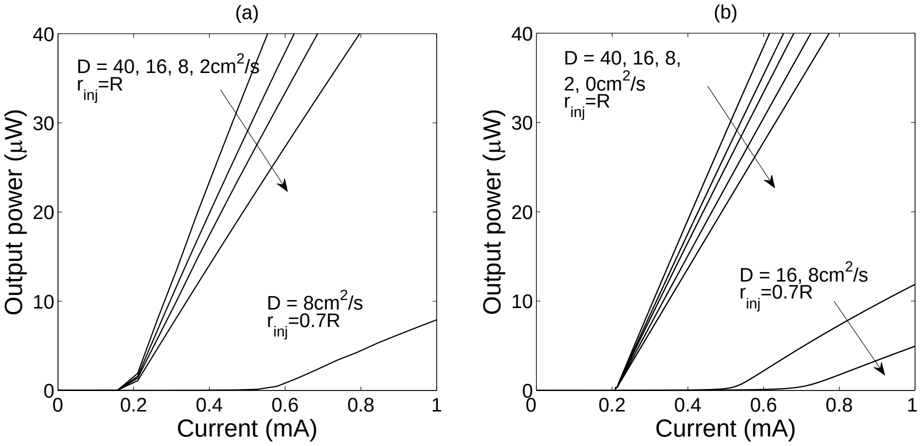

Figure 3.22: Comparison of simulation results for the benchmark 2.5-μm-radius microdisk laser, calculated with (a) fully radially-dependent rate equations and (b) rate-equation system with two lumped carrier densities. A good (qualitative) match is obtained, however with a slight underestimation of the lateral diffusion in the latter case.

slope efficiency, most likely due to the arbitrary definition of the WGM width $W(R)$, at 1% of the maximum mode intensity. With increasing diffusion constant, the simple lumped model slightly underestimates the output power. This slight underestimation of the lateral diffusion is also visible for microdisks with only central injection ($r_{inj} = 0.7R$). However, using higher (effective) values for D can compensate for this underestimation. We will use this model to estimate the dynamic behavior of the microdisk lasers in section 3.10.

3.9 Static performance optimization

Now, we use the approximate laser model described in the previous sections to optimize the global device performance of a TJ-based microdisk laser, using the previously calculated values for bending loss, internal loss, scattering loss and device voltage. More specifically, we will optimize the disk radius R, coupling loss α_c and TJ p-type doping N_a to minimize the required input power P_{in} for a given optical output power P_u. P_{in} can be written as

$$\begin{aligned} P_{in} &= VI && (3.43) \\ &= V\left(I_{th} + \frac{P_u q}{\eta_d h\nu}\right). && (3.44) \end{aligned}$$

In this section, we assumed a vertical injection efficiency $\eta_V = 0.9$ below threshold, and a differential vertical injection efficiency $\eta_V^d = 0.75$ [35]. No lateral carrier diffusion was assumed, resulting in an underestimation of the efficiencies. Surface

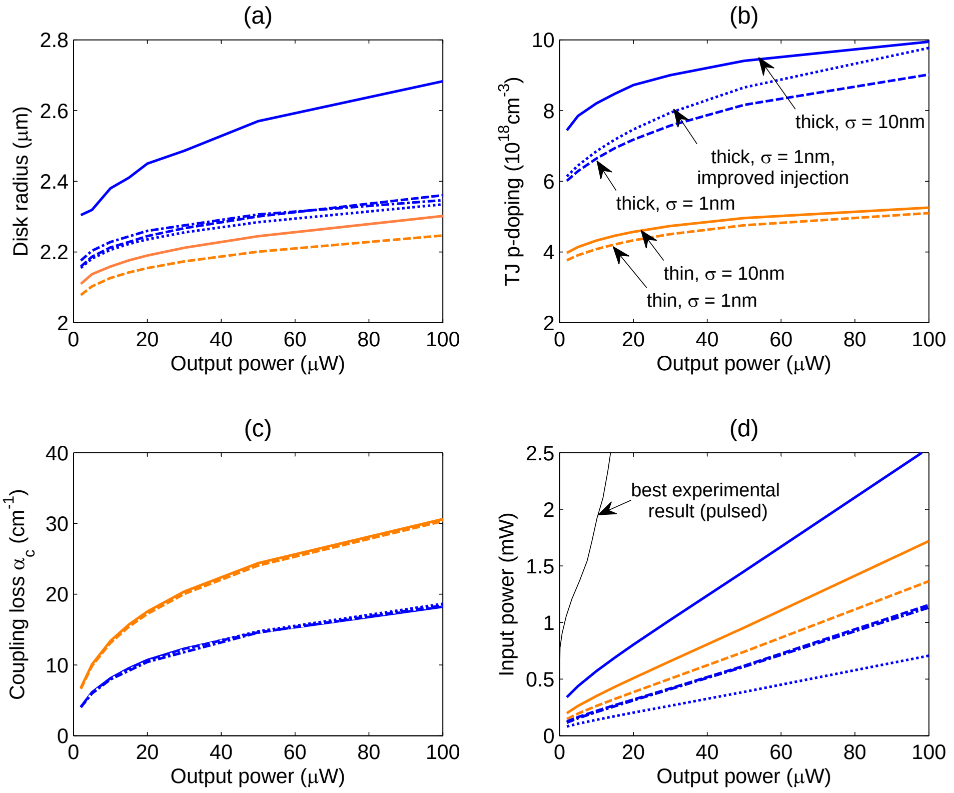

Figure 3.23: Results of the optimization procedure both for the thin (orange) and thick epitaxial structure (blue), for output powers in the range 1-100 μW. The optimized microdisk radius can be found in (a), the optimized tunnel-junction p-type doping in (b) and the optimized coupling loss in (c). The power consumption for devices with these optimized design parameters is shown in (d). Solid lines represent devices with roughness $\sigma = 10\,\text{nm}$, $L_c = 100\,\text{nm}$. The dashed lines have $\sigma = 1\,\text{nm}$, as have the dotted and dashed-dotted cases. Furthermore, the dotted line shows the results for an artificial structure with improved lateral injection efficiency ($\times 1.5$), whereas the dashed-dotted line represents optimized devices with the currently available estimated tunnel-junction optoelectronic performance, coinciding accidentally with the dashed line. The best experimental result (pulsed regime) for a thick, non-optimized 7.5-μm-diameter microdisk laser is also shown, emphasizing the potential for device optimization.

recombination was also neglected. The radially dependent bending loss $\alpha_b(R)$ was fitted to the simulations in 3.2.2, for $t_s = 50\,\text{nm}$. The scattering loss $\alpha_s(R)$ is based on equation (3.9). The device voltage V was calculated with the electrical model in section 3.5. Finally, it was assumed that all SOI-coupled output power is emitted in one direction of the SOI wire, which could be achieved by implementing a well phase-positioned DBR mirror in one of the SOI wire branches.

Again, the above expressions neither include gain suppression nor self-heating effects. While the latter causes early thermal roll-over in current experimental devices, thereby limiting maximum output power, we believe that this effect can be suppressed by incorporating an adequate heat sinking structure together with optimizing the laser structure, as we will show.

The results of the optimization procedure are shown in figure 3.23, both for the thin (orange) and thick epitaxial structure (blue), for output powers in the range 1-100 μW. Solid lines include devices with scattering loss for $\sigma = 10\,\text{nm}$, the other cases have $\sigma = 1\,\text{nm}$. The dotted line shows the results for an artificial structure with improved lateral injection efficiency ($\times$1.5), which could be achieved by etching a hole or applying proton implantation in the center of the disk, thereby removing part of the leakage current. The dashed-dotted line represents ultimate performance with the estimated experimental tunnel-junction characteristics (see chapter 5). For all cases, the optimized disk radius is in the range 2.1-2.7 μm (fig. 3.23a). For smaller disks, the bending loss and/or scattering becomes the dominant optical loss mechanism. Optimized disk radii are slightly smaller for thin structures, since the internal loss is higher, allowing for a higher bending/scattering loss. The thick disks with $\sigma = 10\,\text{nm}$ have slightly bigger optimized disk radii, due to a higher α_s (which scales with t).

The optimum TJ p-type doping N_a is for the thick structure in the range 6-10$\times10^{18}$ cm^{-3} (fig. 3.23b), which results in theoretical operating voltages below 1.5 V. For the thin microdisks, optimized N_a-values are only 4-5$\times10^{18}$cm^{-3}. Clearly, the larger Γ_{TJp} for the latter structures doesn't allow for very high N_a levels. The optimized coupling loss α_c ranges from 7 to 30 cm^{-1} for the thin structures and from 5 to 20 cm^{-1} for the thick microdisks (fig. 3.23c). A larger disk-waveguide coupling is needed for the thin microdisk lasers (about $\times1.5$), since the larger internal loss needs to be overcome to achieve decent differential efficiency. However, this can be obtained with relatively thicker bonding layers, as shown in figure 3.8, and with higher tolerance on the bonding layer thickness.

Finally, figure 3.23d shows the required electrical input power versus optical output power. For microdisks with substantial sidewall roughness, optimized thin microdisk lasers outperform thick structures, since the expression for scattering loss scales linearly with t. For thin (thick) devices, 50 μW output power would require an input power of 0.96 mW (1.45 mW), which is equivalent with 5.2% (3.4%) wall-plug efficiency (WPE). For $\sigma = 1\,\text{nm}$, thick microdisks perform better: 50 μW output power would require 0.74 mW (6.8% WPE) and 0.61 mW (8.2% WPE) input power for the thin and thick microdisks, respectively. The better performance for the thick microdisk is due to the reduced optical overlap with the TJ p-side layer, but comes at the expense of a thinner optimum bonding layer thickness and the associated

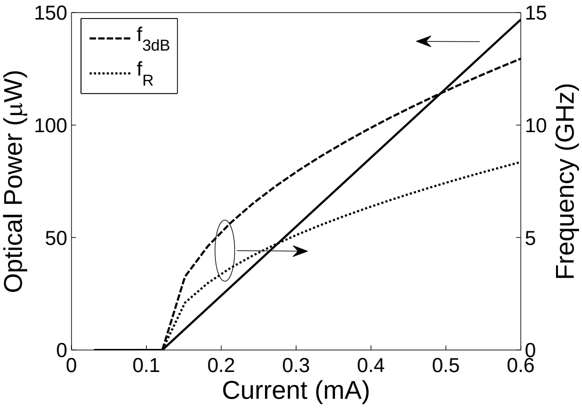

Figure 3.24: Intrinsic relaxation oscillation frequency f_R and modulation bandwidth f_{3dB} for the optimized (50 μW) microdisk laser with currently available TJ performance, as a function of pumping level. The output power is also shown as reference.

reduced tolerance. The hypothetical, thick device with improved lateral injection efficiency would only need 0.39 mW (12.8% WPE). Self heating is expected to be less of a problem for this optimized device, since even with the thermal resistance of 10 K/mW for current experimental devices, temperature increase should remain under 10 °C for output powers up to 100 μW, and even under 4 °C for a structure with an integrated heat sink. Further WPE improvement could be obtained by reducing the TJ layer thickness and by further shrinking the microdisk diameter by using a isolation/planarization layer with lower refractive index than BCB.

3.10 Dynamic laser characteristics

3.10.1 Intrinsic modulation speed

The intrinsic relaxation oscillation frequency of the microdisk laser, ignoring parasitic effects such as carrier diffusion and electrical RC filtering, can be derived from (2.68) as

$$\omega_R^2 \simeq \frac{v_g a \Gamma}{q t_a \pi (R^2 - W(R)^2)} \eta_i^d (I - I_{th}). \tag{3.45}$$

Both $f_R = \omega_R/2\pi$ and the intrinsic modulation bandwidth $f_{3dB} \simeq 1.55 f_R$ are shown in figure 3.24, for the thick microdisk laser optimized for 50 μW output power, with currently available TJ performance (see section 5.3.3). It can be seen that at this output power, the intrinsic modulation bandwidth is about 7.5 GHz. To achieve modulation bandwidths over 10 GHz, the laser should be injected with more than 400 μA, with an associated output power over 100 μW. Therefore, we conclude that for this type of microdisk lasers, it doesn't make sense to target output powers less than 100 μW, if a modulation speed in excess of 10 GHz is required.

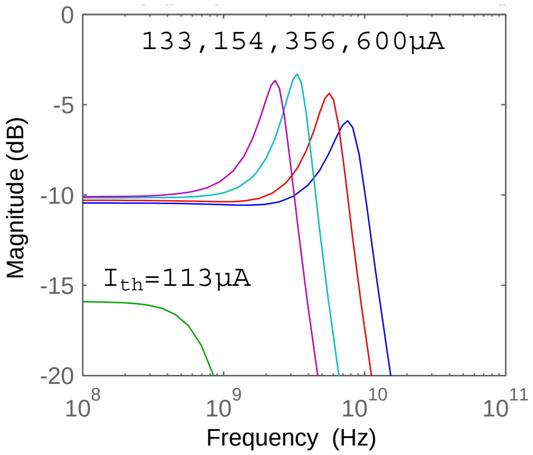

Figure 3.25: Modulation response as function of pumping level for a 4.6-μm-diameter microdisk optimized for 50 μW output, with $D = 8\,\mathrm{cm}^2/\mathrm{s}$.

3.10.2 Influence of lateral diffusion

As already mentioned, equation (3.45) yields the intrinsic modulation bandwidth of a laser, neglecting parasitic effects such as carrier diffusion and RC filtering. Apart from vertical carrier transport (see 2.5.4), spatial hole burning in combination with lateral carrier diffusion is also found to have an impact on the modulation characteristics, causing additional damping of the relaxation oscillation [131]-[132] and the appearance of a tail in the turn-off behavior [133]. Since microdisk lasers exhibit strong spatial hole burning, it could be expected that the interaction between the central carrier reservoir and the WGM lasing region strongly influences the modulation behavior.

Small-signal analysis

Thiyagarajan et al. studied the small-signal modulation characteristics of optically pumped InGaAsP-based microdisk lasers in [134]. They found that the modulation characteristics depend on the radius of the device. For a 2.4-μm-diameter microdisk, they measured a modulation response similar to a conventional laser, with $f_{3dB} = 1.39\,\mathrm{GHz}$ for $P_{pump} = 1.3P_{th}$, but with a strongly damped oscillation relaxation peak. For a 4.8-μm-diameter microdisk at $P_{pump} = 1.3P_{th}$, the oscillation relaxation peak ($f_{3dB} = 1.7\,\mathrm{GHz}$) was less damped, but a partial roll-off was found around $0.4\,\mathrm{GHz}$. The authors attributed this difference to a different diffusive coupling strength between the central region and the lasing region, which was confirmed by a simple lumped rate-equation-based model very similar to Model 2, using two carrier concentrations.

To gain a better understanding of this phenomenon, we carried out a small-signal analysis on laser Model 2 (3.37)-(3.39). First, these calculations were performed for

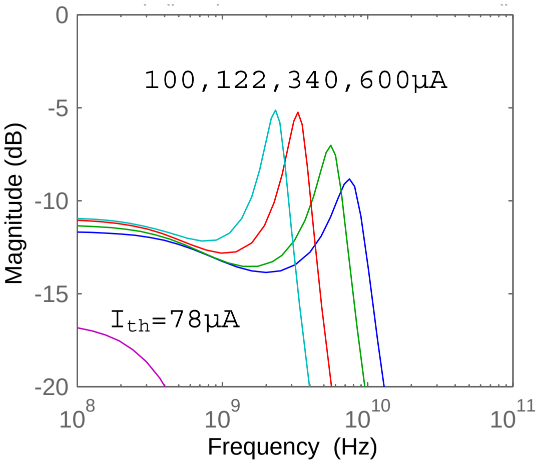

Figure 3.26: Modulation response as function of pumping level for the same microdisk laser as in fig. 3.25, but without improved lateral injection efficiency, with enhanced lateral diffusion $D = 40\,\mathrm{cm}^2/\mathrm{s}$ and assuming a 10× lower Auger recombination rate ($C = 1.63 \times 10^{-29}\mathrm{cm}^6\mathrm{s}^{-1}$).

the 4.6-μm-diameter microdisk laser optimized for $50\,\mu$W output power, assuming the experimental TJ performance, $D = 8\,\mathrm{cm}^2/\mathrm{s}$ and a 1.5×-improved lateral injection efficiency, obtained by etching a hole in the central region. The modulation response as function of pumping level is shown in figure 3.25. The obtained modulation curves are roughly similar to those of conventional lasers, with f_R obeying (3.45).

This result seems to be in contradiction with the measured roll-off observed for a microdisk with similar diameter in [134]. However, since the coupling between the central region and the lasing region is determined by the diffusion length $L = \sqrt{D\tau}$, it depends strongly on the Auger recombination rate C via the carrier lifetime τ. In literature, values for C can be found in the range 10^{-29}–$10^{-27}\mathrm{cm}^6\mathrm{s}^{-1}$ [35], for InGaAsP quantum wells emitting around 1.55μm at room temperature. Therefore, we have performed another small-signal modulation analysis for the same microdisk laser, however assuming $C = 1.63 \times 10^{-29}\mathrm{cm}^6\mathrm{s}^{-1}$, an enhanced diffusion constant $D = 40\,\mathrm{cm}^2/\mathrm{s}$, and no central etched hole. The response is shown in fig. 3.26. In this case, a clear roll-off is apparent in the modulation characteristic, for frequencies below f_R. Our interpretation of this effect is as follows. For slow modulation rates, the lasing region receives an additional current due to lateral diffusion from the central region on top of the vertically injected current, enhancing the laser's response, as is the case in steady-state regime. For higher modulation rates, this diffusion current cannot follow the modulation rate since the carrier lifetime in the center of the disk is relatively high. As a result, the extra modulation response due to lateral current decreases, causing a roll-off. For the highest modulation speeds, the laser region only

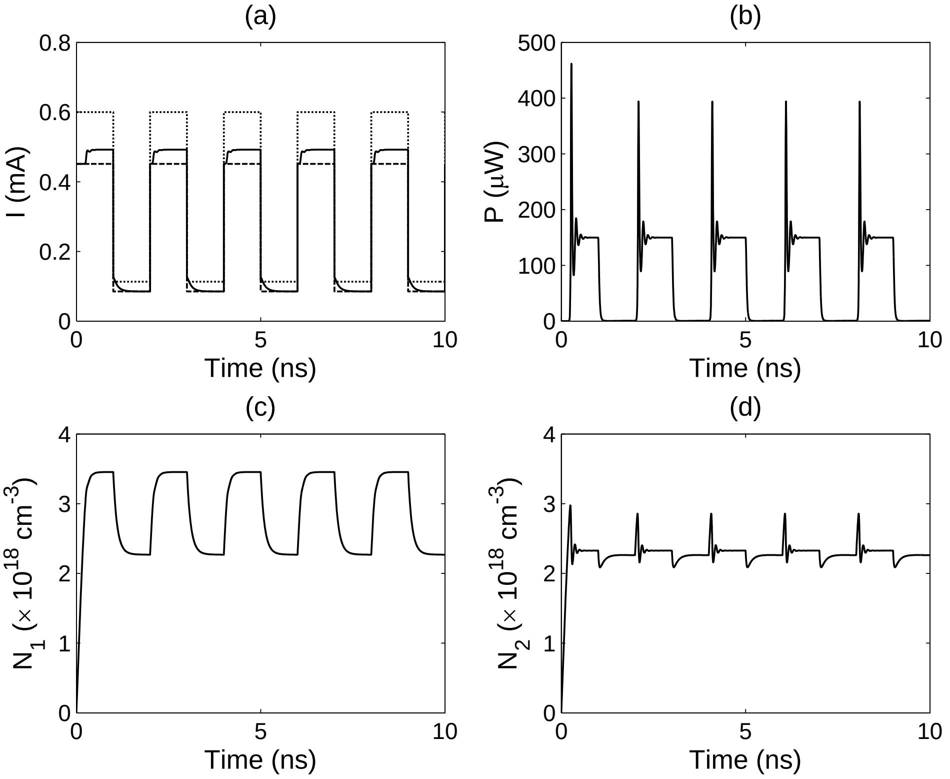

Figure 3.27: Simulated behavior of the optimized 4.6-μm-diameter microdisk laser under above-threshold large-signal modulation at 1 Gb/s. (a) Total injected current (dotted lines), vertical injected current in lasing region (dashed lines) and vertical plus lateral injected current in lasing region (solid lines). (b) Output power. (c) Carrier density N_1 in central region. (d) Carrier density N_2 in laser region.

receives a non-modulated lateral current, and the output modulation amplitude is basically that of a microdisk without any lateral diffusion current.

Large-signal analysis

For the large-signal analysis, the laser was modulated above threshold to avoid turn-on delay (except for the first bit). The simulation results for 1 Gb/s for the first laser are shown in figure 3.27. In (a), the relevant currents are shown, including the total injected current, the vertical current directly injected in the laser region and the sum of vertical and lateral diffusion current injected in the laser region. As could be expected, lateral diffusion results in a higher effective injection current in the on state. In the off state, the laterally injected current vanishes rapidly, resulting in a clean turn-off behavior for the output power, as can be seen in (b). The time evolution

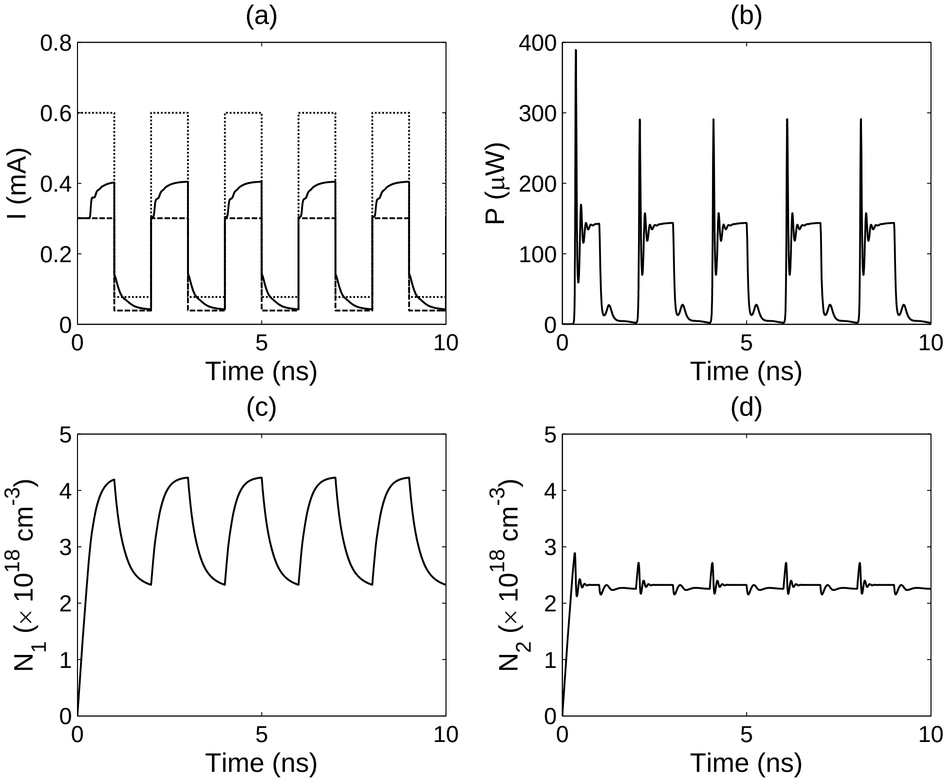

Figure 3.28: Simulated behavior of the 4.6-μm-diameter microdisk laser, with reduced Auger recombination, enhanced diffusion $D = 40\,\mathrm{cm}^2/\mathrm{s}$ and no lateral injection improvement under above-threshold large-signal modulation at 1 Gb/s. (a) Total injected current (dotted lines), vertical injected current in lasing region (dashed lines) and vertical plus lateral injected current in lasing region (solid lines). (b) Output power. (c) Carrier density N_1 in central region. (d) Carrier density N_2 in laser region.

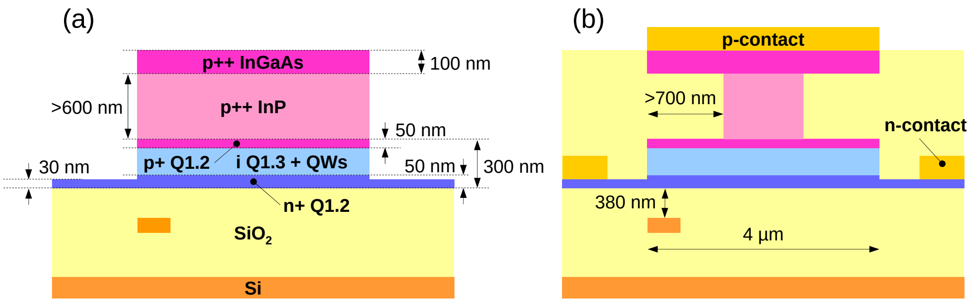

Figure 3.29: Layout and processing for a post-injected ultrathin microdisk laser. (a) Dry etched microcylinder. (b) Selective wet underetch of the InP post and metallization.

of the carrier densities N_1 and N_2 are shown in (c) and (d) respectively, and show above-threshold carrier clamping for N_2 and the lack thereof for N_1.

The simulation results for the case of reduced Auger recombination and an increased diffusion constant is shown in fig. 3.28. In this case, the laterally injected current is more important, and keeps the laser above threshold for several 100 ps after it is turned off. This leads to a secondary pulsation in the turn-off state of the laser, as can be seen in (c). This phenomenon also occurs in some VCSELs [133], and is expected to strongly affect the bit-error-rate (BER) of the full optical link. Once again, the carrier densities N_1 and N_2 are shown in (c) and (d).

Conclusion

From the above examples, it is clear that the modulation response of a microdisk laser depends strongly on the carrier lifetime in the central region and the diffusion constant. While strong Auger recombination results in higher laser thresholds, it also limits the effects of lateral diffusion currents, due to a reduced carrier lifetime. Since the values for the Auger recombination parameter C reported in literature differ up to two orders of magnitude, it is unclear whether lateral diffusion is a true limiting factor for modulation bandwidth. An experimental assessment of the modulation characteristics should bring the final answer to this question. However, with the nominal values for C and D used in this work, the effect of lateral diffusion on laser modulation bandwidth appears to be limited.

3.11 Ultra-thin microdisk lasers

As already discussed in section 3.3, the tolerance on the bonding layer thickness is very tight for 1-μm-thick microdisk lasers (α_c varies 4% per nm). A more relaxed tolerance can be obtained by using thinner microdisks, as illustrated by 0.5-μm-thick structures, which have a sensitivity of 1.9% per nm, at the cost of a higher internal loss. Therefore, we investigate in this section the option of using a 300-nm-thick

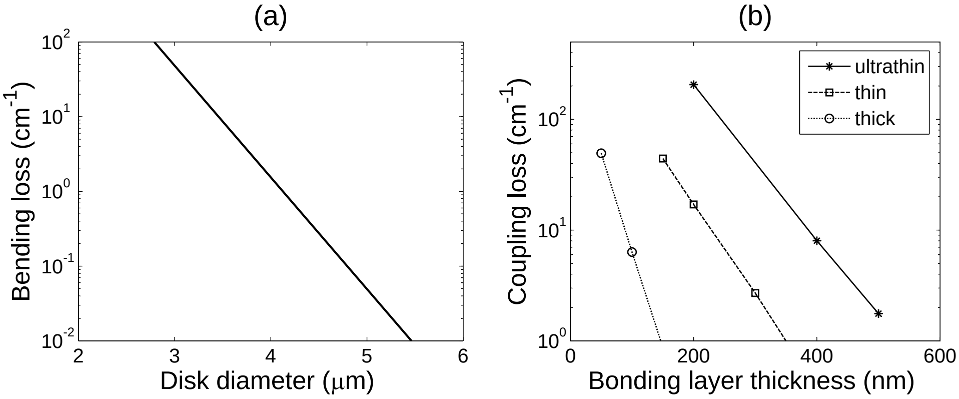

Figure 3.30: (a) Bending loss for the ultrathin microdisk laser with $t_s = 30\,\mathrm{nm}$. (b) Coupling loss to the SOI wire waveguide for a ultrathin microdisk laser ($D = 4\,\mu\mathrm{m}$), without lateral offset. The coupling loss for thick and thin microdisk lasers ($D = 7.5\,\mu\mathrm{m}$) are also shown as reference.

microdisk. The microdisk layout is shown in fig. 3.29. The microdisk has a 200-nm Q1.3-core – containing 3 quantum wells – embedded in 50-nm Q1.2 p+ and n+ layers, forming a conventional p-i-n structure. To avoid excessive optical absorption, the highly-doped, ternary p-type contact layer is implemented in a central post, very similar to pedestal-supported microdisk lasers. The device could be fabricated by dry etching a cylinder, followed by a selective wet etch of the InP post with respect to the ternary contact layer and quaternary disk.

To minimize the threshold current, a disk diameter of $4\,\mu$m was considered. To limit the bending loss, the bottom contact layer thickness should be reduced to $30\,\mathrm{nm}$, which yields a bending loss of $1.6\,\mathrm{cm}^{-1}$, as can be seen in fig. 3.30 (a). For these calculations, the disk was assumed to be embedded in $\mathrm{SiO_2}$. The coupling loss into the SOI wire is shown in 3.30 (b). As could be expected, thicker bonding layers can be used, with $t_{ox} = 380\,\mathrm{nm}$ yielding $\alpha_c = 10\,\mathrm{cm}^{-1}$. Also, the tolerance is slightly improved, with a coupling loss sensitivity of 1.6% per nm.

The doping level N_a in the p-layer is an important design parameter. High N_a values improve the lateral injection efficiency η_L, but result in larger internal loss due to free-carrier absorption. Since the current spreading layers are relatively thin, the depletion layers arising around the intrinsic layer could occupy a substantial fraction of them. To estimate this effect, we calculated the effective depletion lengths W_a and W_d with SIMWINDOWS, for zero bias. The result is shown in figure 3.31 (a), for doping levels $N_a = N_d = 2 \times 10^{18}\mathrm{cm}^{-3}$. From the carrier concentration profiles, we extract $W_a = 9\,\mathrm{nm}$ and $W_a = 6.5\,\mathrm{nm}$. Subsequently, the current density profile was calculated with a lumped electrical network analogous to the one in fig. 3.13, but without vertical resistors, associated with the p-type layer and TJ layer. For the current spreading layers, effective thicknesses $50\,\mathrm{nm} - W_{a/d}$ were used. The resulting

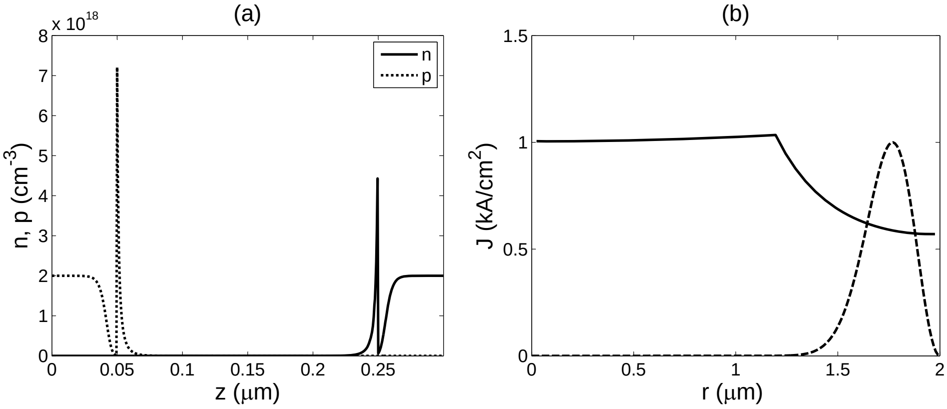

Figure 3.31: (a) Calculated free carrier concentrations n and p for $N_a = N_d = 10^{18}\,\mathrm{cm}^{-3}$, at zero bias. (b) Calculated current density profile for a total current of $100\,\mu\mathrm{A}$ (solid line). The WGM is shown as a dashed line.

current density profile $J(r)$ is shown in figure 3.31 (b), for a total current of $100\,\mu\mathrm{A}$. The lateral injection efficiency is calculated to be $\eta_L = 0.49$.

We calculated the laser performance for this structure, assuming that the coupling loss is equal to the internal loss, neglecting scattering, bending loss and lateral diffusion, and assuming for simplicity that the carrier concentration in the OCLs is 20 times lower than that in the quantum wells. Therefore we have

$$\begin{aligned}
\Gamma_{QW} G_0 \ln\left(\frac{N_{th}}{N_0}\right) &= 2\alpha_i \qquad (3.46)\\
\alpha_i &= \Gamma_n k_n^Q N_d + \Gamma_p k_p^Q N_a + \Gamma_{OCL} k_p^Q \frac{N_{th}}{20} + \Gamma_{QW} k_p^Q N_{th}\\
I_{th} &= \frac{1}{\eta_L \eta_v}\left(AN_{th} + BN_{th}^2 + CN_{th}^3\right)\pi t_a \left(2RW(R) - W^2(R)\right)\\
\eta_d &= \frac{1}{2}\eta_v^d \eta_L
\end{aligned}$$

Since $\Gamma_n = \Gamma_p = 9.1\%$, $\Gamma_{QW} = 7.1\%$ (3 QWs) and $\Gamma_{OCL} = 63.9\%$, we find $I_{th} = 125\,\mu\mathrm{A}$ and a slope efficiency of $145\,\mu\mathrm{W/mA}$. Therefore, we believe that this laser structure offers a good alternative to the TJ-based structure, with a higher tolerance on the bonding layer thickness, at the expense of a more complicated fabrication.

3.12 Conclusion

This chapter provides a detailed theoretical analysis of the performance of electrically-injected, tunnel-junction-based microdisk lasers integrated on and coupled to a SOI wire waveguide. All parasitic losses as well as the coupling loss were numerically evaluated as function of the relevant structural parameters. For the analyzed disk geometry, the requirement of having negligible bending loss was found to imply a minimum disk diameter of about 4.5μm. Evanescent coupling to the underlying SOI wire was found to be strongly dependent on the disk thickness: 1-μm-thick disk require 70-nm-thick bonding layers, as compared to 190-nm-thick bonding layers for 0.5-μm-thick microdisks. Furthermore, the coupling loss is very sensitive to the bonding layer thickness.

Three epitaxial layer designs, compatible with low-voltage electrical injection, were analyzed and optimized to obtain the lowest internal, as function of total epitaxial film thickness. It was found that a tunnel-junction-based design strongly outperforms a design based on a thin ternary contact layer, especially for 0.5-μm-thick films. For 1-μm-thick films with a highly doped TJ, the internal loss was calculated to be as low as 14 cm^{-1}, with the dominant absorption occurring in the p-side of the TJ.

A lumped electrical network was then used to analyze the current path in the microdisk. A uniform injection profile was obtained for typical doping levels in the TJ and the current spreading layers, under the assumption of perfect cylindrical symmetry. For the electrical TJ performance, a model from literature was used. This analysis also revealed operating voltages under 2 V, for adequate TJ doping and typical current densities.

The thermal behavior of the microdisk was analyzed by solving the dynamic heat equation, using a commercial finite-element tool. The calculations revealed a thermal resistance of the order 10 K/mW, and a thermal time constant of about 1.7 μs. The thermal resistance can be reduced by using a planarization layer with a better thermal conductivity such as Al_2O_3, however at the expense of higher bending loss. Alternatively, a thermal short circuit from the top contact to the silicon substrate could be provided, which acts as a heat sink.

The static laser performance was then modeled by using rigorous, radially-dependent rate equations, including the effects of lateral diffusion and surface recombination. Lateral diffusion was found to have a beneficial influence on the slope efficiency, feeding carriers from the central non-lasing microdisk area into the lasing mode located at the disk edge. Surface recombination can be neglected, since InAsP quantum wells were used. Non-uniform injection results in higher threshold currents and a saturating laser output at higher pumping levels.

The static wall-plug efficiency was then optimized, by adjusting the dominant design parameters, being the microdisk radius, the TJ p-type doping, and the coupling loss. This was done both for the theoretical optoelectronic TJ performance, as for the estimated experimental TJ performance, obtained in chapter 5. For the former case, an SOI-coupled output power of 50 μW can be generated with up to 12.8 % wall-plug efficiency, for a microdisk with a diameter of 4.6 μm and with operating voltages below 2 V. For the latter, the WPE is reduced to 8.2 %. For the optimized device with experimental TJ performance, the calculated threshold current is 110 μA, and the slope efficiency is 240 μW/mA. In these calculations, lateral diffusion and surface scattering were neglected, and it was assumed that the lateral injection efficiency can be enhanced by etching a hole in the center of the disk, and that laser emission is unidirectional in the SOI waveguide.

A simple, lumped rate-equation model was proposed to model the laser dynamics, using a separate carrier density for the central non-lasing area and another for the lasing zone. This model reproduced the static results obtained by the rigorous model reasonably well, however with a slight underestimation of the lateral diffusion current. It was subsequently used to estimate the effect of lateral diffusion on the modulation bandwidth. It was found that lateral diffusion can hamper high-speed operation, and that this parasitic effect is worse for devices with a long spontaneous carrier lifetime in the central zone, in combination with high ambipolar diffusion constants.

Finally, an ultrathin microdisk laser design was proposed, featuring a central top post contact. The p-type contact layer can be implemented in this post, effectively shielding it form the lasing mode, as is the case for pedestal-supported microdisk lasers. By reducing the disk thickness to 300 nm, the relative sensitivity of the coupling can be reduced to $1.6\%/\text{nm}$. For these lasers, a threshold current of 125 μA with a slope efficiency of 145 μW/mA seems to be in reach.

From the above considerations, we conclude that a heterogeneous InP-based microdisk laser integrated on SOI has good potential as a compact, low-power, electrically-injected, on-chip integrated light source for PICs. Concerning the possible use as a light source for intra-chip optical interconnect, we note that theoretically all requirements as stated in section 2.1 can be fulfilled, except for the requirement of high-temperature operation. As already stated, the high on-chip temperatures remain the main obstacle for implementing optical intra-chip interconnects with on-chip light sources.

Chapter 4

Fabrication of SOI-integrated microdisk lasers

In this chapter, we give an overview of the most important technological processes that were used to fabricate heterogenous SOI-integrated microdisk lasers. It involves the fabrication of the SOI waveguide circuit, the growth of the InP-based epitaxial structures, the bonding of the InP-based material to the SOI wafer and the III-V processing of the microlasers.

4.1 Global overview

A global overview of the fabrication procedure of SOI-integrated microdisk lasers is shown in figure 4.1. The main elements are the SOI waveguide processing, the InP-based epitaxial growth of the laser structure, the InP-SOI bonding and the InP, BCB and metallization processing steps defining the microdisk and the metal contacts.

Processing runs

In the course of this work, three main processing runs were performed. In the first run, yielding generation-1 (G1) lasers, an InP wafer was molecularly bonded onto a plain silicon wafer with a 1-μm-thick SiO_2 layer, both for dies with 0.5-μm and 1-μm-thick epitaxial layers. The wafer with bonded dies was then sawn into dies, which were processed separately, using optical contact lithography. For the second run, InP epitaxial material was molecularly bonded onto a planarized SOI waveguide wafer. In this case, die-to-wafer bonding was used. Furthermore, on each SOI cell, two different dies were bonded, one with the epitaxial layer structure required for laser operation, and another optimized for fabricating integrated detectors, aiming at demonstrating a full optical link (see section 5.4). However, the bonding yield was low, especially for the detector dies. Laser structures fabricated in this run are referred to as generation-2 lasers (G2). Finally, a third run involved the die-to-wafer bonding for fabricating SOI-coupled generation-3 (G3) laser structures only. The

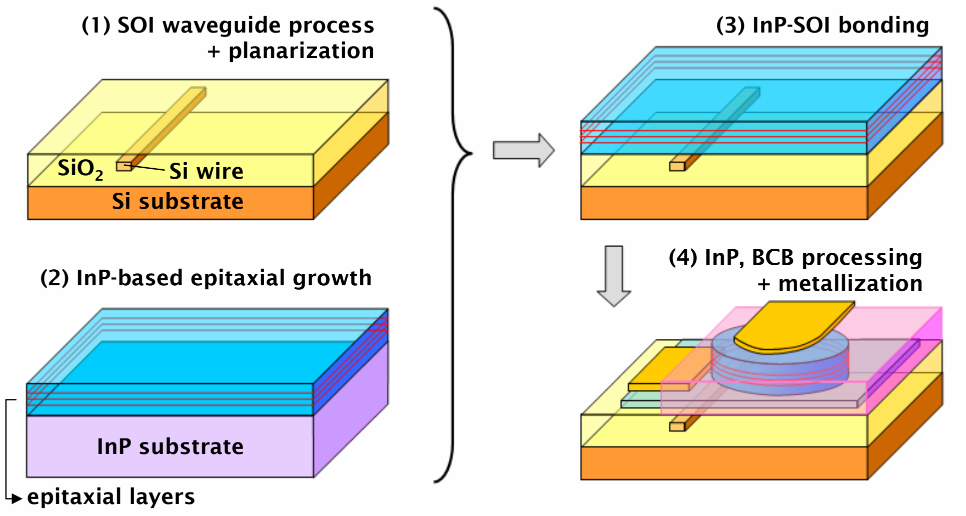
(1) SOI waveguide process
+ planarization
SiO_2
Si wire
Si substrate
(2) InP-based epitaxial growth
InP substrate
epitaxial layers
(3) InP-SOI bonding
(4) InP, BCB processing
+ metallization

Figure 4.1: Global overview of the fabrication process of an SOI-integrated microdisk laser.

bonding yield was slightly better. This run contained advanced designs, such as microdisk lasers coupled to a common SOI waveguide (to demonstrate flip-flop operation, and coarse WDM transmitters) and heat-sink vias.

4.2 SOI waveguide technology

4.2.1 Deep-UV lithography

The SOI waveguide technology used in this work was developed in the PhD work of W. Bogaerts [135]. First, Shipley UV3 photoresist is spun on a bare 200-mm SOI wafer and then prebaked. On top of this photoresist, an anti-reflective coating is spun, to eliminate reflection effects at the air-photoresist interface. These could result in standing-wave effects and therefore inhomogeneous illumination. Subsequently, the wafer is sent to the stepper, which illuminates the photoresist with the pattern on the mask, using a deep-UV (DUV) light source (with 248-nm wavelength). The pattern of a unit cell (typically $10 \times 10\,\mathrm{mm}^2$ large) is repeated over the whole wafer. In this stepping process, the illumination dose and focus can be varied, which results in a variation of the characteristic dimensions of the patterns over the wafer. After exposure, the wafer gets a post-bake treatment, after which the resist is developed.

4.2.2 Si etching

The developed resist is then used as a mask for the silicon etch, which is done with a $Cl_2/O_2/He/HBr$ plasma. The etch process includes a break-through etch and a main etch, with different chemistry. More information on the SOI waveguide fabrication with DUV lithography can be found in [136]. Both DUV lithography and Si etching were carried out at IMEC, Leuven.

4.3 InP-to-Si/SOI bonding technology

4.3.1 Direct molecular bonding

The direct molecular bonding process described here was developed and carried out at CEA-LETI and Tracit Technologies in Grenoble, France.

Principle

Direct molecular bonding is initiated by the van der Waals attraction force that exists between the electrically polarized molecules of two surfaces that are brought into close contact. As this van der Waals effect is a short-range force, a very intimate contact between the two involved materials is needed, resulting in stringent surface requirements. These include very low surface roughness ($\sigma < 0.5\,\mathrm{nm}$), good planarity and low wafer bow, a low concentration of attached particles and a low surface contamination. In this work, direct bonding involves the fusion of two SiO_2 surfaces, although in principle, any material combination could be used.

SiO_2 deposition and planarization

Si/SOI wafer. Prior to bonding, a thick ($\sim 1\,\mu\mathrm{m}$) SiO_2 layer is deposited on the Si or the processed SOI waveguide host wafer, by means of chemical vapour deposition (CVD), for instance starting from TEOS (tetraethyl-orthosilicate). Then, chemical mechanical polishing (CMP) is used to create a surface with high planarity and low roughness. This step is very similar to the polishing of interlayer dielectrics between the metal interconnect layers of conventional microelectronics. It should be noted that in the case of a patterned SOI wafer, the deposited SiO_2 layer should be sufficiently thick, allowing for the planarization of the waveguide topology after deposition and CMP. Also, the amount of deposition and polishing determines the final thickness of the bonding layer, which has a large impact on the laser performance, as indicated in chapter 3. Controlling this thickness can be done by measuring the polishing time, provided that the polishing rate is known and reproducible. Another endpoint detection method is in-situ optical interferometry. In this case, constructive or destructive interference effects of an impinging laser beam on the polished layer can be measured in reflection, and give an indication of the polishing rate and remaining film thickness. With this method, an accuracy of $\pm 10\,\mathrm{nm}$ was obtained [137]. In general, the post-CMP thickness variations (on a non-patterned Si-wafer) are of the same magnitude [138]. However, on a patterned wafer, uniformity can be worse due to variations in the pattern density, and associated effects such as dishing and erosion [137]. These non-uniformities are expected to become more important with increasing CMP time.

Within this work (CMP performed at Tracit Technologies, bonding at CEA-LETI), measured bonding layer thicknesses were 130 nm for a first wafer batch and 180 nm for a second, both with a nominal design value of 200 nm ($\pm 10\%$). In view of the high sensitivity of the laser efficiency to the bonding layer thickness, it is crucial that the CMP accuracy and uniformity should be significantly improved. This requires optimization of the slurry composition, applied pressure, carrier and plate speed, and temperature. Also, the total amount of material removed by CMP polishing should be minimized, while maintaining bonding compatible surface properties.

InP-based wafer. An additional 10-nm-thick SiO_2 layer is deposited on the InP-based epitaxial structure, grown at INL by Molecular Beam Epitaxy (MBE) on 2-inch InP wafers, using a Electron Cyclotron Resonance plasma (ECR). This approach allows one to use the standard SiO_2 bonding technology.

Surface activation and bonding

After planarization, the SiO_2 surfaces need a cleaning treatment to remove attached particles and other contaminations. This can be done by the standard SC-1 solution or by a piranha solution (H_2SO_4:$3H_2SO_4$) [139]. This cleaning step also activates the surface, since it provides the surface with OH groups that are needed to start the hydrophilic bonding process. When these activated surfaces are brought together, van der Waals attraction will occur between the OH groups of both surfaces, forming hydrogen bonds. By curing the wafer for several hours at 200-300°C, the hydrogen bonds are gradually replaced by covalent Si-O-Si bonds, with the release of H_2O. This results in bonding strengths up to 1 J/m^2[139].

4.3.2 Adhesive DVS-BCB bonding

An adhesive die-to-wafer bonding proces, based on the DVS-BCB polymer (1,3-divinyl-1,1,3,3-tetramethyldisiloxane-bisbenzocyclobutene), was developed by G. Roelkens [30], in the context of heterogeneous integration of InP-based Fabry-Perot laser diodes and detectors on SOI. While this type of bonding wasn't used for the fabrication of integrated microlasers, it could be a good alternative to molecular bonding. This bonding process has less stringent requirements on the surface properties of the involved materials, since the bonding polymer planarizes part of the SOI surface topology, especially for thick bonding layers. DVS-BCB has a refractive index of 1.54 at 1.55-μm wavelength, allowing for a large index contrast with Si or InP-based waveguide structures. However, the thermal conductivity is low ($\kappa_{BCB} = 0.3\,\mathrm{W/mK}$), which is three to four times less than for SiO_2. Bonding layer thicknesses as low as 100 nm have already been obtained in [140], where compact metal-semiconductor-metal (MSM) detectors were integrated on an SOI-wire waveguide circuit. For further details on DVS-BCB bonding, we refer to [30].

4.3.3 InP substrate removal

The removal of the InP substrate of the bonded InP epitaxial material is typically done in a two-step process. First, the substrate is thinned from 360 μm down to a few tens of micrometers by using mechanical grinding. Subsequently, the remainder of the InP substrate is removed by selective wet chemical etching, until the InGaAs etch-stop layer is reached. This etch stop layer is then removed by another selective wet etch. When the bonding strength is not adequate, the bonded material detaches typically during the substrate removal procedure.

4.3.4 Wafer-to-wafer versus die-to-wafer bonding

As the diameter of SOI wafers is typically much larger than that of InP wafers (8-12 inch versus 2-4 inch), it is impossible to cover a complete SOI wafer with InP-based material via a wafer-to-wafer bonding approach. However, many applications don't require a complete coverage of the SOI chip with III-V material. Also, for some applications, different III-V epilayer compositions might be needed on different locations on the SOI chip, for instance for a complete optical link that requires specifically optimized III-V heterostructures both for the lasers and detectors. Furthermore, since the cost of InP wafer material is much higher than that of SOI, covering only specific spots of the SOI wafer with InP dies could result in cost reduction. Obviously, die-to-wafer bonding requires an additional dicing step prior to bonding, which can be done by cleaving or sawing the epitaxial wafer.

4.3.5 Bonding results

In the context of the PICMOS project, three (functional) molecular bonding runs were performed. The first run (G1) involved the integration of InP laser dies on a plain Si wafer. The second run (G2) involved die-to-wafer bonding of $9 \times 4.5\,\mathrm{mm}^2$ dies on a 200-mm SOI wafer with a $9 \times 7\,\mathrm{mm}^2$ unit cell, containing SOI waveguide circuitry. Two types of dies were bonded, one containing a tunnel-junction-based laser epitaxial structure and the other containing an epilayer composition optimized for fabricating detectors. The result is shown in figure 4.2. It can be seen that a large fraction of the bonded material was detached after substrate removal, indicating poor bonding quality. This is especially true for the detector dies, which were grow with Metal-Organic Chemical Vapour Deposition (MOCVD), and showed higher surface roughness as opposed to the laser dies, which were grown with Molecular Beam Epitaxy (MBE).

Finally, a third bonding run was performed (with only laser dies), with a higher bonding strength and high fraction of the the bonded material remaining stuck to the SOI wafer after substrate removal (fig. 4.2 (c), (d)). However, during III-V processing, on some of the dies, the epitaxial material became strongly degraded and detached, resulting in a (bonding) yield below 50%. The low yield was attributed to a higher than usual wafer bow, which was already measured on the blank InP wafers, together with unusually high spikes on the epitaxial surface. Also, the bonding involved materials from three project partners: IMEC (SOI wafers), INL (laser epitaxial dies) and TUe (detector epitaxial dies), with different surface topology as compared to previous bonding runs. However, for molecular die-to-wafer bonding with well-known materials, the yield is currently in the range 60-70%.

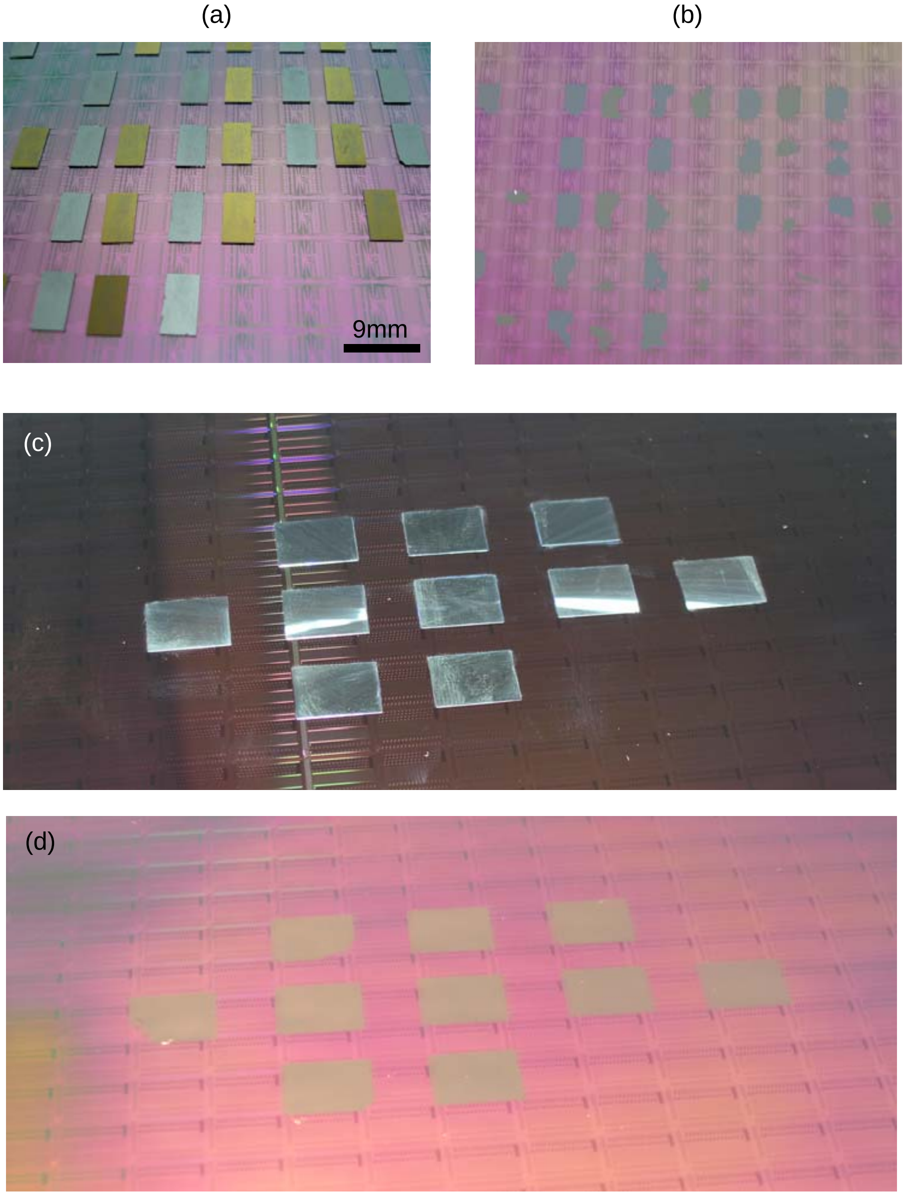

Figure 4.2: SOI wafer with molecularly bonded InP-based dies, used for fabricating generation-2 lasers and detectors, before (a) and after substrate removal (b). During substrate removal, a large fraction of the bonded (mainly detector) material was detached, which severely limited the process yield. (c) shows the result after mechanical grinding and (d) after chemical substrate removal for the generation-3 samples, involving only laser dies, with a higher yield. (bonding performed at CEA-LETI/Tracit).

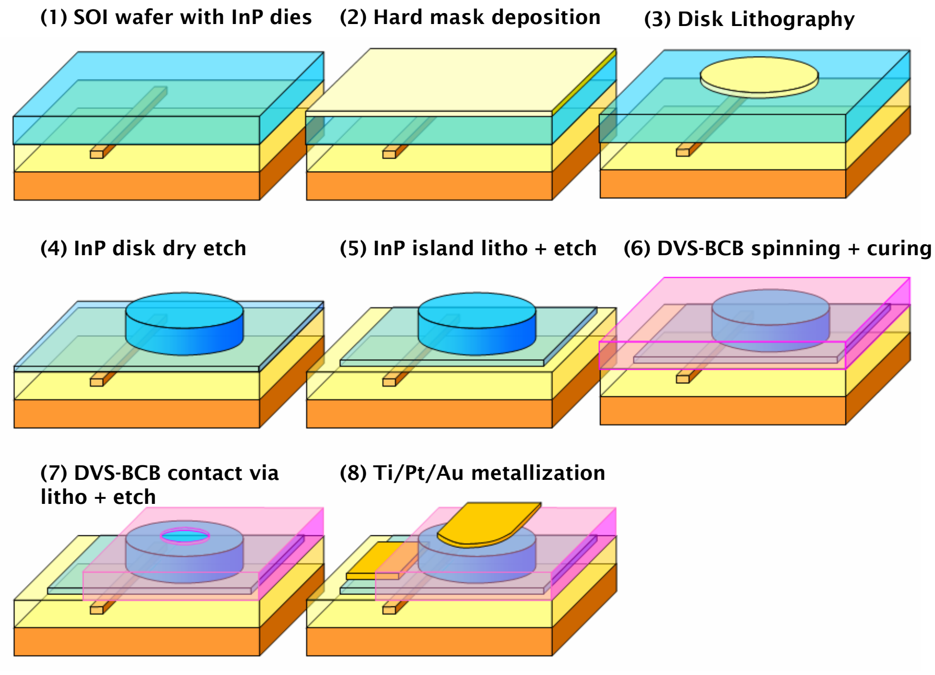
(1) SOI wafer with InP dies
(2) Hard mask deposition
(3) Disk Lithography
(4) InP disk dry etch
(5) InP island litho + etch
(6) DVS-BCB spinning + curing
(7) DVS-BCB contact via litho + etch
(8) Ti/Pt/Au metallization

Figure 4.3: Overview of the InP, BCB and metallization processing steps of the heterogeneous SOI-integrated microdisk laser.

4.4 InP processing

4.4.1 Microdisk definition

In the course of this work, microdisk lasers have been fabricated both with optical contact lithography as with e-beam lithography. The first process was mainly used to fabricate non-coupled G1 lasers integrated on Si, on a die scale (UGent/INL). The latter was applied for SOI-coupled G2 and G3 microdisks, on a wafer scale (CEA-LETI). Both process flows are briefly described hereafter.

Optical contact lithography

In order to define the microdisk patterns in a Ti hard mask on top of the bonded epitaxial layers, contact lithography was used in combination with a Ti lift-off process. For less critical InP etching steps and BCB etching, the developed resist can be directly used as an etch mask. Positive-tone resists were used in this work (AZ5214 or TI09XR), which also can be used for image reversal, using a flood exposure. After spin coating, typically at 3000 RPM, the resist is pre-baked at 100 °C, to obtain the desired resist thickness of 1.4 μm. Then, the glass mask plate – containing the microdisk patterns in chromium – is aligned with respect to the sample in the mask aligner tool (Karl Suss MA-6). Typically, an alignment accuracy of 500 nm can be obtained, depending on the to-be-aligned patterns[1] and the operator. After alignment, the mask plate is pushed against the resist and the sample is illuminated, with 320-nm wavelength and a typical dose of 210 mJ/cm^2. After an additional post bake at 110 °C, the resist is developed. If required, the Ti hard mask is then deposited (100 nm), and followed by the lift-off process, which is done by an aceton-IPA-DI resist removal step with ultrasonic agitation. If the resist is used as etch mask, an additional post bake can be applied to harden the resist.

E-beam lithography

Since the alignment accuracy required for adequate microdisk-wire coupling (± 100 nm) cannot be obtained with contact lithography, e-beam lithography was chosen as a tool to define SOI-integrated microdisk lasers (on a wafer scale). Prior to entering the clean rooms of CEA, the SOI wafers with bonded epitaxial dies were subjected to a backside decontamination procedure with different etchants. Then, the SiO_2 hard mask (150 nm) was deposited with PECVD at 220°C, using SiH_4[2], which also protects the lithography tool from contamination. Subsequently, an e-beam resist (PMMA) is spun on the wafer and the microdisk patterns are written into it, with an alignment accuracy of about 150 nm. After development, the patterns are transferred into the SiO_2 hard mask with CF_4 etching. Since InP can be slightly attacked during this step, this processing is performed before the weekly cleaning of the etching chamber to avoid contamination of other wafers. Finally, the PMMA is removed and a thick protective resist is deposited.

While e-beam lithography was chosen as a convenient tool to define hundreds of microdisk lasers per die, it should be noted that this a serial and thus slow process (several hours/wafer). For mass fabrication with high throughput, the microdisks should be defined with DUV lithography, as is used in the SOI patterning. First tests to test the viability of this scheme have already successfully been performed at CEA-LETI.

E-beam alignment markers. In order to align the microdisk structures with the SOI wire waveguides, alignment markers visible with an SEM tool need to be provided in the SOI structure. For this purpose, $10 \times 10\,\mu\text{m}^2$ squares were defined by DUV lithography and etched down to the silicon substrate. This was only done for some SOI cells at the edge of the SOI wafer, where no die bonding was planned. The e-beam marker development was carried out with the help of W. Bogaerts.

4.4.2 InP etching

After the e-beam lithography of the microdisks, all further processing steps were performed on a die scale, since the III-V processing equipment at UGent and INL

---

[1] While mask-sample alignment is mostly done with the help of specific alignment patterns predefined on the sample, sometimes a better accuracy can be obtained by aligning the patterns on the structures itself.

[2] only a low-temperature deposition technique is acceptable at this stage, since InP decomposes at temperatures above 450°C.

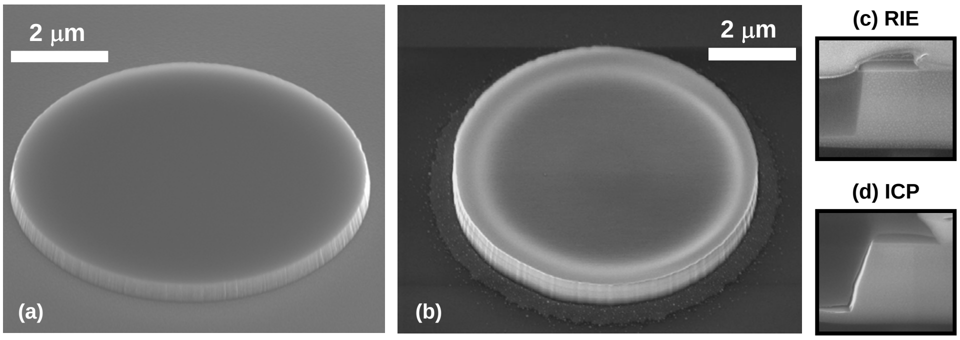

Figure 4.4: Dry-etched microdisks with SiO_2 hard mask: (a) ICP-RIE-etched 0.5-μm-thick disk, and (b) RIE-etched 1-μm-thick disk (etching performed at INL). (c) and (d) show cross sections of the disk edge of 1-μm-thick microdisks, comparing RIE and ICP-RIE etching results.

only allows for the processing of dies of a few cm^2. However, there is no fundamental reason why these InP processing steps couldn't be carried out on wafer scale with CMOS tools, as indicated by first encouraging tests at CEA. Before die-scale processing, the SOI wafers with bonded InP dies were diced into pieces of $18.4 \times 14.2\,mm^2$, each containing (at least) one bonded InP die. After removal of the protective resist, the samples are ready for InP etching, mainly performed with a reactive-ion etch (RIE) tool or an inductively-coupled plasma (ICP-RIE) etching tool.

Reactive-ion etching

In the RIE tool, both the energy and density of the plasma ions are determined by the table RF power. In this work, a CH_4/H_2 30/60 sccm gas mixture was used, with 100 W RF power and 20 mTorr pressure. When etching with a methane-based gas, polymers are formed and deposited at the etched surfaces. Therefore, an O_2 plasma cleaning step should be included (50 sccm, 100 W). A typical RIE cycle includes 6 minutes plasma etching, followed by 0.6 minutes of O_2 plasma cleaning. The RIE method was used in INL to etch the microdisks (with an SiO_2 hard mask), in combination with an end-point detection tool based on in-situ interferometry, in order to control the thickness of the bottom contact layer (see figure 4.4 (b) and (c)). At UGent, RIE was used in combination with a Ti hard mask, and also for etching the InP islands in the bottom contact layer (with a resist mask).

Inductively-coupled plasma etching

In the ICP-RIE tool, the plasma density is determined by the ICP coil power. The etching parameters that were used are: a CH_4/H_2 30/60 sccm gas mixture, with 240 W RF power, 100 W ICP power, 20 mTorr pressure at 100 °C. The O_2 plasma cleaning step consisted of 50 sccm, 150 W RF power, 50 W ICP power at 40 mTorr. A

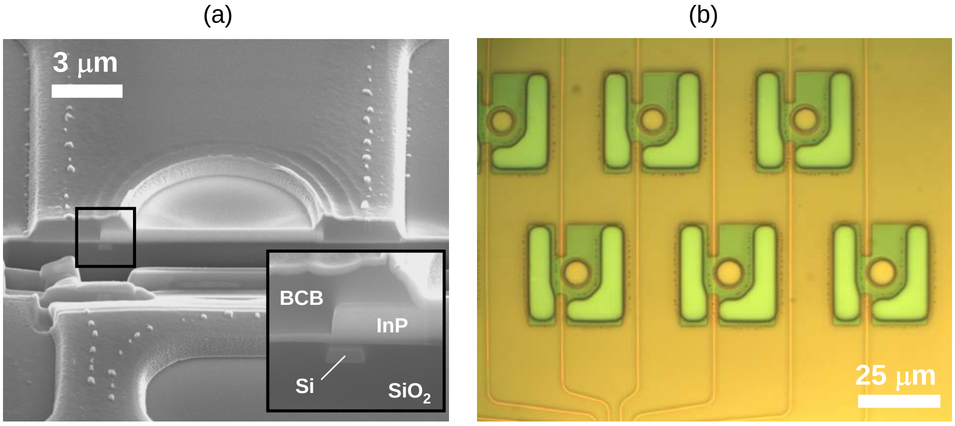

Figure 4.5: (a) FIB cross section of a microdisk laser after the DVS-BCB planarization and opening of the contact windows. (b) Top down microscope image of the same structures, showing the shape of the top and bottom contact vias, and the underlying SOI waveguides.

typical ICP-RIE cycle includes 90 seconds etching, followed by 60 seconds of plasma cleaning. Such a cycle typically removes 20-30 nm of InP. During ICP-RIE at UGent, the etching depth was controlled by Talystep measurements in between a number of etching cycles. For ultimate precision, a FIB cross section was made on one of the microdisk lasers.

These ICP-RIE process parameters were found to be the optimum values for obtaining deeply etched (few μm) laser facets with low surface roughness and steep sidewall slopes, in combination with a Ti mask [30]. For the microdisk lasers, this process was used in combination with a SiO_2 hard mask, and resulted in microdisk edges with a substantial sidewall slope, as a result of strong mask erosion (see figure 4.4 (a) and (d)). Since sidewall slope is of less importance in a microdisk resonator, no specific effort was paid for optimizing the process for use with a SiO_2 hard mask. However, it should be noted that optimizing the etching parameters could be very rewarding in terms of lowering the scattering loss, which do have a strong impact on laser performance.

4.4.3 DVS-BCB planarization and isolation

In order to optically isolate the waveguides – both SOI wires and the microdisk resonator – from the absorptive metal contacts, a DVS-BCB polymer is spun over the etched microdisk structures, before they are metallized. The DVS-BCB Cyclotene 3022-35 was used for this purpose (purchased from Dow Chemical). The polymer is spin coated at 2000-2500 RPM, resulting in a BCB thickness around 1.5 μm. Then, the DVS-BCB is baked in a N_2 atmosphere to avoid oxidation, with the following temperature evolution. First the temperature is increased to 150 °C at a rate of 5°C/min.

Then the temperature is increased to 250 °C at a rate of 1.6°C/min, and kept at that temperature for 60 minutes. Finally, the sample is left to cool down.

Etching contact vias in DVS-BCB

The shape and position of the (top) contact via in the DVS-BCB layer are of crucial importance for proper device operation, since it defines where the subsequently deposited metal will be in contact with the microdisk. The first requirement is that no (standard) metal contacts should be deposited on top of the whispering-gallery zone, as this would cause excessive optical absorption. Using a *shiny* metal contact can bring some relief to this requirement (see section 4.4.4). Also, the DVS-BCB layer should be thick enough in the WGM zone, to provide adequate optical isolation (a few 100 nm typically provide sufficient isolation). This thickness is largely determined by the spin-coating process, but can also be affected during etching. Finally, the sidewall slope of the via should be not to steep to allow for good metal step coverage.

The bottom and top contact vias were defined in separate lithography and etching steps, since they require different etch depths. Contact lithography was used in combination with the AZ5124 resist, which was also used as etch mask. Both the bottom and top vias were etched by ICP-RIE, using a SF_6/O_2 gas mixture (5/40 sccm) at 60 mTorr and 150 W RF power and 50 W ICP power. To soften the sidewall edges of the deep bottom vias, they were subsequently treated to a RIE step using the same gas flow, but at a high pressure (1000 mTorr) and 100 W RF power. This high etching power results in strong resist mask erosion, which in turn results in angled sidewall profiles. The result of this via process is shown in figure 4.5. Due to the limited alignment accuracy during contact lithography, the top vias are typically misaligned with respect to the microdisks with a few 100 nm.

4.4.4 Metal contacts

With the tunnel-junction-based injection scheme, only ohmic metal contacts to n-type InP are required, which are easily obtained, provided that the doping level is high enough and that an alloying treatment is performed. For the bottom contact, a Ti/Pt/Au metallization with typical thicknesses 25/50/200 nm was applied. For the top contact, Ti/Pt/Au metallization with typical thicknesses 2/5/200 nm or shiny Au contact was used (see section 4.4.4), in order to minimize any excess optical absorption at the (slightly) misaligned top contacts, while also limiting the risk on severe Au spiking into the InP during subsequent thermal annealing, as compared to a pure Au contact.

The metallization is done with a lift-off process, using contact lithography on the AZ5124 resist, which is twice spin coated at 3500 RPM to obtain a resist thickness of about 3 μm. This increased resist thickness allows for the lift off of thicker metal layers. After deposition, the samples are subjected to a rapid thermal annealing process (RTA) at 325 °C, in a N_2/H_2 (90/10) atmosphere. This relatively low annealing temperature (conventional RTA is done at 400 °C) was chosen to limit the risk on Au spiking. Typical results of the metallization are shown in figure 4.6: (b) shows a top

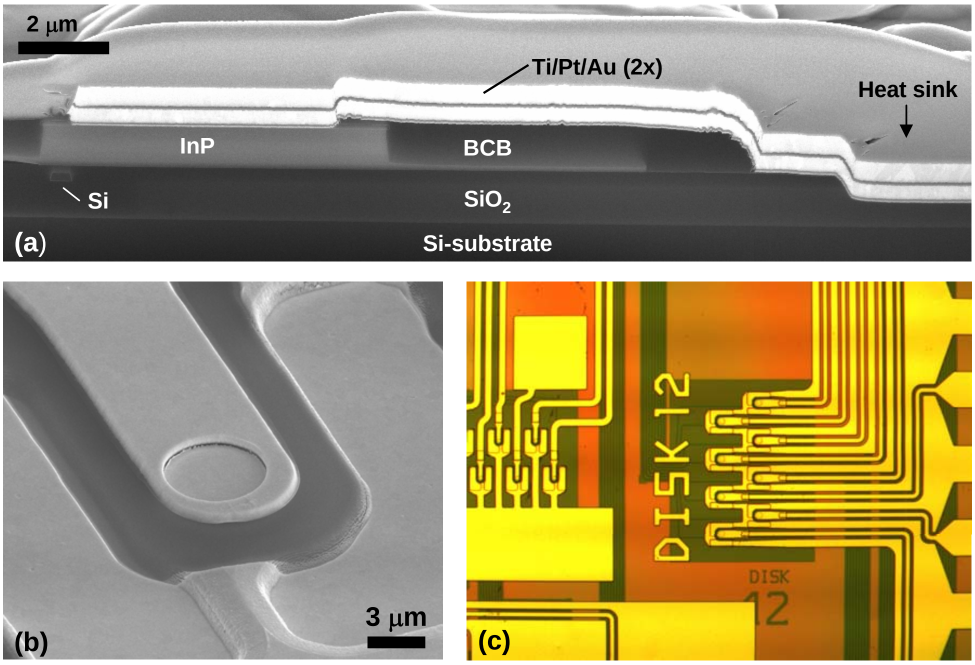

Figure 4.6: (a) FIB cross section of a 1-μm-thick G3 microdisk laser after metallization, including a heat sinking structure. (b) Top SEM image of a metallized G2 structure, showing a poor metal step coverage at the top contact due to too steep BCB via sidewalls. (c) Top down microscope image of block of eight metallized G2 microdisks.

view of the metal contacts, with an apparent step coverage problem at the top via. Increasing the metal thickness can solve this problem, as shown in (a). In this case the top metal was as thick as possible ($\sim 1\,\mu$m, with two subsequent lithography and deposition steps), in order to improve the heat sinking capacity. (c) shows a top view of a group of 8 metallized microdisk lasers, with large contact pads for external probing.

Shiny, ohmic Au contacts to n-type InP

As already mentioned in 2.2.2, purely Au-based contacts on InP have the lowest optical absorption loss. However, as-deposited Au on n-type InP doesn't result in low-resistance ohmic contacts, unless they are alloyed. Unfortunately, during alloying, Au spikes are formed that can penetrate deep into the InP, thereby causing very high optical absorption and possibly creating shunt current pads to the diode. In [88], a purely Au-based contact with low spiking and low contact resistance was proposed. It is formed by first depositing a very thin Au layer of a few nm, which is alloyed (RTA) at 400 °C. It was found that in this process a thin Au_2P_3 layer is formed, which

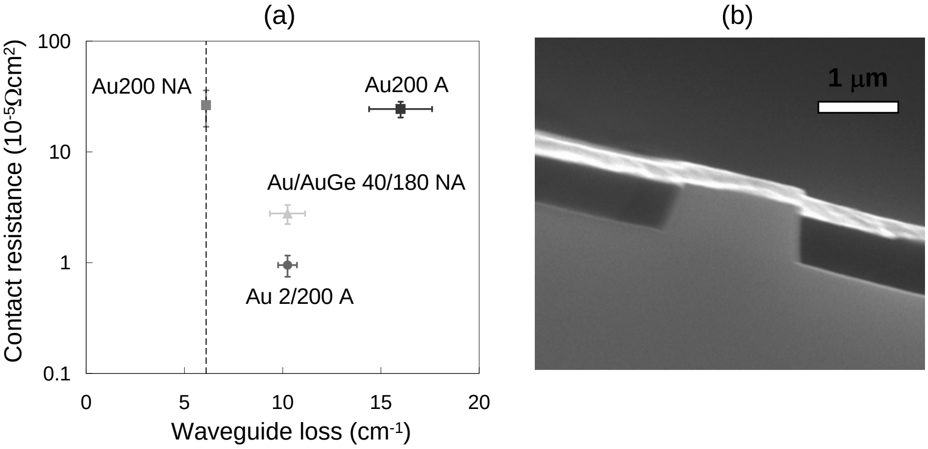

Figure 4.7: (a) Contact resistance and absorption loss for different Au-based contacts to n-type InP (A=alloyed, NA=non-alloyed). The vertical line represents the calculated absorption loss for the associated 1D slab waveguide. (b) SEM image of a metallized waveguide, used to extract the metal absorption loss.

results in a two-to-three order of magnitude drop in the contact resistivity. Then, a thick Au layer is deposited, without further alloying.

We have studied the potential of this special Au-based metallization scheme to obtain a low-loss, low-resistance contact to n-type InP. Transmission-line measurements (TLM) were performed to obtain the contact resistance R_c, on an InP-based epitaxial structure with a 100-nm, highly doped n-type top contact layer (5×10^{18} cm^{-3}), for different Au-based metallizations and alloying conditions. The epitaxial layer structure also included a Q1.28 waveguide core, separated from the contact layer with a 150-nm InP cladding layer. Ridge waveguides were etched into this layer structure down to the bottom of the Q1.28 layer. After DVS-BCB planarization, the same Au-based metallizations as above were deposited on top of the waveguides. Subsequently, the samples were cleaved to obtain 1-mm-long waveguides with high-quality waveguide facets, as shown in figure 4.7(b). Waveguide losses were then extracted by inspecting the Fabry-Perot resonance quality factors, by injecting light using the end-fire method. The loss was extracted for waveguide widths of 3, 5 and 7 μm.

The results of both measurements are summarized in figure 4.7(a). Four different metallizations were considered: (1) a non-alloyed 200-nm Au layer (Au200 NA), (2) an alloyed 200-nm Au layer (Au200 A), (3) a non-alloyed 180-nm AuGe layer (7-at%Ge) on top of a 40-nm Au layer (Au/AuGe 40/180 NA) and (4) the special Au contact from [88], with a non-alloyed 200-nm Au layer on top of a thin alloyed 2-nm Au layer[3] (Au 2/200 A). All alloying steps consisted of a RTA of 3 minutes at

---

[3] It should be noted that the error on the thickness of the deposited Au-layer can also be in the nm range, especially for very short deposition times.

440°C. Both Au200 NA and Au200 A exhibit non-ohmic behavior. Therefore, R_c was extracted at a current density of 1kA/cm^2, yielding $R_c \sim 2.5 \times 10^{-4}\Omega\text{cm}^2$. The Au/AuGe 40/180 NA contact exhibit ohmic behavior, with $R_c \sim 2.5 \times 10^{-5}\Omega\text{cm}^2$. Finally, the Au 2/200 A metallization yielded the lowest contact resistivity, $R_c \sim 1 \times 10^{-5}\Omega\text{cm}^2$. These observations are in (qualitative) agreement with results presented in [88]-[141].

The waveguide loss for the Au200 NA metallization agreed very well with the calculated waveguide loss for the metallized (1D) slab waveguide, indicated by the dashed line in figure 4.7(a) (6.1 cm^{-1}). Fast alloying this 200-nm Au contact resulted in an increase of the waveguide loss by almost a factor 3. This increase is associated with Au-InP interaction, and can be partly suppressed by alloying only a thin Au layer, as is evident from the waveguide loss for the Au 2/200 A metallization ($\sim 10.3\,\text{cm}^{-1}$). The Au/AuGe 40/180 NA contact has comparable waveguide loss. It can be expected that a further reduction of the amount of alloyed Au will result in lower waveguide losses, without a significant increase in contact resistance.

From these results, it is clear that alloying only a thin Au layer can be beneficial to both waveguide loss and contact resistivity. However, the reliability of such a contact remains an issue, as an increased temperature – for instance due to self heating – might result in additional InP-Au intermixing.

4.5 Conclusion

This chapter reviews the processing steps that are required for the fabrication of heterogeneous Si- and SOI-integrated microdisk lasers. The most critical steps involve the molecular InP-to-SOI bonding, which requires ultra-flat and ultra-clean surfaces. Currently, the yield of this process is low, and the control on the bonding layer thickness is insufficient, given the high sensitivity of the microdisk-wire coupling loss to this thickness. A further yield-limiting step is the alignment of the top BCB vias during contact lithography. However, this could be solved by using wafer-scale DUV lithography.

Chapter 5

Experimental results

This chapter gives an overview of the measurements performed on integrated microdisk lasers. The measurement procedure is first explained, both for optically-pumped and for electrically-injected operation. In the course of this work, measurements were performed both on Si-integrated generation-1 (G1) microdisk lasers, without coupling to a waveguide, and on generation-2 (G2) microdisk lasers integrated on SOI waveguide circuits. Generation 2 also included samples with a complete optical link, with both integrated microlasers and microdetectors. Some preliminary full-link experimental results will be presented. Generation-3 (G3) samples with advanced SOI-coupled microdisk laser designs arrived too late for a complete experimental characterization.

5.1 Measurement setups

Both optically pumped and electrically-injected measurements were performed in the course of this work. While the ultimate goal was the demonstration of electrically-injected integrated microlasers, optically-pumped experiments can often yield valuable information on the laser performance, such as threshold power and coupling efficiency. They are also useful as an in-line tool during processing, to check for laser operation prior to the metallization step.

5.1.1 Optical pumping

Optically pumped lasing operation is typically characterized in a micro-photoluminescence setup (μPL). In such a setup, an optical pumping beam – with a wavelength considerably shorter than the expected emission wavelength[1] – is focused onto a microdisk laser through a microscope objective. The absorption of the pumping light creates electron-hole pairs throughout the disk, which can recombine within

---

[1] Pumping wavelengths too close to the emission wavelength could exhibit too small absorption, whereas carriers generated by too short pumping wavelengths relax thermally before potentially recombining radiatively , thereby contributing to device heating.

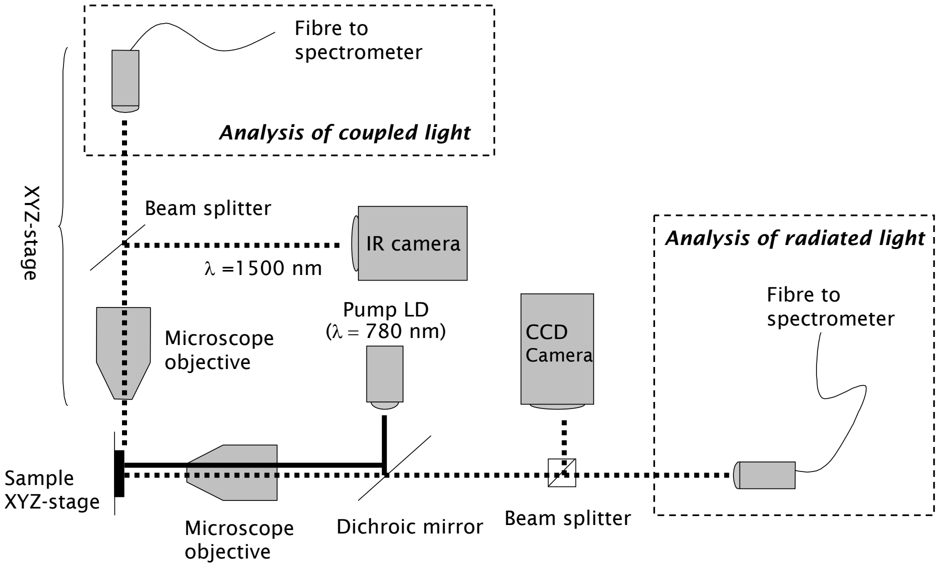
Fibre to spectrometer
Analysis of coupled light
XYZ-stage
Beam splitter
IR camera
λ =1500 nm
Analysis of radiated light
Fibre to spectrometer
Pump LD
(λ = 780 nm)
Microscope objective
CCD Camera
Sample XYZ-stage
Microscope objective
Dichroic mirror
Beam splitter

Figure 5.1: Schematic representation of the optical pumping setup, as available at INL.

the active region to contribute to laser operation. The emitted light is then collected through the same objective, and separated from the pumping light – typically with a dichroic mirror – after which it is fed to a spectrometer for spectral analysis.

An advanced version of such a μPL setup was already available at INL at the start of this PhD work, together with extensive expertise on fabricating and characterizing Si-integrated, optically pumped microlasers. A schematic representation of the μPL setup at INL is shown in figure 5.1. As can be seen, this setup also allows for the characterization of light coupled to the in-plane SOI waveguide, by collecting the light emanating at the cleaved facet of the SOI waveguide with a second (long working-distance, IR) objective. The pumping light has a wavelength of 780 nm, which is still visible for the CCD camera used to align the pumping spot with the microlaser. An infrared camera is used to visualize the laser light emitted at the SOI waveguide facet. A grating-based monochromator in combination with a liquid-N_2-cooled InGas detector was used as spectrometer. The spectral resolution is 25 pm.

During this work, a simple μPL setup was built at UGent, with a pumping wavelength[2] of 660 nm. A GRIN-lensed fibre was used to collect the light and feed it to an optical spectrum analyzer. This setup was mainly used to confirm optically-pumped lasing on a sample prior to metallization, for instance to check if the disk etch depth was sufficient to allow for low bending loss.

---

[2] A pumping beam in the visible is easier to align in the measurement setup, but results in less efficient pumping.

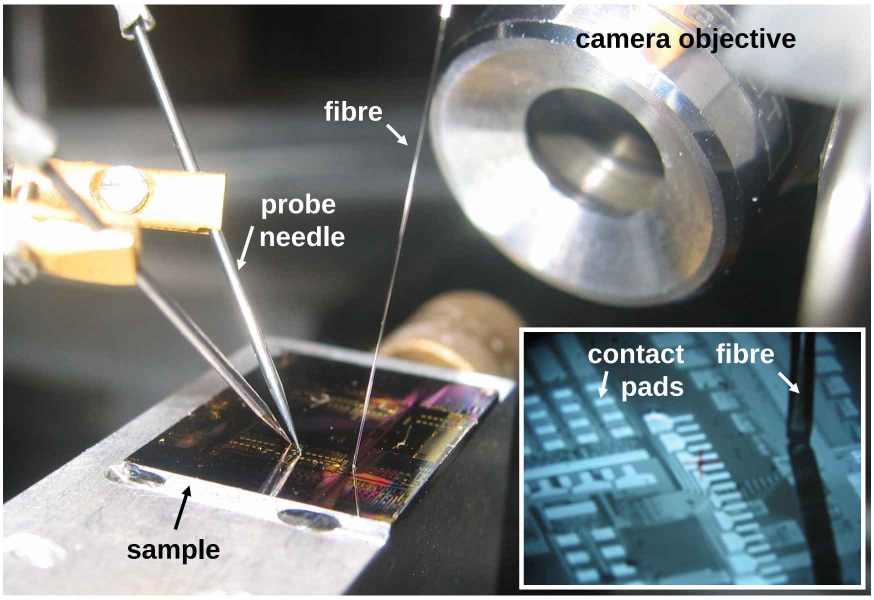

Figure 5.2: Photograph of the electrically-injected laser measurement setup, showing the electrical probe needles positioned on top of the contact pads and the optical fibre positioned above the fibre coupler of the corresponding SOI waveguide (inset: camera image).

5.1.2 Electrical injection

For electrically-injected measurements, the electrical drive signal was delivered to the microlaser by probe needles that are positioned on top of large contact pads that are defined in one of the metallization steps. A photo of the measurement setup is shown in figure 5.2. Part of the emitted light is collected by a fibre, which is aligned under an angle with the surface normal. For G1 microlasers, a multi-mode fibre was used to enhance the collection efficiency, and is aligned on top of the biased microdisk. The angle with the surface normal is in the range 30-50 °. Typically, up to 1 nW of the emitted optical power is collected. For SOI-coupled G2 microdisk lasers, a single-mode fibre is aligned under an angle of 8 ° above a grating coupler etched into the output SOI waveguide. Coupling efficiencies up to 30% have been measured for this type of grating couplers [6]. The fibre alignment is done with the help of a camera image taken at an angle of roughly 45 ° with the sample plane. The probe needles are positioned using a top-down microscope image, prior to aligning the fibre.

Typically, driving a laser diode is done with a current source, since a small error on a voltage drive signal would result in a large error in the applied current, due to the non-linear diode I-V behavior. However, for reliable pulsed measurements, specific care has to be taken to avoid parasitic transmission line effects (such as reflection at interfaces), and capacitive loading and inductive effects, to avoid ringing

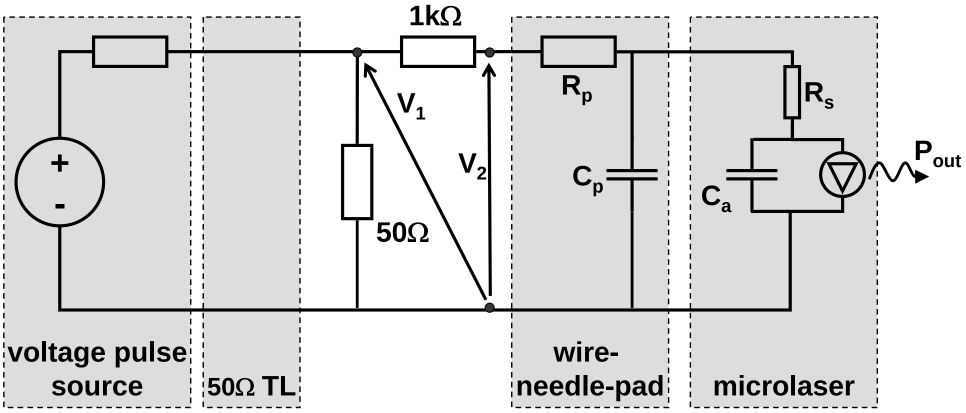

Figure 5.3: Equivalent electrical network of the electrical injection setup. A pulsed voltage source is connected to the laser diode through a 50 Ω transmission line, terminated with a 50 Ω resistor. The device current is determined by measuring the voltage drop over a series resistor.

on fast pulses. The equivalent electrical network of the used setup is shown in figure 5.3. A (pulsed) voltage source is connected to the probe needles through a 50 Ω transmission line, which is terminated by a 50 Ω resistor[3]. By measuring the voltage drop $V_r = V_1 - V_2$ over a resistance in series with the laser diode, the current running through the laser diode can be determined, after transient effects have disappeared. Since typical device currents are on the order of 1 mA, a 1kΩ-resistance was chosen, resulting in resistor voltages in the order of 1 V. To minimize parasitic inductance, the wires between the probe needles and the 50 Ω transmission line connected to the voltage source were made as short as possible. The voltages V_1 and V_2 are measured with electrical probes, with an input resistance of 10 MΩ and a capacitance of 15 pF. Therefore, capacitive loading will take at least 15 ns, which limits the minimum pulse duration. Parasitic capacitance of the contact wires and pads further add to the loading time. For high-speed measurements, high-speed probes should be used, in combination with specifically designed high-speed contact pads with 50 Ω impedance. However, such RF contacts occupy a large area on the sample, thereby limiting the amount of available devices on a sample.

5.2 Generation 1: Si-integrated microdisk lasers

For electrically-injected G1 microdisk lasers, the epitaxial composition is given in table 5.2[4]. Samples with a nominal epitaxial thickness of 0.5 and 1 μm were available. They were bonded on plain Si dies, with an intermediate SiO_2 bonding layer

---

[3] The voltage pulse source has an output impedance of 50 Ω.

[4] This material was already available at the start of this PhD work, however no successful laser operation or even electroluminescent operation was obtained prior to this PhD work.

Description	Material	Type	Doping	Thickness (nm)	
			(10^{18}cm^{-3})	Thin	Thick
n-contact	InP	n+	2	150	380
OCL	Q1.2	nid	n/a	51	83
barrier	Q1.2	nid	n/a	20 (×4)	20 (×4)
quantum well	$InAs_{0.65}P_{0.35}$	nid	n/a	6 (×3)	6 (×3)
OCL	Q1.2	nid	n/a	51	83
p-layer	InP	p+	2-5	30	302
TJ p-layer	Q1.2	p++	20	20	20
TJ n-layer	Q1.2	n++	20	20	20
n-contact	InP	n+	2	80	100

Table 5.1: Epitaxial layer design for G1 microlasers.

thickness of 1 μm. However, for MBE growth on 2-inch InP wafers, intra-wafer non-uniformities on the measured layer thickness in the range 10-20% are not uncommon. As a result, the thick epitaxial samples were found to have a thickness as low as 800 nm, whereas the thin microdisks had a thickness of 480 nm. The microdisk diameters were in the range 4-10 μm.

5.2.1 Thick G1 microdisk lasers

The first successful demonstration of electrically injected lasing was achieved on a 0.8-μm-thick microdisk laser, as shown in figure 5.4. For this early sample, the BCB processing was not yet optimized, leaving the complete top surface of microdisk open to metal coverage. To minimize the impact of absorption loss at this interface, a shiny Au top contact was used (see section 4.4.4). Electrically-injected lasing in pulsed regime was observed on two 8-μm-diameter microdisk lasers with the electroluminescence measurement setup in INL. The lasing threshold was about 1.5 mA (2.9 kA/cm^2), and the lasing wavelength was 1520 nm, as can be seen on the output spectrum in fig. 5.4 (b). However, a voltage of more than 5 V was needed to reach the threshold current. Even so, to the best of our knowledge, this was the world-wide first demonstration of a Si-integrated, electrically-injected microlaser. This result was published in [142].

A number of likely causes can be mentioned to explain the small number of lasing devices (2 out of 48 on the sample). First, the reliability of the shiny-Au contact is low, exhibiting a very low adhesion to the InP disk. This was found to be a particular problem when biasing the lasers in continuous-wave regime. In this regime, self heating results in a serious increase of the microdisk temperature (see further). Thermal stress in combination with poor adhesion causes the top contact to literally be torn apart from the microdisk. However, this burn-in treatment was required to obtain adequate current injection at the top contact. Further, due to misalignment

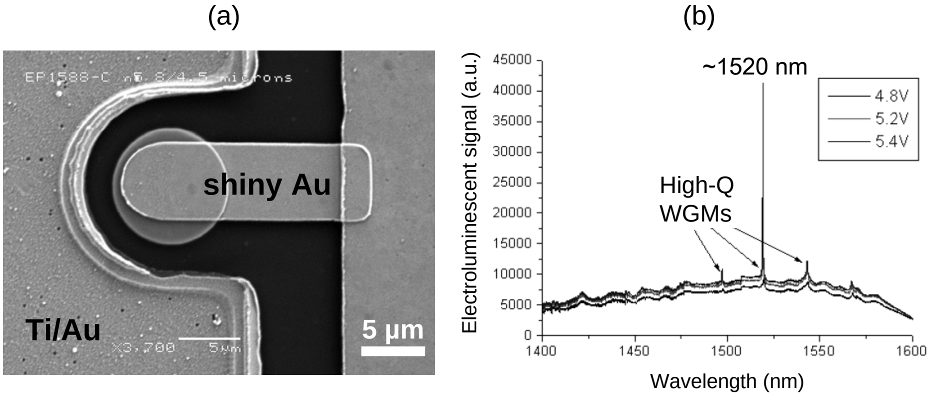

Figure 5.4: Fabrication and measurement results of a G1 0.8-μm-thick microdisk laser. (a) top-down SEM image of 8-μm-diameter microdisk, with shiny-Au top contact. (b) Lasing spectrum taken at various bias voltages (6-ns pulses (nominal), 333-ns period). Fabrication performed at UGent/INL, measurements at INL.

during lithography, the metal coverage on the top microdisk surfaces was not the same for all devices. Lasing was only obtained for structures with the least amount of metal coverage. Lastly, some microdisks exhibit very rough sidewalls, with irregularities as big as several 100 nm. The high operating voltage can be attributed to a too low tunnel-junction p-type doping level (see further).

5.2.2 Thin G1 microdisks lasers

For the thin G1 microdisks, the BCB processing was optimized such that the disk top surface was covered with at least 500 nm BCB, efficiently isolating the whispering-gallery modes from the top metal contact (see inset figure 5.5 (b)). Microdisks with diameters in the range 4-10 μm were available, with top contact vias in the range 2.5-8.5 μm. Due to steep BCB via sidewalls, two top Au metallization steps were needed for adequate metal coverage. Again, a burn-in treatment (high current in pulsed regime) was needed to obtain lasing. On this sample, lasing was obtained for the majority of the microdisks with diameter larger than or equal to 4 μm. For smaller devices, the top vias weren't etched open. A typical set of P-I and V-I data is shown in figure 5.5 (a), for a 6-μm-diameter microdisk. The threshold current was 0.55 mA. However, the required threshold voltages were in the range 7-8 V, resulting in strong self heating and making lasing only possible in pulsed regime. The above-threshold spectrum is shown in fig. 5.5 (b). It reveals a clear laser peak superimposed on the spontaneous emission background, mainly emitted form the center of the microdisk and also picked up by the multi-mode optical fibre. This spontaneous emission contribution blurs the onset of lasing in the P-I curve when recording the total emitted power. Therefore, to determine the laser threshold current, in figure 5.5 (a), the laser

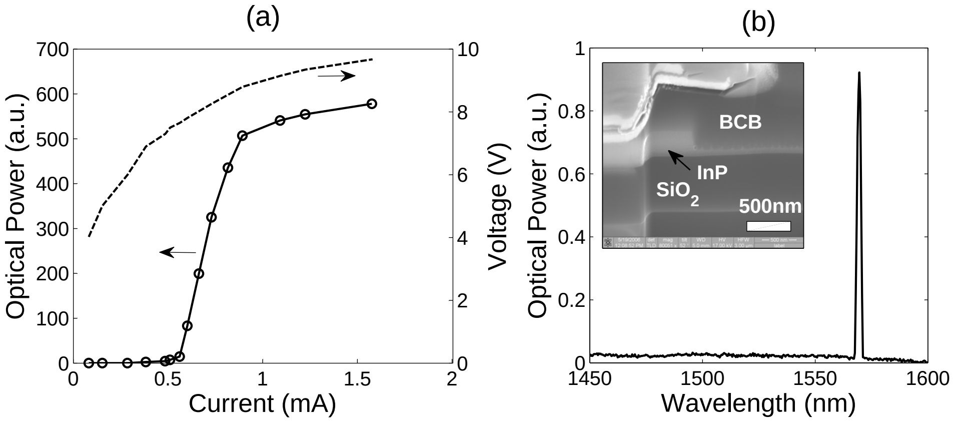

Figure 5.5: (a) Laser peak power versus current and V-I curve for a 6-μm-diameter, 0.48-μm-thick G1 microdisk laser in pulsed regime (360-ns pulses, 3.6-μs period). (b) Spectrum taken at 0.78 mA. The inset shows a FIB cross section of the microdisk edge.

peak power is plotted as function of device current, instead of total emitted power[5]. The saturation of the peak laser power at currents larger than 0.75 mA is due to self heating, as will be discussed below.

The threshold current versus microdisk radius is shown in figure 5.6 (a). The measured data (circles) are compared to calculated threshold values (see equations (3.34) and (3.36)), under the assumption of uniform injection. Various values for the internal loss α_i and scattering loss α_s were considered to obtain a good match with the experimental values. The bending loss was calculated for a 80-nm bottom contact layer. From figure 3.12, an internal loss of 50 cm^{-1} could be expected (assuming an on-target TJ p-doping of 2$\times$10^{19}cm^{-3}), even if the G1 epitaxial layer structure isn't completely identical to the optimized layer structures considered in fig. 3.12. The expected threshold values for $\alpha_i = 50\,\mathrm{cm}^{-1}$ and without scattering loss ($\alpha_s = 0$) are shown in grey, and clearly overestimate the measured threshold values. Based on the poor electrical behavior of the TJ, exhibiting a high turn-on voltage, the TJ p-doping is most likely more than an order of magnitude lower than the target value, resulting in a much lower internal loss. The calculated threshold values for $\alpha_i = 10\,\mathrm{cm}^{-1}$ and with various values for scattering loss, based on the model (3.9) with $\sigma = 1, 10, 20\,\mathrm{nm}$ ($L_c = 100\,\mathrm{nm}$) are indicated with the solid, dashed and dotted black lines respectively. The decreasing trend in threshold with decreasing microdisk radius, as predicted by the (simple) model, are confirmed by the measurements, assuming sidewall roughness in the range 10-20 nm, which are common values for InP waveguides.

The lasing wavelengths as function of microdisk radius are shown in fig. 5.6 (b). At high injection, the lasers with radius in the range 3-3.75 μm exhibit two lasing modes. The ground lasing modes are indicated by the circles, whereas the second

---

[5] This is often done in literature for the determination of the threshold current of microdisk lasers.

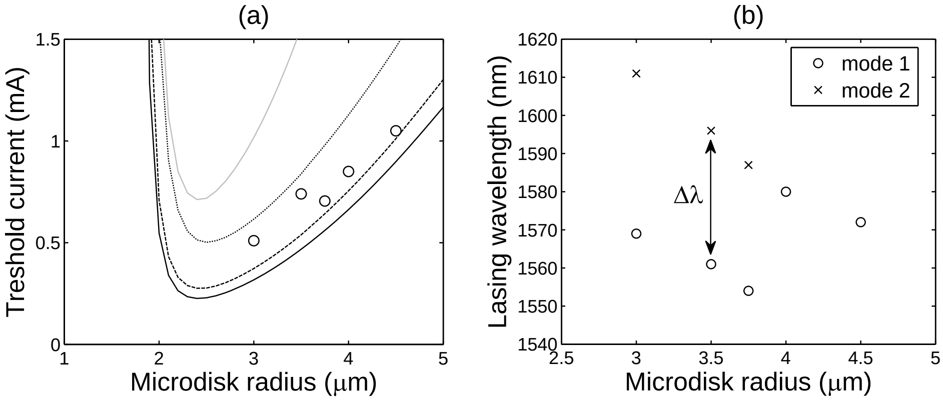

Figure 5.6: Lasing characteristics versus microdisk radius for G1 lasers (pulsed regime: 360-ns pulses, 3.6-μs period). (a) Measured threshold current (circles). Calculated threshold values for $\alpha_i = 50\,\mathrm{cm}^{-1}$, $\alpha_s = 0$ (grey line), and $\alpha_i = 10\,\mathrm{cm}^{-1}$, $\sigma = 1, 10, 20\,\mathrm{nm}$ ($L_c = 100\,\mathrm{nm}$) in solid, dashed and dotted black lines respectively. (b) Measured lasing wavelengths.

modes are shown by the crosses. From the mode separation $\Delta\lambda$ (free spectral range), the WGM group index n_g can be deduced from equation (3.6). From the measured $\Delta\lambda$ values, n_g is calculated to be about 3.2. This value agrees reasonably well with the eigenmode expansion calculations, as shown in figure 3.5. The slight underestimation of the simulated values is due to the simplified simulated structure, assuming a homogeneous disk with $n = 3.2$. Nevertheless, this result confirms that the microdisks are lasing in the fundamental WGMs.

Lasing at elevated temperatures

All previously reported lasing measurements were performed at room temperature (20°C). To study the performance penalty under elevated temperature, the sample was heated by means of a Peltier element, while keeping pulsed drive conditions with as short as possible pulse durations[6], to suppress self heating. The measured P-I curves for different ambient temperatures ($D = 6\,\mu$m) are shown in figure 5.7 (a). It can be seen that the threshold current increases gradually with increasing temperature, while the slope efficiency drops dramatically. However, it should be noted that only the laser peak power at the ground mode (around 1570 nm) is considered, while at higher temperatures the second mode at 1612 nm starts lasing. Therefore, the total laser output is higher than shown here. Also, it should be noted that it was difficult to maintain the same fibre coupling conditions for the G1 lasers over the relatively long time needed to perform a complete thermal characterization, which takes several tens of minutes. Therefore, it was difficult to accurately compare the absolute output powers of measurements at different temperatures.

---

[6] 50 ns for the measurement setup available at that time.

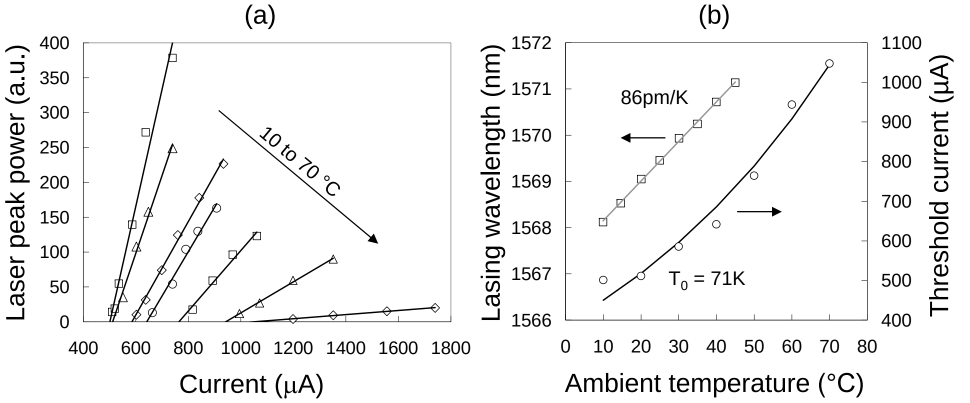

Figure 5.7: Lasing characteristics for mode 1 versus ambient temperature for a 6-μm-diameter G1 laser (pulsed regime: 50-ns pulses, 3-μs period). (a) Laser peak power at 1570 nm versus current, (b) lasing wavelength versus ambient temperature.

Nevertheless, the threshold current and lasing wavelength can be extracted with reasonable accuracy, and are shown in fig. 5.7 (b). A characteristic temperature of 71 K can be fitted for the threshold current, which agrees well with reported values in literature for InP-based lasers. The red shift of the lasing wavelength $d\lambda_r/dT$ was measured to be 86 pm/K, which is somewhat lower than the 100 pm/K that is typical for InP-based (DFB-)lasers. This reduced thermal red shift is attributed to the BCB cladding, for which the refractive index increases with temperature, as is the case for most polymers. For a 7.5-μm-diameter microdisk laser, a red shift of 95 pm/K was measured, due to the reduced mode intensity in the BCB cladding for larger disk radii. This reduced thermal red shift was also reported in [46] for BCB-covered pedestal-supported microdisk lasers.

Self heating

Knowing the thermal red shift $d\lambda_r/dT$ with changing ambient temperature, we now can use this data to characterize the cavity temperature increase due to self heating, at a fixed sample temperature. During self heating, the laser emits gradually at a longer wavelength within a single pulse, provided it is long enough. The thermal turn-on response of the microdisk can thus be extracted by measuring the spectral broadening in pulsed regime for varying pulse durations, provided that the pulse period is long enough to allow the device to cool down. Under such conditions, the maximum attained cavity temperature within a pulse can be estimated as

$$T(s) = T_{hs} + \frac{\Delta\lambda(s) - \Delta\lambda_0}{d\lambda_r/dT}, \tag{5.1}$$

where s is the pulse duration, T_{hs} the heat-sink (sample) temperature, $\Delta\lambda(s)$ the measured linewidth, and $\Delta\lambda_0$ the finite linewidth due to the resolution of the mea-

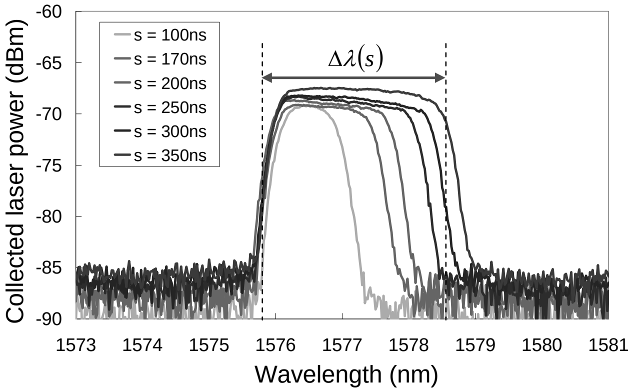

Figure 5.8: Spectral broadening due to self heating (mode 1) versus pulse duration s for a 6-μm-diameter G1 laser (850-μA pulses, fixed 5-μs period, spectra recorded with 200-pm resolution)

.

surement setup. The measured spectra for varying s are shown for a 6-μm-diameter laser in figure 5.8, for a pulsed drive current of 0.85 mA and a 5-μs pulse period. Self heating results in an increasing spectral red shift of the long-wavelength tail of the laser peak with increasing pulse duration, while the short-wavelength edge remains almost constant, as expected. It should be noted that for an injection current of 0.85 mA, the total peak drive power was approximately 6 mW, as a result of the high operating voltage. Using this spectral data, the cavity temperature was extracted using equation (5.1), by measuring the laser linewidth $\Delta\lambda(s)$ at -5 dB, -10 dB and -15 dB respectively. The linewidth $\Delta\lambda_0$ was assumed to be determined by the limited resolution of the measurement setup (200 pm at -3 dB), and was calculated at the relevant power level, assuming a lorentzian lineshape.

The results are indicated in figure 5.9 by the markers. Additional measurements were performed for higher pumping powers of 9 mW and 11 mW. For these measurements, the heat sink was kept at 15 °C. The lasing wavelength could be traced up to an equivalent cavity temperature of 60 °C. The extracted data are compared to the simulated data, obtained by the thermal model in section 3.6, for which the simulated geometry was obtained using the FIB cross section in figure 5.5. For the simulations, two SiO_2 thermal conductivities κ_{ox} were considered: 1 and 1.27 W/mK, which covers the range of reported values in literature. All injected power is assumed to be dissipated as heat, which is reasonable considering the high operating voltage. The experimental data is found to be in good agreement with the thermal model, especially when assuming $\kappa_{ox} = 1\,\mathrm{W/mK}$. In this graph, the horizontal error bars indicate the uncertainty on the true pulse duration, due to parasitic electrical effects.

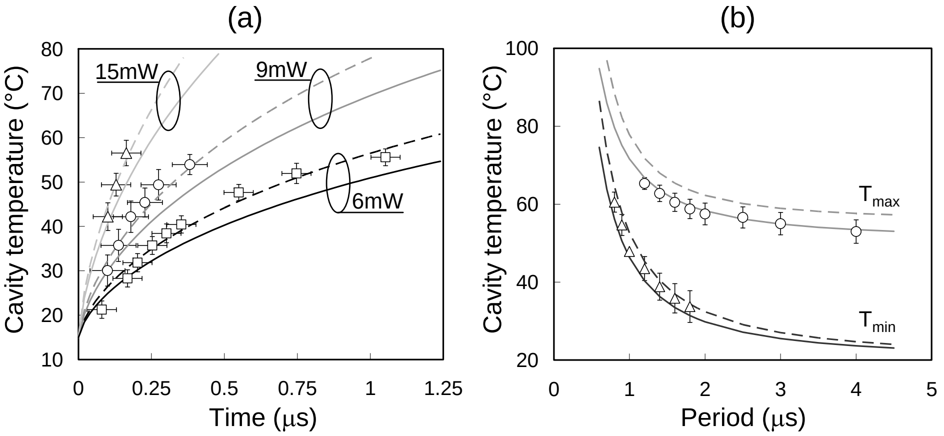

Figure 5.9: Comparison of experimentally extracted self heating with thermal simulation. (a) Thermal turn-on response of a 6-μm-diameter G1 laser for different pumping levels. (b) Maximum and minimum regime temperatures versus pulse period for a fixed pulse duration (360 ns), for a 7.5-μm-diameter laser at 11 mW pumping power. Experimental data are indicated with markers. Lines show simulated data (solid lines $\kappa_{ox} = 1.27\,\mathrm{W/mK}$, dashed lines $\kappa_{ox} = 1\,\mathrm{W/mK}$)

.

In a second experiment, the pulse duration was fixed while the period was varied. With decreasing period, the laser doesn't get the chance to cool down completely and heat is accumulated during each period. After some periods, a thermal regime is reached, for which the temperature oscillates between T_{min} and T_{max}, which depend both on the drive power, pulse length and period. This experiment thus also involves the cooling behavior. To check the general validity of the thermal model, for this experiment the temperature extraction was performed on a 7.5-μm-diameter microdisk, with a heat sink temperature of 20 °C. The results are shown in figure 5.9 (b). Again, excellent agreement was obtained with the simulated data, however in this case, agreement is better when assuming $\kappa_{ox} = 1.27\,\mathrm{W/mK}$. For a period larger than 2 μs, mode competition prevented a straightforward extraction of the minimum regime temperature.

From these measurements, we conclude that the thermal model provides a good framework to predict the thermal behavior of the microdisk lasers. Furthermore, it confirms that the device current and voltage as measured with the electrical setup are reliable. This result was published in [143].

5.3 Generation 2: SOI-integrated microdisk lasers

The epitaxial layer structure design for G2 microdisk lasers is given in table 5.3. The internal loss and confinement factors are similar to the optimized structures of designs A and B, which were discussed in section 3.4. Again, thin and thick structures

Description	Material	Type	Doping (10^{18}cm^{-3})		Thickness (nm)	
			Thin	Thick	Thin	Thick
n-contact	InP	n+	5-1	5-1	50	340
OCL	Q1.2	n+	1	n/a	165	100
barrier	Q1.2	nid	n/a	n/a	20 (×4)	20 (×4)
quantum well	InAsP	nid	n/a	n/a	6 (×3)	6 (×3)
OCL	Q1.2	nid	n/a	n/a	0	80
p-layer	InP	p+	2-5	0.1-1	95	220
TJ p-layer	Q1.2	p++	20	20	20	20
TJ n-layer	Q1.2	n++	10	10	20	20
n-contact	InP	n+	5	5	80	100

Table 5.2: Epitaxial layer design for G2 microlasers.

with respective thicknesses 0.5 and 1 μm were grown, with particular attention to enhance the TJ doping levels. The InP dies were molecularly bonded onto waveguide SOI wafers, as discussed in section 4.3. Microdisks with diameters 5, 7.5 and 10 μm were available on the mask plate. To compensate for possible alignment errors between the disk and the SOI waveguide, the mask also contained microdisks with intentional lateral wire-disk offsets of ±100 nm. Due to an error during Si lithography, the SOI wires were fabricated about 10 % too wide. As a result, InP dies were bonded on SOI cells containing wires with widths in the range 530-565 nm. However, due to the poor yield of the G2 bonding run, only a limited amount of samples was available for complete processing.

5.3.1 Optical pumping

After bonding and InP etching steps, optical pumping was performed at INL to test for laser operation and coupling into the SOI waveguide, using the setup sketched in fig. 5.1. Lasing was obtained in pulsed regime from all tested microdisks. Typical pulsed measurement results for thin, 7.5-μm-diameter microdisk lasers are shown in figure 5.10. For this sample, the bonding layer thickness was measured to be around 150 nm, for which a coupling loss $\alpha_c = 50\,\text{cm}^{-1}$ can be expected. The threshold pump power P_{th} can be estimated using (3.36) and

$$P_{th} = \left(AN_{th} + BN_{th}^2 + CN_{th}^3\right) \pi R^2 t_a h\nu_p, \tag{5.2}$$

where ν_p is the frequency of the pumping light. Assuming $\alpha_i = 30\,\text{cm}^{-1}$ (see further) and $\alpha_s = 10\,\text{cm}^{-1}$ and accounting for the 780-nm pumping wavelength results in a pumping threshold of 1.3 mW. The measured P_{th} values[7] are in the range

---

[7] The effective pumping power is assumed to be around 1/3 of the total power impinging on the sample, to account for reflection and partial absorption.

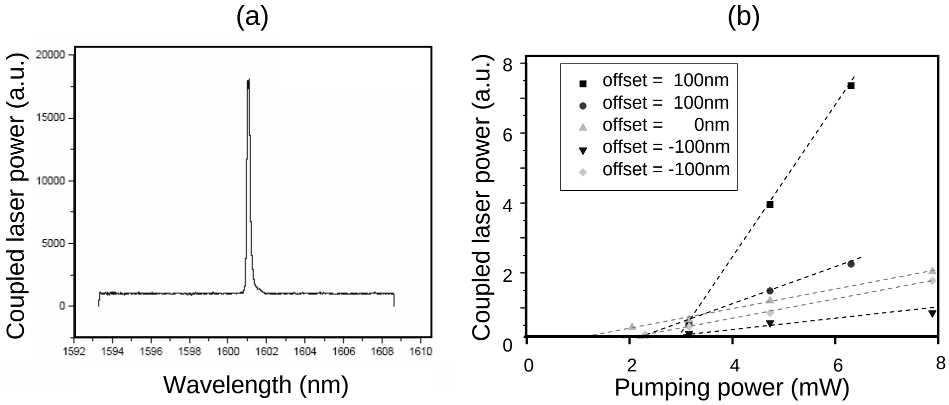

Figure 5.10: Measurement results under pulsed optical pumping for 0.5-μm-thick G2 microdisk lasers with 150-nm-thick bonding layer. (a) Above-threshold SOI-coupled output spectrum of a 10-μm-diameter microdisk laser, showing laser operation at 1601 nm. (b) SOI-coupled output signal versus pumping power for 7.5-μm-diameter microdisk lasers, for different lateral waveguide offsets. Measurements were performed at INL. Lines are drawn as guide to the eye.

1-3 mW, depending on the wire-disk offset, but also with considerable variance between nominally identical microdisks (see fig. 5.10). This variance is attributed to differences in scattering losses, but also to differences in experimental pumping conditions. The resonant wavelength of the guided light was found to be identical to that of the radiated light, confirming that the laser mode is coupled to the SOI wire. For 10-μm-diameter microdisks, the laser linewidth around threshold was smaller than the resolution of the setup (25 pm). For 5-μm-diameter microdisk lasers, threshold linewidths were found to be in the range 140-190 pm, which is equivalent with $Q = 8400 - 11400$. The intensity of the coupled light was found to be only a factor 2-7 smaller than the intensity of the radiated light, indicating relatively efficient coupling. Furthermore, from fig. 5.10 (b), it is also (qualitatively) clear that the coupling efficiency is the highest for the lasers with zero wire-disk offset, which agrees with simulation. Due to misalignment during e-beam lithography, no disks with +100 nm wire-disk offset were available (which should have exhibited the highest coupling).

While optically pumped laser operation from an InP microdisk coupled with an SOI wire was already demonstrated at INL [58] prior to this PhD work, the current measurements confirmed this achievement with epitaxial structures that are ready for electrical injection, and thus have higher internal losses.

5.3.2 Electrical pumping

For electrically injected operation, microdisks were available with top BCB via diameters in the range 0.7-0.84R. A FIB cross section of a thick 7.5-μm-diameter G2 microdisk is shown in fig. 5.11. The BCB top via was found to be misaligned by

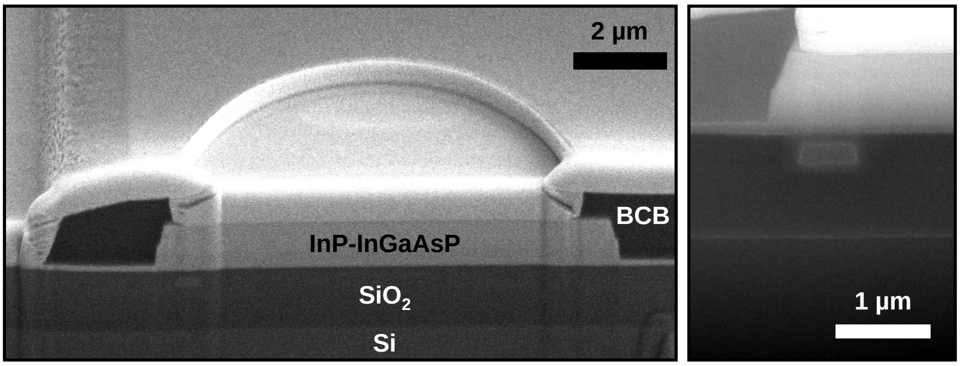

Figure 5.11: FIB cross section of a thick 7.5-μm-diameter G2 microdisk, before metallization.

400 nm, whereas the disk-wire misalignment introduced during lithography was about 150 nm. The bonding layer thickness was found to be about 130 nm. These samples were part of the effort in the PICMOS project to fabricate a full heterogeneous optical link on SOI. Therefore, one branch of the output SOI wire is guided towards a heterogeneously integrated InP-based detector, whereas the other branch is terminated on a standard fibre grating coupler. As a result, it was only possible to directly assess the laser output in one output direction for lasers on this type of samples. The fibre grating efficiency was measured to be maximum at 1594 nm, when using a fibre under 8° with the surface normal. For all measurements reported hereafter, a maximum grating coupler efficiency of 25 % was assumed. Furthermore, an on-chip attenuation of 2 dB was considered, since the laser light has to travel about 5 mm through the SOI circuit before reaching the grating coupler (see Appendix B) and the SOI wire propagation losses were estimated at 4 dB/cm.

On a sample with a 1-μm-thick InP film, lasing was observed in continuous-wave (CW) regime for 7.5-μm-diameter microdisks. Before lasing was obtained, the lasers required a burn-in treatment, typically performed by applying 10 V in pulsed regime with a 5 % duty cycle for several minutes. During this treatment, an increase in (lateral) injection efficiency is observed, which is apparent from the increasing output intensity at the fundamental resonant WGM wavelengths. During this burn-in, the top contact is most likely further alloyed, with additional Au-InP intermixing. In some cases, this treatment results in device failure, most probably due to heavy Au spiking into the microdisk, despite the thin, protective Pt layer.

The measurement results for CW operation of 7.5-μm-diameter microdisk lasers are shown in figures 5.12 and 5.13. Fig. 5.12 (a) shows the output power coupled into the SOI wire for microdisks with -50 nm disk-wire offset, and two different BCB top via diameters $R_{top} = 0.7R$ and $0.76R$. For the first device, the CW threshold current is 0.5 mA, with a CW slope efficiency of 20 μW/mA just above threshold. The output power saturates at 10 μW, due to thermal roll-over. For the second device, performance is much worse, with a threshold current around 0.8 mA and a maximum output power of 1.25 μW. Considering the 400-nm top contact misalignment,

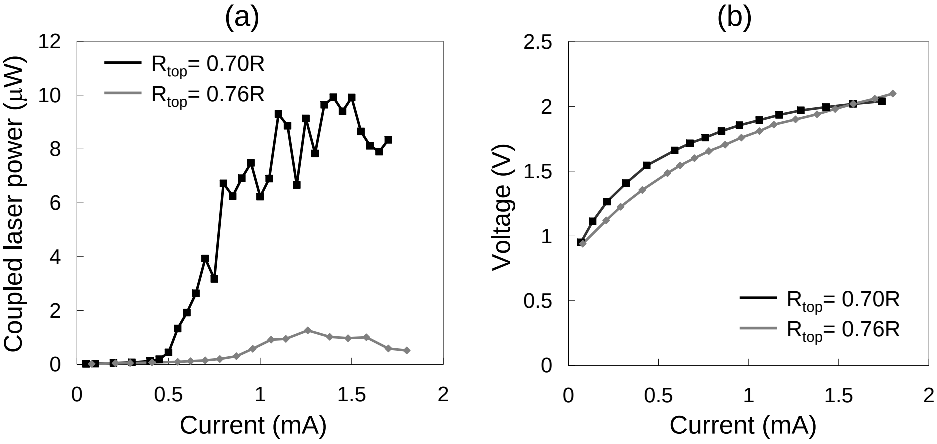

Figure 5.12: Measurement results of CW electrically injected 7.5-μm-diameter 1-μm-thick microdisk lasers, with $-50\,\text{nm}$ wire-disk offset, for various top BCB via diameters R_{top}. (a) SOI-coupled laser output power versus current. (b) Device voltage versus current.

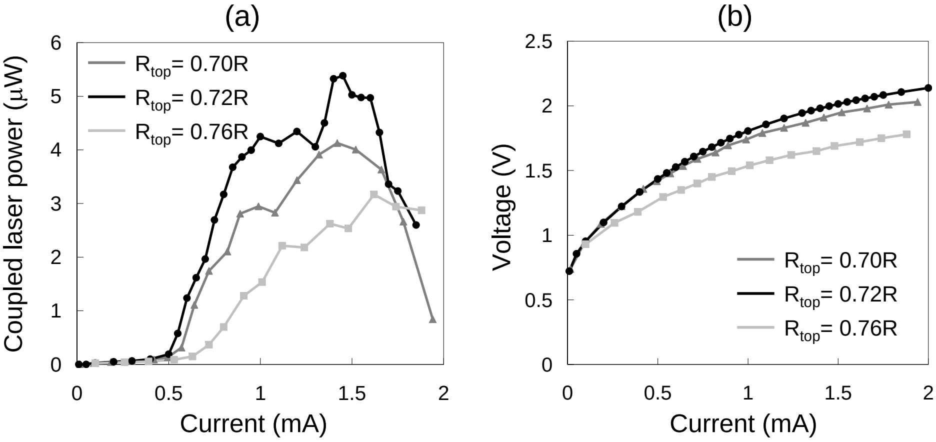

Figure 5.13: Measurement results of CW electrically injected 7.5-μm-diameter 1-μm-thick microdisk lasers, with $-150\,\text{nm}$ wire-disk offset, for various top BCB via diameters R_{top}. (a) SOI-coupled laser output power versus current. (b) Device voltage versus current.

it is clear that for this laser, a fraction of the WGM area is covered by the top metal, which induces excessive modal loss. For both devices, the CW operating voltage remains below 2 V. Clearly, the electrical resistance of the G2 epitaxial structure is much lower than in the G1 structures, due to an enhanced TJ doping level. This reduction in electrical resistance allows for CW operation.

For the laser with $0.7R$, the abrupt kinks in the P-I curve for currents larger than 0.75 mA are most likely due to mode competition between the clockwise and counterclockwise laser mode, which is a typical behaviour for ring lasers [144]. For an ideal microdisk, these counterpropagating modes are degenerate. However, the presence of surface roughness induces contradirectional coupling between the two modes, lifting the degeneracy and causing mode splitting [75]. Monitoring the laser output at both SOI waveguide ends should bring more insight in the competition between these two modes, but this was not possible on these samples.

Fig. 5.13 (a) shows the measurement results for similar microdisk lasers but with -150 nm disk-wire offset. As could be expected, these lasers exhibit a lower slope efficiency (up to 10 μW/mA). Once again, the laser with the biggest top contact has the worst performance, and operating voltages are below 2 V.

In figure 5.14, the SOI-coupled laser spectra of the best performing laser are shown. Fig. 5.14 (a) shows an overview spectrum recorded at 1.4 mA, normalized for the grating coupler efficiency and on-chip loss. Three fundamental WGM modes are clearly visible, with lasing occurring in the mode at 1601 nm. Higher order WGMs are also apparent, with much lower quality factors. Fig. 5.14 (b) shows detailed lasing spectra for several injection levels, recorded with the finest available resolution (60 pm). Above threshold, the measured linewidth is found to be limited by this resolution, indicating that the actual laser linewidth is (much) smaller. No evidence of mode splitting due to contradirectional coupling was observed, suggesting that it is much smaller than the resolution limit, or that lasing occurs in only one of the laser modes at a time for a given pumping level. Self heating is again apparent from the red shift of the lasing wavelength with increasing pumping level. Thermal simulations for this structure yield $R_{th} = 10.4 - 12\,\mathrm{K/mW}$, depending on the value used for κ_{ox}. Assuming that all power is dissipated as heat results in a thermal resistance $R_{th} = 9.5 \pm 0.5\,\mathrm{K/mW}$. Since this assumption overestimates the dissipated power, the true R_{th} is expected to be closer to the simulated value.

For 7.5-μm-diameter microdisk lasers with larger top BCB vias, lasing was only obtained in pulsed regime, with thresholds in the mA range. For 10-μm-diameter microdisks, no CW lasing was found, regardless of R_{top}. Lasing in pulsed regime was obtained for some devices, with a threshold of more than 2 mA and slope efficiencies well below 1 μW/mA. Since CW lasing was obtained for these devices under optical pumping, we speculate that the poor performance under electrical injection is due to a poor lateral injection efficiency. Clearly, the assumption of uniform injection doesn't hold. We note that in the calculations leading to this assumption, perfect cylindrical symmetry was assumed, which is clearly not the case for the bottom contact in fabricated devices. Therefore, we speculate that current crowding occurs in some parts of the disk, resulting in non-uniform injection and a poor lateral injection efficiency. For 7.5-μm-diameter microdisks, this effect seems to be less important.

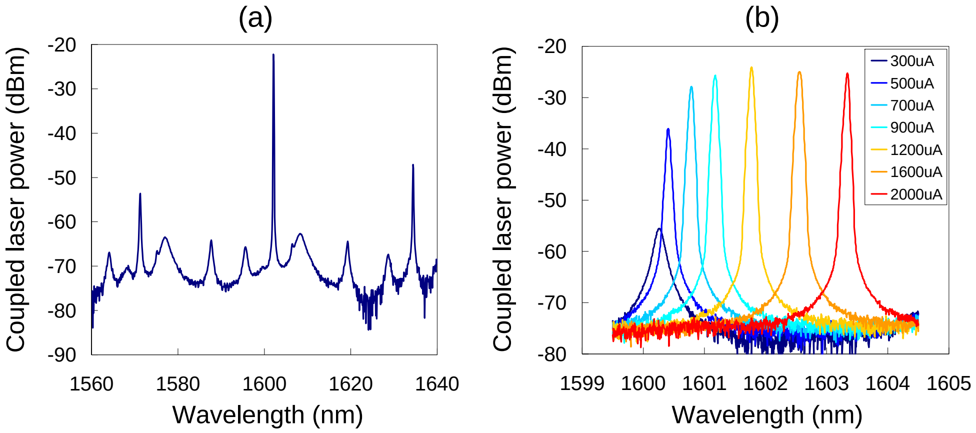

Figure 5.14: SOI-coupled laser output spectrum for the best laser. (a) Overview spectrum for 1.4 mA pumping current. (b) Spectrum detail recorded at finest available resolution (60 pm), as function of injected current.

.

No lasing at all was obtained for 5-μm-diameter microdisk lasers, which we believe is due to their stronger sensitivity to a misalignment of the top contact.

To the best of our knowledge, this was the world-wide first demonstration of an electrically-injected microlaser integrated on and coupled to a Si-based waveguide circuit, operated under continuous-wave regime at room temperature. This result was published in [145].

For 0.5-μm-thick microdisks, lasing was obtained only in pulsed regime, with threshold currents in the mA-range and slope efficiencies around 1 μW /mA. Only one thin device exhibited CW lasing (see section 5.4). Again, this poor performance can most likely be attributed to a poor injection efficiency, which seems to be worse as compared to thick devices.

5.3.3 Theoretical fit to measured lasing characteristics

In order to test the validity of the theoretical laser model, we now attempt to fit this model to the measured (best) lasing characteristics. To eliminate the influence of self heating, which isn't included in the model, pulsed measurements must be considered. This exercise was performed for the best performing 7.5-μm-diameter lasers, for -50 nm and -150 nm disk-wire offset respectively. The results are shown in figure 5.15, where the pulsed measurements are denoted by the markers. The device voltages are higher than in continuous-wave regime. A good fit to the I-V data is provided by assuming a TJ p-type doping level $N_a = 2{\times}10^{18}\text{cm}^{-3}$. This doping level is an order of magnitude lower than the design value. However, an analysis with Secondary-Ion Mass Spectroscopy (SIMS) at INL revealed a doping level around $8{\times}10^{18}\text{cm}^{-3}$. Therefore, we conclude that the electro-optical performance

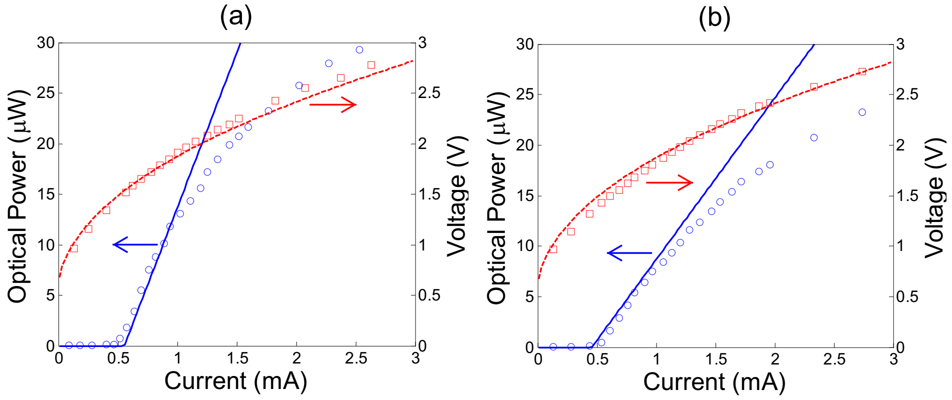

Figure 5.15: Fit to pulsed lasing characteristics of 1-μm-thick 7.5-μm-diameter microdisk lasers. (a) Best performing laser with -50 nm disk-wire offset. (b) Best performing laser with -150 nm disk-wire offset. Rectangles denote measured voltages, circles denote coupled output power. Lines represent the fit to the experiment.

of the tunnel junction is somewhat lower than could be theoretically expected by Demassa's model. Therefore, we have assumed $N_a = 2{\times}10^{18}\text{cm}^{-3}$ to calculate the device voltage, while $N_a = 8{\times}10^{18}\text{cm}^{-3}$ to calculate internal loss. This assumption was also used in section 3.9 to calculate the near-term performance for a microdisk laser with an optimized geometry.

The slope efficiency just above threshold is measured to be 30 μW/mA and 15 μW /mA respectively. A good fit to both P-I curves is provided by the simplest model (3.8), assuming $\alpha_s = 12\,\text{cm}^{-1}$ ($L_c = 100\,\text{nm}$, $\sigma = 10\,\text{nm}$), and $\alpha_c = 3$ and $7\,\text{cm}^{-1}$ respectively. These coupling loss values compare reasonably well with the simulated values of $\alpha_c = 3$ and $9\,\text{cm}^{-1}$, obtained by 3-D FDTD on the simplified disk structure.

The saturation effect at higher pumping levels was observed for all microdisk lasers, fabricated with this mask set. Obviously, it isn't reproduced by the simple laser model. Since no substantial red shift was noticed at these higher pumping levels, this effect neither can be explained by self heating. However, this phenomenon could be another indication for non-uniform injection, which we already suggested to be the causing the poor performance of 10-μm-diameter microdisks. As demonstrated in section 3.7.3, non-uniform injection can also result in such a saturation effect. However, rigorous 3-D electro-optical modeling might be required to gain more insight in this effect.

5.4 Full optical link on G2 samples

In the context of the PICMOS project, a full optical link consisting of heterogeneously integrated InP-based p-i-n detector and a microdisk laser, connected by an SOI wire waveguide, was developed. The basic layout of the implemented detector, which

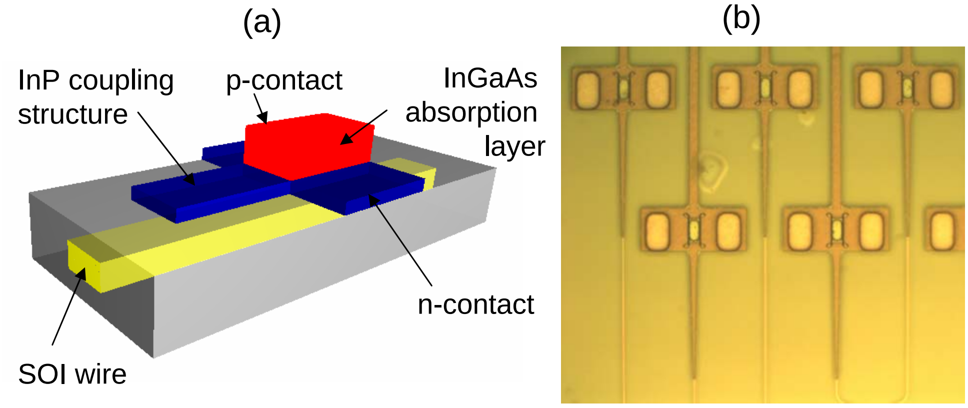

Figure 5.16: (a) Schematic layout of the heterogeneous SOI-integrated p-i-n detector, implemented in the full optical link. (b) Top-down microscope image of a fabricated detector before metallization . This device was developed by P. Binetti at Technical University Eindhoven.

was developed at Technical University Eindhoven, is shown in figure 5.16. It consists of an intrinsic InGaAs absorption layer embedded in a reversely biased p-i-n structure, with a total thickness of 1 μm. Evanescent coupling occurs between the SOI wire and a thin InP waveguide, which is butt-coupled to the detector itself. The n-type contacts are implemented as thin lateral bottom layers, whereas the p-contact covers the top of the detector mesa. Simulations indicate a theoretical responsivity at 1.55 μm of 0.85 A/W and a bandwidth of 25 GHz, for a $5 \times 10\,\mu\text{m}^2$ detector and a 15-μm-long InP coupling waveguide. However, substantial detection is also possible without the input InP waveguide. Responsivities up to 0.45 A/W have been measured for fabricated devices, with a dark current of a few nA at -5 V bias.

The fabrication of both integrated microdisk lasers and p-i-n detectors on a single SOI circuit required many processing steps carried out in four different clean rooms, limiting the yield of the process. Combined with the very low yield of the bonding process for detector epitaxial material and the sensitivity of the microdisk lasers to the dimension and alignment of the top contact, only a very small number of links with good potential for successful operation was available. On one of those links, we found a microdisk laser with CW operation.

To characterize the full link, two more probe needles were added to the measurement setup. For the measurements, the laser was injected in pulsed or continuous-wave regime, while the detector was always operated in CW regime. The detectors on the available full links exhibited a significant dark current when applying a reverse bias, most likely due to the presence of deep pits in the top surface of the detector, which were observed during processing. These pits were found during only some processing runs and their cause is unknown. To eliminate the effect of this excessive dark current, the measurements were performed at zero detector bias. Since the microdisk lasers emit in both directions of the output SOI waveguide, the laser

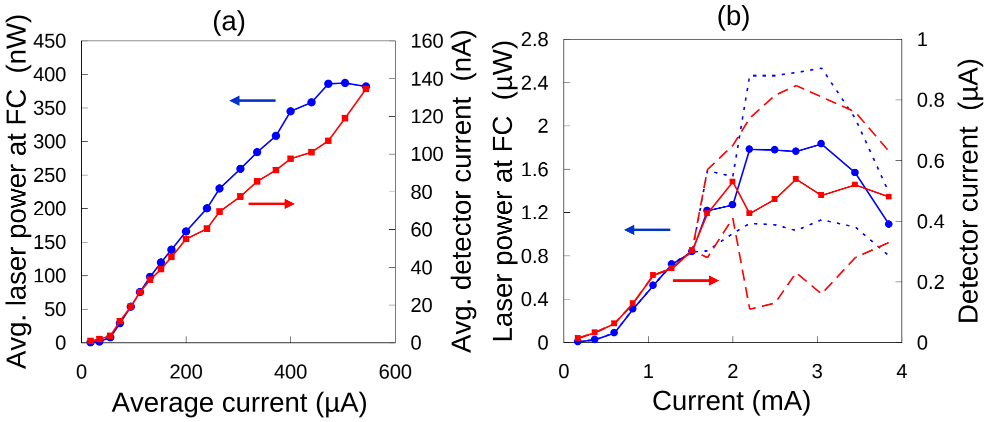

Figure 5.17: Measurement results of a complete optical link. (a) Average laser power detected at the fibre coupler (FC) and average detector current versus average laser current in pulsed regime. (b) Laser power at the fibre coupler and detector current versus laser current in CW regime. The detector current and output power at the FC are unstable versus time and pump level, varying between the dashed and dotted lines. The detector was not biased.

output was simultaneously monitored at the end of the SOI waveguide not leading to the detector, with a fibre coupler (FC).

The highlights of the measurements are shown in figure 5.17, for a link including a 1-μm-thick 7.5-μm-diameter microdisk laser, and a $5 \times 30\,\mu\text{m}^2$ detector without input InP waveguide coupler, connected through a 6-mm-long SOI waveguide. In (a), the pulsed measurement results are summarized, showing the average laser power detected at the fibre coupler and the average detector current versus the average laser current. The pulse period was 1 μs, and the pulse duration was 80 ns. The laser threshold current was about 0.69 mA, and the slope efficiency was approximately 1.8 μW/mA. As can be seen on graph (a), the detector current follows roughly the same trend as the detected power at the FC, with a clear kink in the curve at the laser threshold. Assuming that the same power arrives at the detector as at the fibre coupler results in an estimated detector responsivity of 0.33 ± 0.04 A/W.

In fig. 5.17 (b), the measurements under CW operation are shown. The threshold current is 0.6 mA and the slope efficiency was approximately 1.25 μW/mA. In this case, the interpretation of the experimental data was less straightforward. First, both the monitored output power at the FC and the detector current were found to be very unstable, both as function of time as as function of injected laser current. However, there was a clear correlation between them, such that a minimum power at the FC was associated with a maximum value for the detector current. This effect is visualized in fig. 5.17 (b) by the dashed and dotted lines. The solid lines represent an average value. This correlation is a clear indication for the mode competition between the clockwise and counterclockwise laser mode, each emitting dominantly in a single SOI wire direction. The second effect that makes characterization more

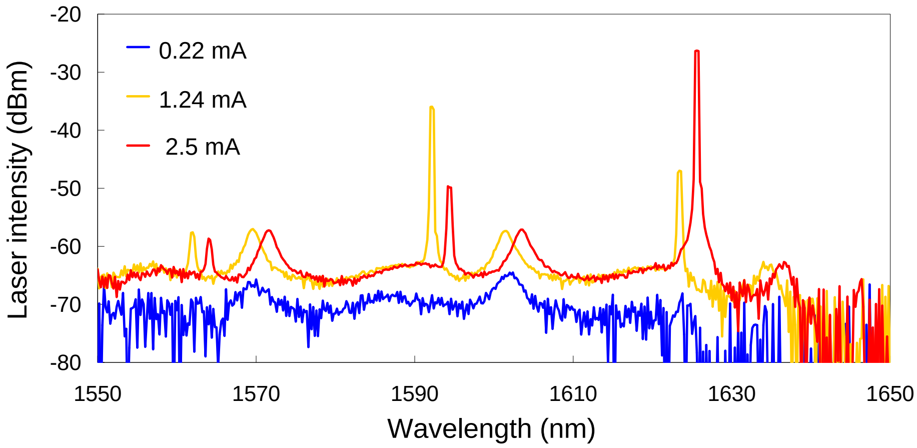

Figure 5.18: Laser spectrum for the microdisk laser implemented in the full optical link, under CW operation. The data was normalized for the FC efficiency and on-chip loss.

difficult is self heating. As shown in fig. 5.18, the microdisk laser exhibits two lasing modes, one at 1593 nm and another at 1624 nm. The first is dominant for currents smaller than 1.5 mA, while the latter is dominant for larger currents. Therefore, for determining the P-I curve, we assumed a FC efficiency of 0.25 for $I < 1.5\,\mathrm{mA}$ and 0.15 for $I > 1.5\,\mathrm{mA}$, obeying the gaussian coupling spectrum of the FC. Considering the average data, we extracted a detector efficiency $0.35 \pm 0.07\,\mathrm{W/A}$, which agrees well with the pulsed measurements.

While the extracted detector performance is within expectations, it should be noted that a fit to the lasing characteristics of the thin microdisk requires $\alpha_c = 1\,\mathrm{cm}^{-1}$, while an FDTD simulation based on a FIB cross section yields $\alpha_c = 11\,\mathrm{cm}^{-1}$. Clearly, the simple laser model fails to reproduce this sub-optimal laser performance, most likely as a result of non-uniform injection. Another explanation could be found in the presence of additional optical loss in the SOI waveguide, for instance due to non-optimal processing of the bottom InP contact layer.

5.5 Preliminary results from G3 samples

While the G3 samples arrived too late for a complete experimental characterization, some preliminary measurements were made, with the assistance of dr. Liu Liu. CW operation was found for 7.5 and 10-μm-diameter microdisk lasers. However, due to a thicker bonding layer as compared to G2, the output powers were generally lower than that of the best G2 lasers.

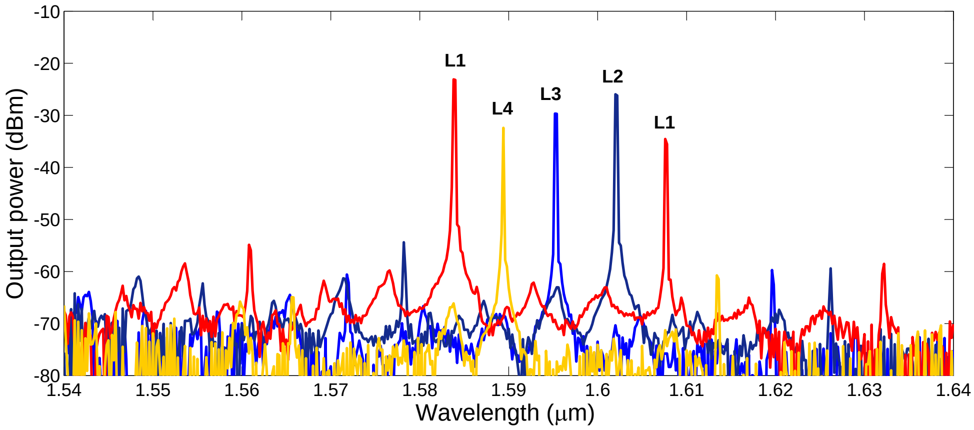

Figure 5.19: Laser spectra under CW operation (4.5 mA each) for 4 microdisk lasers coupled to a common SOI wire. The nominal disk diameters are 10, 10.044 μm, 10.088 μm and 10.132 μm for laser L4, L3, L2 and L1 respectively. The data was normalized for the FC efficiency. L1 is the laser closest to the fibre coupler used for extraction.

CWDM transmitters

CW lasing was found for a set of 4 microdisk lasers coupled to a common SOI wire, as shown in fig. C.3. The nominal disk diameters are 10, 10.044μm, 10.088μm and 10.132μm for laser L4, L3, L2 and L1 respectively. This set of diameters should theoretically result in 4 WDM channels, with uniform spectral distribution within the free spectral range of the 10-μm-diameter microdisk. The normalized spectra obtained by biasing each laser separately at 4.5 mA are superimposed in figure 5.19. However, biasing all lasers together results in a comparable output spectrum.

It can be seen that emission wavelengths are indeed nicely distributed within the free spectral range of a single microdisk. However, the uniformity of the output power is clearly not optimal yet, as the L4 signal – coming from the microdisk positioned the furthest away form the fibre coupler – is approximately 8 dB weaker than that of laser L1. This non-uniformity is believed to be due to optical loss through coupling to the higher-order modes of the other disks, which exhibit high disk-waveguide coupling and are very lossy. Reducing the microdisk thickness to suppress these modes appears to be the only solution to improve the output non-uniformity.

5.6 Conclusion

In this chapter, the highlights of the measurement results on integrated microdisk lasers were discussed, in a chronological order. First, the used measurement setups were discussed. Optically pumped measurements were mainly performed at INL, due to the availability of an advanced μPL setup. A simple μPL setup was built at

Ghent university as a tool to check for laser operation during processing of electrically injected lasers. Also, a setup was built for reliable pulsed electrical injection. Measurement results were presented both for uncoupled, Si-integrated microdisk lasers (G1) as for SOI-integrated microdisk lasers (G2).

G1 lasers only exhibited lasing in pulsed regime with high operating voltage (7-8 V), due to poor electrical tunnel-junction performance. Lasing was observed for microdisks with diameters in the range 6-10 μm. The measured threshold currents (0.55-1.1 mA) were consistent with the simple standard laser model from chapter 3. A thermal analysis revealed a thermal resistance of the order 10 K/mW. The thermal behavior was found to be in perfect agreement with simulations in chapter 3.

On several G2 microdisk lasers, lasing was observed in continuous-wave regime. This was possible due the a decrease in tunnel-junction resistance, and the associated decrease in dissipated power. Threshold currents were as low as 0.5 mA for 1-μm-thick 7.5-μm-diameter microdisk lasers, with up to 30 μW/mA coupled unidirectionally into the SOI wire. It was found that the lasing performance is very sensitive to misalignment and size of the top contact. Once again, the simple laser model could be fitted to the measured laser performance, using realistic values for the model parameters, consistent with simulation. However, the measured saturation in the output power couldn't be explained by the simple model. In CW regime, mode competition between the clockwise and counterclockwise laser mode resulted in unstable laser output in a single direction of the SOI waveguide. Also, for 10-μm-diameter microdisks, only pulsed lasing was observed, as well as for 0.5-μm-thick lasers (except for 1 device). We speculate that these effects are due to non-uniform current injection due to the non-cylindrosymmetric shape of the bottom contacts, and the fact that we have shown through simulations in chapter 3 that non-uniform injection can indeed result in a saturating laser output. However, fully 3-D electro-optical simulations should be performed to gain a better understanding of this phenomenon. Also, the processing scheme can be slightly adapted to yield more symmetrical bottom contacts.

Finally, some preliminary measurement results of a full optical link containing heterogenous microdisk lasers and p-i-n detectors, were presented. For one link, we found operation in continuous-wave regime, with a clear response in the detector current (up to 0.85 μA) when driving the microdisk laser.

Chapter 6

Conclusions and Outlook

6.1 Overview

The ever increasing computation power of modern electronic ICs is creating a need for low-power interconnections with high bandwidth density. However, electrical interconnects suffer from a physical, aspect-ratio limited bandwidth. Therefore, optical interconnections are increasingly being considered on all system levels to alleviate the interconnection bottleneck, typically when the 10 Mb/s×km bandwidth-distance product is reached. It is expected that through further dimensional scaling and parallelization in microelectronics, this transition threshold will also be reached for on-chip interconnections, within 15-20 years. Therefore, there is a growing research interest for intra-chip optical interconnects.

A major technological requirement for on-chip optical networks is CMOS compatibility. The fabrication of such networks should as much as possible be compatible with existing microelectronics processing infrastructure, in order to obtain a cost-effective solution that can be integrated with electronics. The basic CMOS material – silicon – is an excellent material to implement passive optical functions such as waveguiding and filtering. The nanophotonic silicon-on-insulator (SOI) waveguide platform enables a high photonic integration density. Unfortunately, light emission is very inefficient in silicon due to its indirect bandgap. While there is some encouraging progress being made on purely silicon-based light emitters, in a short-to-medium time frame, direct bandgap materials such as InP will need to be integrated for efficient on-chip light emission and amplification.

The goal of this work was to demonstrate an SOI-integrated microlaser, fabricated in a thin InP-based film on top of the SOI layer stack. Electrical injection was a prerequisite to allow for seamless photonic-electronic integration. A small footprint and low power consumption were required to enable a high integration density. Finally, the laser output was to be efficiently coupled into the on-chip SOI waveguide.

When designing a thin-film, electrically-injected microcavity laser, two main issues arise. First, the parasitic losses of the optical resonator should be kept as low as possible to ensure low threshold currents and high efficiencies. Second, efficient current injection should be possible, with low applied voltages. The latter typically requires the use of highly absorptive contact layers and metals, possibly in close proximity with the optical field, causing excessive optical absorption. As a result, a trade-off exists between obtaining low cavity loss and efficient current injection.

A structure with such a balanced trade-off was found in the form of a tunnel-junction-based microdisk laser. The tunnel junction enables the use of two ohmic n-type contacts, which are easily obtained without requiring absorptive contact layers. The microdisk resonator supports high-quality whispering-gallery modes, which are confined to the edges of the disk. As a result, a metal contact can be applied in the center of the disk without causing extra loss. A numerical analysis and optimization suggested that – at room temperature – such structures have the potential for SOI-coupled wall-plug efficiencies on the order of $10\,\%$, with a threshold current and slope efficiency of the order of $100\,\mu$A and $240\,\mu$W/mA respectively, for a microdisk with a diameter smaller than $5\,\mu$m. The operating voltages would remain under 2 V.

In the framework of a EU-funded research project, our project partners at CEA-LETI developed a molecular wafer-to-wafer and die-to-wafer bonding process, which enables heterogenous integration of a thin InP film on the SOI circuit. Microdisk lasers were fabricated using this technology and a combination a wafer-scale and die-based InP processing. However, in principle, all InP processing steps could be carried out on a wafer scale, enabling high through-put fabrication.

A first processing run yielded microdisk lasers integrated on a plain silicon wafer. Electrically-injected laser operation at room temperature was obtained for several devices, with diameters in the range $6 - 9\,\mu$m. Only pulsed operation was possible due to a high electrical resistance in combination with poor heat sinking, which resulted in excessive self heating. The high resistance was attributed to inadequate doping levels in the tunnel junction. Nevertheless, this was the first demonstration of an electrically-injected, silicon-integrated microlaser. The experimental thermal behavior was also found to be in good agreement with thermal simulations.

A second processing run involved the integration of microdisk lasers on the SOI waveguide platform. In order to reduce the electrical resistance, additional effort was paid to optimize the doping levels in the tunnel-junction layers. This tunnel-junction optimization was carried out by our project partners at INL. Several fabricated lasers exhibited electrically-injected lasing, with substantial optical coupling into the SOI waveguide. Furthermore, the operating voltages were found to be in the range 1.5-3 V. The threshold current was found to be strongly correlated to the size and position of the top contact. The best lasers featured threshold currents around $500\,\mu$A (microdisks with a diameter of 7.5μm). These lasers could be operated in continuous-wave regime at room temperature, with up to $20\,\mu$W/mA CW power coupled unidirectionally into the SOI waveguide. To our knowledge, this was the first demonstration of an electrically-driven microlaser, integrated on and coupled to a SOI waveguide circuit. The performance of the best performing lasers was in agreement with the theoretical laser model, using realistic parameter values, except for the measured saturation in the output power at higher pumping levels.

6.2 Conclusion

Heterogeneous integration of InP on SOI enables the implementation of ultra-compact, integrated, electrically-injected microlasers. The output power can be efficiently coupled to the passive waveguide circuit. By optimizing the structural parameters, these ultra-compact integrated lasers can theoretically reach an efficiency and modulation bandwidth comparable to those of conventional InP-based laser diodes, however with a strongly reduced threshold current.

While the theoretical performance at room temperature appears to be good enough to consider these devices as on-chip light sources for intra-chip optical interconnect, it should be noted that the performance will be strongly affected by the high on-chip temperature, as would be the case for any InP-based laser diode operating at that temperature. Therefore, we believe that the potential use of integrated laser diodes for on-chip interconnect mainly depends on the success of enhancing the high-temperature properties of the gain material (e.g. optimizing barrier heights and strain levels of the quantum wells).

For applications at room temperature, the integrated microdisk laser could be a key component for many systems. Coupling several lasers through a common waveguide can yield low-power ultra-fast optical flip-flops, as was demonstrated for ring lasers on an InP substrate. Such memory elements are an important building block for digital optical signal processing. High-capacity WDM transmitters could be developed by coupling several microdisk lasers – each emitting at a different wavelength by having slightly different diameters – to a common waveguide. These transmitters could also be used for inter-chip interconnect, provided that the output power can be increased, which requires adequate heat sinking structures to avoid self heating.

On a general note, the heterogeneous InP-SOI platform shows great promise to implement both high-density active-passive optical integration as well as intimate electronic-photonic integration.

6.3 Recommendations

Improvement is possible on several fronts:

- On the **fabrication** side, many issues still exist. The yield of the bonding process was typically lower than 50 %, leaving plenty of room for improvement. Also, the reproducibility and uniformity of the bonding layer thickness should be improved considerably, as the coupling strength is highly sensitive to this thickness. Another yield-limiting factor is the lithography of the top via. The alignment accuracy of 0.5 μm that can be obtained with contact lithography isn't sufficient. Logically, the next step would be to use wafer-scale DUV-lithography also for the processing of the microdisk, as this tool typically has 50 nm alignment accuracy. Better aligned top vias would also allow to use a TiPtAu-metallization for the top contact, and a conventional alloying temperature. It is expected that such devices wouldn't require a burn-in treatment.

Finally, the dry etching process should be optimized for low surface roughness. These technological improvements are required to obtain the optimized microdisk lasing structure.

- Concerning the general **laser design**, the ultra-thin microdisk laser design as proposed in chapter 3.11 could be further explored, in order to obtain devices that are less sensitive to the bonding layer thickness. Additionally, post-injected photonic-crystal cavities could be considered, to achieve the ultimate mode confinement and to unleash the benefits associated with the Purcell effect.

- On the **modeling** side, a fully 3-D model – with coupled electro-optical equations – should be implemented to gain more insight in the current flow in the disk at different bias levels. Such calculations could reveal the origin of the output power saturation for measured microdisk lasers.

- When a high-yield and reproducible process is available, **advanced functionality** such as flip-flop operation and WDM transmitters can be evaluated. A first step toward this goal was already taken at the end of this work. Samples from the third processing run contain such coupled lasers and are ready to be measured. Additionally, the microdisk laser dynamics should be evaluated experimentally.

Appendix A

DBR microlaser modeling

DBR microlaser layout

The layout of the Distributed-Bragg-Reflector (DBR) microlaser is shown in figure A.1. It consists of a ridge waveguide with length L and width W, etched in the InP-based film, and is terminated by fully-etched DBR mirrors. The DBR period is a and the filling factor is FF. The laser mode is evanescently coupled to an underlying SOI waveguide, with the same width as the InP ridge. The bonding layer thickness is t_{ox}. The top contact covers the complete ridge waveguide (but not the DBR mirrors).

The lasing performance of such a structure was estimated by performing a 2-D eigenmode expansion analysis, in the xz-plane. Such an analysis obviously gives optimistic results, as the optical radiation loss in the y-direction is not taken into account. However, for large W ($> 5\,\mu$m), this loss can be neglected, as indicated by 2-D simulations in the xy-plane.

Internal loss

The internal loss was calculated for 1-D slab waveguides, for various epitaxial layer compositions. The active layer is assumed to be consisting of four 5-nm-wide QWs embedded in 20-nm barrier layers. Designs with TJ-based injection schemes for the top of bottom contact were compared with designs with 15-nm-thick ternary contact layers (similar analysis as for the microdisk laser in section 3.4). For each of the designs, the thicknesses of the OCLs were optimized to achieve the lowest internal loss α_{int} for the fundamental TE$_0$-mode (**E**-field parallel to y-axis), as function of total thickness t. The layer structure and the to-be-optimized thicknesses for the case of the TJ-based top contact is shown in figure A.2 (b). The results are shown in figure A.2 (a). All loss values include absorption loss at the Au top contact, except for the simulation results indicated by the triangles, which involve a TJ-based top contact with TiPtAu (4/10/200 nm) metallization. As can be seen, for $t < 1\,\mu$m, the TJ-based top contact outperforms all other designs. For larger thicknesses, the internal losses of the different designs converge, except for the ternary-based bottom contact, which has significantly higher loss.

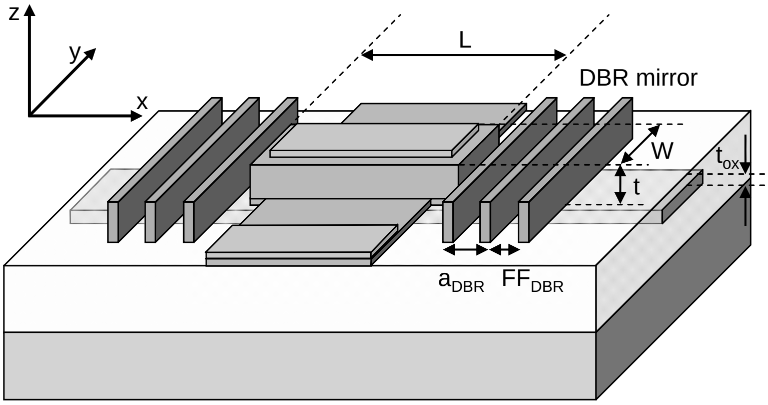
z
y
x
L
DBR mirror
W
t_ox
t
a_DBR
FF_DBR

Figure A.1: Schematic drawing of the SOI-coupled DBR-microlaser.

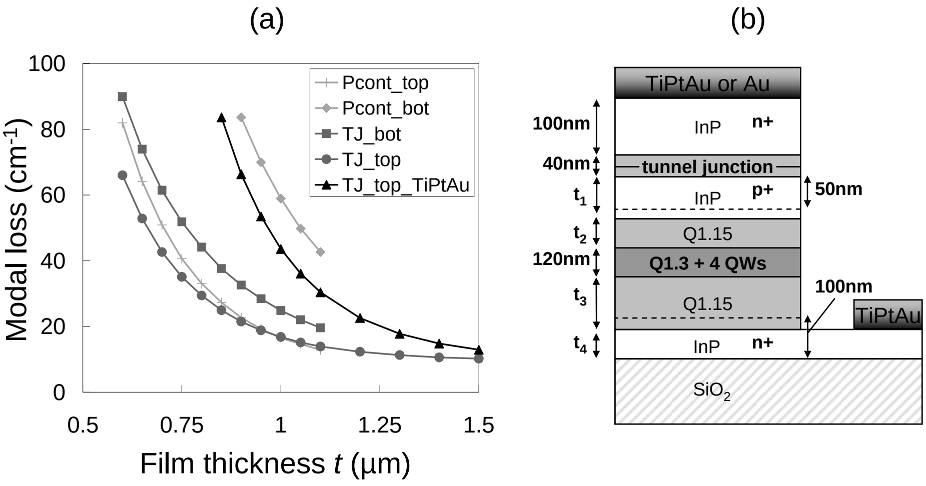

Figure A.2: (a) Internal loss α_{int} of the fundamental TE$_0$-mode at $1.5\ \mu$m versus film thickness t, for various epitaxial designs. (b) Epitaxial layer design for structure with TJ-based top contact.

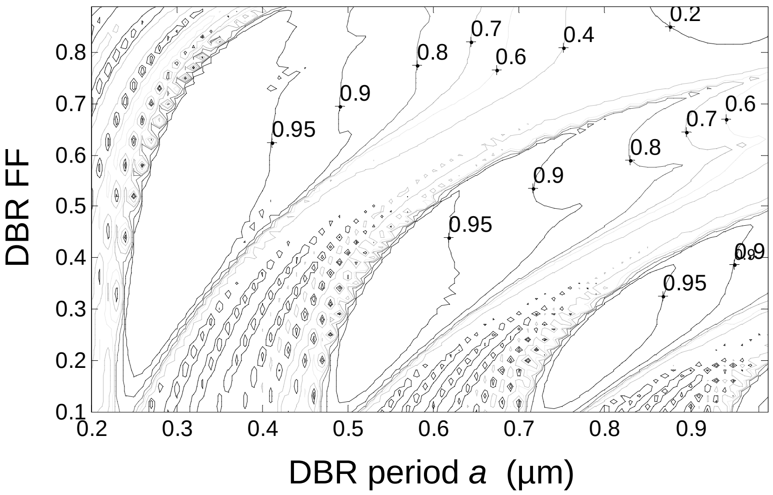

Figure A.3: DBR mirror reflectivity of the fundamental TE_0-mode at $1.5\,\mu$m, for $t = 1\,\mu$m versus DBR period a and filling factor FF (for 8 DBR periods).

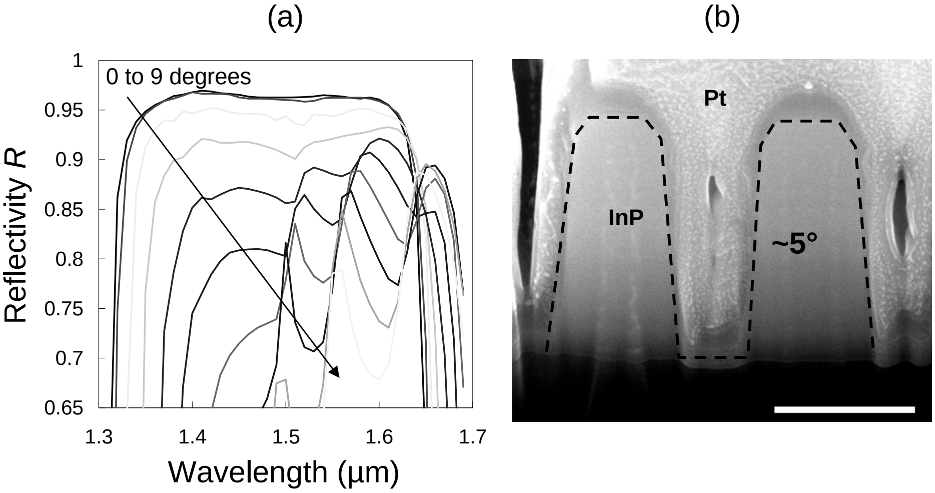

Figure A.4: (a) DBR mirror reflectivity spectrum versus sidewall angle. (b) FIB cross section of RIE-etched DBR structure.

DBR mirror reflectivity

We have calculated the DBR mirror reflectivity of the fundamental TE_0-mode for $t = 1\,\mu$m versus DBR period a and filling factor FF, defined as the ratio of the slit width to the period. The results are shown in fig. A.3. For these calculations, it was assumed that the QWs are not pumped and therefore exhibit a material absorption loss of $10^4\,\mathrm{cm}^{-1}$. The DBR slits were assumed to be filled with air, and the mirror contains 8 slits. However, a BCB-filled DBR exhibits similar performance, albeit at adjusted DBR parameters.

As can be seen from fig. A.3, the highest reflectivities can be found for a first-order DBR mirror, around a period $a = 0.3\,\mu$m and filling factor $FF = 0.5$. However, to relax the etching requirements somewhat, further calculations involve second-order DBR mirrors, with parameters around $a = 0.55\,\mu$m and $FF = 0.33$ and a reflectivity around $96\,\%$.

The above calculations all assume DBR slit sidewalls that are perfectly vertical. The impact of non-vertical sidewall slopes on the DBR reflectivity was estimated by performing eigenmode-expansion calculations on a sliced DBR structure with tilted sidewalls. The resulting reflection spectra for $t = 1\,\mu$m, and $a = 0.55\,\mu$m, $FF = 0.33$ are shown in fig. A.4 (a). It can be seen that the maximum reflectivity drops quickly with increasing sidewall tilt (defined with respect to the z-axis). At the same time, the reflection spectrum features a strong wavelength-dependent behavior within the (decreasing) reflection window, most likely due to multi-mode interference with higher-order modes.

For 1-μm-deep DBR mirrors etched with the standard RIE process using a SiO_2 hard mask, the obtained sidewall angle is about 5 degrees. For this value, a theoretical reflectivity of 0.85-0.9 is to be expected. However, sidewall roughness is expected to further reduce the experimental reflectivity.

Laser performance

With the waveguide and DBR mirror in place, we proceeded with analyzing the complete cavity, for perfectly vertical DBR slits. The fundamental resonant modes were calculated for DBR microlasers including an evanescently coupled SOI waveguide, as a function of cavity length L. These calculations directly yield the material gain lasing threshold G_{th} and the extraction efficiency η_e. For each cavity length, the lasing mode with resonant wavelength closest to $1.5\,\mu$m was considered.

The simulation results for an optimized 0.75-μm-thick laser structure with a TJ-based top contact with pure Au metallization, BCB-filled DBR mirrors with $a = 0.57\,\mu$m and $FF = 0.33$, and $t_{ox} = 200\,$nm, are shown in fig. A.5. The G_{th} values show a generally decreasing trend with increasing L due to a reducing distributed DBR mirror loss. However, a clear modulation on G_{th} with a period of roughly 5.4 μm is apparent, on top of sharp spikes with a period of about 1.2 μm. The former modulation period is very close to the evanescent coupling length $L_c = 5.32\,\mu$m that was deduced by calculating the supermodes of the SOI-InP waveguide, and using the formula

$$L_c = \frac{\pi}{\beta_1 - \beta_2}, \tag{A.1}$$

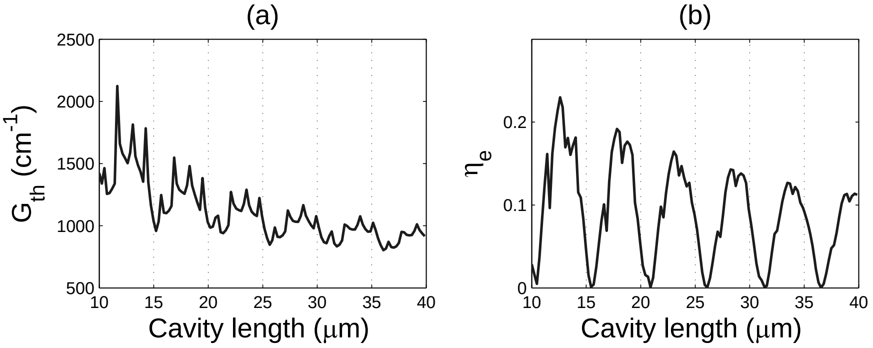

Figure A.5: Simulation results for a 0.75-μm-thick DBR microlaser with Au top contact and $t_{ox} = 200\,\text{nm}$, as function of the cavity length L. (a) Material threshold gain G_{th}. (b) Extraction efficiency η_e.

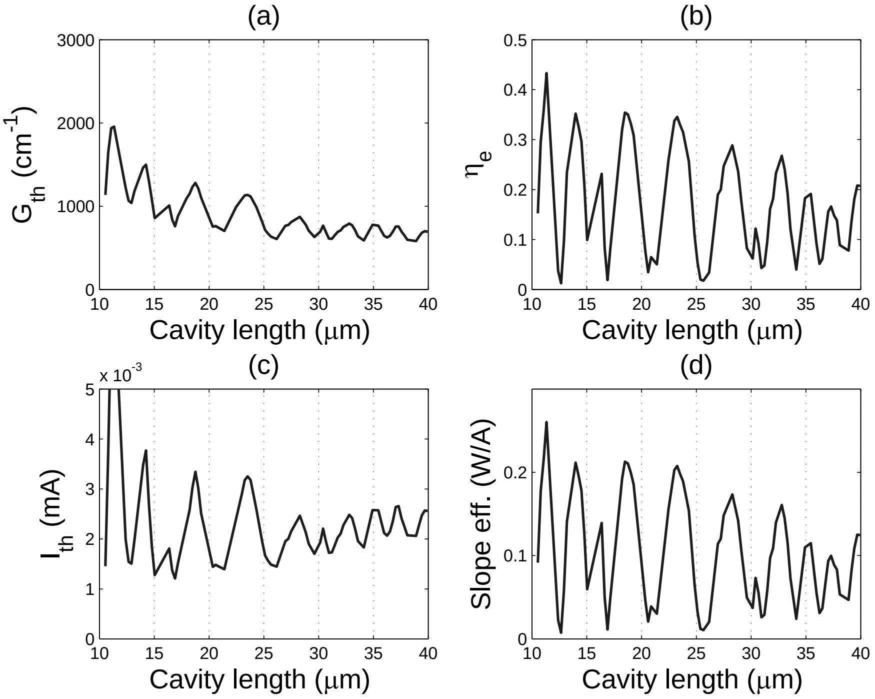

Figure A.6: Simulation results for a 1.5-μm-thick DBR microlaser with TiPtAu top contact and $t_{ox} = 150\,\text{nm}$, as function of the cavity length L. (a) Material threshold gain G_{th}. (b) Extraction efficiency η_e. (c) Threshold current I_{th}, assuming $W = 5\,\mu\text{m}$. (d) Slope efficiency.

where $\beta_{1,2}$ are the propagation constants of the fundamental supermodes. This modulation is also clearly apparent for η_e. The spikes with smaller period were identified as multi-mode interference effects between the fundamental and higher-order InP-confined modes.

The simulation results for an optimized 1.5-μm-thick laser structure with a TJ-based top contact with TiPtAu metallization, BCB-filled DBR mirrors with $a = 0.57\,\mu$m and $FF = 0.33$, and $t_{ox} = 150\,$nm, are shown in fig. A.6. In this case the identification of the spikes in the G_{th} and η_e-curves is less straightforward, due to the higher number of waveguide modes as a result of the increased film thickness. In this case, we also calculated the theoretical laser threshold – assuming $W = 5\,\mu$m not to induce additional mirror loss – and the slope efficiency. The results are shown in fig. A.6 (c) and (d). Threshold currents are in the range 1.5-3.5 mA, for associated slope efficiencies in the range 0-0.21 W/A, for cavity lengths L is in the range 15-35μm.

A E_y-field plot of the resonant mode for the 1.5-μm-thick laser is shown in fig. A.7, with (a) showing the real part and (b) the imaginary part. Due to the specific normalization in CAMFR, (a) shows the field when the laser-mode standing wave is at its maximum, while (b) shows the field when it is at its minimum. Therefore, the field contribution in (b) belongs to leaking light, and thus gives a visual indication of the cavity losses. It should be noted that the scale in (a) and (b) are different.

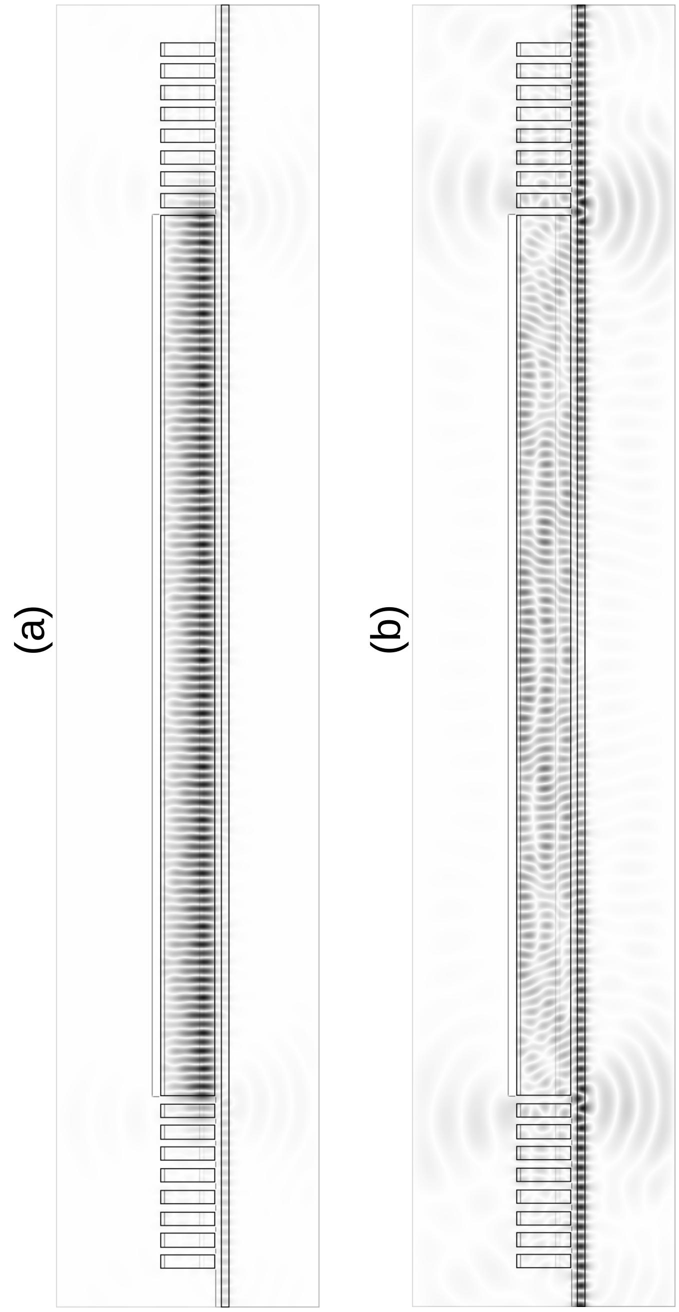

Figure A.7: Mode plot of the E_y laser field for the 1.5-μm-thick DBR microlaser with $t_{ox} = 100\,\text{nm}$, with the real part plotted in (a) and the imaginary part plotted in (b).

Appendix B

Radially-dependent rate equations: calculation details

To solve the radially-dependent rate equations in (3.27) for a given the total current I, the calculation procedure as depicted in fig. B.1 was used. The scheme starts with setting initial guesses for the photon density $S = 0$ and the carrier profile $N(r) \equiv N_0 = 2 \times 10^{18}\,\mathrm{cm}^{-3}$. An iterative loop – with index i – is then initiated, starting with calculating an updated carrier profile $N(r)$ associated with the input photon density $S[i]$, using MATLABs boundary-value solver `bvp4c`, obeying the boundary conditions (3.27). From $N(r)$, an updated photon density S_{new} is derived, using

$$S_{new} = \frac{-b - \sqrt{b^2 - 4ac}}{2a}, \tag{B.1}$$

with

$$\begin{aligned} a &= -\frac{\epsilon}{\tau_p}\Gamma \qquad \text{(B.2)} \\ b &= \frac{1}{\tau_p} + \epsilon\Gamma\beta\int_0^R BN^2(r)\Psi^2(r)2\pi r dr + \int_0^R G\left[N(r)\right]\Psi^2(r)2\pi r dr \\ c &= \beta\int_0^R BN^2(r)\Psi^2(r)2\pi r dr. \end{aligned}$$

As long as the absolute value of the error $|e[i]| = |S_{new} - S[i]|$ exceeds the required tolerance or the maximum number of iterations hasn't been reached, the iterative loop is repeated, with an updated input photon density $S[i+1]$:

$$S[i+1] = S[i] - \frac{1}{4}e[i]\frac{S[i-1] - S[i]}{e[i-1] - e[i]}. \tag{B.3}$$

When the required precision or the maximum allowed number of iterations is reached, the calculated S and $N(r)$ values are returned. Typically, we required the relative error $e[i]/S[i]$ to be smaller than 1%.

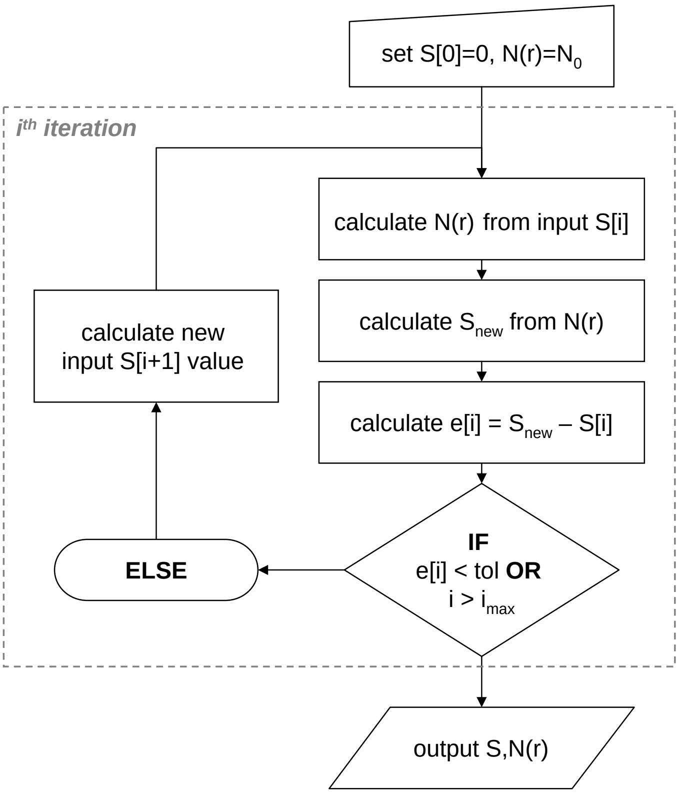
set S[0]=0, N(r)=N_0
i^{th} iteration
calculate N(r) from input S[i]
calculate S_{new} from N(r)
calculate e[i] = S_{new} – S[i]
IF
e[i] < tol OR
i > i_{max}
ELSE
calculate new input S[i+1] value
output S,N(r)

Figure B.1: Calculation flowchart used for solving radially-dependent, static rate equations.

Appendix C

Mask layouts

Here, we give further information on the mask design for the G2 microdisk lasers and the full link, as well as for the latest G3 microdisk lasers. An overview of the G2 cell is shown in figure C.1. Both the SOI- as InP-related mask levels are shown.

This cell was designed with the goal of demonstrating a full optical link on SOI, and therefore includes both microlasers and microdetectors, as is also illustrated in fig. 4.2 (a). The position of the respective epitaxial dies is indicated by the gray rectangles. The bonded laser die contains 256 microlasers, clustered in groups of 8 at the top part of the cell. The left part contains 128 microdisk lasers whereas the right part contains 128 DBR microlasers. Within each group, the microdisk laser design parameters are identical, except for the size of the top contact. Almost every laser on the cell is coupled to an underlying SOI waveguide. One branch of the waveguide is terminated on a fibre grating coupler, which are located in arrays at the left and right edge of the cell. The other branch leads toward a microdetector at the bottom of the cell. In the center of the cell, the SOI wires are tapered to 3-μm-wide multimode SOI waveguides, which can be used for coupling light by the end-fire method, provided that the die is cleaved.

A mask detail of the G2 microdisk lasers is shown in figure C.2. In (a), a group of 8 microdisk lasers is shown, including the metal contact pads used for probing and the underlying SOI wires. In (b), the mask layout of the laser with the best experimental performance is shown, illustrating the size and position of the contact vias and metallization, the bottom contact layer, and the underlying SOI wire. Note that the bottom contact via doesn't cover the SOI wire region, in order to avoid absorption of the SOI-coupled laser output.

In fig. C.3, some details of the G3 microdisk lasers are shown. In (a), a group of 4 microdisk lasers with slightly different radii ($\Delta R = 16\,\text{nm}$) – coupled to a common SOI waveguide – is shown. The goal of this laser array is to demonstrate an on-chip, coarse-WDM transmitter. They also contain a thermal via at the top contact, with the goal of reducing the thermal resistance. In (b), two nominally identical microdisk lasers are coupled to a common SOI wire. This structure can be used to explore the flip-flop operation capacity, analogous to the coupled microring lasers on an InP substrate in [37].

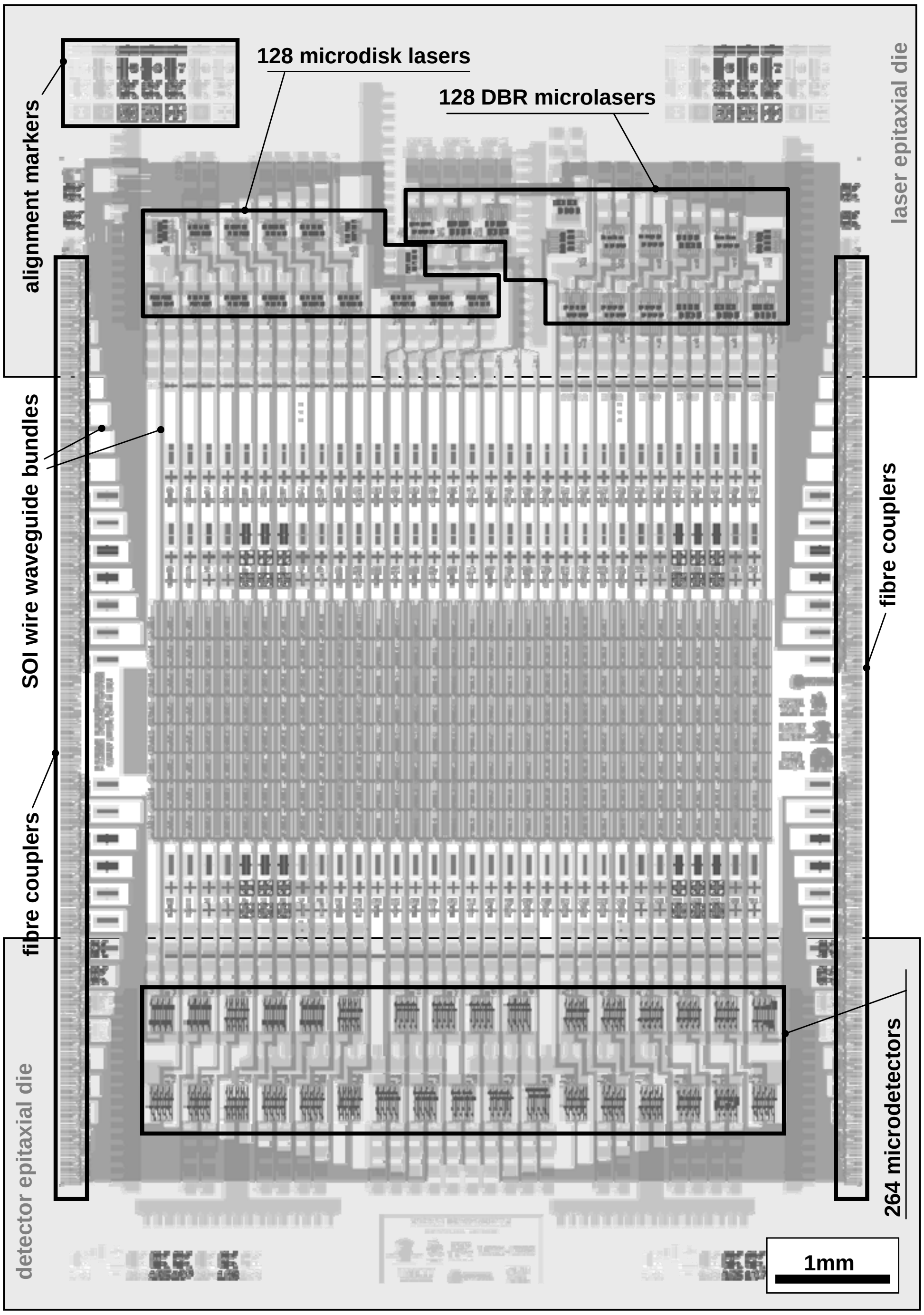
128 microdisk lasers
128 DBR microlasers
laser epitaxial die
alignment markers
SOI wire waveguide bundles
fibre couplers
fibre couplers
detector epitaxial die
264 microdetectors
1mm

Figure C.1: Mask layout of G2 microdisk lasers and microdetectors.

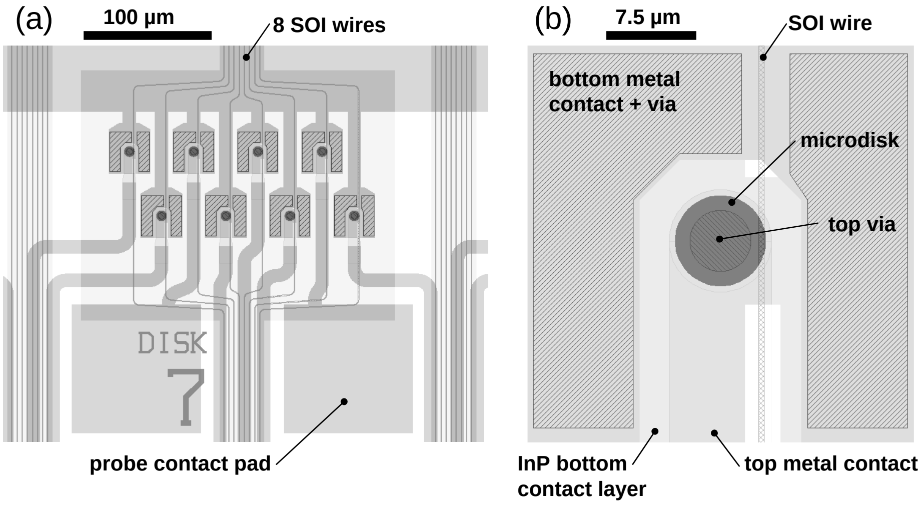
(a)
100 µm
8 SOI wires
DISK
7
probe contact pad
(b)
7.5 µm
SOI wire
bottom metal contact + via
microdisk
top via
InP bottom contact layer
top metal contact

Figure C.2: Mask layout detail of G2 microdisk lasers.

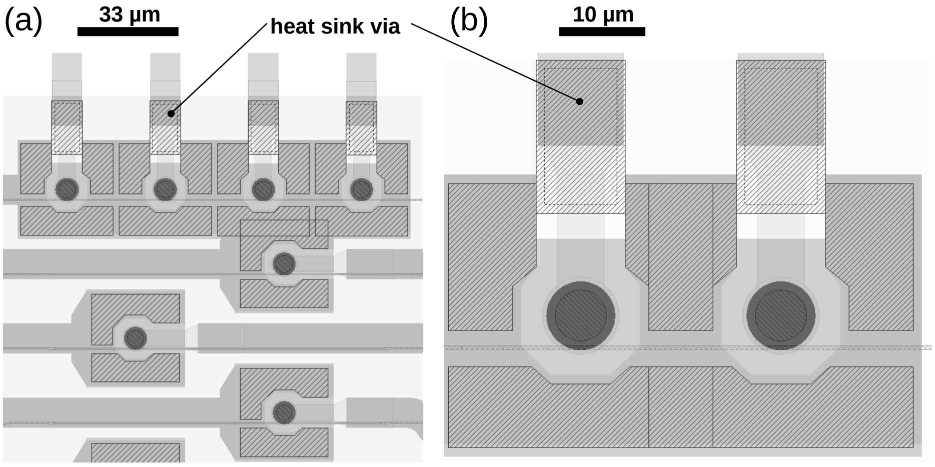
(a)
33 µm
heat sink via
(b)
10 µm

Figure C.3: Mask layout details of G3 microdisk lasers.

Appendix D

Publications and awards

D.1 International Journals

1. **J. Van Campenhout**, P. Rojo-Romeo, D. Van Thourhout, C. Seassal, P. Regreny, L. Di Cioccio, J. M. Fedeli, and R. Baets. Design and Optimization of Electrically Injected InP-based Microdisk Lasers Integrated on and Coupled to a SOI Waveguide Circuit. *Journal of Lightwave Technology*, to be published.

2. **J. Van Campenhout**, P. Rojo-Romeo, D. Van Thourhout, C. Seassal, P. Regreny, L. Di Cioccio, J. M. Fedeli, C. Lagahe, and R. Baets. Electrically pumped InP-based microdisk lasers integrated with a nanophotonic silicon-on-insulator waveguide circuit. *Optics Express*, 15(11):6744–6749, 2007.

3. **J. Van Campenhout**, P. Rojo-Romeo, D. Van Thourhout, C. Seassal, P. Regreny, L. Di Cioccio, J. M. Fedeli, and R. Baets. Thermal characterization of electrically injected thin-film InGaAsP microdisk lasers on Si. *Journal of Lightwave Technology*, 25(6):1543–1548, 2007.

4. G. Roelkens, **J. Van Campenhout**, J. Brouckaert, D. Van Thourhout, R. Baets, P. Rojo Romeo, P. Regreny, A. Kazmierczak, C. Seassal, X. Letartre, G. Hollinger, J.M. Fedeli, L. Di Cioccio, C. Lagahe-Blanchard, A die-to-wafer bonding approach to photonic integration on a silicon platform (invited), *Materials Today*, 10(7-8):36–43, 2007.

5. I. O'Connor, F. Tissafi-Drissi, F. Gaffiot, J. Dambre, M. De Wilde, J. Van Campenhout, D. Van Thourhout, **J. Van Campenhout**, and D. Stroobandt. Systematic simulation-based predictive synthesis of integrated optical interconnect. *IEEE Transactions on Very Large Scale Integration (VLSI) Systems*, 15(8):927–940, 2007.

6. P. R. Romeo, **J. Van Campenhout**, P. Regreny, A. Kazmierczak, C. Seassal, X. Letartre, G. Hollinger, D. Van Thourhout, R. Baets, M. Fedeli, and L. Di Cioccio. Heterogeneous integration of electrically driven microdisk based laser sources for optical interconnects and photonic ICs. *Optics Express*, 14(9):3864–3871, 2006.

7. **J. Van Campenhout**, P. Bienstman, and R. Baets. Band-edge lasing in gold-clad photonic-crystal membranes. *IEEE Journal on Selected Areas in Communications*, 23(7):1418–1423, 2005.

8. W. Bogaerts, R. Baets, P. Dumon, V. Wiaux, S. Beckx, D. Taillaert, B. Luyssaert, **J. Van Campenhout**, P. Bienstman, and D. Van Thourhout. Nanophotonic waveguides in silicon-on-insulator fabricated with CMOS technology. *Journal of Lightwave Technology*, 23(1):401–412, 2005.

9. W. Bogaerts, P. Dumon, D. Taillaert, V. Wiaux, S. Beckx, B. Luyssaert, **J. Van Campenhout**, D. Van Thourhout, R. Baets, SOI Nanophotonic Waveguide Structures Fabricated with Deep UV Lithography (invited), *Photonics and Nanostructures: Fundamentals and Applications*, 2(2):81–86, 2004.

10. P. Dumon, W. Bogaerts, V. Wiaux, J. Wouters, S. Beckx, **J. Van Campenhout**, D. Taillaert, B. Luyssaert, P. Bienstman, D. Van Thourhout, R. Baets, Low-loss SOI Photonic Wires and Ring Resonators Fabricated with Deep UV Lithography, *IEEE Photonics Technology Letters*, 16(5):1328–1330, 2004.

11. W. Bogaerts, D. Taillaert, B. Luyssaert, P. Dumon, **J. Van Campenhout**, P. Bienstman, D. Van Thourhout, R. Baets, V. Wiaux, S. Beckx, Basic structures for photonic integrated circuits in Silicon-on-insulator (invited), *Optics Express*, 12(8):1583–1591, 2004.

D.2 International Conference Proceedings

12. **J. Van Campenhout**, P. Rojo Romeo, P. Regreny, C. Seassal, D. Van Thourhout, L. Di Cioccio, L. Lagahe, J.-M. Fedeli, R. Baets, Electrically injected InP microdisk lasers integrated with nanophotonic SOI circuits (invited), *Photonics West 2008*, San Jose, California, United States, to be published.

13. **J. Van Campenhout**, P. Rojo Romeo, P. Regreny, C. Seassal, D. Van Thourhout, L. Di Cioccio, J. M. Fedeli, R. Baets, Optimization of Electrically Pumped Microdisk Lasers Integrated with a Nanophotonic SOI Waveguide Circuit, *IPNRA 2007*, Salt Lake City, United States, p. 35, July 2007.

14. **J. Van Campenhout**, P. Rojo Romeo, P. Regreny, C. Seassal, D. Van Thourhout, L. Di Cioccio, J. M. Fedeli, R. Baets, Electrically Pumped InP-based Microdisk Lasers Integrated with a Nanophotonic SOI Waveguide Circuit, *OFC 2007*, United States, PDP p. 35, Apr. 2007.

15. **J. Van Campenhout**, P. Rojo-Romeo, D. Van Thourhout, C. Seassal, P. Regreny, L. Di Cioccio, J.M. Fedeli, R. Baets, ”Electrically injected thin-film InGaAsP microdisk lasers integrated on a Si-wafer, *Annual Symposium of the IEEE/LEOS Benelux Chapter*, Eindhoven, Netherlands, pp. 29-32, Nov. 2006.

16. **J. Van Campenhout**, P. Rojo-Romeo, D. Van Thourhout, C. Seassal, P. Regreny, L. Di Cioccio, J. M. Fedeli, R. Baets, Electrically Injected InGaAsP Microdisk

Lasers Heterogeneously Integrated on a Si-wafer, *International Semiconductor Laser Conference*, Big Island of Hawaii, United States, pp. 133-134, Sep. 2006

17. P. Rojo-Romeo, **J. Van Campenhout**, P. Regreny, F. Mandorlo, C. Seassal, X. Letartre, G. Hollinger, D. Van Thourhout, R. Baets, J.M. Fedeli, L. Di Cioccio, InP on silicon electrically driven microdisk lasers for photonic ICs, *International Conference on Indium Phosphide and Related Materials*, May 2006.
18. D. Van Thourhout, W. Bogaerts, P. Dumon, G. Roelkens, **J. Van Campenhout**, R. Baets, Functional Silicon Wire Waveguides, *Integrated Photonics Research and Application, Nanophotonics, OSA Topical Meetings*, Uncasville, United States, p. IWA6, Apr. 2006.
19. D. Van Thourhout, G. Roelkens, **J. Van Campenhout**, J. Brouckaert, R. Baets, Technologies for on-chip optical interconnects, *18th Annual meeting IEEE/LEOS*, Sydney, Australia, p. TuE2, Nov. 2005.
20. **J. Van Campenhout**, P. Rojo-Romeo, D. Van Thourhout, C. Seassal, P. Regreny, L. Di Cioccio, J.M. Fedeli, R. Baets, An electrically driven membrane microdisk laser for the integration of photonic and electronic ICs, *18th Annual meeting IEEE/LEOS*, Sydney, Australia, p. PD1.7, Oct. 2005.
21. **J. Van Campenhout**, P. Bienstman, D. Van Thourhout, R. Baets, Membrane-type DBR-microlasers for the integration of electronic and photonic ICs, *Workshop on Photonic and Electromagnetic Crystal Structures (PECS-VI)*, Crete, Greece, p. 32, Jun. 2005.
22. **J. Van Campenhout**, P. Bienstman, R. Baets, Membrane-type photonic-crystal microlasers for the integration of electronic and photonic ICs, *IEEE/LEOS BENELUX Chapter - Annual Symposium*, Ghent, Belgium, pp. 279-282, Dec. 2004.
23. R. Baets, W. Bogaerts, P. Dumon, G. Roelkens, I. Christiaens, K. De Mesel, D. Taillaert, B. Luyssaert, **J. Van Campenhout**, P. Bienstman, D. Van Thourhout, Wiaux, Vincent, Wouters, Johan, Beckx, Stefan, Integration of photonic functions in and with Silicon (invited), *ESSDERC/ESSCIRC*, Leuven, Belgium, Sep. 2004.
24. P. Dumon, W. Bogaerts, **J. Van Campenhout**, V. Wiaux, J. Wouters, S. Beckx, R. Baets, Low-loss photonic wires and compact ring resonators in Silicon-on-insulator, *SPIE International Symposium Photonics Europe*, Strasbourg, France, Apr. 2004.
25. **J. Van Campenhout**, P. Bienstman, R. Baets, Band edge lasing in metal-clad multimode photonic crystal slabs, *Photonic and Electromagnetic Crystal Structures (PECS-V)*, Kyoto, Japan, p. 233, Mar. 2004.
26. P. Dumon, W. Bogaerts, **J. Van Campenhout**, V. Wiaux, J. Wouters, S. Beckx, R. Baets, Low-loss photonic wires and compact ring resonators in silicon-on-insulator, *LEOS Benelux Annual Symposium*, Enschede, Netherlands, Nov. 2003.

27. P. Dumon, W. Bogaerts, **J. Van Campenhout**, V. Wiaux, J. Wouters, S. Beckx, R. Baets, ”Low-loss, single-mode photonic wires ring resonators in Silicon-on-Insulator”, LEOS 2003, vol. 1, Tuscon, United States, pp. 289-299, Oct. 2003.

28. W. Bogaerts, P. Dumon, **J. Van Campenhout**, V. Wiaux, J. Wouters, S. Beckx, D. Taillaert, B. Luyssaert, D. Van Thourhout, R. Baets, Deep UV Lithography for Planar Photonic Crystal Structures (invited), *LEOS 2003*, vol. 2, Tuscon, United States, pp. 754-755, Oct. 2003.

29. W. Bogaerts, V. Wiaux, P. Dumon, D. Taillaert, J. Wouters, S. Beckx, **J. Van Campenhout**, B. Luyssaert, D. Van Thourhout, R. Baets, Large-scale production techniques for photonic nanostructures (invited), *SPIE*, San Diego, United States, pp. 101-112, Aug. 2003.

D.3 National Conference Proceedings

30. **J. Van Campenhout**, D. Van Thourhout, P. Bienstman, C. Seassal, P. Rojo-Romeo, L. Di Cioccio, J.M. Fedeli, Membrane microlasers for the integration of photonic and electronic ICs, 6th UGent-FirW PhD Symposium, Ghent, Belgium, p.39 (paper nr. 29), 2005.

31. W. Bogaerts, P. Dumon, V. Wiaux, J. Wouters, S. Beckx, D. Taillaert, B. Luyssaert, **J. Van Campenhout**, D. Van Thourhout, R. Baets, Nanophotonic waveguides in Silicon-on-Insulator Fabricated with CMOS Technology, 1st UGent FTW PhD Symposium, Ghent, Belgium, p.63, 2003.

32. W. Bogaerts, P. Dumon, V. Wiaux, J. Wouters, S. Beckx, D. Taillaert, B. Luyssaert, **J. Van Campenhout**, D. Van Thourhout, R. Baets, Nanophotonic waveguides in Silicon-on-Insulator Fabricated with CMOS Technology, 4th UGent FTW PhD Symposium, Ghent, Belgium, p.56, 2003.

33. **J. Van Campenhout**, W. Bogaerts, D. Taillaert, R. Baets, Compact photonic-crystal waveguides in Silicon-on-Insulator: design and experimental verification, LEOS Benelux Photonic Crystal Workshop, Ghent, Belgium, 2002.

D.4 Awards

- Third prize presentation award, 6th FirW PhD symposium, Ghent University, Belgium, 2005
- IEEE-LEOS Graduate Student Fellowship, USA, 2007

Figures

4 (a) Schematic representation of the SOI-integrated microdisk laser. (b) Whispering-gallery mode, evanescently coupled to the SOI wire. . . . xii
5 (a) FIB cross section, and (b) top down microscope image of a microdisk laser before metallization. xiii
6 (a) Measured output power and voltage versus current for 7.5-μm-diameter microdisk. (b) Output spectrum for 1.4 mA drive current. . . xiv

1.1 Layout of the Cell processor, containing 8 processor cores. 2
1.2 Evolution of the information capacity for various electrical and optical communication technologies (reproduced from [1]). 3
1.3 Physical interconnect hierarchy of interconnects in digital systems. The interconnects span a wide range of covered distances. Figures are reproduced from [2]. 5
1.4 Ultra-compact passive 16-channel wavelength router based on an arrayed waveguide grating, fabricated on the silicon-on-insulator wire waveguide platform [5]. 7
1.5 Bandgap energy and wavelength versus lattice constant for various III-V semiconductors, silicon and germanium [21]. 10
1.6 III-V/Si integration technology. (a) Hetero-epitaxy of AlSb on Si [25], (b) InP-based lasers flip chipped on SOI [27], and (c) InP-based layer bonded to SOI with adhesive BCB bonding [28]. 12
1.7 Schematic representation of future global on-chip interconnects. (a) Optical interconnect with on-chip lasers, (b) optical interconnect with off-chip laser source and on-chip modulators, and (c) electrical interconnect with repeaters. 14
1.8 (a) Metallization levels in a modern electronic IC (AMD Athlon 64, 2003). (b) Proposed SOI-based optical interconnect (OI) layer, as studied in the PICMOS research project. Only the longest global electrical interconnections (EI) would be replaced by optical interconnects. The OI layer is based on a nanophotonic SOI waveguide with heterogeneous InP-based microlasers and microdetectors. 15
1.9 (a) Pedestal-supported microdisk laser structure [50]. (b) Pedestal-supported photonic-crystal laser structure [51]. 18

2.1 Schematic representation of a Fabry-Pérot laser 24

2.2 Minimum required mirror reflectivity to achieve lasing resonance versus cavity length and propagation loss. 25
2.3 Absorption processes in a direct band semiconductor. 27
2.4 (a) Real part of the effective index n_e for an InP-based film waveguide, with (solid lines) and without (dashed lines) Au cladding, versus film thickness t (TE polarization). (b) Modal propagation loss of the fundamental TE_0 mode due to metal absorption, for various Au-based metal cladding versus waveguide thickness t. For both graphs, the InP waveguide contains a Q1.25 core with thickness $t/2$, and the wavelength is $1.55\,\mu$m. 28
2.5 (a) Substrate loss for a thin-film slab waveguide consisting of a InP film bonded on a Si substrate vs. bonding layer thickness (TE modes, $\lambda = 1.55\,\mu$m). (b) **E**-field profile for $t_{ox} = t_{InP} = 300\,$nm. 30
2.6 Conformal transformation, mapping a bent waveguide in the xy plane (or $r\varphi$ plane) to an equivalent straight waveguide in the uv plane. . . . 30
2.7 Carrier recombination processes 32
2.8 (a) Band structure. (b) Gain spectrum 37
2.9 (a) Gain spectrum and peak material gain versus injected current for different quantum confinement. Reproduced from [81]. (b) Comparison of QW and QD modal gain ($\lambda = 980\,$nm) as function of current density [82]. 38
2.10 (a) Calculated quantum well peak material gain versus carrier concentration N, for increasing temperature. (b) Calculated gain spectrum for $N = 2 \times 10^{18}\mathrm{cm}^{-1}$ for increasing temperature [35]. 39
2.11 (a) Tunnel-junction current-voltage characteristic. Simplified band diagram for reverse bias (b) and forward bias V_P (c). 42
2.12 Calculated tunnel-junction J-V characteristic in reverse bias for an InP-based TJ as function of p-type doping N_a [90]. 43
2.13 Origin of leakage current contributing to the threshold current. (a) Lateral and vertical leakage current in a ridge waveguide laser. (b) Vertical leakage is due to thermionic emission out of the active region (quantum wells), allowing carriers to recombine elsewhere without contributing to the laser operation. 45
2.14 Vertical injection efficiency η_{iV} as function of τ_e and t_{OCL} for $t_{QW} = 20\,$nm. 46
2.15 (a) Calculated band diagram under forward bias for a thin-film p-i-n diode structure with a InGaAs contact layer, (b) carrier concentrations, and (c) recombination rate for $0.9\,V$ forward bias. Calculations are performed with SIMWINDOWS. For all heterobarriers, $Q_C = 0.4$ was assumed. Band bending at the contacts is not included. 48
2.16 In-plane micron-sized optical confinement schemes. (a) DBR microlaser (SEM image from [82]). (b) Defect-based photonic-crystal laser (SEM image from [101]). (c) Band-edge photonic crystal laser (SEM image from [102]). (d) Microdisk cavity. 54

2.17 Band structure for a triangular 2D photonic crystal (2D calculation with $n_{eff} = 2.8$ in TE polarization, where only the four lower bands are shown). 56

2.18 Overview of some promising thin-film microlaser contacting schemes. Double metal-clad film (a), single metal-clad film (b), microdisk resonator (c) and defect-based PhC resonator (d) with lateral contacts, post-contacted microdisk resonator (e) and defect-based PhC resonator (f), thin-film ridge (g) laser and PhC laser with lateral p-n junction. . . 58

3.1 Schematic representation of the heterogeneous SOI-integrated microdisk laser. 66

3.2 Definition of cylindrical coordinate system (a), and whispering-gallery mode H_z profiles for an InP disk with a radius of $4\,\mu$m (TE), calculated with 3-D FDTD, for $(K, L, M) = (0, 0, 45)$ (b), and $(K, L, M) = (0, 1, 40)$ (c). 67

3.3 Cross-sectional $H_z(r, z)$, $E_r(r, z)$, $E_\phi(r, z)$ profiles for the fundamental TE-polarized WGM in a 5-μm-diameter 1-μm-thick microdisk (FimmWave, $\lambda = 1.55\,\mu$m). The contour level values are different for each graph. . . 69

3.4 (a) Normalized $H_z^2(r)$, $E_r^2(r)$, $E_\phi^2(r)$ and $E^2(r)$ profiles at half microdisk thickness for the fundamental TE-polarized whispering-gallery mode, for 5-μm-diameter 1-μm-thick microdisk (FimmWave, $\lambda = 1.55\,\mu$m). A good approximation for the mode profile consists of a Bessel function of the first kind J_M inside the disk and a vanishing field outside the disk. (b) The WGM width $W(R)$ as a function of disk radius, calculated for $J_M(r)$. 70

3.5 Effective index n_e and group index n_g for the fundamental TE-polarized WGM in a 0.5-μm-thick microdisk versus bend radius, calculated with FimmWave. 71

3.6 Bending loss α_b for the fundamental TE-polarized WGM, for thin microdisks versus diameter for different bottom contact layer thicknesses t_s. Lines represent eigenmode-expansion calculations, whereas the markers show 2-D FDTD results. 71

3.7 Calculated scattering loss [77] as a function of disk radius and sidewall roughness rms value σ, assuming a roughness correlation length S_c of 50 nm (left) and 100 nm (right). 72

3.8 Distributed coupling loss α_c for thin and thick microdisks with 7.5-μm diameter and a 500-nm-wide SOI wire waveguide (without offset) versus bonding layer thickness t_{ox}. 74

3.9 Left: distributed coupling loss α_c for a thick 7.5-μm microdisk, a bonding layer thickness $t_{ox} = 100\,$nm and SOI wire waveguide widths $w_{Si} = 500\,$nm and $600\,$nm, versus lateral disk-wire offset. Right: H_z profile in a plane between the disk and the Si waveguide, showing the evanescent tails of the WGM and the coupled light propagating in the Si wire. 75

3.10 Three epitaxial layer structure designs are under study: design A and B include a tunnel junction, whereas design C incorporates a thin ternary contact layer. 76
3.11 Optimized transparency gain G_{tr}, compensating for the internal loss, as a function of III-V film thickness t. 77
3.12 Breakdown of the internal loss contributions for design A versus III-V film thickness t. α_{int} is the total internal loss, α_{TJp} is the loss in the p-side of the tunnel junction, α_{QW} is the quantum-well contribution, $\alpha_{p/n}$ the loss in the diode p/n-doped layer and α_{OCL} is the loss in the optical confinement layers. 78
3.13 Lumped electrical network, used for analyzing the current path in the microdisk laser. 79
3.14 Current density versus radial position calculated for a 7.5-μm disk and $I = 0.5\,$mA, calculated with the network shown in fig. 3.13, with the material parameters listed in table 3.5. Structures (a)-(d) include thick devices with $R_{top} = 0.4R$ or $0.8R$, and $N_a = 2 \times 10^{18}$cm^{-3} or 2×10^{19}cm^{-3}, and show uniform current injection. Thin structures have comparable behavior. Structure (e) has a $10\times$ worse conducting top n-layer and a $10\times$ better conducting bottom n-layer, while (f) has the opposite composition. 80
3.15 Calculated V-I curve for a thick 7.5-μm microdisk, assuming uniform injection, versus TJ p-doping level N_a. A breakdown of the device voltage is shown for $N_a = 2 \times 10^{18}$ cm^{-3}. For this doping level, the TJ voltage dominates other non-diode related voltage contributions. . . . 82
3.16 Left: geometry used for thermal simulations of generation 1 microdisk lasers. Right: steady-state temperature increase distribution for $P = 1\,$mW. 83
3.17 Left: temperature step response for $P = 1\,$mW. Right: Thermal resistance versus microdisk radius, for disk geometry as in fig. 3.16 (a), 1D approximation $R_{th} = t_{ox}/\kappa_{ox}\pi R^2$ (b), BCB planarization layer replaced by amorphous Al_2O_3 (c), SiO_2 bonding layer replaced by crystalline Al_2O_3 (d), and microdisk with heat sink structure (e). 85
3.18 Lateral diffusion feeds extra carriers to the laser region, resulting in a higher differential efficiency (a), and a less distinct spatial hole burnt into the carrier density profile (b). The left part (a) also shows the P-I curve calculated under the assumption of no lateral current and an injection efficiency determined by the geometrical width of the WGM (grey line). 88
3.19 Radial carrier profile for a 5-μm-diameter microdisk as function of injection current. (a) $v_s = 10^4$cm/s, (b): $v_s = 10^5$cm/s, with $D = 8\,$cm^2/s. The WGM profile $\Psi^2(r)$ is also plotted as reference (dashed lines). 88
3.20 Impact of surface recombination on static laser performance. Enhanced lateral diffusion increases the performance penalty due to surface recombination. 89

3.21 Impact of non-uniform injection (radially symmetric) on static laser performance ($D = 8\,\mathrm{cm}^2/\mathrm{s}$). (a) benchmark 2.5-$\mu$m-radius microdisk laser. (b) 3.75-μm-radius microdisk laser. The dashed line is a visual guide to illustrate the saturation effect. 90

3.22 Comparison of simulation results for the benchmark 2.5-μm-radius microdisk laser, calculated with (a) fully radially-dependent rate equations and (b) rate-equation system with two lumped carrier densities. A good (qualitative) match is obtained, however with a slight underestimation of the lateral diffusion in the latter case. 92

3.23 Results of the optimization procedure both for the thin (orange) and thick epitaxial structure (blue), for output powers in the range 1-100 μW. The optimized microdisk radius can be found in (a), the optimized tunnel-junction p-type doping in (b) and the optimized coupling loss in (c). The power consumption for devices with these optimized design parameters is shown in (d). Solid lines represent devices with roughness $\sigma = 10\,\mathrm{nm}$, $L_c = 100\,\mathrm{nm}$. The dashed lines have $\sigma = 1\,\mathrm{nm}$, as have the dotted and dashed-dotted cases. Furthermore, the dotted line shows the results for an artificial structure with improved lateral injection efficiency ($\times 1.5$), whereas the dashed-dotted line represents optimized devices with the currently available estimated tunnel-junction optoelectronic performance, coinciding accidentally with the dashed line. The best experimental result (pulsed regime) for a thick, non-optimized 7.5-μm-diameter microdisk laser is also shown, emphasizing the potential for device optimization. 93

3.24 Intrinsic relaxation oscillation frequency f_R and modulation bandwidth f_{3dB} for the optimized (50 μW) microdisk laser with currently available TJ performance, as a function of pumping level. The output power is also shown as reference. 95

3.25 Modulation response as function of pumping level for a 4.6-μm-diameter microdisk optimized for 50 μW output, with $D = 8\,\mathrm{cm}^2/\mathrm{s}$. 96

3.26 Modulation response as function of pumping level for the same microdisk laser as in fig. 3.25, but without improved lateral injection efficiency, with enhanced lateral diffusion $D = 40\,\mathrm{cm}^2/\mathrm{s}$ and assuming a 10× lower Auger recombination rate ($C = 1.63 \times 10^{-29}\mathrm{cm}^6\mathrm{s}^{-1}$). . . . 97

3.27 Simulated behavior of the optimized 4.6-μm-diameter microdisk laser under above-threshold large-signal modulation at 1 Gb/s. (a) Total injected current (dotted lines), vertical injected current in lasing region (dashed lines) and vertical plus lateral injected current in lasing region (solid lines). (b) Output power. (c) Carrier density N_1 in central region. (d) Carrier density N_2 in laser region. 98

3.28 Simulated behavior of the 4.6-μm-diameter microdisk laser, with reduced Auger recombination, enhanced diffusion $D = 40\,\text{cm}^2/\text{s}$ and no lateral injection improvement under above-threshold large-signal modulation at 1 Gb/s. (a) Total injected current (dotted lines), vertical injected current in lasing region (dashed lines) and vertical plus lateral injected current in lasing region (solid lines). (b) Output power. (c) Carrier density N_1 in central region. (d) Carrier density N_2 in laser region. 99
3.29 Layout and processing for a post-injected ultrathin microdisk laser. (a) Dry etched microcylinder. (b) Selective wet underetch of the InP post and metallization. 100
3.30 (a) Bending loss for the ultrathin microdisk laser with $t_s = 30\,\text{nm}$. (b) Coupling loss to the SOI wire waveguide for a ultrathin microdisk laser ($D = 4\,\mu$m), without lateral offset. The coupling loss for thick and thin microdisk lasers ($D = 7.5\,\mu$m) are also shown as reference. . . 101
3.31 (a) Calculated free carrier concentrations n and p for $N_a = N_d = 10^{18}\,\text{cm}^{-3}$, at zero bias. (b) Calculated current density profile for a total current of $100\,\mu$A (solid line). The WGM is shown as a dashed line. 102

4.1 Global overview of the fabrication process of an SOI-integrated microdisk laser. 106
4.2 SOI wafer with molecularly bonded InP-based dies, used for fabricating generation-2 lasers and detectors, before (a) and after substrate removal (b). During substrate removal, a large fraction of the bonded (mainly detector) material was detached, which severely limited the process yield. (c) shows the result after mechanical grinding and (d) after chemical substrate removal for the generation-3 samples, involving only laser dies, with a higher yield. (bonding performed at CEA-LETI/Tracit). 110
4.3 Overview of the InP, BCB and metallization processing steps of the heterogeneous SOI-integrated microdisk laser. 111
4.4 Dry-etched microdisks with SiO_2 hard mask: (a) ICP-RIE-etched 0.5-μm-thick disk, and (b) RIE-etched 1-μm-thick disk (etching performed at INL). (c) and (d) show cross sections of the disk edge of 1-μm-thick microdisks, comparing RIE and ICP-RIE etching results. 113
4.5 (a) FIB cross section of a microdisk laser after the DVS-BCB planarization and opening of the contact windows. (b) Top down microscope image of the same structures, showing the shape of the top and bottom contact vias, and the underlying SOI waveguides. 114
4.6 (a) FIB cross section of a 1-μm-thick G3 microdisk laser after metallization, including a heat sinking structure. (b) Top SEM image of a metallized G2 structure, showing a poor metal step coverage at the top contact due to too steep BCB via sidewalls. (c) Top down microscope image of block of eight metallized G2 microdisks. 116

4.7 (a) Contact resistance and absorption loss for different Au-based contacts to n-type InP (A=alloyed, NA=non-alloyed). The vertical line represents the calculated absorption loss for the associated 1D slab waveguide. (b) SEM image of a metallized waveguide, used to extract the metal absorption loss. 117

5.1 Schematic representation of the optical pumping setup, as available at INL. 120
5.2 Photograph of the electrically-injected laser measurement setup, showing the electrical probe needles positioned on top of the contact pads and the optical fibre positioned above the fibre coupler of the corresponding SOI waveguide (inset: camera image). 121
5.3 Equivalent electrical network of the electrical injection setup. A pulsed voltage source is connected to the laser diode through a 50 Ω transmission line, terminated with a 50 Ω resistor. The device current is determined by measuring the voltage drop over a series resistor. 122
5.4 Fabrication and measurement results of a G1 0.8-μm-thick microdisk laser. (a) top-down SEM image of 8-μm-diameter microdisk, with shiny-Au top contact. (b) Lasing spectrum taken at various bias voltages (6-ns pulses (nominal), 333-ns period). Fabrication performed at UGent/INL, measurements at INL. 124
5.5 (a) Laser peak power versus current and V-I curve for a 6-μm-diameter, 0.48-μm-thick G1 microdisk laser in pulsed regime (360-ns pulses, 3.6-μs period). (b) Spectrum taken at 0.78 mA. The inset shows a FIB cross section of the microdisk edge. 125
5.6 Lasing characteristics versus microdisk radius for G1 lasers (pulsed regime: 360-ns pulses, 3.6-μs period). (a) Measured threshold current (circles). Calculated threshold values for $\alpha_i = 50\,\mathrm{cm}^{-1}$, $\alpha_s = 0$ (grey line), and $\alpha_i = 10\,\mathrm{cm}^{-1}$, $\sigma = 1, 10, 20\,\mathrm{nm}$ ($L_c = 100\,\mathrm{nm}$) in solid, dashed and dotted black lines respectively. (b) Measured lasing wavelengths. 126
5.7 Lasing characteristics for mode 1 versus ambient temperature for a 6-μm-diameter G1 laser (pulsed regime: 50-ns pulses, 3-μs period). (a) Laser peak power at 1570 nm versus current, (b) lasing wavelength versus ambient temperature. 127
5.8 Spectral broadening due to self heating (mode 1) versus pulse duration s for a 6-μm-diameter G1 laser (850-μA pulses, fixed 5-μs period, spectra recorded with 200-pm resolution) 128
5.9 Comparison of experimentally extracted self heating with thermal simulation. (a) Thermal turn-on response of a 6-μm-diameter G1 laser for different pumping levels. (b) Maximum and minimum regime temperatures versus pulse period for a fixed pulse duration (360 ns), for a 7.5-μm-diameter laser at 11 mW pumping power. Experimental data are indicated with markers. Lines show simulated data (solid lines $\kappa_{ox} = 1.27\,\mathrm{W/mK}$, dashed lines $\kappa_{ox} = 1\,\mathrm{W/mK}$) 129

5.10 Measurement results under pulsed optical pumping for 0.5-μm-thick G2 microdisk lasers with 150-nm-thick bonding layer. (a) Above-threshold SOI-coupled output spectrum of a 10-μm-diameter microdisk laser, showing laser operation at 1601 nm. (b) SOI-coupled output signal versus pumping power for 7.5-μm-diameter microdisk lasers, for different lateral waveguide offsets. Measurements were performed at INL. Lines are drawn as guide to the eye. 131
5.11 FIB cross section of a thick 7.5-μm-diameter G2 microdisk, before metallization. 132
5.12 Measurement results of CW electrically injected 7.5-μm-diameter 1-μm-thick microdisk lasers, with -50 nm wire-disk offset, for various top BCB via diameters R_{top}. (a) SOI-coupled laser output power versus current. (b) Device voltage versus current. 133
5.13 Measurement results of CW electrically injected 7.5-μm-diameter 1-μm-thick microdisk lasers, with -150 nm wire-disk offset, for various top BCB via diameters R_{top}. (a) SOI-coupled laser output power versus current. (b) Device voltage versus current. 133
5.14 SOI-coupled laser output spectrum for the best laser. (a) Overview spectrum for 1.4 mA pumping current. (b) Spectrum detail recorded at finest available resolution (60 pm), as function of injected current. . . 135
5.15 Fit to pulsed lasing characteristics of 1-μm-thick 7.5-μm-diameter microdisk lasers. (a) Best performing laser with -50 nm disk-wire offset. (b) Best performing laser with -150 nm disk-wire offset. Rectangles denote measured voltages, circles denote coupled output power. Lines represent the fit to the experiment. 136
5.16 (a) Schematic layout of the heterogeneous SOI-integrated p-i-n detector, implemented in the full optical link. (b) Top-down microscope image of a fabricated detector before metallization . This device was developed by P. Binetti at Technical University Eindhoven. 137
5.17 Measurement results of a complete optical link. (a) Average laser power detected at the fibre coupler (FC) and average detector current versus average laser current in pulsed regime. (b) Laser power at the fibre coupler and detector current versus laser current in CW regime. The detector current and output power at the FC are unstable versus time and pump level, varying between the dashed and dotted lines. The detector was not biased. 138
5.18 Laser spectrum for the microdisk laser implemented in the full optical link, under CW operation. The data was normalized for the FC efficiency and on-chip loss. 139
5.19 Laser spectra under CW operation (4.5 mA each) for 4 microdisk lasers coupled to a common SOI wire. The nominal disk diameters are 10, 10.044 μm, 10.088 μm and 10.132 μm for laser L4, L3, L2 and L1 respectively. The data was normalized for the FC efficiency. L1 is the laser closest to the fibre coupler used for extraction. 140

A.1 Schematic drawing of the SOI-coupled DBR-microlaser. 148

A.2 (a) Internal loss α_{int} of the fundamental TE$_0$-mode at $1.5\,\mu$m versus film thickness t, for various epitaxial designs. (b) Epitaxial layer design for structure with TJ-based top contact. 148
A.3 DBR mirror reflectivity of the fundamental TE$_0$-mode at $1.5\,\mu$m, for $t = 1\,\mu$m versus DBR period a and filling factor FF (for 8 DBR periods). 149
A.4 (a) DBR mirror reflectivity spectrum versus sidewall angle. (b) FIB cross section of RIE-etched DBR structure. 149
A.5 Simulation results for a 0.75-μm-thick DBR microlaser with Au top contact and $t_{ox} = 200\,$nm, as function of the cavity length L. (a) Material threshold gain G_{th}. (b) Extraction efficiency η_e. 151
A.6 Simulation results for a 1.5-μm-thick DBR microlaser with TiPtAu top contact and $t_{ox} = 150\,$nm, as function of the cavity length L. (a) Material threshold gain G_{th}. (b) Extraction efficiency η_e. (c) Threshold current I_{th}, assuming $W = 5\,\mu$m. (d) Slope efficiency. 151
A.7 Mode plot of the E_y laser field for the 1.5-μm-thick DBR microlaser with $t_{ox} = 100\,$nm, with the real part plotted in (a) and the imaginary part plotted in (b). 153

B.1 Calculation flowchart used for solving radially-dependent, static rate equations. 156

C.1 Mask layout of G2 microdisk lasers and microdetectors. 158
C.2 Mask layout detail of G2 microdisk lasers. 159
C.3 Mask layout details of G3 microdisk lasers. 159

Tables

3.1 Parameters for the two benchmark structures 78
3.2 Parameter values used for the electrical analysis 81
3.3 Material parameters used in the thermal simulation 84
3.4 Model parameters used in rate equations 87

5.1 Epitaxial layer design for G1 microlasers. 123
5.2 Epitaxial layer design for G2 microlasers. 130

Bibliography

[1] MIT Microphotonics Center Industry Consortium. Communications technology roadmap. Technical report, MIT, 2005.

[2] A. F. Benner, M. Ignatowski, J. A. Kash, D. M. Kuchta, and M. B. Ritter. Exploitation of optical interconnects in future server architectures. *IBM Journal of Research and Development*, 49(4-5):755–775, 2005.

[3] D. A. B. Miller. Physical reasons for optical interconnection. *International Journal of Optoelectronics*, 11(3):155–168, 1997.

[4] D. A. B. Miller. Rationale and challenges for optical interconnects to electronic chips. *Proceedings of the IEEE*, 88(6):728–749, 2000.

[5] P. Dumon. *Ultra-Compact Integrated Optical Filters in Silicon-on-insulator by Means of Wafer-Scale Technology*. Phd thesis, Ghent University, 2007.

[6] D. Taillaert, F. Van Laere, M. Ayre, W. Bogaerts, D. Van Thourhout, P. Bienstman, and R. Baets. Grating couplers for coupling between optical fibers and nanophotonic waveguides. *Japanese Journal of Applied Physics Part 1-Regular Papers Brief Communications*, 45(8A):6071–6077, 2006.

[7] M. J. Chen, J. L. Yen, J. Y. Li, J. F. Chang, S. C. Tsai, and C. S. Tsai. Stimulated emission in a nanostructured silicon pn junction diode using current injection. *Applied Physics Letters*, 84(12):2163–2165, 2004.

[8] L. Pavesi, L. Dal Negro, C. Mazzoleni, G. Franzo, and F. Priolo. Optical gain in silicon nanocrystals. *Nature*, 408(6811):440–444, 2000.

[9] R. J. Walters, G. I. Bourianoff, and H. A. Atwater. Field-effect electroluminescence in silicon nanocrystals. *Nature Materials*, 4(2):143–146, 2005.

[10] S. G. Cloutier, P. A. Kossyrev, and J. Xu. Optical gain and stimulated emission in periodic nanopatterned crystalline silicon. *Nature Materials*, 4(12):887–891, 2005.

[11] B. Zheng, J. Michel, F. Y. G. Ren, L. C. Kimerling, D. C. Jacobson, and J. M. Poate. Room-Temperature Sharp Line Electroluminescence at Lambda=1.54-Mu-M from an Erbium-Doped, Silicon Light-Emitting Diode. *Applied Physics Letters*, 64(21):2842–2844, 1994.

[12] H. S. Han, S. Y. Seo, and J. H. Shin. Optical gain at 1.54 mu m in erbium-doped silicon nanocluster sensitized waveguide. *Applied Physics Letters*, 79(27):4568–4570, 2001.

[13] A. Polman, B. Min, J. Kalkman, T. J. Kippenberg, and K. J. Vahala. Ultralow-threshold erbium-implanted toroidal microlaser on silicon. *Applied Physics Letters*, 84(7):1037–1039, 2004.

[14] C. A. Barrios and M. Lipson. Electrically driven silicon resonant light emitting device based on slot- waveguide. *Optics Express*, 13(25):10092–10101, 2005.

[15] H. S. Rong, A. S. Liu, R. Jones, O. Cohen, D. Hak, R. Nicolaescu, A. Fang, and M. Paniccia. An all-silicon Raman laser. *Nature*, 433(7023):292–294, 2005.

[16] O. Boyraz and B. Jalali. Demonstration of a silicon Raman laser. *Optics Express*, 12(21):5269–5273, 2004.

[17] M. A. Foster, A. C. Turner, J. E. Sharping, B. S. Schmidt, M. Lipson, and A. L. Gaeta. Broad-band optical parametric gain on a silicon photonic chip. *Nature*, 441(7096):960–963, 2006.

[18] Q. F. Xu, B. Schmidt, S. Pradhan, and M. Lipson. Micrometre-scale silicon electro-optic modulator. *Nature*, 435(7040):325–327, 2005.

[19] Q. F. Xu, S. Manipatruni, B. Schmidt, J. Shakya, and M. Lipson. 12.5 Gbit/s carrier-injection-based silicon micro-ring silicon modulators. *Optics Express*, 15(2):430–436, 2007.

[20] A. S. Liu, L. Liao, D. Rubin, H. Nguyen, B. Ciftcioglu, Y. Chetrit, N. Izhaky, and M. Paniccia. High-speed optical modulation based on carrier depletion in a silicon waveguide. *Optics Express*, 15(2):660–668, 2007.

[21] E. F. Schubert. *Light Emitting Diodes*. Cambridge Univ. Press, 2005.

[22] D. G. Deppe, N. Holonyak, D. W. Nam, K. C. Hsieh, G. S. Jackson, R. J. Matyi, H. Shichijo, J. E. Epler, and H. F. Chung. Room-Temperature Continuous Operation of P-N Alxga1-Xas-Gaas Quantum-Well Heterostructure Lasers Grown on Si. *Applied Physics Letters*, 51(9):637–639, 1987.

[23] D. Fehly, A. Schlachetzki, A. S. Bakin, A. Guttzeit, and H. H. Wehmann. Monolithic InGaAsP optoelectronic devices with silicon electronics. *IEEE Journal of Quantum Electronics*, 37(10):1246–1252, 2001.

[24] Z. Mi, J. Yang, P. Bhattacharya, and D. L. Huffaker. Self-organised quantum dots as dislocation filters: the case of GaAs-based lasers on silicon. *Electronics Letters*, 42(2):121–123, 2006.

[25] G. Balakrishnan, A. Jallipalli, P. Rotella, S. H. Huang, A. Khoshakhlagh, A. Amtout, S. Krishna, L. R. Dawson, and D. L. Huffaker. Room-temperature optically pumped (Al)GaSb vertical-cavity surface-emitting laser monolithically grown on an Si(100) substrate. *IEEE Journal of Selected Topics in Quantum Electronics*, 12(6):1636–1641, 2006.

[26] K. Chilukuri, M. J. Mori, C. L. Dohrman, and E. A. Fitzgerald. Monolithic CMOS-compatible AlGaInP visible LED arrays on silicon on lattice-engineered substrates (SOLES). *Semiconductor Science and Technology*, 22(2):29–34, 2007.

[27] T. Mitze, M. Schnarrenberger, L. Zimmermann, J. Bruns, F. Fidorra, K. Janiak, J. Kreissl, S. Fidorra, H. Heidrich, and K. Petermann. CWDM transmitter module based on hybrid integration. *IEEE Journal of Selected Topics in Quantum Electronics*, 12(5):983–987, 2006.

[28] G. Roelkens, J. Brouckaert, D. Van Thourhout, R. Baets, R. Notzel, and M. Smit. Adhesive bonding of InP/InGaAsP dies to processed silicon-on-insulator wafers using DVS-bis-benzocyclobutene. *Journal of the Electrochemical Society*, 153(12):G1015–G1019, 2006.

[29] A. L. Lentine, K. W. Goossen, J. A. Walker, J. E. Cunningham, W. Y. Jan, T. K. Woodward, A. V. Krishnamoorthy, B. J. Tseng, S. P. Hui, R. E. Leibenguth, L. M. F. Chirovsky, R. A. Novotny, D. B. Buchholz, and R. L. Morrison. Optoelectronic VLSI switching chip with greater than 1 Tbit/s potential optical I/O bandwidth. *Electronics Letters*, 33(10):894–895, 1997.

[30] G. Roelkens. *Heterogeneous III-V/Silicon Photonics: Bonding Technology and Integrated Devices*. Phd thesis, Ghent University, 2007.

[31] ITRS roadmap, http://www.itrs.net/, 2005.

[32] M. J. Kobrinsky, B. A. Block, J. F. Zheng, B. C. Barnett, E. Mohammed, M. Reshotko, F. Robertson, S. List, I. Young, and K. Cadien. On-chip optical interconnects. *Intel Technology Journal*, (2), 2004.

[33] G. Q. Chen, H. Chen, M. Haurylau, N. A. Nelson, D. H. Albonesi, P. M. Fauchet, and E. G. Friedman. Predictions of CMOS compatible on-chip optical interconnect. *Integration-the Vlsi Journal*, 40(4):434–446, 2007.

[34] I. O'Connor, F. Tissafi-Drissi, F. Gaffiot, J. Dambre, M. De Wilde, J. Van Campenhout, D. Van Thourhout, J. Van Campenhout, and D. Stroobandt. Systematic simulation-based predictive synthesis of integrated optical interconnect. *IEEE Transactions on Very Large Scale Integration (Vlsi) Systems*, 15(8):927–940, 2007.

[35] J. Piprek. *Semiconductor Optoelectronic Devices. Introduction to Physics and Simulation*. Elsevier, San Diego, 2003.

[36] F. Ramos, E. Kehayas, J. M. Martinez, R. Clavero, J. Marti, L. Stampoulidis, D. Tsiokos, H. Avramopoulos, J. Zhang, P. V. Holm-Nielsen, N. Chi, P. Jeppesen, N. Yan, I. T. Monroy, A. M. J. Koonen, M. T. Hill, Y. Liu, H. J. S. Dorren, R. Van Caenegem, D. Colle, M. Pickavet, and B. Riposati. IST-LASAGNE: Towards all-optical label swapping employing optical logic gates and optical flip-flops. *Journal of Lightwave Technology*, 23(10):2993–3011, 2005.

[37] M. T. Hill, H. J. S. Dorren, T. de Vries, X. J. M. Leijtens, J. H. den Besten, B. Smalbrugge, Y. S. Oei, H. Binsma, G. D. Khoe, and M. K. Smit. A fast low-power optical memory based on coupled micro-ring lasers. *Nature*, 432(7014):206–209, 2004.

[38] E. C. Mos, J. J. L. Hoppenbrouwers, M. T. Hill, M. W. Blum, Jjhb Schleipen, and H. de Waardt. Optical neuron by use of a laser diode with injection seeding and external optical feedback. *IEEE Transactions on Neural Networks*, 11(4):988–996, 2000.

[39] D. Taillaert, W. Van Paepegem, J. Vlekken, and R. Baets. A thin foil optical strain gage based on silicon-on-insulator microresonators, July 2007 2007.

[40] K. De Vos, I. Bartolozzi, E. Schacht, P. Bienstman, and R. Baets. Silicon-on-Insulator microring resonator for sensitive and label-free biosensing. *Optics Express* , 15(12):7610–7615, 2007.

[41] J. Yang and L. J. Guo. Optical sensors based on active microcavities. *IEEE Journal of Selected Topics in Quantum Electronics*, 12(1):143–147, 2006.

[42] S. L. Mccall, A. F. J. Levi, R. E. Slusher, S. J. Pearton, and R. A. Logan. Whispering-Gallery Mode Microdisk Lasers. *Applied Physics Letters*, 60(3):289–291, 1992.

[43] A. F. J. Levi, R. E. Slusher, S. L. Mccall, T. Tanbunek, D. L. Coblentz, and S. J. Pearton. Room-Temperature Operation of Microdisk Lasers with Submilliamp Threshold Current. *Electronics Letters*, 28(11):1010–1012, 1992.

[44] M. Fujita, K. Inoshita, and T. Baba. Room temperature continuous wave lasing characteristics of GaInAsP/InP microdisk injection laser. *Electronics Letters*, 34(3):278–279, 1998.

[45] M. Fujita, R. Ushigome, and T. Baba. Continuous wave lasing in GaInAsP microdisk injection laser with threshold current of 40 uA. *Electronics Letters*, 36(9):790–791, 2000.

[46] R. Ushigome, M. Fujita, A. Sakai, T. Baba, and Y. K. Kubun. GaInAsP microdisk injection laser with benzocyclobutene polymer cladding and its athermal effect. *Japanese Journal of Applied Physics*, 41(11A):6364–6369, 2002.

[47] M. Hovinen, J. Ding, A. V. Nurmikko, D. C. Grillo, J. Han, L. He, and R. L. Gunshor. Blue-Green Laser-Emission from Znse Quantum-Well Microresonators. *Applied Physics Letters*, 63(23):3128–3130, 1993.

[48] S. S. Chang, N. B. Rex, R. K. Chang, G. Chong, and L. J. Guido. Stimulated emission and lasing in whispering-gallery modes of GaN microdisk cavities. *Applied Physics Letters*, 75(2):166–168, 1999.

[49] A. C. Tamboli, E. D. Haberer, R. Sharma, K. H. Lee, S. Nakamura, and E. L. Hu. Room-temperature continuous-wave lasing in GaN/InGaN microdisks. *Nature Photonics*, 1(1):61–64, 2007.

[50] T. Baba, M. Fujita, A. Sakai, M. Kihara, and R. Watanabe. Lasing characteristics of GaInAsP-InP strained quantum-well microdisk injection lasers with diameter of 2-10μm. *IEEE Photonics Technology Letters*, 9(7):878–880, 1997.

[51] H. G. Park, S. H. Kim, S. H. Kwon, Y. G. Ju, J. K. Yang, J. H. Baek, S. B. Kim, and Y. H. Lee. Electrically driven single-cell photonic crystal laser. *Science*, 305(5689):1444–1447, 2004.

[52] L. D. Zhang and E. Hu. Lasing from InGaAs quantum dots in an injection microdisk. *Applied Physics Letters*, 82(3):319–321, 2003.

[53] T. Ide, T. Baba, J. Tatebayashi, S. Iwamoto, T. Nakaoka, and Y. Arakawa. Room temperature continuous wave lasing in InAs quantum-dot microdisks with air cladding. *Optics Express*, 13(5):1615–1620, 2005.

[54] K. Srinivasan, M. Borselli, and O. Painter. Cavity Q, mode volume, and lasing threshold in small diameter AlGaAs microdisks with embedded quantum dots. *Optics Express*, 14(3):1094–1105, 2006.

[55] S. J. Choi, K. Djordjev, S. J. Choi, and P. D. Dapkus. Microdisk lasers vertically coupled to output waveguides. *IEEE Photonics Technology Letters*, 15(10):1330–1332, 2003.

[56] B. Corbett, J. Justice, L. Considine, S. Walsh, and W. M. Kelly. Low-threshold lasing in novel microdisk geometries. *IEEE Photonics Technology Letters*, 8(7):855–857, 1996.

[57] C. Seassal, P. Rojo-Romeo, X. Letartre, P. Viktorovitch, G. Hollinger, E. Jalaguier, S. Pocas, and B. Aspar. InP microdisk lasers on silicon wafer: CW room temperature operation at 1.6 μm. *Electronics Letters*, 37(4):222–223, 2001.

[58] H. T. Hattori, C. Seassal, E. Touraille, P. Rojo-Rmeo, X. Letartre, G. Hollinger, P. Viktorovitch, L. Di Cioccio, M. Zussy, L. El Melhaoui, and J. M. Fedeli. Heterogeneous integration of microdisk lasers on silicon strip waveguides for optical interconnects. *IEEE Photonics Technology Letters*, 18(1-4):223–225, 2006.

[59] X. Liu, W. Fang, Y. Huang, X. H. Wu, S. T. Ho, H. Cao, and R. P. H. Chang. Optically pumped ultraviolet microdisk laser on a silicon substrate. *Applied Physics Letters*, 84(14):2488–2490, 2004.

[60] O. Painter, R. K. Lee, A. Scherer, A. Yariv, J. D. O'Brien, P. D. Dapkus, and I. Kim. Two-dimensional photonic band-gap defect mode laser. *Science*, 284(5421):1819–1821, 1999.

[61] M. Loncar, T. Yoshie, A. Scherer, P. Gogna, and Y. M. Qiu. Low-threshold photonic crystal laser. *Applied Physics Letters*, 81(15):2680–2682, 2002.

[62] K. Srinivasan, P. E. Barclay, O. Painter, J. X. Chen, A. Y. Cho, and C. Gmachl. Experimental demonstration of a high quality factor photonic crystal microcavity. *Applied Physics Letters*, 83(10):1915–1917, 2003.

[63] K. Nozaki, S. Kita, and T. Baba. Room temperature continuous wave operation and controlled spontaneous emission in ultrasmall photonic crystal nanolaser. *Optics Express*, 15(12):7506–7514, 2007.

[64] M. K. Seo, K. Y. Jeong, J. K. Yang, Y. H. Lee, H. G. Park, and S. B. Kim. Low threshold current single-cell hexapole mode photonic crystal laser. *Applied Physics Letters*, 90(17):–, 2007.

[65] H. Wada and T. Kamijoh. Room-temperature CW operation of InGaAsP lasers on Si fabricated by wafer bonding. *IEEE Photonics Technology Letters*, 8(2):173–175, 1996.

[66] G. Roelkens, D. Van Thourhout, R. Baets, R. Notzel, and M. Smit. Laser emission and photodetection in an InP/InGaAsP layer integrated on and coupled to a Silicon-on-Insulator waveguide circuit. *Optics Express*, 14(18):8154–8159, 2006.

[67] A. W. Fang, H. Park, O. Cohen, R. Jones, M. J. Paniccia, and J. E. Bowers. Electrically pumped hybrid AlGaInAs-silicon evanescent laser. *Optics Express*, 14(20):9203–9210, 2006.

[68] A. W. Fang, R. Jones, H. Park, O. Cohen, O. Raday, M. J. Paniccia, and J. E. Bowers. Integrated AlGaInAs-silicon evanescent racetrack laser and photodetector. *Optics Express*, 15(5):2315–2322, 2007.

[69] M. Haurylau, G. Q. Chen, H. Chen, J. D. Zhang, N. A. Nelson, D. H. Albonesi, E. G. Friedman, and P. M. Fauchet. On-chip optical interconnect roadmap: Challenges and critical directions. *IEEE Journal of Selected Topics in Quantum Electronics*, 12(6):1699–1705, 2006.

[70] M. Heiblum and J. H. Harris. Analysis of Curved Optical-Waveguides by Conformal Transformation. *IEEE Journal of Quantum Electronics*, QE11(2):75–83, 1975.

[71] J. H. Jang, W. Zhao, J. W. Bae, D. Selvanathan, S. L. Rommel, I. Adesida, A. Lepore, M. Kwakernaak, and J. H. Abeles. Direct measurement of nanoscale sidewall roughness of optical waveguides using an atomic force microscope. *Applied Physics Letters*, 83(20):4116–4118, 2003.

[72] S. Mitsugi, F. Koyama, and A. Matsutani. Correlation length measurement of sidewall roughness of dry etched facet and its effect on reflectivity. *Optical Review*, 6(4):378–379, 1999.

[73] W. Zhao, J. W. Bae, I. Adesida, and J. H. Jang. Effect of mask thickness on the nanoscale sidewall roughness and optical scattering losses of deep-etched InP/InGaAsP high mesa waveguides. *Journal of Vacuum Science and Technology B*, 23(5):2041–2045, 2005.

[74] P. K. Tien. Light waves in thin films and integrated optics. *Applied Optics*, 10(11):2395–2313, 1971.

[75] B. E. Little, J. P. Laine, and S. T. Chu. Surface-roughness-induced contradirectional coupling in ring and disk resonators. *Optics Letters*, 22(1):4–6, 1997.

[76] M. Borselli, K. Srinivasan, P. E. Barclay, and O. Painter. Rayleigh scattering, mode coupling, and optical loss in silicon microdisks. *Applied Physics Letters*, 85(17):3693–3695, 2004.

[77] J.E. Heebner, T. C. Bond, and J. S. Kallman. Generalized formulation for performance degradations due to bending and edge scattering loss in microdisk resonators . *Optics Express*, 15(8):4452–4473, 2007.

[78] V. N. Bessolov, E. V. Konenkova, and M. V. Lebedev. A comparison of the effectiveness of GaAs surface passivation with sodium and ammonium sulfide solutions. *Physics of the Solid State*, 39(1):54–57, 1997.

[79] L. A. Coldren and S. W. Corzine. *Diode Lasers and Photonic Integrated Circuits*. Wiley, New York, 1995.

[80] A. A. Dikshit and J. M. Pikal. Carrier distribution, gain, and lasing in 1.3-mu m InAs-InGaAs quantum-dot lasers. *IEEE Journal of Quantum Electronics*, 40(2):105–112, 2004.

[81] M. Asada, Y. Miyamoto, and Y. Suematsu. Gain and the Threshold of 3-Dimensional Quantum-Box Lasers. *IEEE Journal of Quantum Electronics*, 22(9):1915–1921, 1986.

[82] J. P. Reithmaier and A. Forchel. Single-mode distributed feedback and microlasers based on quantum-dot gain material. *IEEE Journal of Selected Topics in Quantum Electronics*, 8(5):1035–1044, 2002.

[83] D. Bimberg, M. Grundmann, F. Heinrichsdorff, N. N. Ledentsov, V. M. Ustinov, A. E. Zhukov, A. R. Kovsh, M. V. Maximov, Y. M. Shernyakov, B. V. Volovik, A. F. Tsatsul'nikov, P. S. Kop'ev, and Z. I. Alferov. Quantum dot lasers: breakthrough in optoelectronics. *Thin Solid Films*, 367(1-2):235–249, 2000.

[84] X. D. Huang, A. Stintz, C. P. Hains, G. T. Liu, J. Cheng, and K. J. Malloy. Efficient high-temperature CW lasing operation of oxide-confined long-wavelength InAs quantum dot lasers. *Electronics Letters*, 36(1):41–42, 2000.

[85] II Novikov, N. Y. Gordeev, M. V. Maximov, Y. M. Shernyakov, A. E. Zhukov, A. P. Vasil'ev, E. S. Semenova, V. M. Ustinov, N. N. Ledentsov, D. Bimberg, N. D. Zakharov, and P. Werner. Ultrahigh gain and non-radiative recombination channels in 1.5 mu m range metamorphic InAs-InGaAs quantum dot lasers on GaAs substrates. *Semiconductor Science and Technology*, 20(1):33–37, 2005.

[86] O. B. Shchekin and D. G. Deppe. 1.3 mu m InAs quantum dot laser with T-o=161 K from 0 to 80 degrees C. *Applied Physics Letters*, 80(18):3277–3279, 2002.

[87] E. Hokelek and G. Y. Robinson. A Study of Schottky Contacts on Indium-Phosphide. *Journal of Applied Physics*, 54(9):5199–5205, 1983.

[88] V. G. Weizer and N. S. Fatemi. The Influence of Interstitial Ga and Interfacial Au2p3 on the Electrical and Metallurgical Behavior of Au-Contacted Iii-V-Semiconductors. *Journal of Applied Physics*, 69(12):8253–8260, 1991.

[89] M. Vanwolleghem, P. Gogol, P. Beauvillain, W. Van Parys, and R. Baets. Design and optimization of a monolithically integratable InP-based optical waveguide isolator. *Journal of the Optical Society of America B-Optical Physics*, 24(1):94–105, 2007.

[90] M. Mehta, D. Feezell, D. A. Buell, A. W. Jackson, L. A. Coldren, and J. E. Bowers. Electrical design optimization of single-mode tunnel-junction-based long-wavelength VCSELs. *IEEE Journal of Quantum Electronics*, 42(7-8):675–682, 2006.

[91] T. A. Demassa and D. P. Knott. The prediction of tunnel diode voltage-current characteristics. *Solid-State Electronics*, 13(2):131–138, 1970.

[92] E. Kane. Theory of Tunneling. *Journal of Applied Physics* , 32(1):83–91, 1961.

[93] C. Monier, M. F. Vilela, I. Serdiukova, and A. Freundlich. Band discontinuity in strained In(As,P)/InP heterostructures. *Applied Physics Letters*, 72(13):1587–1589, 1998.

[94] M. Irikawa, T. Ishikawa, T. Fukushima, H. Shimizu, A. Kasukawa, and K. Iga. Improved theory for carrier leakage and diffusion in multiquantum-well semiconductor lasers. *Japanese Journal of Applied Physics*, 39(4A):1730–1737, 2000.

[95] N. Tansu and L. J. Mawst. Current injection efficiency of InGaAsN quantum-well lasers. *Journal of Applied Physics*, 97(5):–, 2005.

[96] J. Piprek, P. Abraham, and J. E. Bowers. Self-consistent analysis of high-temperature effects on InGaAsP/InP lasers. *Compound Semiconductors 1999*, (166):379–382, 2000.

[97] J. Piprek, P. Abraham, and J. E. Bowers. Carrier nonuniformity effects on the internal efficiency of multiquantum-well lasers. *Applied Physics Letters*, 74(4):489–491, 1999.

[98] R. Nagarajan, M. Ishikawa, T. Fukushima, R. S. Geels, and J. E. Bowers. High-Speed Quantum-Well Lasers and Carrier Transport Effects. *IEEE Journal of Quantum Electronics*, 28(10):1990–2008, 1992.

[99] J. Boucart, C. Starck, F. Gaborit, A. Plais, N. Bouche, E. Derouin, J. C. Remy, J. Bonnet-Gamard, L. Goldstein, C. Fortin, D. Carpentier, P. Salet, F. Brillouet, and J. Jacquet. Metamorphic DBR and tunnel-junction injection: A CW RT monolithic long-wavelength VCSEL. *IEEE Journal of Selected Topics in Quantum Electronics*, 5(3):520–529, 1999.

[100] M. Ortsiefer, S. Baydar, K. Windhorn, G. Bohm, J. Rosskopf, R. Shau, E. Ronneberg, W. Hofmann, and M. C. Amann. 2.5-mW single-mode operation of 1.55-mu m buried tunnel junction VCSELs. *IEEE Photonics Technology Letters*, 17(8):1596–1598, 2005.

[101] O. Painter, J. Vuckovic, and A. Scherer. Defect modes of a two-dimensional photonic crystal in an optically thin dielectric slab. *Journal of the Optical Society of America B-Optical Physics*, 16(2):275–285, 1999.

[102] S. H. Kwon, H. Y. Ryu, G. H. Kim, Y. H. Lee, and S. B. Kim. Photonic bandedge lasers in two-dimensional square-lattice photonic crystal slabs. *Applied Physics Letters*, 83(19):3870–3872, 2003.

[103] L. Raffaele, R. M. De La Rue, J. S. Roberts, and T. E. Krauss. Edge-emitting semiconductor microlasers with ultrashort-cavity and dry-etched high-reflectivity photonic microstructure mirrors. *IEEE Photonics Technology Letters*, 13(3):176–178, 2001.

[104] M. Ariga, Y. Sekido, A. Sakai, T. Baba, A. Matsutani, F. Koyama, and K. Iga. Low threshold GaInAsP lasers with semiconductor/air distributed Bragg reflector fabricated by inductively coupled plasma etching. *Japanese Journal of Applied Physics*, 39(6A):3406–3409, 2000.

[105] T. Baba, M. Hamasaki, N. Watanabe, P. Kaewplung, A. Matsutani, T. Mukaihara, F. Koyama, and K. Iga. A novel short-cavity laser with deep-grating distributed Bragg reflectors. *Japanese Journal of Applied Physics*, 35(2B):1390–1394, 1996.

[106] M. M. Raj, J. Wiedmann, Y. Saka, H. Yasumoto, and S. Arai. 1.5 mu m wavelength DBR lasers consisting of 3 lambda/4-semiconductor and 3 lambda/4-groove buried with benzocyclobutene. *Electronics Letters*, 35(16):1335–1337, 1999.

[107] T. Asano, B. S. Song, and S. Noda. Analysis of the experimental Q factors (similar to 1 million) of photonic crystal nanocavities. *Optics Express*, 14(5):1996–2002, 2006.

[108] S. Nojima. Optical-gain enhancement in two-dimensional active photonic crystals. *Journal of Applied Physics*, 90(2):545–551, 2001.

[109] K. Sakoda. Enhanced light amplification due to group-velocity anomaly peculiar to two- and three-dimensional photonic crystals. *Optics Express*, 4(5):167–176, 1999.

[110] J. Van Campenhout, P. Bienstman, and R. Baets. Band-edge lasing in gold-clad photonic-crystal membranes. *IEEE Journal on Selected Areas in Communications*, 23(7):1418–1423, 2005.

[111] H. G. Park, S. H. Kim, M. K. Seo, Y. G. Ju, S. B. Kim, and Y. H. Lee. Characteristics of electrically driven two-dimensional photonic crystal lasers. *IEEE Journal of Quantum Electronics*, 41(9):1131–1141, 2005.

[112] A. Sugitatsu and S. Noda. Proposal of line-defect-waveguide laser with transverse current injection structure in 2d photonic crystal slab. In *PECS-V*, page 230, Kyoto, Japan, 2004.

[113] S. Strauf, K. Hennessy, M. T. Rakher, Y. S. Choi, A. Badolato, L. C. Andreani, E. L. Hu, P. M. Petroff, and D. Bouwmeester. Self-tuned quantum dot gain in photonic crystal lasers. *Physical Review Letters*, 96(12):–, 2006.

[114] E. M. Purcell. Spontaneous emission probabilities at radio frequencies. *Phys. Rev.*, 69:681, 1946.

[115] D. Englund, D. Fattal, E. Waks, G. Solomon, B. Zhang, T. Nakaoka, Y. Arakawa, Y. Yamamoto, and J. Vuckovic. Controlling the spontaneous emission rate of single quantum dots in a two-dimensional photonic crystal. *Physical Review Letters*, 95(1):–, 2005.

[116] H. Altug, D. Englund, and J. Vuckovic. Ultrafast photonic crystal nanocavity laser. *Nature Physics*, 2(7):484–488, 2006.

[117] G. Bjork and Y. Yamamoto. Analysis of Semiconductor Microcavity Lasers Using Rate-Equations. *IEEE Journal of Quantum Electronics*, 27(11):2386–2396, 1991.

[118] T. Baba. Photonic crystals and microdisk cavities based on GaInAsP-InP system. *IEEE Journal of Selected Topics in Quantum Electronics*, 3(3):808–830, 1997.

[119] N. C. Frateschi and A. F. J. Levi. Resonant Modes and Laser Spectrum of Microdisk Lasers. *Applied Physics Letters*, 66(22):2932–2934, 1995.

[120] A. Morand, K. Phan-Huy, Y. Desieres, and P. Benech. Analytical study of the microdisk's resonant modes coupling with a waveguide based on the perturbation theory. *Journal of Lightwave Technology*, 22(3):827–832, 2004.

[121] E. I. Smotrova, A. I. Nosich, T. M. Benson, and P. Sewell. Cold-cavity thresholds of microdisks with uniform and nonuniform gain: Quasi-3-D modeling with accurate 2-D analysis. *IEEE Journal of Selected Topics in Quantum Electronics*, 11(5):1135–1142, 2005.

[122] A. Farjadpour, D. Roundy, A. Rodriguez, M. Ibanescu, P. Bermel, J. D. Joannopoulos, S. G. Johnson, and G. W. Burr. Improving accuracy by subpixel smoothing in the finite-difference time domain. *Optics Letters*, 31(20):2972–2974, 2006.

[123] P. J. A. Thijs, L. F. Tiemeijer, P. I. Kuindersma, J. J. M. Binsma, and T. Vandongen. High-Performance 1.5 Micro-M Wavelength Ingaas-Ingaasp Strained Quantum-Well Lasers and Amplifiers. *IEEE Journal of Quantum Electronics*, 27(6):1426–1439, 1991.

[124] P. Bienstman and R. Baets. Optical modelling of photonic crystals and VCSELs using eigenmode expansion and perfectly matched layers. *Optical and Quantum Electronics*, 33(4-5):327–341, 2001.

[125] T. P. Pearsall. *Properties, Processing and Applications of Indium Phosphide*. EMIS datareview. IEE Publishing, London, 2000.

[126] M. G. Burzo, P. L. Komarov, and P. E. Raad. Thermal transport properties of gold-covered thin-film silicon dioxide. *IEEE Transactions on Components and Packaging Technologies*, 26(1):80–88, 2003.

[127] G. Chen and P. Hui. Thermal conductivities of evaporated gold films on silicon and glass. *Applied Physics Letters*, 74(20):2942–2944, 1999.

[128] S. M. K. Thiyagarajan, A. F. J. Levi, C. K. Lin, I. Kim, P. D. Dapkus, and S. J. Pearton. Continuous room-temperature operation of optically pumped InGaAs/InGaAsP microdisk lasers. *Electronics Letters*, 34(24):2333–2334, 1998.

[129] S. M. Lee, D. G. Cahill, and T. H. Allen. Thermal-Conductivity of Sputtered Oxide-Films. *Physical Review B*, 52(1):253–257, 1995.

[130] M. Fujita, A. Sakai, and T. Baba. Ultrasmall and ultralow threshold GaInAsP-InP microdisk injection lasers: Design, fabrication, lasing characteristics, and spontaneous emission factor. *IEEE Journal of Selected Topics in Quantum Electronics*, 5(3):673–681, 1999.

[131] R. S. Tucker and D. J. Pope. Circuit Modeling of the Effect of Diffusion on Damping in a Narrow-Stripe Semiconductor-Laser. *IEEE Journal of Quantum Electronics*, 19(7):1179–1183, 1983.

[132] N. Chinone, K. Aiki, M. Nakamura, and R. Ito. Effects of Lateral Mode and Carrier Density Profile on Dynamic Behaviors of Semiconductor-Lasers. *IEEE Journal of Quantum Electronics*, 14(8):625–631, 1978.

[133] J. J. Morikuni, P. V. Mena, A. V. Harton, K. W. Wyatt, and S. M. Kang. Spatially independent VCSEL models for the simulation of diffusive turn-off transients. *Journal of Lightwave Technology*, 17(1):95–102, 1999.

[134] S. M. K. Thiyagarajan and A. F. J. Levi. Dynamic behavior of scaled microdisk lasers. *Solid-State Electronics*, 45(10):1821–1826, 2001.

[135] W. Bogaerts. *Nanophotonic Waveguides and Photonic Crystals in Silicon-on-Insulator*. Phd thesis, Ghent University, 2004.

[136] W. Bogaerts, R. Baets, P. Dumon, V. Wiaux, S. Beckx, D. Taillaert, B. Luyssaert, J. Van Campenhout, P. Bienstman, and D. Van Thourhout. Nanophotonic waveguides in silicon-on-insulator fabricated with CMOS technology. *Journal of Lightwave Technology*, 23(1):401–412, 2005.

[137] M. Quirk and J. Serda. *Semiconductor manufacturing technology*. Prentice-Hall, Upper Saddle River, 2001.

[138] Y. J. Seo. Oxide-chemical mechanical polishing characteristics using silica slurry retreated by mixing of original and used slurry. *Microelectronic Engineering*, 77(3-4):263–269, 2005.

[139] C. S. Tan, K. N. Chen, A. Fan, and R. Reif. Low-temperature direct CVD oxides to thermal oxide wafer bonding in silicon layer transfer. *Electrochemical and Solid State Letters*, 8(1):G1–G4, 2005.

[140] J. Brouckaert, G. Roelkens, D. Van Thourhout, and R. Baets. Thin-film III-V photodetectors integrated on silicon-on-insulator photonic ICs. *Journal of Lightwave Technology*, 25(4):1053–1060, 2007.

[141] V. G. Weizer and N. S. Fatemi. Simple, Extremely Low Resistance Contact System to N-Inp That Does Not Exhibit Metal-Semiconductor Intermixing during Sintering. *Applied Physics Letters*, 62(21):2731–2733, 1993.

[142] P. R. Romeo, J. Van Campenhout, P. Regreny, A. Kazmierczak, C. Seassal, X. Letartre, G. Hollinger, D. Van Thourhout, R. Baets, M. Fedeli, and L. Di Cioccio. Heterogeneous integration of electrically driven microdisk based laser sources for optical interconnects and photonic ICs. *Optics Express*, 14(9):3864–3871, 2006.

[143] J. Van Campenhout, P. Rojo-Romeo, D. Van Thourhout, C. Seassal, P. Regreny, L. Di Cioccio, J. M. Fedeli, and R. Baets. Thermal characterization of electrically injected thin-film InGaAsP microdisk lasers on Si. *Journal of Lightwave Technology*, 25(6):1543–1548, 2007.

[144] M. Sorel, G. Giuliani, A. Scire, R. Miglierina, S. Donati, and P. J. R. Laybourn. Operating regimes of GaAs-AlGaAs semiconductor ring lasers: Experiment and model. *IEEE Journal of Quantum Electronics*, 39(10):1187–1195, 2003.

[145] J. Van Campenhout, P. Rojo-Romeo, D. Van Thourhout, C. Seassal, P. Regreny, L. Di Cioccio, J. M. Fedeli, C. Lagahe, and R. Baets. Electrically pumped InP-based microdisk lasers integrated with a nanophotonic silicon-on-Insulator waveguide circuit. *Optics Express*, 15(11):6744–6749, 2007.